Resolution Improvement in Multidimensional Nuclear Magnetic Resonance Spectroscopy of Proteins

Luminita Duma

N° d'ordre : 287   Année 2004
N° attribué par la bibliothèque : 04ENSL0 287

<div align="center">

ÉCOLE NORMALE SUPÉRIEURE DE LYON
Laboratoire de Chimie
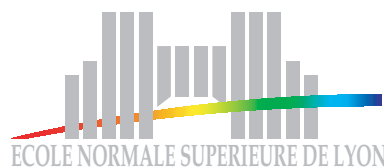
Thèse de doctorat

En vue d'obtenir le titre de :
Docteur de l'École Normale Supérieure de Lyon
Spécialité : Physique

Présentée et soutenue publiquement le 17 septembre 2004 par :

Luminita DUMA

</div>

<div align="center">

Amélioration de la Résolution dans la Résonance Magnétique Nucléaire Multidimensionnelle des Protéines

</div>

Directeur de thèse :   Lyndon EMSLEY

Après avis de :   Monsieur Geoffrey BODENHAUSEN, Membre/Rapporteur
Monsieur Hartmut OSCHKINAT, Membre/Rapporteur

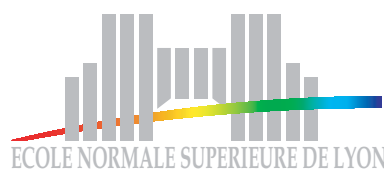*Devant la Commission d'examen formée de :*

Monsieur Geoffrey BODENHAUSEN, Membre/Rapporteur
Monsieur Yannick CRÉMILLIEUX, Membre
Monsieur Lyndon EMSLEY, Membre
Monsieur Alain MILON, Membre
Monsieur Hartmut OSCHKINAT, Membre/Rapporteur

<div align="center">

Lyon, 2004

</div>

ÉCOLE NORMALE SUPÉRIEURE DE LYON
Chemistry Laboratory

Doctoral Thesis

For the degree of:
Doctor in Physics of the École Normale Supérieure de Lyon

Presented and defended the 17th of September 2004 by:

Luminita DUMA

Resolution Improvement in Multidimensional Nuclear Magnetic Resonance Spectroscopy of Proteins

Supervisor: *Lyndon EMSLEY*

After recommendation of: *Mr Geoffrey BODENHAUSEN, Member/Referee*
                            Mr Hartmut OSCHKINAT, Member/Referee

In front of the jury made up of:

                            Mr Geoffrey BODENHAUSEN, Member/Referee
                            Mr Yannick CRÉMILLIEUX, Member
                            Mr Lyndon EMSLEY, Member
                            Mr Alain MILON, Member
                            Mr Hartmut OSCHKINAT, Member/Referee

Lyon, 2004

Părinţilor mei.
À mes parents.
To my parents.

"The principle
of science, the definition, almost,
is the following: *The test of all knowledge
is experiment*. Experiment is the *sole judge* of sci-
entific "truth". But what is the source of knowledge?
Where do the laws that are to be tested come from? Exper-
iment, itself, helps to produce these laws, in the sense that it
gives us hints. But also needed is *imagination* to create from these
hints the great generalizations - to guess at the wonderful, simple,
but very strange patterns beneath them all, and then to experiment
to check again whether we have made the right guess... *Everything
is made of atoms*. That is the key hypothesis. The most important hy-
pothesis in all of biology, for example, is that *everything that animals
do, atoms do*. In other words, *there is nothing that living things do
that cannot be understood from the point of view that they are made
of atoms acting according to the laws of physics*. This was not
known from the beginning: it took some experimenting and
theorizing to suggest this hypothesis, but now it is accepted,
and it is the most useful theory for producing new ideas
in the field of biology." from "Six easy pieces. Es-
sentials of physics explained by its most
brilliant teacher" by Richard
P. Feynman

Contents

Introduction

The development of the magnetic resonance phenomenon originates in the concept of spin[1] as quantum mechanical property.[3,4] If the discovery of nuclear magnetic resonance (NMR) spectroscopy was identified with the independent works of the Purcell and Bloch groups in 1945,[5,6] its origin is undoubtedly based on the experiments which verified the original ideas of nuclear and electron spin. Indeed, developments like the interpretation of hyperfine spectral structures given by Pauli in 1924[7] and the application of atomic and molecular beams to nuclear magnetic moments and hyperfine structures measurements performed by Rabi[8] and Stern[9] largely contributed to the discovery of the NMR spectroscopy.

Soon after its discovery, NMR spectroscopy imposed itself as a powerful technique with applications in numerous fields. The impact of magnetic resonance on physics and chemistry was its ability to give detailed information about processes at atomic level. In fact, the technique originally developed into an important tool for chemistry research and became nowadays also a powerful method in biochemistry and biophysics for obtaining structure elucidation and molecular dynamics of complex systems like for example biomolecules[10] and polymers.[11] NMR is also widely used in medical imaging to diagnose different types of pathologies. Additionally, NMR has a variety of other applications: searching for oil or water, studying the composition and structure of various foods, testing wine adulteration, quantum computing, etc.

The exploitation of structural and dynamical properties by NMR requires high resolution and sensitivity in order to accurately interpret the NMR spectra. Due to the orientation dependence of the anisotropic magnetic interactions, the anisotropy is the major contribution to the broadening of the lineshapes. In liquid-state NMR, the spectra show sharp lines because of the averaging of the anisotropic interactions by the molecular tumbling of the molecules.[2,12,13] On the other hand, in the solid state, the anisotropic interactions are all retained in addition to the isotropic chemical shifts and indirect spin-spin couplings. For powder samples, the anisotropic interactions usually dominate the spectrum and depend on the orientation of the crystallites with respect to the external magnetic field.[11,12,14] Therefore, the spectra of powdered samples show broad lines which overlap each other whereas sharp lines in a liquid-like fashion can only be obtained for single crystals and oriented samples.[15,16] Narrow lines can however be obtained for solids by spinning the solid sample about an axis which forms an angle of 54.74° with the direction of the external magnetic field and which is referred to as the "magic angle".[17,18,19] The idea behind the magic-angle spinning is to average out the second-rank tensor interactions (i.e., chemical shift anisotropy (CSA), dipole-dipole (DD) interactions and a part of the quadrupole anisotropy). As the sample starts to rotate, the spin Hamiltonian becomes time dependent and spinning sidebands appear in the resulting spectrum.[20] When the spinning frequency exceeds the magnitude of the anisotropic interactions, these are averaged out and the intensity of the spinning sidebands is concentrated

---

[1]Even though getting a picture about the abstract concept of spin is very difficult, it is worth introducing the idea here. The entity called spin is a property of any elementary particle which possesses an intrinsic angular momentum (i.e., a spin) and is intimately linked to the particle itself.[1,2] The spin angular momentum confers a magnetic moment and therefore, for a non-zero spin angular momentum and in the presence of strong static magnetic field, the associated energy results in an ensemble of discrete values. Basically, the transitions between these nuclear spin energy levels give rise to the NMR phenomenon.

on the central line located at the position of the isotropic chemical shift.

The low sensitivity of nuclei with low gyromagnetic ratio like ^{13}C or ^{15}N, also called rare or insensitive spins, can be enhanced by using the magnetisation reservoir of the abundant spins (i.e., protons). The technique is called cross polarisation and consists in transferring magnetisation from sensitive spins to insensitive ones. In liquid-state NMR, polarisation transfer is driven by the J-coupling between abundant and rare nuclei. The polarisation transfer can be performed either by the INEPT (Insensitive Nuclei Enhanced by Polarisation Transfer) approach,[21,22] or by spin-locking the radio-frequency (rf) fields such that the Hartmann-Hahn[23] condition is satisfied. In solid-state NMR, the polarisation transfer is driven by the flip-flop terms of the dipolar interaction between sensitive and insensitive spins. Among the existing techniques proposed for increasing the sensitivity of rare nuclei in solid-state NMR, the most commonly used is Hartmann-Hahn cross polarisation in the rotating frame.[23] Further, at high-rotation frequencies, adiabatic-passage Hartmann-Hahn cross polarisation is expected to efficiently transfer the entire magnetisation of the sensitive spins to the insensitive ones.[24] It is worth pointing out that polarisation transfer from one spin species to another is an essential tool for spectral editing, double resonance experiments and multidimensional correlation spectroscopy. The magic-angle spinning technique is frequently used in combination with cross polarisation and powerful decoupling sequences[25,26] for improving both resolution and sensitivity of the spectra.

As mentioned above, lines in solid-state NMR spectra are often broad. Two distinct dynamic processes are responsible for this spectral broadening: first, incoherent processes induced by the stochastically fluctuating local magnetic fields (i.e., relaxation[27]), and second, coherent processes occuring essentially in rigid solids, such as chemical-shift dispersion. Since incoherent broadening is due to irreversible processes, it cannot be reduced by pulses. On the contrary, coherent broadening generated by coherent interactions can be eliminated by appropriate pulse sequences.[11] Chemical-shift anisotropy, chemical-shift dispersion as well as magnetic field inhomogeneity are characteristic examples of coherent broadening. The technique allowing to separate the two types of broadening is the spin-echo experiment.[28]

The present thesis is concerned with both solid-state and solution NMR spectroscopy. However, most of this work is focused on the investigation by solid-state NMR of fully ^{13}C-labelled compounds with the principal aim of presenting techniques devised for further improving the spectral resolution and sensitivity in multidimensional NMR of microcrystalline proteins. Resolution enhancement can be obtained by removing the J-coupling contribution responsible for the broadening of carbon lineshapes in fully ^{13}C-labelled biomolecular systems. Additionally, under high-spinning conditions, sensitivity enhancement can be performed in multidimensional correlation spectroscopy by using adiabatic polarisation transfer techniques.[29,30] The techniques introduced in the last part of this work are tailored for solution NMR and are the result of the research training I spent in the CERM Laboratory in Florence, Italy, in the framework of a Marie Curie fellowship.

The first chapter of this thesis presents and analyses in detail the experimental lineshapes of the carboxyl and methyl carbon resonances of fully ^{13}C-enriched L-Alanine observed at different sample-spinning frequencies and decoupling field strengths. Experimental results show that the effect of the decoupling power on the lineshape is modest while the sample spinning significantly influences the carbon lineshapes. Thus, for the carboxyl resonance, for example, the asymmetric lineshapes at low spinning frequency have a complex behaviour at intermediate spinning frequency before reaching the expected symmetry at high spinning frequencies. The complex lineshapes at intermediate spinning speeds were explained by the *joint effect* of off rotational resonance and coherent CSA-DD cross correlation. Whereas off rotational-resonance effects lead to complex lineshapes due to the splitting of some (i.e., $|\alpha\beta\rangle$, $|\beta\alpha\rangle$) energy levels, coherent CSA-DD cross correlation introduces either a differential intensity or a differential broadening of the J-multiplet components. The experimental conditions leading to such effects are explained and experimentally verified. The differential broadening expected for the two transitions of the methyl resonance was experimentally confirmed by using the state-selection IPAP approach[31,32] (described in detail in chapter 2). Additionally, we show by means of computer simulations that these effects are not restricted to the particular case of L-Alanine and can be present over a wide range of static magnetic fields.

The study of carbon lineshapes in fully enriched compounds and the differential broadening of the methyl doublet components lead us to spin-state-selective experiments. Spin-state selection in solid-state NMR will be illustrated in the chapter 2 using elements similar to that used in liquid-state NMR (i.e., S3E,[33] IPAP,[31,32] DIPSAP,[34] INADEQUATE-CR[35,36]). Therefore, using the IPAP selection filter, the transitions of all three carbon resonances of fully ^{13}C-labelled L-Alanine can be separated in different subspectra. The state-selection approach allows to remove the contribution of the J-coupling to the linewidth, thus improving the spectral resolution. The single-transition selection, with the IPAP filter[31,32] element, is illustrated for a wide range of magic-angle-spinning frequencies going from 6 to 35 kHz. The use of state-selection techniques implies the insertion of an additional block in the pulse sequence. Thus, the step preceding any implementation of the spin-state selection into a multidimensional experiment is the investigation of those experimental conditions susceptible to affect the sensitivity of state-selection techniques. We analysed the sensitivity losses due to the introduction of the spin-state-selective filter and found them to be acceptable.

Structural investigation of biomolecules by solid-state NMR spectroscopy demands high resolution and sensitivity. In uniformly ^{13}C-labelled biomolecular compounds, the ^{13}C - ^{13}C scalar couplings represent a significant contribution to the linewidth in magic-angle-spinning spectra. We mentioned previously, that the use of spin-state-selective techniques allows to remove the J-coupling contribution in simple 1D experiments. For large compounds however, multidimensional experiments have to be used in order to accurately assign the large number of resonances. We illustrate in chapter 3 that single-transition-selection techniques in combination with transition-selective transfer schemes are well suited for removing the J-induced broadening in multidimensional solid-state NMR correlation experiments of ^{13}C-labelled proteins. First, we show that single-transition selection removes the line broadening due to the C' - C$^\alpha$ scalar coupling in both direct and indirect dimensions of a 2D COCA correlation experiment recorded on a microcrystalline sample of uniformly [^{13}C - ^{15}N]-enriched Crh, a protein of 85 amino acids existing under the form of a dimer in the solid state. State selection and selective transfer can be further combined with homonuclear J-decoupling techniques[37] in order to obtain enhanced resolution in a 2D CACB correlation spectrum. Furthermore, the sensitivity of this kind of ^{13}C - ^{13}C correlation experiments can also be increased by using adiabatic polarisation transfer schemes[38] at fast MAS frequencies where their efficiency is optimised.

In the preceding chapters we show that useful inspiration for new solid-state NMR experiments can come from liquid-state NMR. New ideas can also come from other disciplines, not really concerned with magnetic resonance.[39] Solution NMR can equally take advantage from the advances made in solid-state NMR. To illustrate this, we will show in the chapter 4 that heteronuclear assignment experiments, widely used in solid-state NMR for protein structure determination because of the low proton resolution, can be successfully applied in liquid state NMR as well. Therefore, the content of chapter 4 is concerned with two techniques designed for liquid-state NMR and based on the direct detection of carbon nuclei.

First, we present the CBCACO experiment tailored for intra-residue assignment of C$^\beta$, C$^\alpha$ and C' nuclei. Next, the CANCO experiment will be introduced, as a technique complementary to CBCACO and devised for sequential correlations. Among the various alternatives which are open for sequential transfer without involving protons, the ^{13}C-based approach starting on ^{13}C$^\alpha$, passing through ^{15}N, and ending on ^{13}C' takes advantage of the simultaneous presence of intra- and inter-residue J-couplings for achieving the optimum magnetisation transfer. The CANCO experiment provides increased sensitivity for inter-residue correlations which are privileged with respect to intra-residue ones. The feasibility of CBCACO and CANCO experiments is demonstrated with uniformly [^{15}N, ^{13}C] - labelled oncomodulin, a protein of 109 residues. These techniques are very attractive for the systems where the TROSY[40] effects are absent or the broadening due to the fast ^{1}H transverse nuclear spin relaxation cannot be recovered by using the TROSY approach. Additionally, these ^{13}C direct detection approaches could be useful for the investigation of paramagnetic proteins which cannot be deuterated and for which the contribution of the paramagnetic center to the line broadening renders the ^{1}H signals undetectable in a wide sphere around the metal ion.

Chapter 5 will tackle, from a theoretical point of view, the spin-echo J-modulation in magic-angle-

spinning solids. Most of the experiments presented in chapters 1-4 are based on the idea that pure J-modulation is present during a τ - π - τ echo sequence. However, theoretically it is not obvious that one can discard the dipolar and CSA contributions. The theory of J-induced spin-echo modulation to be presented in this chapter allowed us to derive a set of modulation regimes which apply under different experimental conditions. In most cases, the dominant spin-echo modulation frequency is exactly equal to the J-coupling. Interestingly, the chemical-shift anisotropies and dipolar couplings tend to stabilise the J-modulation, rather than obscuring it. The theoretical conclusions are supported by numerical simulations and experimental results obtained for three representative samples containing ^{13}C spin pairs.

"... ne fût-ce que pour vous en donner une idée!"

Stephane Mallarmé, Villiers

Carbon-13 lineshapes in solid-state NMR of labelled compounds. Coherent CSA-DD cross-correlation effects.

1.1 Introduction

In the past several years, significant advances have been made in multidimensional solid-state nuclear-magnetic-resonance spectroscopy. Much effort has been focused on developing new techniques to study large molecular systems like proteins in non-oriented environment.[41, 42, 43, 44, 45, 46, 47] This is mainly the result of technical improvement in high magnetic field, radio-frequency fields, magic-angle spinning, and sample preparation techniques. With these tools, in combination with sophisticated pulse sequences for decoupling[25, 26, 48, 49] and/or recoupling[50, 51, 52, 53, 54, 55, 56, 57, 58] different interactions, a resonance assignment approach similar to that done in liquid-state NMR is being developed for the study of non-oriented biomolecules with the solid-state NMR techniques.[44, 46, 47] Most of the pulse sequences developed for this purpose are designed, as in solution NMR, for fully ^{13}C, ^{15}N-labelled molecules. The extensive use of ^{13}C labelling leads however to a broadening of the carbon lines due partly to the presence of the homonuclear J-couplings.

Apart from line broadening, the presence of the J-coupling in isotopically enriched biological compounds does not induce the expected multiplet structure, but rather unusual broadened and asymmetric lineshapes.[43] A simple illustration of this behaviour is provided in Figure 1.1 which shows expected and measured carbon resonances of L-Alanine. Since natural abundance of ^{13}C nuclei is only 1%, the appearance of the carbon spectrum of natural abundance L-Alanine is determined by singlet resonances, one for each distinct carbon nucleus. Uniform enrichment results in increased sensitivity but also, due to the presence of spin-spin coupling, in more complex spectra. The scalar interaction being symmetric in general, the schematic spectra for fully ^{13}C-enriched L-Alanine show symmetric multiplet structures. Due to the indirect interaction with the C$^\alpha$ nucleus, both C' and C$^\beta$ resonances are split into symmetric doublets. Furthermore, the four components of the C$^\alpha$ multiplet, a doublet of doublets, arise from simple combinations of distinct J-coupling to C' and C$^\beta$ nuclei. Contrary to what we whould expect to see, intriguing asymmetric lineshapes are experimentally observed for fully ^{13}C-enriched L-Alanine under magic-angle spinning. It is therefore important to have a good understanding of the different contributions causing these distorted and broadened lineshapes in solids because this could enable the development of new techniques for enhancing the resolution in solid-state NMR. In this chapter a detailed explanation of physical mechanisms leading to these lineshapes will be given.

Several effects, which have been described separately in literature, will be invoked to explain the observed lineshapes. Broadening of the lineshape in a powder pattern like fashion under MAS was already predicted in 1979 by Maricq and Waugh for homonuclear coupled spin systems.[20] Rotational-resonance effects[59, 60] where the sample spinning frequency matches the difference of isotropic chemical shift of both

nuclei must also be considered to explain complex lineshapes, even far from the exact rotational-resonance condition.[61, 62] Finally, the interplay of the dipole-dipole interaction and chemical-shift anisotropy tensors was shown to introduce an asymmetry in the intensity of the two peaks split by the isotropic J-coupling constant in a heteronuclear spin-1/2 pair system under slow sample spinning.[63] This kind of asymmetry was observed as well by Nakai and McDowell in homonuclear ^{31}P spin systems.[64]
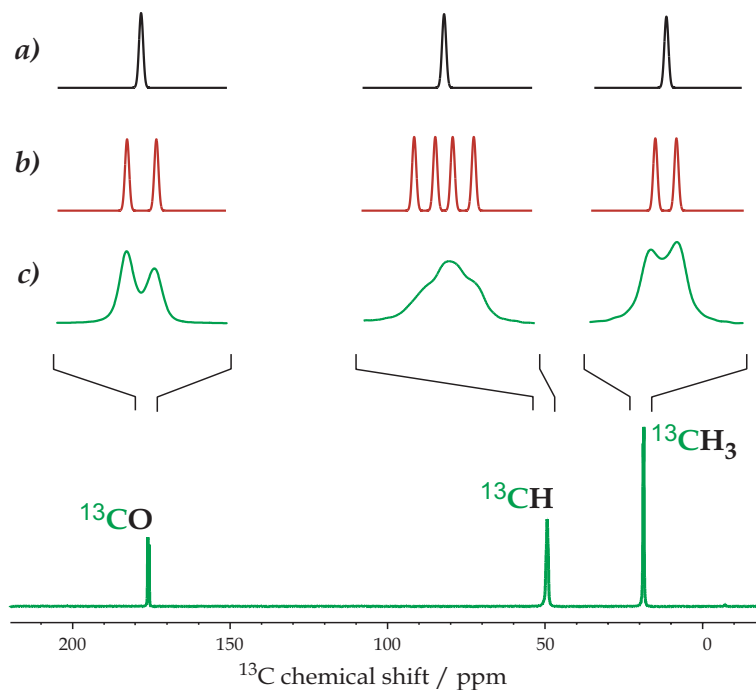

FIGURE 1.1: *Schematic and experimental spectra of L-Alanine. a) Appearance of carbon spectrum of natural abundance L-Alanine. b) Symmetric multiplet structures induced by the presence of J-coupling in fully ^{13}C-enriched L-Alanine. c) Specific carbon lineshapes observed experimentally for fully ^{13}C-enriched L-Alanine under MAS. The experimental spectrum was obtained with a standard CPMAS experiment.*

Our interest for carbon lineshapes was originally motivated by the observation of unusual asymmetric ^{13}C doublets in 10 % ^{13}C-enriched L-Alanine by Dimitri Sakellariou. The 10% ^{13}C-enriched L-Alanine sample was diluted by a factor of 10 into natural abundance alanine. This leads to an attenuation of the intermolecular ^{13}C - ^{13}C interactions while retaining the full intramolecular effects. The results obtained on the 10% ^{13}C-enriched sample show that the carbon resonances present also a non-negligible contribution from the naturale abundance L-Alanine. In order to eliminate this effect, we replaced the 10% ^{13}C-enriched sample by a fully ^{13}C-labelled L-Alanine. In theory, both intermolecular and intramolecular ^{13}C - ^{13}C interactions will give a contribution to the carbon resonances. However, results which will be presented latter show that, at least for the carboxyl resonance, the intermolecular contribution is negligible for this sample.

Herein, we will investigate and discuss in detail the specific experimental lineshapes observed for carboxyl and methyl carbons of fully ^{13}C-enriched L-Alanine under a range of experimental conditions. By means of computer simulations, we will show the relative impact of the different parts of the Hamiltonian on the spectral lineshape of a homonuclear coupled spin system. We will show that in the case of a carboxyl resonance, the observed asymmetric powder lineshape can be explained by the *joint effect* of off rotational resonance[61, 62] and a coherent cross-correlation effect between the chemical-shift anisotropy of the carboxyl and the dipole-dipole interaction between carboxyl and C^{α} carbons, leading to an asymmetry in intensity between the two components of the multiplet.[63, 64] For the methyl resonance in L-Alanine, a coherent cross-correlation effect is present as well, but is manifested this time by a *differential broadening* of the doublet components. The

differential broadening, determined initially by deconvolving the CPMAS carbon lineshapes, was experimentally confirmed using the In-Phase Anti-Phase selection filter,[31,32] which allows for individually probing the components of the carbon lineshapes. Finally, the conditions leading to such distorted carbon lineshapes in homonuclear coupled spin systems will be discussed.

In liquid-state NMR, cross correlation is a very well known phenomenon, which manifests itself in the relaxation behaviour of the spin system. The modulation by molecular motion of two different anisotropic spin interactions whose orientations are correlated (for example, the magnetic dipole-dipole interaction and the chemical-shift anisotropy) can give rise to this kind of relaxation process, generally called cross-correlated relaxation or cross correlation (for reviews about that subject, see the works of Brutscher[65] and Kumar *et al.*[66]). Such relaxation induced (incoherent) cross-correlation effects, which lead to a differential-line broadening of the J-multiplets, have also been seen in solids under magic-angle spinning for compounds showing extensive molecular motion like liquid crystals or highly mobile solid polymers.[67,68,69,70]

1.2 Experimental results for carboxyl and methyl resonances

The experiments shown in this section were all performed on a Bruker 500 Avance spectrometer (proton and carbon frequencies at 500.13 MHz and 125.76 MHz) equipped with a 2.5 mm double resonance CPMAS probehead. The 99 % ^{13}C-labelled L-Alanine powder sample was purchased from Eurisotop and used without further purification. The carbon spectrum was measured for different spinning (6, 7, 9, 12, 18, 21, 23, 28, 30, and 35 kHz) and decoupling (60, 100, and 160 kHz) frequencies. Attention was paid in choosing the MAS frequencies that none of the carboxyl and methyl rotational-resonance conditions were matched at the magnetic field used. The isotropic chemical-shift differences are 15.9 kHz between the COO$^-$ (C') and CH (C$^\alpha$), 19.8 kHz between the C' and CH$_3$ (C$^\beta$), and 3.9 kHz between the C$^\alpha$ and C$^\beta$ resonances (see FIGURE 1.2). The rotational-resonance (R^2) conditions are then expected at the following spinning frequencies:

$$\begin{cases} 15.9\,\text{kHz}\ (n=1), & 8.0\,\text{kHz}\ (n=2), & 5.3\,\text{kHz}\ (n=3) & \text{for the C' - C}^\alpha \text{ spin pair} \\ 19.8\,\text{kHz}\ (n=1), & 9.9\,\text{kHz}\ (n=2), & 6.6\,\text{kHz}\ (n=3) & \text{for the C' - C}^\beta \text{ spin pair} \\ 3.9\,\text{kHz}\ (n=1), & 1.95\,\text{kHz}\ (n=2), & 1.3\,\text{kHz}\ (n=3) & \text{for the C}^\beta \text{ - C}^\alpha \text{ spin pair} \end{cases} \qquad (1\text{-}1)$$
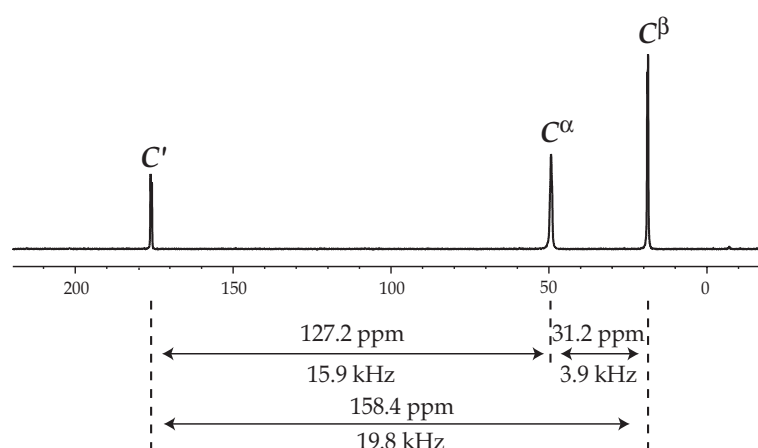
FIGURE 1.2: *Isotropic chemical-shift differences of carbon resonances of fully ^{13}C-enriched L-Alanine. The values in Hz were calculated for a corresponding static magnetic field of 11.8 T (i.e., 125 MHz ^{13}C Larmor frequency).*

All chosen rotation frequencies are at least 1.2 kHz off the $n = 1$ and 900 Hz off the $n = 2$ R^2 conditions. As the C'C$^\beta$ dipolar-coupling constant is much smaller than the C'C$^\alpha$ one, off rotational-resonance effects from dipolar recoupling of the carboxyl spin with the C$^\beta$ and vice-versa should be less important. The

carboxyl and methyl resonances are shown in FIGURE 1.3 and 1.4, respectively, for different sample rotation frequencies and decoupling field strengths.

Under high spinning speed and decoupling field, and well off rotational-resonance conditions, we expect the carboxyl and methyl resonances to be split into a symmetric doublet by the homonuclear J-coupling to the carbon C^α. Indeed, to zero order, the effect of the heteronuclear C-H dipole-dipole coupling is removed by both magic-angle spinning and decoupling, the heteronuclear C-H J-coupling is removed by decoupling, and the homonuclear carbon-carbon dipolar coupling is removed by MAS, as long as rotational-resonance conditions are avoided. The effect of the carboxyl CSA should also be removed by MAS. However, the spectra of FIGURES 1.3 and 1.4 show that the experimental carbon lineshape is far from the expected symmetric doublet, except for spinning speeds well above 25 kHz. The methyl CSA being smaller, the expected symmetric doublet is already observed at 18 kHz spinning frequency for the C^β resonance.

For the carboxyl resonance, below 9 kHz and above 20 kHz sample rotation frequency, the lineshape looks like a more or less asymmetric doublet, with two components of different intensity but same linewidth. This is especially marked at low spinning speeds. In the lower spinning regime, broadening of the doublet is observed for the exact $n = 3$ R^2 conditions at 5.3 and 6.6 kHz and $n = 2$ R^2 conditions at 8 kHz MAS, respectively. Examples of these broadened lineshapes observed for L-Alanine are given in FIGURE 1.5. Note that off rotational-resonance effects from those conditions are small and appear negligible at 6 and 7 kHz for the carboxyl resonance. At 9, 12 and 18 kHz MAS, we obtain a powder-pattern like line, with a different shape at each spinning speed. It is difficult to follow more closely the lineshape change between the different spinning speeds, as rotational-resonance conditions would then be close to match and their effects clearly dominate the lineshape. It is also noticeable that the center of gravity of the resonance moves slightly between 6 and 35 kHz; this isotropic chemical-shift change, observable in fully labelled compounds, is a known effect of off rotational-resonance conditions and is due to the interaction between non-secular components of the dipolar and Zeeman terms.[61,62]

The methyl lineshapes show a different behaviour, principally due to the smaller CSA and different rotational-resonance conditions. The methyl lineshapes are slightly affected by the off rotational-resonance effects of the $n = 3$ R^2 condition between methyl and carboxyl nuclei. Thus, broad lineshapes are observed between 5.3 and 8 kHz MAS (see FIGURE 1.5). We can see in FIGURE 1.4 that, between 9 and 18 kHz rotation frequency, the lineshapes look like asymmetric doublets. As expected, the isotropic doublets appear at spinning frequencies smaller than for carboxyl resonance, as the magnitude of the methyl anisotropy is smaller than that of carboxyl nucleus. The shift of the center of gravity of the methyl resonance is less pronounced due to the smaller rotational-resonance effects.

The influence of the decoupling power on the lineshape is less drastic for both carboxyl and methyl resonances. Reduction of the decoupling power introduces a broadening of the lines due to less efficient proton decoupling, but the shape of the carbon line is not essentially modified. With a proton nutation frequency of 60 kHz, the decoupling is not effective any more for spinning speeds higher than 20 kHz, reflecting probably the combined effect of less efficient proton decoupling and the onset of rotary-resonance recoupling effect expected at 30 kHz MAS.[75,76]

The effects on the lineshape that we describe here with the example of the carboxyl and methyl resonances of L-Alanine is a general problem in fully ^{13}C-labelled samples. Unexpected lineshapes were indeed also observed in carbon spectra of fully isotopically enriched proteins.[43]

1.3   Theoretical aspects and simulations

The theory concerning the different aspects considered in this contribution has already been treated in the literature individually. However, in order to separate the different contributions to the lineshape and understand the experimental observations, we will recall here a broad outline of the theory.

Proton nutation frequency / kHz
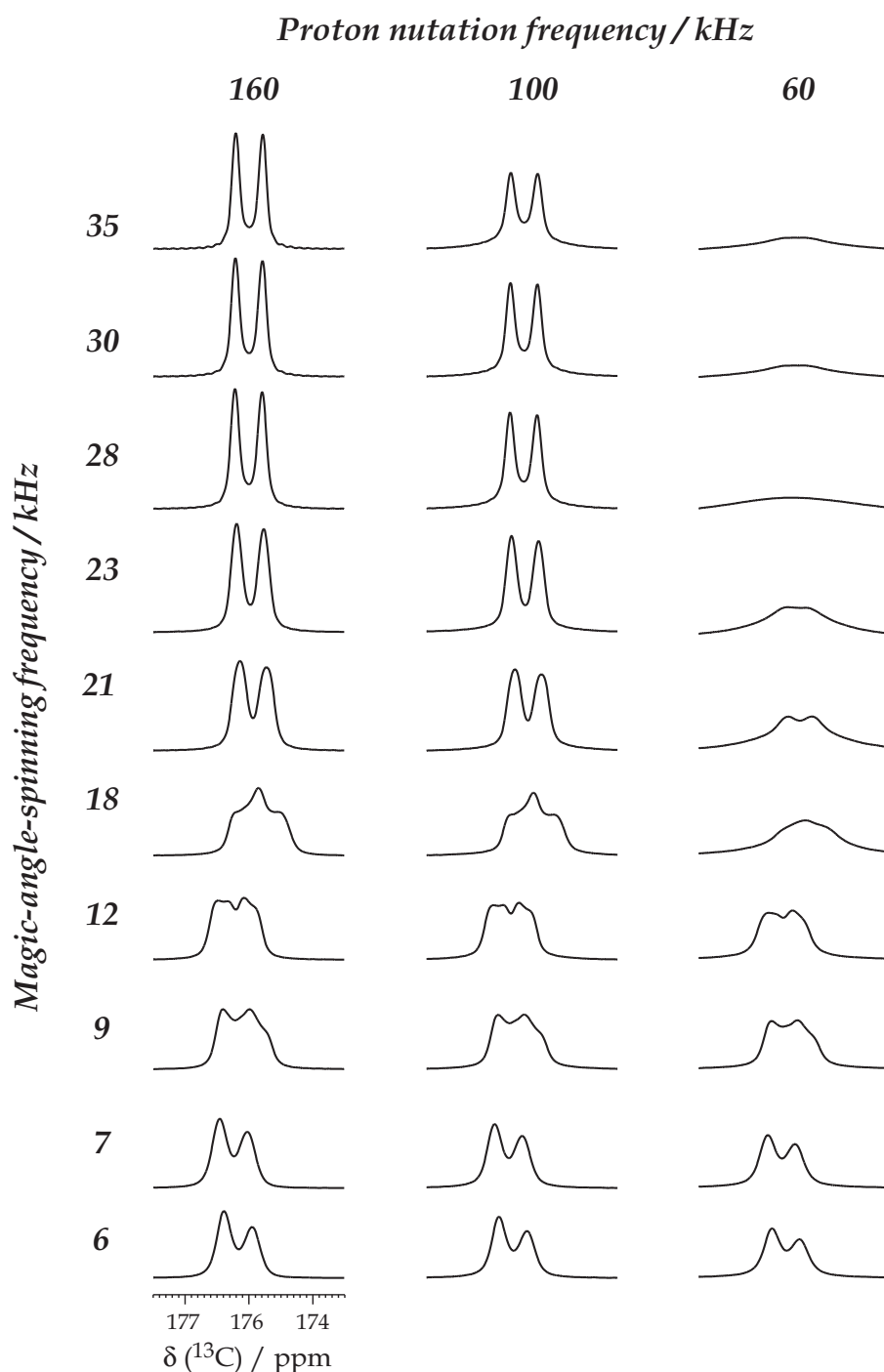
FIGURE 1.3: *Experimental carboxyl lineshapes for 99 % ^{13}C enriched L-Alanine at different spinning speeds and decoupling field strengths. The carbon spectra were obtained using the standard cross-polarisation technique, with a ramped spin-lock on the proton channel to broaden the Hartmann-Hahn condition.[23, 24, 71, 72, 73] The contact time was set to 1 ms. Detection was performed under TPPM decoupling.[74] To ensure the best resolution, the acquisition time was set to 60 ms at all spinning rates, thus ensuring complete decay of the free induction decay (FID). No exponential line broadening was applied.*

We consider a model of an isolated spin-$1/2$ pair experiencing anisotropic chemical-shift interactions and interacting by a through-space dipole-dipole coupling and by a scalar J-coupling which is assumed to be isotropic. We also assume that interactions with heteronuclei such as protons are strongly suppressed by decoupling irradiation. The case of a static sample will be first considered. The nuclear spin Hamiltonian of a

Proton nutation frequency / kHz
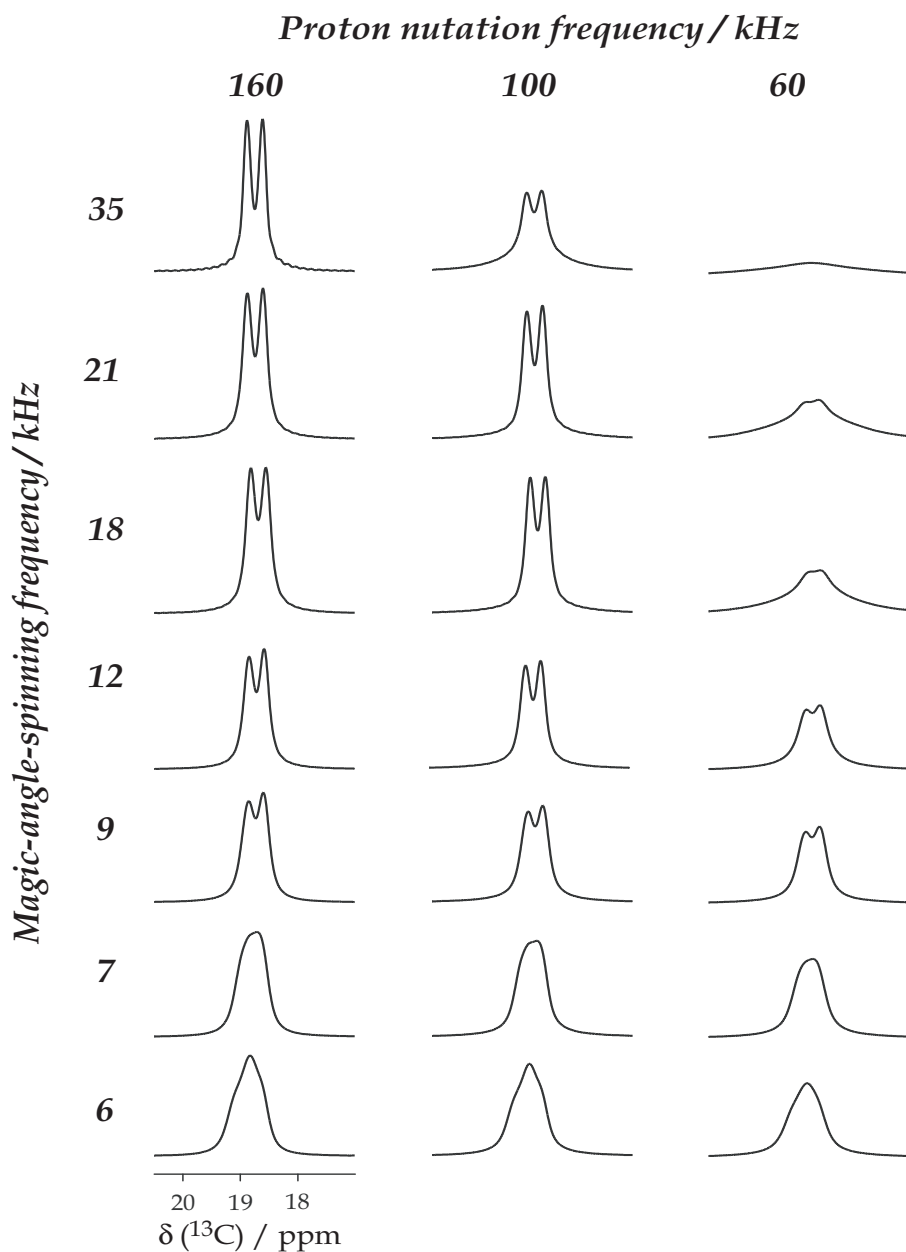
FIGURE 1.4: *Experimental methyl lineshapes for 99 % ^{13}C-enriched L-Alanine at different spinning speeds and decoupling field strengths. All experimental parameters are similar to those indicated in the legend of FIGURE 1.3.*

static homonuclear two-spin system, in the rotating frame of the Zeeman interaction, is given by the following expression:

$$\mathcal{H} = \mathcal{H}_{iso} + \mathcal{H}_{CSA} + \mathcal{H}_{DD} + \mathcal{H}_{J} \tag{1-2}$$

with $\mathcal{H}_{iso}$ the isotropic chemical shift of both spins I and S, $\mathcal{H}_{CSA}$ the anisotropic part of the chemical shift considered here only for the spin I, $\mathcal{H}_{DD}$ the dipole-dipole interaction between both spins, and $\mathcal{H}_{J}$ the scalar
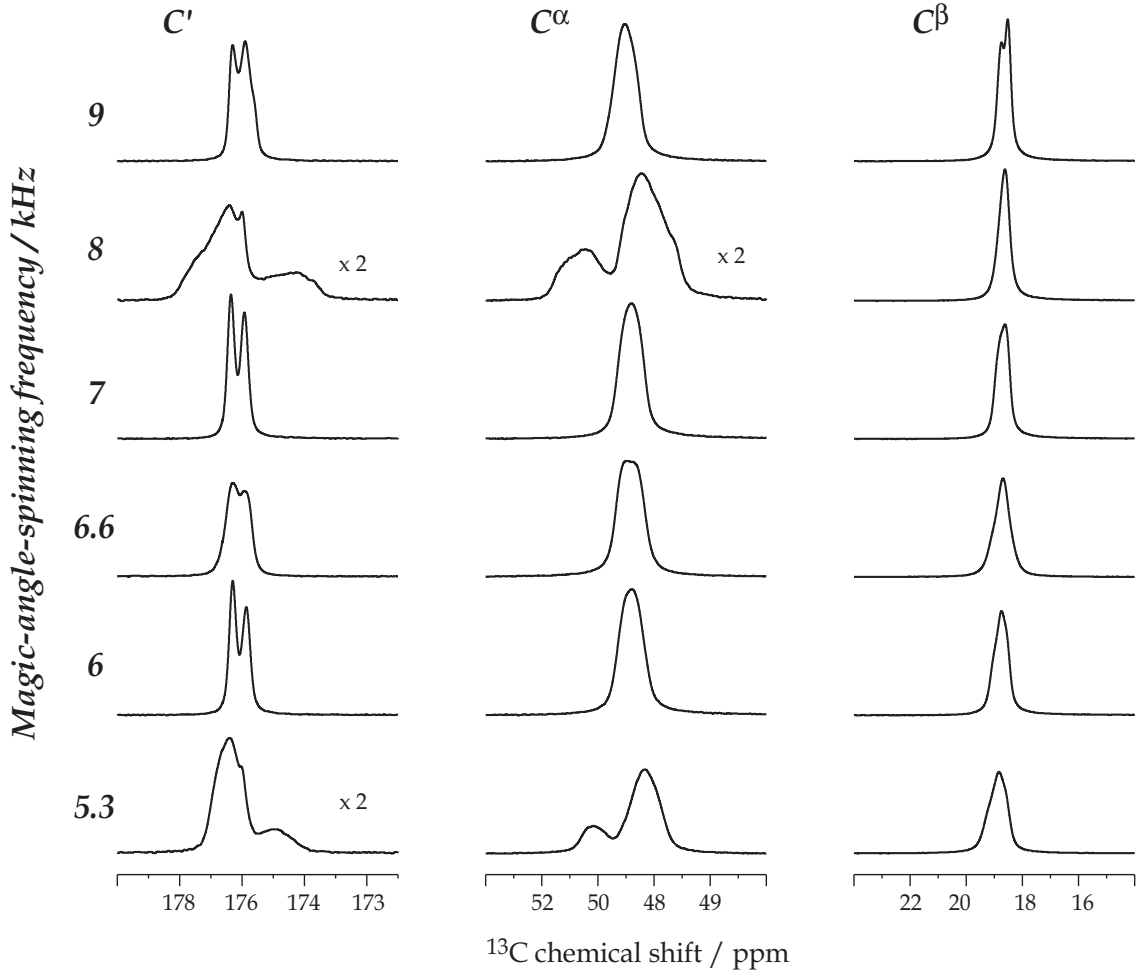
FIGURE 1.5: *Carbon lineshapes for spinning frequencies ranging from 5.3 kHz to 9 kHz. 5.3 and 8 kHz spinning frequencies represent the $n = 3$ and $n = 2$ C'C$^\alpha$ R^2 conditions whereas 6.6 kHz is the $n = 3$ C'C$^\beta$ R^2 condition. All experimental parameters are indicated in the legend of FIGURE 1.3.*

coupling. Their explicit expressions are:

$$
\begin{cases}
\mathcal{H}_{iso} &= \omega_{0I}I_z + \omega_{0S}S_z \\
\mathcal{H}_{CSA} &= \omega_{CSA}(\Omega)I_z \\
\mathcal{H}_{DD} &= \omega_{DD}(\Omega')(3I_zS_z - \mathbf{I}\cdot\mathbf{S}) = \omega_{DD}(\Omega')(2I_zS_z - I_xS_x - I_yS_y) \\
\mathcal{H}_J &= \pi J 2I_zS_z
\end{cases}
\tag{1-3}
$$

where Ω and Ω' represent the two sets of Euler angles connecting the principal axes system (PAS) of the CSA and DD tensors, respectively, to the crystallite orientation in the laboratory frame (LF). The relation between Ω and Ω' depends on the geometry of the spin system. The matrix representation of the Hamiltonian in the product basis is given by:

$$
\mathcal{H} = \begin{pmatrix}
\omega_{0I} + \omega_{0S} + \pi J + \omega_{CSA} + \omega_{DD} & 0 & 0 & 0 \\
0 & \omega_{0I} - \omega_{0S} - \pi J + \omega_{CSA} - \omega_{DD} & -\omega_{DD} & 0 \\
0 & -\omega_{DD} & -\omega_{0I} + \omega_{0S} - \pi J - \omega_{CSA} - \omega_{DD} & 0 \\
0 & 0 & 0 & -\omega_{0I} + \omega_{0S} + \pi J - \omega_{CSA} + \omega_{DD}
\end{pmatrix}
\tag{1-4}
$$

where the elements of the basis are: $|1\rangle = |\alpha,\ \alpha\rangle$, $|2\rangle = |\alpha,\ \beta\rangle$, $|3\rangle = |\beta,\ \alpha\rangle$ and $|4\rangle = |\beta,\ \beta\rangle$ the first symbol representing the state of the I spin and the second one of the S spin.

We consider now the case when the isotropic chemical-shift difference is larger than all other interactions ($\omega_{iso}^{\Delta} \gg \omega_k$; $k = CSA, DD, J$). This is for example always the case in heteronuclear spin systems in the high magnetic field approximation. In this case, the off-diagonal elements of this matrix can be considered as non-secular and can be neglected. The two single-quantum (SQ) transitions for the I spin appear therefore at the frequencies:

$$\begin{cases} \omega_{\alpha\alpha\to\beta\alpha} & = & \omega_{0I} + \pi J + \omega_{CSA}(\Omega) + \omega_{DD}(\Omega^{'}) \\ \omega_{\alpha\beta\to\beta\beta} & = & \omega_{0I} - \pi J + \omega_{CSA}(\Omega) - \omega_{DD}(\Omega^{'}) \end{cases} \tag{1-5}$$

The two transitions separated by the J-coupling have a powder lineshape due to the orientation-dependent contributions of the CSA and DD terms. However, due to the fixed relative orientation of both tensors, the contribution of the two terms are "added" for one transition and "subtracted" for the other one. This leads to powder patterns of different shapes and widths for the two transitions of the I spin. The difference in width of the powder patterns depends on the relative size and orientation of the CSA and the DD tensors. A detailed analysis of the pattern of both transitions was given by Zilm and Grant.[77]

In a homonuclear spin system, the off-diagonal elements of Eq. 1-4 lead to a change in the powder pattern of the line, but the relative contribution of the CSA and DD terms are still added for one transition and subtracted for the other, leading once again to components of different widths. This is illustrated in FIGURE 1.6 where simulations of the I spin transitions in the static case are shown. An isolated two-spin system interacting by direct DD and indirect scalar couplings and with the detected spin experiencing anisotropic chemical-shift interactions was considered for these simulations.

In FIGURE 1.6a the geometry of L-Alanine was considered with the I spin representing the carboxyl and the S spin the C^{α}. It is clear from this simulation that the first carboxyl transition $\alpha\alpha \to \beta\alpha$, e.g., with the C^{α} in α state, is broader than the second transition $\alpha\beta \to \beta\beta$ with C^{α} in β state. Since only the I spin signal is shown in FIGURE 1.6a for reasons of clarity, a small dispersive signal appears at the chemical shift of the S spin due to the mixing of the spin states by the off-diagonal elements of Eq. 1-4, which are not completely non-secular in this homonuclear spin system. In FIGURE 1.6b the I spin represents the C^{β} of L-Alanine coupled to the C^{α} (S spin). Here again, the difference in width of both components is evident, whereby the relative orientation of the C^{β} CSA and the dipole-dipole coupling lead this time to a broader pattern for the transition with C^{α} in β state ($\alpha\beta \to \beta\beta$). The geometry of all the tensors with respect to the molecular frame (MF) is given in FIGURE 1.6c using the SIMMOL package.[80] The exact values considered for the different CSA and DD tensors were taken or calculated from the works of Naito et al.,[81] Ye et al.[82] and Levitt et al.,[83] and are summarized in TABLE 1.1 (see Appendix A on page 101 for details on extracting CSA and DD orientational parameters from direction cosines).

In the static case, the correlated effect of the CSA and DD tensors appears directly to zero order in the Hamiltonian, leading for the I spin to two transitions of different shape. The introduction of sample spinning will affect both transitions. The Hamiltonian of Eq. 1-2 becomes in this case time-dependent:

$$\mathcal{H}(t) = \mathcal{H}_{iso} + \mathcal{H}_{CSA}(\Omega, t) + \mathcal{H}_{DD}(\Omega^{'}, t) + \mathcal{H}_J \tag{1-6}$$

with the time-dependent terms:

$$\begin{cases} \mathcal{H}_{CSA}(\Omega, t) & = & \omega_{CSA}(\Omega, t) I_z \\ \mathcal{H}_{DD}(\Omega^{'}, t) & = & \omega_{DD}(\Omega^{'}, t)(2 I_z S_z - I_x S_x - I_y S_y) \end{cases} \tag{1-7}$$

In the following sections we will give a detailed analysis of two different cases.
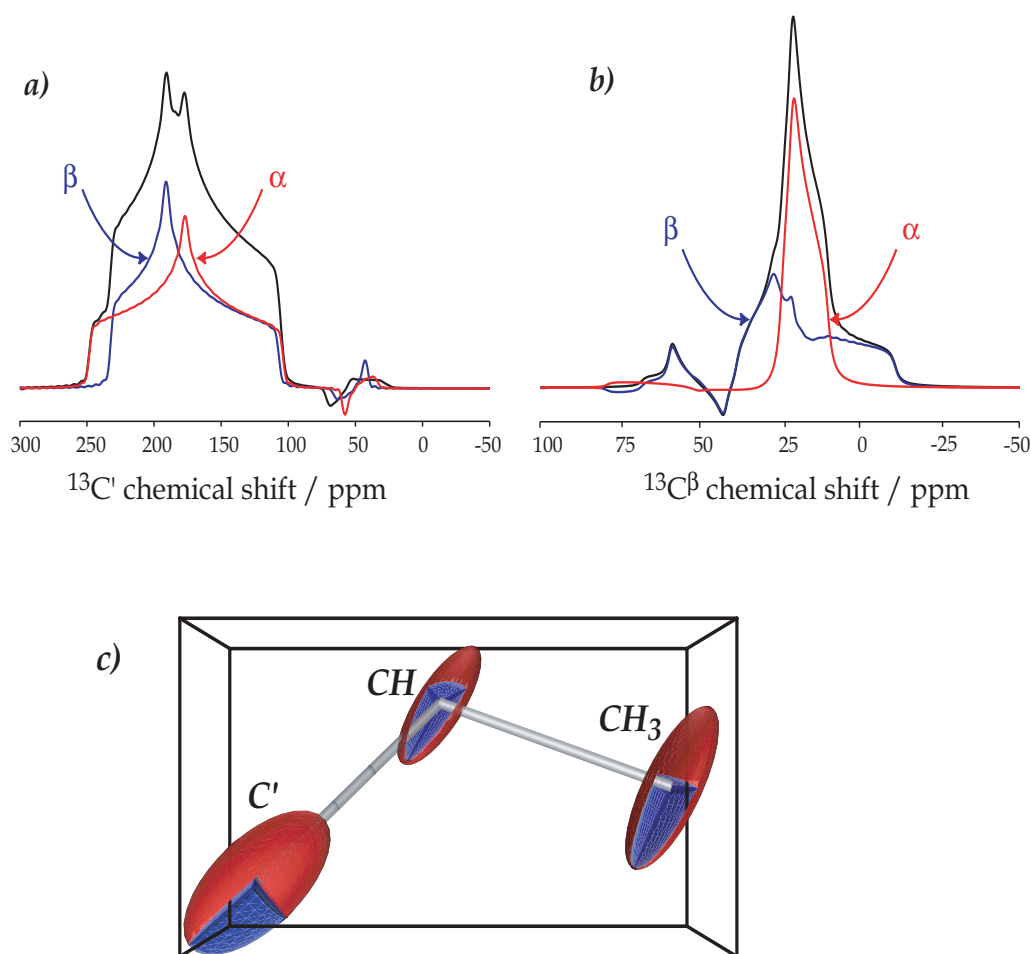
FIGURE 1.6: *Simulated static powder pattern for the (a) C' and (b) C^β in L-Alanine. For the carboxyl, the transition $\alpha\alpha \rightarrow \beta\alpha$, e.g., with C^α in α state, is broader than the transition $\alpha\beta \rightarrow \beta\beta$ with C^α in β state. Regarding the methyl, the transition $\alpha\alpha \rightarrow \beta\alpha$ is narrower than the transition $\alpha\beta \rightarrow \beta\beta$. For both simulations, the spin system was reduced to two spins under the Hamiltonian of Eqs. 1-2, 1-3, the S spin being in both cases the C^α nucleus. The different parameters for the CSA and DD tensors, as well as their relative orientation are given in TABLE 1.1. In both cases, the CSA of the S spin was neglected. The $^1J_{C'C^\alpha}$ and $^1J_{C^\beta C^\alpha}$ scalar couplings were set to 54 and 34 Hz, respectively. A planar grid powder average over 1000000 different crystal orientations was performed to obtain the simulated spectra.[78] These simulations were obtained with the Matlab[79] software using standard techniques.[78] (c) Geometry of the CSA and DD tensors with respect to the molecular frame, for all carbons in L-Alanine. This picture was obtained with the SIMMOL package.[80]*

The inhomogeneous case

If the secular approximation made above is valid, the dipolar contribution in Eq. 1-7 can be reduced to its $2I_zS_z$ component, and the Hamiltonian then commutes with itself at any time during the rotation. In such a situation, the spin system is considered to behave *inhomogeneously* in the sense of Maricq and Waugh.[20] Spinning at the magic angle will lead to a perfect refocusing of the anisotropic part of the Hamiltonian at integer multiples of the rotor period, thus leading to two well-resolved spinning sideband manifolds, one for each transition of the I spin. The static powder pattern of these two transitions being however different from each other, with for instance different widths, the sideband manifolds for each transition will be different. An asymmetry in intensity between both central transitions will therefore normally be present for spinning speeds lower than the static transition width, with the most intense line belonging to the transition with the narrowest static pattern. This was indeed already observed for an heteronuclear spin system by Harris *et al.*,[63] where both sideband manifolds corresponding to the two transitions of a carbon coupled to a phosphorus had different

TABLE 1.1: *Parameters for the CSA and DD tensors, and J-coupling constants of L-Alanine.*

CSA parameters	^{13}C'	^{13}C$^{\alpha}$	^{13}C$^{\beta}$
$\delta_{iso}{}^{a}$	176 ppm	50 ppm	19 ppm
$\delta_{aniso}{}^{a}$	- 70 ppm	- 20 ppm	- 12 ppm
η^{a}	0.78	0.32	1.0
$\Omega_{PM}{}^{b}$	$\{11.7°, 86.3°, - 53°\}$	$\{81.7°, 24.5°, 29.1°\}$	$\{52.9°, 77.4°, 140.5°\}$
DD parameters	^{13}C' - ^{13}C$^{\alpha}$	^{13}C' - ^{13}C$^{\beta}$	^{13}C$^{\alpha}$ - ^{13}C$^{\beta}$
$d_{jk}/2\pi^{c}$	- 2092.5 Hz	- 474.76 Hz	- 2104.8 Hz
Ω'_{PM}	$\{0°, 21.5°, - 154°\}$	$\{0°, 46.6°, 160.4°\}$	$\{0°, 78.4°, 144.7°\}$
J parameters	^{13}C' - ^{13}C$^{\alpha}$	^{13}C' - ^{13}C$^{\beta}$	^{13}C$^{\alpha}$ - ^{13}C$^{\beta}$
$J_{jk}{}^{d}$	54 Hz	0 Hz	34 Hz

[a] The signs of frequencies are conform to that given by Levitt.[84] The isotropic chemical shift frequencies and the chemical-shift principal values were taken from the work of Ye *et al.*[82] with respect to TMS. The isotropic chemical shift, anisotropic chemical-shift frequency and asymmetry parameter are defined as $\delta_{iso} = (\delta_{xx} + \delta_{yy} + \delta_{zz})/3$, $\delta_{aniso} = \delta_{zz} - \delta_{iso}$ and $\eta = (\delta_{yy} - \delta_{xx})/\delta_{aniso}$. The chemical-shift principal values are ordered as $|\delta_{zz} - \delta_{iso}| \geq |\delta_{xx} - \delta_{iso}| \geq |\delta_{yy} - \delta_{iso}|$.

[b] The set of Euler angles specifies the relative orientations of the interaction principal axes (P) system of the tensor and the molecular reference frame (M) assumed here to coincide with the crystallographic reference frame.[83] The set of Euler angles was determined from the atomic parameters given in the work of Naito and coworkers.[81]

[c] Dipole-dipole coupling constant $d_{jk} = -\frac{\mu_0 \gamma^2 \hbar}{4\pi r_{jk}^3}$, with the internuclear distances r_{jk} taken from the paper of Simpson and Marsh.[85]

[d] The scalar coupling constants were measured on the liquid-state NMR spectrum of ^{13}C fully enriched L-Alanine.

intensities at slow spinning speeds, resulting directly from the difference in shape of the two transitions in the static case. It was also observed by Nakai and McDowell[64] in a homonuclear two-spin system with a large difference in isotropic chemical shifts (i.e., doubly labelled sodium acetate).

We see here in the case of the carboxyl of fully ^{13}C-enriched L-Alanine that this effect of coherent cross correlation between CSA and DD tensors can be seen in an amino acid as well. Indeed the chemical-shift difference between C' and C$^{\alpha}$ is large enough for this homonuclear two-spin system to behave inhomogeneously under MAS. FIGURE 1.7 shows a comparison between experimental and simulated carboxyl lineshapes of fully ^{13}C-labelled L-Alanine. The same two-spin C' - C$^{\alpha}$ system interacting by through-space dipole-dipole coupling and by a scalar J-coupling was considered as for the static simulations including only the C' CSA. The asymmetry in the line intensities of the doublet is very clear at 6 and 7 kHz MAS, and remarkably well predicted by the numerical simulations, despite the simple two-spin system approximation and the omission of the C$^{\alpha}$ CSA. Only at spinning speeds higher than the width of the static pattern (above 20 kHz), are the CSA-DD terms fully averaged and the whole spectral intensity concentrated in the centerband for each transition, thus leading to a symmetric doublet for the carboxyl resonance.

At intermediate spinning speeds, the lines are additionally broadened by so called off rotational-resonance effects. This broadening mechanism was extensively discussed by Levitt *et al.*[61] and Nakai and Mc-Dowell.[62] When the MAS spinning speed comes close to a rotational-resonance condition $|\omega_{0I} - \omega_{0S}| \cong n\omega_r$, with n a small integer, the non-secular time-dependent off diagonal elements of Eq. 1-4 contain a component
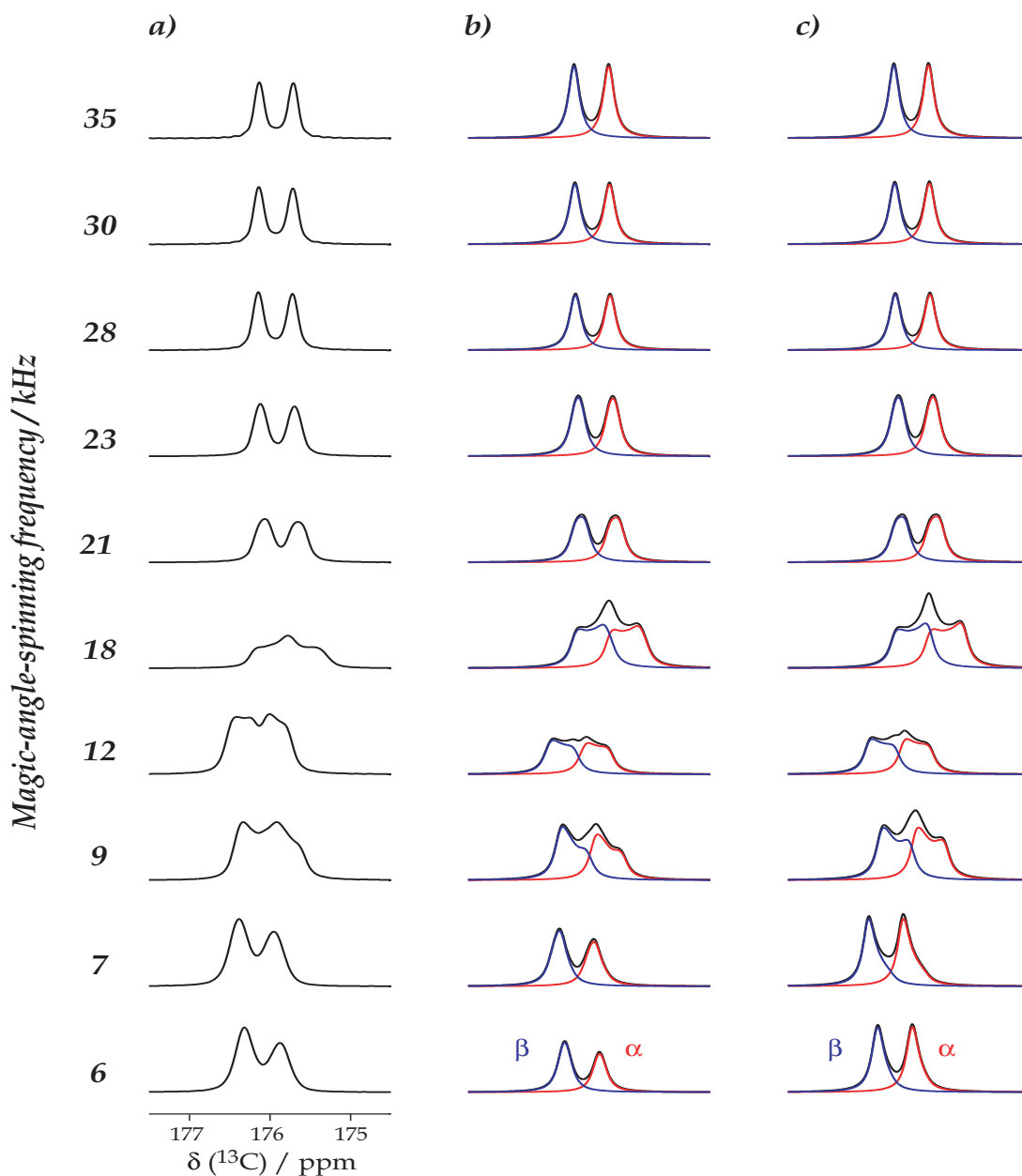
FIGURE 1.7: *Comparison of (a) the experimental lineshapes of the carboxyl resonance of L-Alanine at different spinning speeds with (b-c) numerical simulations. The experimental spectra are those measured at 160 kHz proton nutation frequency (see legend of FIGURE 1.3 for experimental details). For the simulations, the same spin system was considered as for the static simulation of FIGURE 1.6. In the simulations of column (c), the CSA part of the Hamiltonian ($\mathcal{H}_{CSA} = \omega_{CSA}(\Omega, t)I_z$) was omitted. For the simulated spectra, a line broadening of 24 Hz was applied prior to Fourier Transform. The powder average was performed using a set of 4180 molecular angles $\{\alpha_{MR}, \beta_{MR}\}$ generated by the ZCW algorithm[78, 86, 87, 88] and 15 evenly-spaced values for the third Euler angle γ_{MR}. The simulations were obtained with the NMR package SIMPSON[89] using standard techniques.[78]*

which starts to be resonant with the energy levels $|\alpha, \beta\rangle$ and $|\beta, \alpha\rangle$. This induces a splitting of each of these two levels into a pair of time-independent virtual states, leading to a splitting of all single-quantum (SQ) resonances.[61] The SQ spectrum of the I spin is no longer made up of two components (see Eq. 1-5) but four for each crystallite orientation. As the splitting depends upon the dipole-dipole coupling constant and the crystallite orientation, experimental conditions at or close rotational resonance lead to complex powder lineshapes.

At exact rotational resonance, the broadenings can be several hundred Hertz (see FIGURE 1.5). Although

the broadening drops off rapidly away from match, it can still be relevant to the lineshapes we observe, where the dominant interactions are only a few tens of Hertz. Indeed, in the case of the carboxyl resonance in L-Alanine, this phenomenon dominates the lineshape for spinning speeds between 9 and 20 kHz (see FIGURE 1.7). The different powder shapes are again extremely well predicted by the numerical simulations of the two-spin system given in the middle column of FIGURE 1.7. The separate simulations of the two J-components $\omega_{\alpha\alpha\rightarrow\beta\alpha}$ and $\omega_{\alpha\beta\rightarrow\beta\beta}$ clearly show the splitting due to broad rotational-resonance effects. It is worth noting that these two J-components have the same lineshape: the off rotational-resonance effects act in the same way on both transitions. The intensity of the two broadened transitions may however differ due to the coherent cross correlation between CSA and DD interactions described above. This is particularly noticeable at 9 and 12 kHz, where the simulations including the carboxyl CSA match very well the experimental lineshapes, and clearly show two resonances of different intensity. The simulations without CSA (right column of FIGURE 1.7) exhibit, as expected, two identical transitions split by the J-coupling.

The homogeneous case

If the chemical-shift difference between both spins, I and S, is comparable to the dipole-dipole interaction, the system behaves under MAS *homogeneously*.[20] In that case, the Hamiltonian does not commute with itself at all times, and MAS only partly refocuses the anisotropic component at multiples of the rotor period. The linewidth therefore now depends on the MAS frequency, with the resolution improving with increasing spinning speed. In that case, we expect coherent CSA-DD cross correlation to lead to a *differential broadening* of both lines in the doublet. Indeed for a given spinning frequency, the narrower static transition will be better averaged and will be therefore narrower than the broader transition. This effect will of course decrease with increasing spinning speed.

We have tried to simulate the differential broadening induced by coherent cross correlation using the tensors' geometry found in L-Alanine. It was impossible to obtain components of significantly different width with only two spins (C^β and C^α), even by considering both CSAs, and modifying the tensor parameters to force the system to behave as homogeneously as possible. However, a difference in width of the doublet components was obtained only when dipolar couplings to a third spin (C') were introduced. This is in agreement with Filip *et al.*[90] who claim that the lineshape of homogeneous system is dominated at lower spinning speed by three-spin (and higher) terms. Only at higher spinning speeds do these terms get smaller, and the lineshape can be explained using a spin-pair approximation.

Simulations of the C^β resonance of L-Alanine are given in FIGURE 1.8. The J-coupling between C^β and C^α, all the DD couplings between the three spins in one molecule of L-Alanine, and CSA of C^β were taken into account. The simulated spectra which are shown with a small line broadening (3 Hz) do not reproduce exactly the experimental spectra given in first column of FIGURE 1.8. Homogeneous spin systems are very difficult to simulate accurately, and we assume that more spins need to be added to the simulation to properly reproduce the experimental spectra but this kind of simulations are very time consuming. However, it is important to note that, in contrast to the inhomogeneous simulations of FIGURE 1.7, we clearly see that the two simulated transitions show *different lineshapes and widths*.

Of course, off rotational-resonance effects will additionally affect the lineshape in the homogeneous case. For the particular case of the CH_3 in L-Alanine shown here, the MAS frequencies were chosen such that off rotational-resonance effects were negligible.

All simulations under MAS, for carboxyl and methyl resonances of L-Alanine, were performed with the NMR simulation package SIMPSON[89] using γ-compute algorithm.[78,91] The powder average was performed using a set of 4180 molecular orientational angles $\{\alpha_{MR}, \beta_{MR}\}$ generated by the ZCW algorithm[78,86,87,88] and 15 evenly-spaced values for the third Euler angle γ_{MR}. These angles define the relative orientation of the molecular reference frame M, defined with the z-axis along the internuclear vector, and a rotor reference frame R, defined with the z-axis along the spinning axis. We verified that increasing further the number of orientations
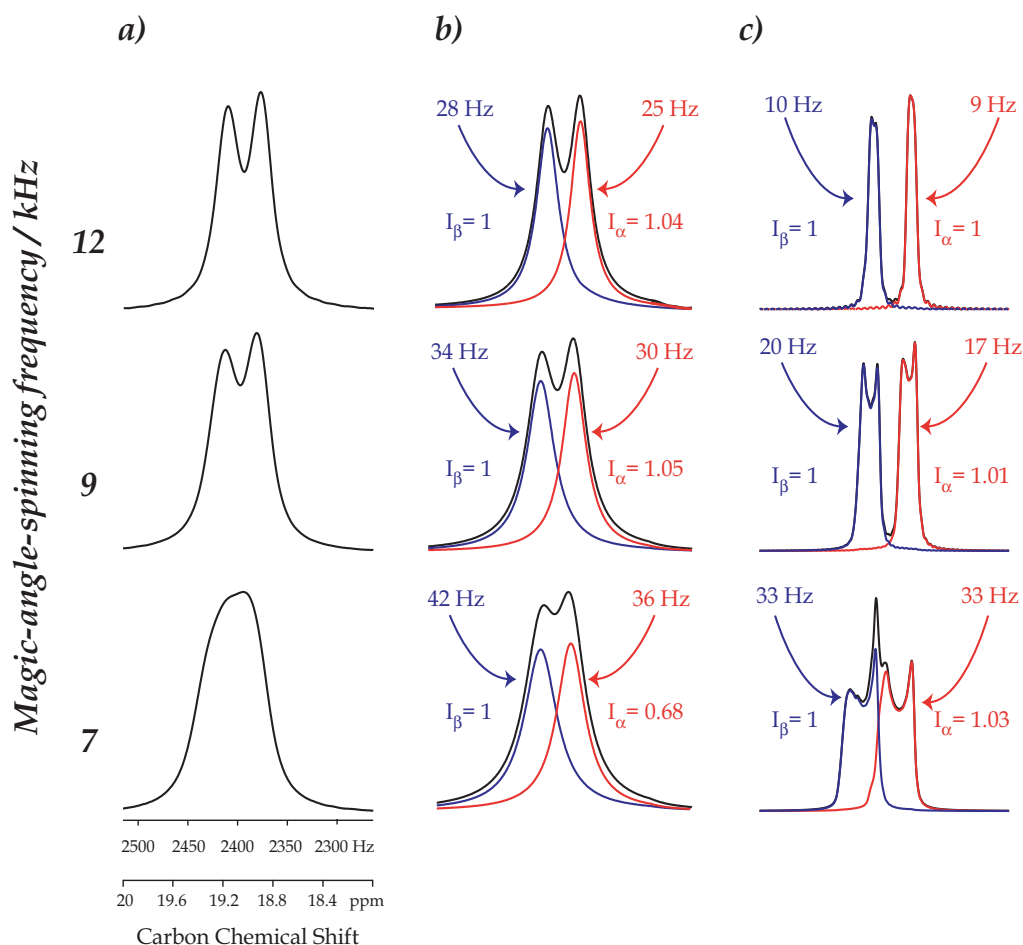
FIGURE 1.8: *(a) Experimental lineshapes of the C^β resonance of fully ^{13}C-enriched L-Alanine at different spinning frequencies at 160 kHz proton nutation frequency. Experimental details are given in the legend of FIGURE 1.3. No linebroadening was applied prior to Fourier transform. Each experimental line was deconvoluted with two Lorentzian functions. The result of the deconvolution in given in column (b), with the linewidth at half height and integral over each component (I). (c) Simulations under magic-angle spinning for the C^β in L-Alanine. To simulate the differential linebroadening for methyl resonance, the dipolar couplings to a third spin are necessary, here C' was considered.[90] The powder average was performed using a set of 4180 molecular angles $\{\alpha_{MR}, \beta_{MR}\}$ generated by the ZCW algorithm[78, 86, 87, 88] and 15 evenly-spaced values for the third Euler angle γ_{MR}. The SIMPSON[89] package was used for these simulations. A small line broadening (3 Hz) was applied prior to Fourier transform to smooth down the lines.*

did not lead to appreciable changes of the lineshapes. The simulations took no account of the interactions with protons which are assumed to be strongly suppressed by the decoupling irradiation. The simulated free-induction decays were multiplied by an exponential function $e^{-\lambda t_2}$, corresponding to a Lorentzian spectral broadening with the width at half height of $\lambda/(2\pi)$ being the applied line broadening in Hz. The static simulations as well as the deconvolution of the CH_3 resonance (see FIGURE 1.8) were obtained with MATLAB[79] using standard techniques.[78]

In order to quantify the theoretically predicted differential broadening of the CH_3 resonance in fully ^{13}C-enriched L-Alanine we started by performing a deconvolution of the doublet. The differential broadening obtained in this way together with the resulting lines are shown in FIGURE 1.8b. Between 7 and 12 kHz MAS, the doublet induced by the J-coupling to the C^α starts to be resolved and for these conditions particularly the doublet separation reveals components of different widths, with the downfield component (C^α in the β state) being wider (see FIGURE 1.8b). The differential broadening decreases as expected with the MAS frequency, going in this case from approximately 6 Hz at 7 kHz MAS (an effect of $\sim$ 15 %) to 3 Hz (an effect of $\sim$ 11 %) at

12 kHz MAS. Increasing further the spinning speed leads to a symmetric doublet (within the limit of uncertainty of the measurement). We should note that the difference in linewidth also leads to a different intensity for the two components. However, the integrated intensity over both deconvoluted components is the same in almost all the spectra. This indicates that the inhomogeneous contribution to the lineshapes is very small here. Thus, the difference in intensity arises only from the differential broadening, and not from differences in spinning sidebands intensity distribution, as is the case for the carboxyl resonance (whose lineshape is dominated by inhomogeneous interactions).

Since the methyl lineshapes at 6 and 7 kHz are not well resolved to easily identify the J-coupling and consequently to precisely determine the linewidths by deconvolution, we looked for a method well adapted for accurately measuring the differential broadening. The spin-state-selective techniques originally introduced in liquid-state NMR for heteronuclear spin systems are well suited for this purpose. The pulse sequence allowing to separately measure the doublet components and thus to prove the methyl differential broadening at low spinning speed, uses the In-Phase Anti-Phase (IPAP)[31,32] selective filter. The spin-state-selective approach and the IPAP filter sequence will be largely described in the next chapter of this thesis. Basically, the selection of one of the doublet components is based on the combination of two separately recorded experiments. The sum and difference of the resulting spectra yield two sub-spectra, one containing the α and the other the β transition. The experimentally measured linewidths for α and β transitions are given in TABLE 1.2. The difference in linewidth is shown as a function of the spinning rate in FIGURE 1.9a. The largest difference in width between α and β transitions is, as expected, obtained at slow spinning frequencies. For example, a difference of 10 Hz is obtained at 6 kHz MAS. The measurement of the differential broadening at even lower spinning frequencies would be difficult due to the presence of off rotational-resonance effects which lead to additional broadening of the resonances. By increasing the spinning speed, the difference in linewidth of the two components decreases and disappears at 18 kHz MAS. These measured values are in good agreement with the above predicted linewidts from the deconvolution of the CPMAS lineshapes.

TABLE 1.2: *Full widths at half height (FWHH) of the two methyl resonance components in fully ^{13}C-enriched L-Alanine determined with the IPAP experiment at different magic-angle-spinning frequencies.*

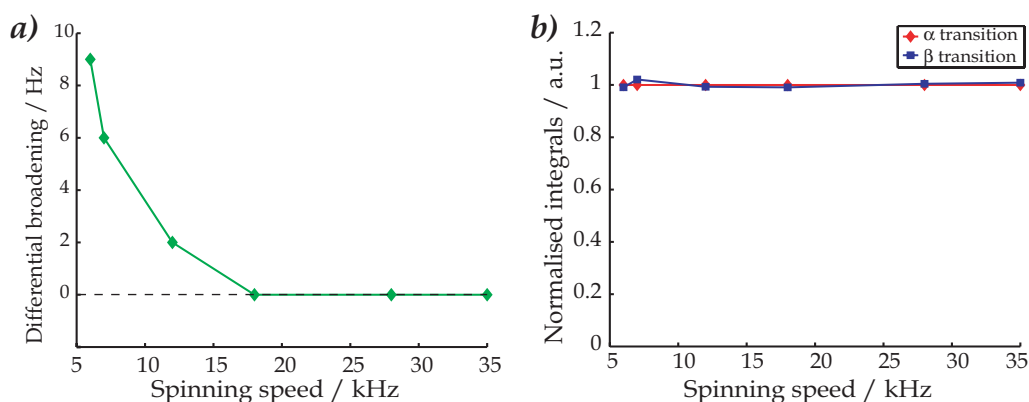| $\frac{\omega_r}{2\pi}$ / kHz	Δ_α / Hz	Δ_β / Hz	%
6	58	68	15
7	43	50	14
12	24	27	11
18	24	24	0
28	20	20	0
33	19	19	0

FIGURE 1.9: *Differential linewidth (a) and normalised integral intensity (b) for both components of the CH$_3$ resonance of fully ^{13}C-labelled L-Alanine measured with the IPAP pulse sequence as a function of the magic-angle-spinning frequency.*

In conclusion, the IPAP experiment allows us to accurately measure the differential broadening induced

by the coherent CSA-DD correlation effects for the case where the involved spins behave homogeneously.[20] For the carboxyl lineshape in L-Alanine, only a difference in intensity was found, showing that the chemical-shift difference to the C^α is big enough for the homonuclear pair spin system to behave inhomogeneously. A completely opposite situation is found for the CH_3 in L-Alanine. The integrals of each doublet component are the same over the whole range of magic-angle-spinning frequencies (see FIGURE 1.9b). The coherent cross-correlation effect between the C^β and C^α is only characterised by a differential broadening of the CH_3 doublet, thus indicating a homogeneous coupled spin pair, as actually expected for a homonuclear spin system. This kind of effects are refocusable by a π pulse in a spin-echo type experiment.[92]

1.4 Discussion

These results show that the experimental lineshapes observed for fully ^{13}C-labelled L-Alanine can be explained by the joint effect of off rotational-resonance conditions and cross correlation between CSA and DD interactions. Such effects are not limited to the special case considered in detail here, but also appear *at other magnetic fields or in other amino acids*, and are therefore relevant for all ^{13}C-labelled compounds as for example the proteins.

To show the generality of this effect with respect to the spin system, we have simulated the carboxyl and methyl lineshapes of L-Threonine for different MAS spinning speeds. These simulations are drawn in FIGURE 1.10. The size and geometry of the different interactions considered are summarised in TABLE 1.3. The broadening of the L-Threonine simulated lines is quite similar to that described above for L-Alanine.
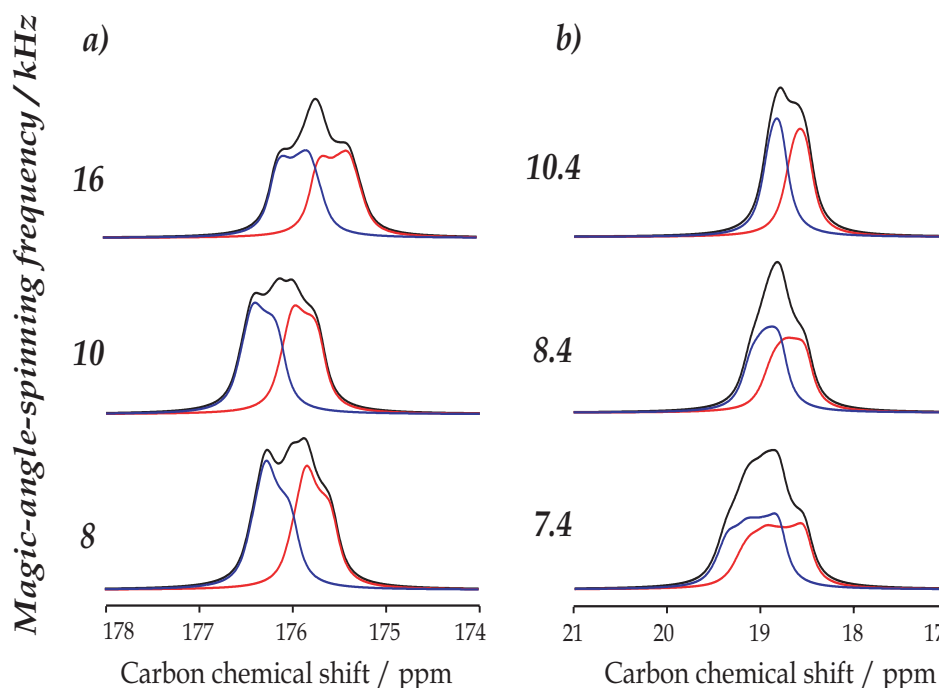
FIGURE 1.10: *Simulated (a) carboxyl and (b) methyl resonances of L-Threonine at intermediate spinning frequencies and 11.8 T (i.e., 500 MHz proton frequency). The different parameters for the CSA and DD tensors, as well as their relative orientations are given in TABLE 1.3. For the simulations of carboxyl lineshape a two-spin system C' - C^α was considered. Only the CSA of the carboxyl spin was taken into account. For the methyl lineshape simulations, a four-spin system C' - C^α - C^β - C^γ was chosen. All CSA tensors and dipolar couplings between all fours spins were considered. The powder average was performed using a set of 376 molecular angles $\{\alpha_{MR}, \beta_{MR}\}$ generated by the ZCW algorithm[78, 86, 87, 88] and 15 evenly-spaced values for the third Euler angle γ_{MR}. The SIMPSON[89] package was used for these simulations. A line broadening of 24 Hz was applied prior to Fourier transform.*

The presence of this effect at other magnetic fields is illustrated in Figure 1.11 where the simulated carboxyl lineshapes of L-Alanine are shown for a series of different static magnetic fields going from 9.4 T (400 MHz) to 23.5 T (1 GHz). In order to keep the size of the off rotational-resonance effects constant, the magic-angle-spinning frequency was adjusted such that its ratio to the static magnetic field remained the same for all the simulated spectra. Even if the distortion of the lineshape from the expected symmetric doublet tends to be smaller at high magnetic fields, it still leads to noticeable effects at 800 MHz proton frequency. We predict therefore that coherent cross-correlation and off rotational-resonance effects can broaden the carbon lineshapes, even at the highest available magnetic field strengths. The asymmetric lineshapes observed in the work of Pauli *et al.* for SH3 domain resonances C^γ of 53Val (17.0 ppm) and C^β of 55Ala (15.9 ppm) are good examples of this.[43]

As was briefly mentioned by Nakai and McDowell,[60] we note that coherent cross-correlation effect observed for carbon lineshapes could potentially be used to determine the orientation of the CSA tensor in the molecular frame, if the principle components are known (or vice-versa). This is illustrated in Figure 1.12 where the predicted lineshapes of the C' carbon in L-Alanine are shown as a function of the angle β between the z-component of the CSA tensor and the C' - C^α internuclear vector. The change is clear, and only the previously determined geometry of the Table 1.1 agrees with the experimental result.

TABLE 1.3: *Parameters for the CSA and DD tensors, and J-coupling constants in L-Threonine.*

CSA parameters	^{13}C'	^{13}C$^\alpha$	^{13}C$^\beta$	^{13}C$^\gamma$	
$\delta_{iso}{}^a$	170 ppm	60.2 ppm	65.4 ppm	18.9 ppm	
$\delta_{aniso}{}^a$	70.2 ppm	8.8 ppm	- 26.6 ppm	- 17.5 ppm	
η^a	0.85	0.71	0.35	0.51	
$\Omega_{PM}{}^b$	{83.7°, 69.4°, 154.4°}	{149°, 58.3°, 88.7°}	{50°, 110.4°, 150.9°}	{1.7°, 147°, 72.8°}	
DD parameters	^{13}C'- ^{13}C$^\alpha$	^{13}C' - ^{13}C$^\beta$	^{13}C$^\alpha$ - ^{13}C$^\beta$	^{13}C$^\alpha$ - ^{13}C$^\gamma$	^{13}C$^\beta$ - ^{13}C$^\gamma$
$d_{jk}/2\pi^c$	- 2176.5 Hz	- 454.5 Hz	- 2072.3 Hz	- 467 Hz	- 2229 Hz
Ω'_{PM}	{0°, 126.8°, 147.7°}	{0°, 125.2°, 18.6°}	{0°, 104.3°, 59.2°}	{0°, 50.4°, 64.5°}	{0°, 20.9°, (73.3°}
J parameters	^{13}C' - ^{13}C$^\alpha$	^{13}C' - ^{13}C$^\beta$	^{13}C$^\alpha$ - ^{13}C$^\beta$	^{13}C$^\alpha$ - ^{13}C$^\gamma$	^{13}C$^\beta$ - ^{13}C$^\gamma$
J_{jk}	54 Hz	0 Hz	34 Hz	0 Hz	34 Hz

^{a} The signs of frequencies are conform that given by Levitt.[84] The isotropic chemical shift frequencies and the chemical shift principal values were taken from the work of Janes *et al.*[93] with respect to TMS. The isotropic chemical shift, anisotropic chemical shift frequency and asymmetry parameter are defined as in the legend of Table 1.1.

^{b} The set of Euler angles was determined from the atomic parameters given in the paper of Shoemaker and coworkers.[94]

^{c} Dipole-dipole coupling constant taken from Shoemaker *et al.*.[94]

1.5 Conclusion

We have shown in this chapter that ^{13}C spectra of fully labelled compounds can reveal at intermediate spinning speeds broad and asymmetric lineshapes instead of the expected multiplet structure induced by the
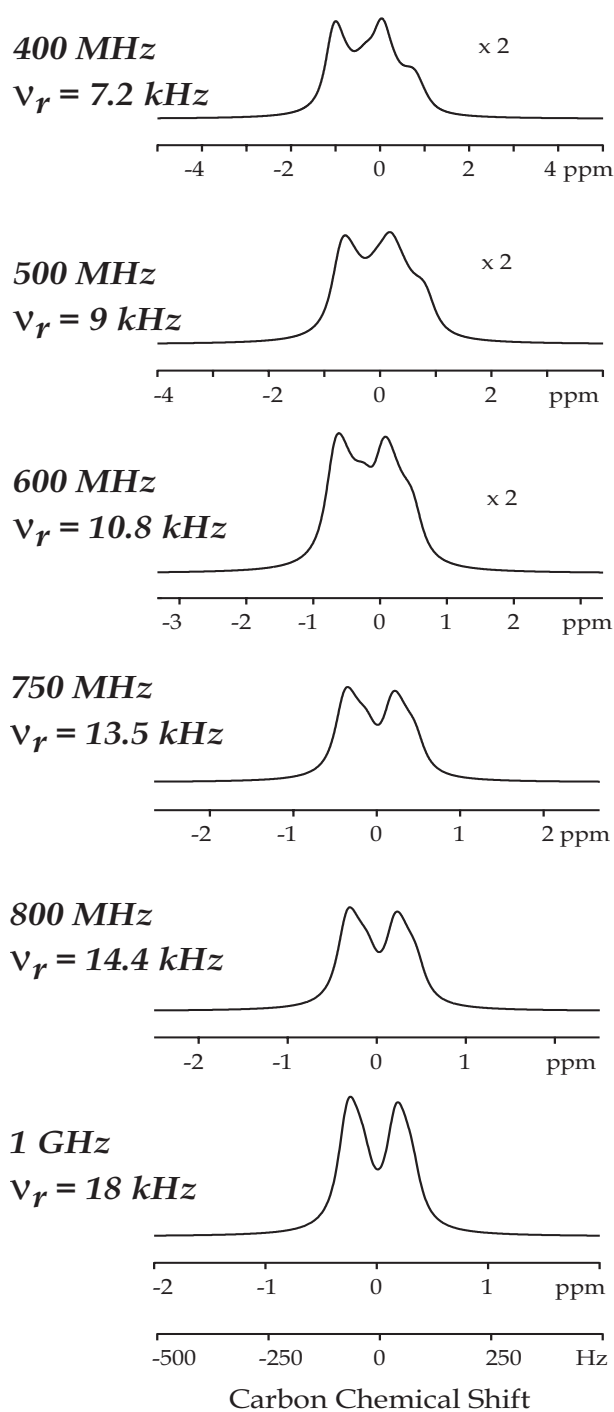
FIGURE 1.11: *Simulations under magic-angle spinning of the carboxyl lineshapes of L-Alanine at different static magnetic fields ranging from 9.4 T (i.e., 400 MHz proton frequency) to 23.5 T (i.e., 1 GHz proton frequency). The spinning frequency was chosen such that its ratio to the magnetic field was kept constant. The same spin system was considered as for the static simulations of FIGURE 1.6. A ZCW[78, 86, 87, 88] powder average over 376 molecular angles {α_{MR}, β_{MR}} and 15 evenly-spaced values for the third Euler angle γ_{MR} were necessary for obtaining these simulations. The SIMPSON[89] package was used for these simulations. A line broadening of 24 Hz was applied prior to Fourier transform.*

presence of carbon-carbon scalar couplings. Whereas the broadening of the lines originates mainly from well-known off rotational-resonance effects, coherent CSA-DD cross correlation was shown to induce an asymmetry in intensity for systems behaving *inhomogeneously*,[20, 62, 63] and this will be the case for the vast majority of

$$\delta\,(^{13}\mathrm{C})\,/\,\mathrm{ppm}$$

FIGURE 1.12: *a) Experimental C' lineshapes at 7 kHz spinning frequency, taken from FIGURE 1.3. b) Simulations similar to those shown in FIGURE 1.7, but varying the β angle between the z-component of the C' CSA tensor and the C' - C$^\alpha$ internuclear vector, showing the sensitivity of the lineshape to this structurally relevant parameter. The simulations of FIGURE 1.7 were done for a β angle equal to 64.8°, which is the value inferred from.*[85]

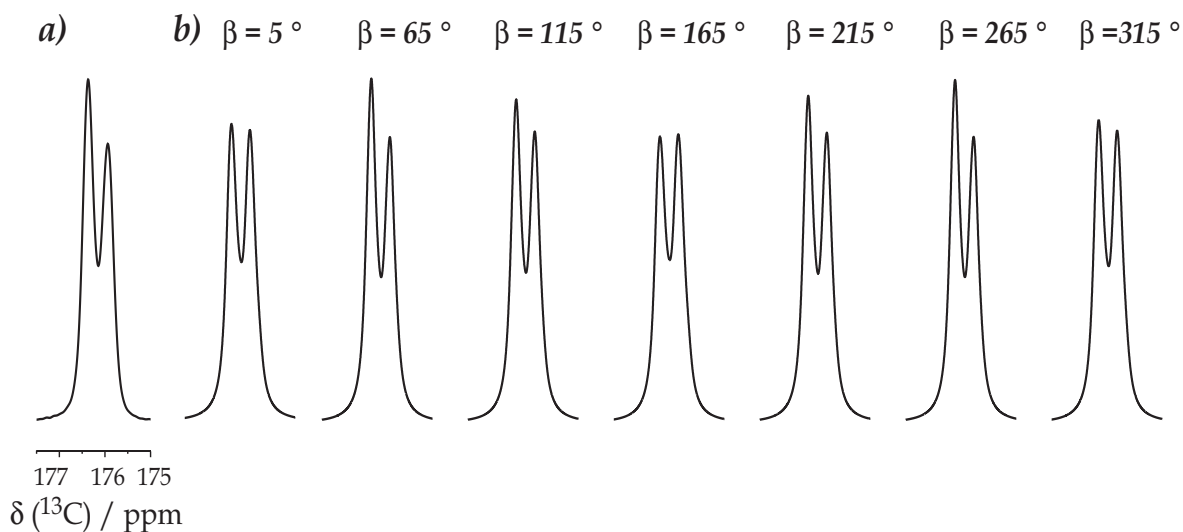carboxyl resonances in proteins for example. On the contrary, the coherent cross-correlation effects produce a differential broadening for the systems behaving homogeneously under MAS. This will be the case, for example, for many aliphatic groups in proteins. The effect we describe here is widespread and *is particularly relevant for solid-state NMR studies of proteins*, where current experimental practice favors the use of intermediate spinning speeds that appear to maximize these effects, and we show that these effects are still noticeable at the highest available magnetic fields. In all cases these coherent cross-correlation effects disappear at high spinning frequencies.

More generally, cross-correlation effects in liquid-state NMR have been successfully used as sensitive structural probes[95, 96] and differential broadening has recently been exploited in the TROSY experiment[40] to yield resolution enhancement in spectroscopy of proteins. It is conceivable that the exploitation of these effects in solids could also lead to new, unexpected applications.

Contrary to the liquid state, in solids these effects are small and sensitive to the spinning frequency. Consequently, since the largest differential broadening is observed at low spinning speeds exploitation of these effects for solids in a way similar to that used in liquid-state NMR (i.e., selection of the transition associated with the longer dephasing time) would not provide a major resolution enhancement because, at these spinning rates, the lineshapes are still dominated by residual second-order dipole-dipole interactions which are only partly refocused by the magic–angle spinning. Owing to the weakness of these effects, other strategies can be considered for fully labelled solid systems at low spinning rates. One of them is the removal of the coherent cross-correlation effects by refocusing the homonuclear J-coupling in a manner similar to that proposed in 1996 by Straus and coworkers.[37, 97] Another possibility is to individually separate each transition of the J-coupled multiplets using spin-state-selection filters as those presented in the next chapter.

Spin-state-selection techniques in solid-state NMR

2.1   Introduction

This chapter focuses on the possibility of using spin-state-selection techniques in solids. It results in the removal of the J-coupling broadening by selecting only one component of the multiplet. Spin-state-selective experiments are well known in liquid-state NMR and are mainly used for the measurement of scalar and residual dipolar coupling constants,[31, 32, 33, 34, 98, 99, 100] for coherence transfer using single-transition cross-polarisation,[101, 102] or in the context of TROSY, where the selection of the slowly relaxing doublet component leads to improved resolution and sensitivity in heteronuclear correlation experiments of biomolecules.[40]

Techniques for spin-state selection can essentially be separated into two categories. In the former, a direct-selective excitation of a single spin state is obtained, either through single-quantum coherences (SQC) in the S3E (Spin-State-Selective Excitation) experiment,[33] or through zero- or double-quantum coherences (ZQC or DQC) as in the S3CT (Spin-State-Selective Coherence Transfer) experiment.[100] In the second category, the spin-state separation is achieved by linear combination of experiments containing in-phase or anti-phase signals. These sequences are known as IPAP (for In-Phase Anti-Phase)[31, 32] and DIPSAP (for Double-In-Phase Single-Anti-Phase)[34] and were developed in liquid-state NMR for heteronuclear spin pairs using non-selective pulses.

The INADEQUATE-CR (Incredible Natural Abundance DoublE QUAntum Transfer Experiment and Composite Refocusing) experiment introduced in 1995 by Nielsen *et al.*[35] has been already applied to solids, where it was shown to work for two-spin systems.[36] The sequence was originally developed to enhance the sensitivity of the basic INADEQUATE experiment.[103, 104, 105, 106, 92] Tailored for homonuclear spin pairs, the experiment uses non-selective pulses to excite and efficiently reconvert the double-quantum coherences to only one component of the J-doublet. However, the sequence is specifically limited to homonuclear double-quantum-single-quantum correlation experiment.

In this chapter, we will show that spin-state selection can be achieved in solid-state NMR in a general manner, even when the J-coupling is not well resolved in the spectrum. Using semi-selective pulses, we measured all the different homonuclear spin states of all three carbon resonances in fully ^{13}C-labelled L-Alanine with a pulse sequence based on the IPAP block filter. The resulting resolution and sensitivity obtained with the IPAP filter will be mainly discussed. In a manner similar to that used for IPAP, the spin-state selection can also be accomplished by using S3E, DIPSAP or INADEQUATE-CR techniques. The degree of selection of the spin states of the latter methods was experimentally tested on carboxyl and/or methyl doublets of fully ^{13}C-enriched L-Alanine.

2.2   Spin-state selection in solid-state NMR

The general pulse sequence used for performing state selection is given in FIGURE 2.1a. All the spin-state-selective filters are adapted for a homonuclear spin pair by the use of semi-selective pulses. The pulse sequence including the spin-state-selective filter was adjusted to make it compatible with conventional solid-state NMR sequences allowing polarisation transfer, magic-angle-spinning, and heteronuclear dipolar decoupling. The carbon magnetisation of all spins is first enhanced by conventional cross polarisation from protons, using simultaneous radio-frequency fields on both the proton and carbon channels.[23, 24, 71, 73] The carbon polarisation is then stored along the static magnetic field direction by a non-selective (i.e., broadband or hard) ^{13}C $\pi/2$ pulse. The following z filter of duration δ removes any residual transverse coherences and ensures proper z magnetisation for the spin-state-selection element which precedes the acquisition.

2.2.1   Spectral selection using IPAP

Pulse sequence and experimental details

For the particular case of spin-state selection with IPAP, the filter block in FIGURE 2.1a has to be replaced by the In-Phase Anti-Phase element (see FIGURE 2.1b).[31, 32] We consider a spin system of two J-coupled carbon-13 nuclei, denoted I and S. The IPAP filter is based on a semi-selective τ - π - τ element, with $2\tau = (2J_{IS})^{-1}$. The selection of one of the I-spin transitions consists in combining two separately recorded experiments, denoted (A) and (B). They differ in the position of the two π pulses on the S spin and the phase φ_3 of the subsequent $\pi/2$ pulse on the I spin.

In the first experiment (A), the homonuclear I - S scalar coupling is removed by the π pulses on the S spin applied in the middle of each τ evolution period. This corresponds to an ε value of $\tau/2$. Thus, no net evolution occurs during the IPAP filter (except for relaxation) and an in-phase signal, with a splitting due to the presence of the J-coupling to the S spin, is observed for the I spin (after an additional z filter) in the detection period t_2. All other interactions are removed either by magic-angle spinning (heteronuclear ^{13}C - ^{1}H and homonuclear ^{13}C - ^{13}C dipolar couplings, and ^{13}C chemical-shift anisotropy), by heteronuclear decoupling (heteronuclear ^{13}C - ^{13}C dipolar and scalar couplings), or by the refocusing π pulses (isotropic chemical shifts). In the second experiment (B), the ε delay is set to zero. This results in a net evolution under the J-coupling during the total delay $2\tau = 1/(2J_{IS})$ leading therefore, after the final z filter, to an anti-phase signal of the I spin with respect to the S one during the detection period t_2. Addition and subtraction of these two experiments yield spectra containing only one of the I spin doublet components, corresponding to the I magnetisation with the coupled S spin being either in the $|\alpha\rangle = |\text{-}1/2\rangle$ or $|\beta\rangle = |1/2\rangle$ state.

In order to achieve optimum separation of the spin states in the combined spectra, it is essential that both (A) and (B) experiments have exactly the same duration and the same number and type of semi-selective pulses. This ensures that "relaxation effects" will occur in the same way in both experiments. For this reason, the two "simultaneous" semi-selective π pulses in the (B) experiment, where $\varepsilon = 0$, are for example applied sequentially. In the same experiment, the second π pulse on the S spin is kept for the same reason. It has additionally the effect of refocusing the transient Bloch-Siegert phase shifts effects[107] potentially introduced on the I-spin coherence by the first π pulse applied on the S spin. Furthermore, it was experimentally noticed that a complete phase cycle of the π pulse on the I spin is required for a good selection of the spin-state transitions.

The feasibility of spin-state selection using IPAP is shown on the fully ^{13}C-enriched L-Alanine. The pulse sequence of FIGURE 2.1 with IPAP as spin-state-selective block filter was applied to all three carbon resonances of L-Alanine at different magic-angle-spinning frequencies (6, 7, 12, 18, 28, 35 kHz). Since all three resonances are well separated and only one resonance at one time is concerned by each soft pulse of the sequence, we used simple Gaussian[108, 109] shaped $\pi/2$ and π pulses as semi-selective pulses. The Gaussian shape was produced by the ShapeTool extension of the Bruker XWINNMR package,[110] using 200 points with
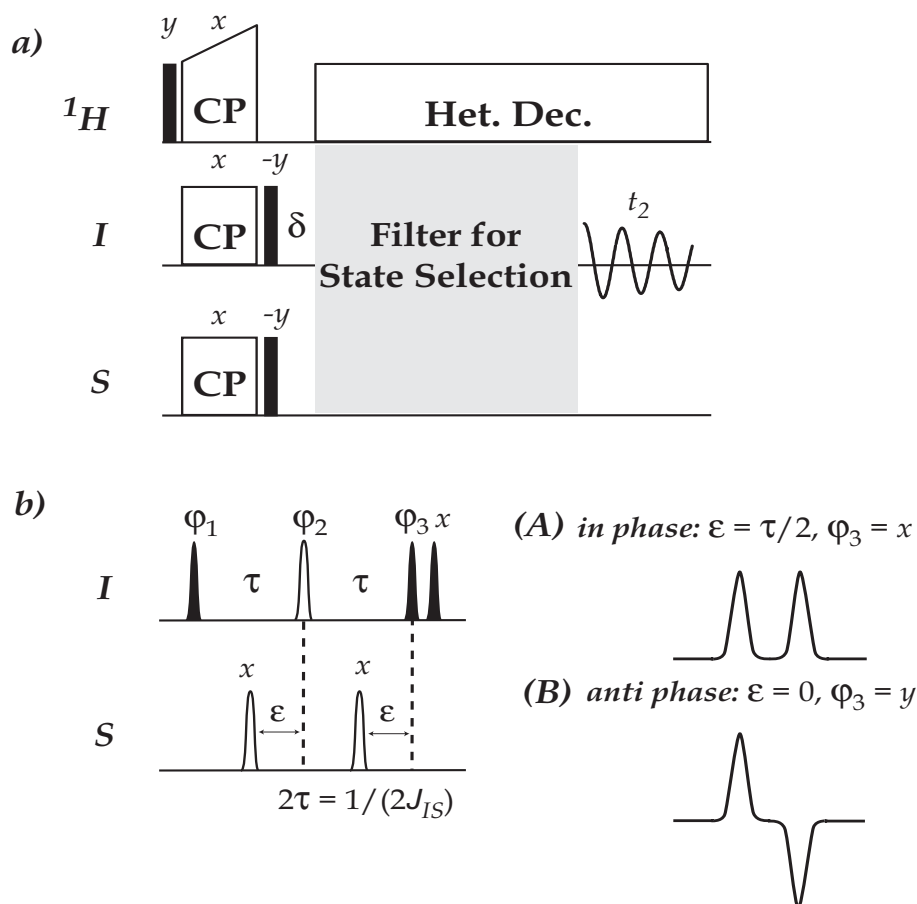
FIGURE 2.1: *a) Pulse sequence for spin-state selection used for selecting individual state transitions with selective filters (drawn in grey box). b) IPAP selection filter. $\pi/2$ and π rf pulses are represented by filled and open bars for hard pulses and shapes for semi-selective pulses, respectively. For optimal performance of the IPAP state-selection filter, the delay 2τ has to be adjusted to $(2^1 J_{IS})^{-1}$ (i.e., 9.26 ms for $C'C^\alpha$ spin pair and 14.706 ms for $C^\beta C^\alpha$ spin system). Two data sets (A) and (B) are recorded using the following settings: (A) $\varepsilon = \tau/2$, $\varphi_3 = x$ and (B) $\varepsilon = 0$, $\varphi_3 = y$.[31, 32] The resulting spectra are schematically given next to the pulse sequence. The phase cycle we used is: $\varphi_1 = x$ -x; $\varphi_2 = x\ x\ y\ y$ -x -x -y -y; $\varphi_{rec} = x$ -x -x x. Addition and subtraction of the (A) and (B) experiments yield two spectra, each of them containing only one of the doublet components.*

a truncation level of 1 %. The amplitude of the Gaussian pulses was calibrated using carbon-13 magnetisation in the following pulse sequence:

$$\text{CP - } \pi/2\text{(hard) - delay (5 ms) - } \pi/2 \text{ (soft) or } \pi \text{ (soft)} \tag{2-1}$$

with simultaneous TPPM[74] decoupling. Due to the symmetry of the Gaussian shape, the refocusing pulse is identical to that optimised for inversion. In order to minimise the imperfections introduced by the π pulse applied on the I spin, the amplitude of the Gaussian $\pi(I)$ pulse was further fine tunned directly on the IPAP pulse sequence. At low spinning frequencies, it was found necessary that Gaussian pulses were selective enough to not affect the other resonances over their whole range of frequencies, including their chemical-shielding anisotropy (i.e., spinning sidebands of other resonances were avoided). At higher spinning frequencies, we found it only necessary to avoid the isotropic chemical-shift resonances of other spins. We therefore used 1 ms Gaussian pulses in the slow spinning regime (i.e., 6 and 7 kHz), and 200 and 800 μs pulses for C' and C^α/C^β resonances, at higher spinning speeds.

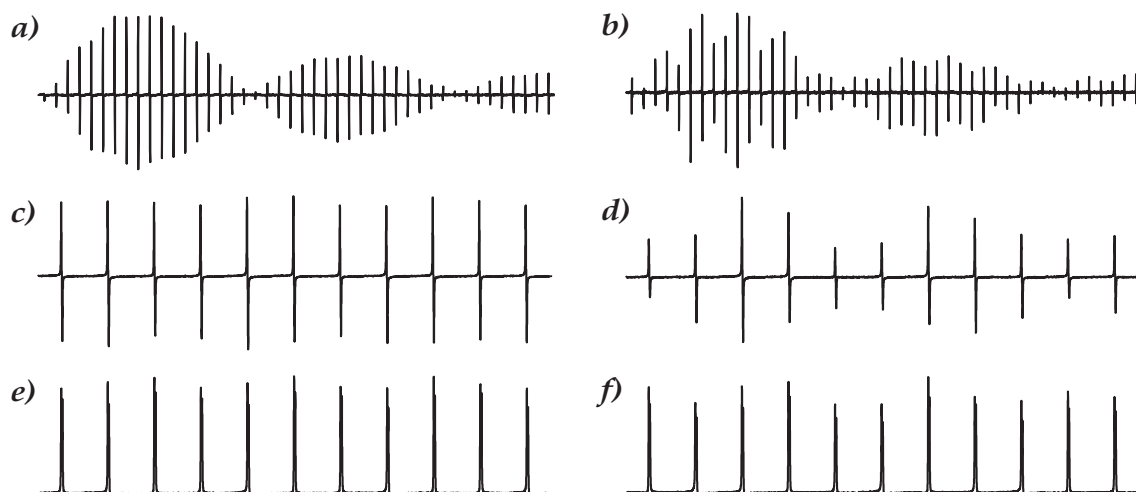Since the IPAP pulse sequence is based on the spin-echo method which requires sychronisation of the

FIGURE 2.2: *$2I_y S_z \sin(2\pi J\tau)$ (a-d) and $I_y \cos(2\pi J\tau)$ (e, f) modulation curves with respect to the τ delay obtained at 6 kHz rotation frequency. The semi-selective pulses were calibrated with the pulse sequence 2-1. The J-modulated curves were recorded with (a, c, e) and without (b, d, f) reoptimising the I spin π pulse directly on the IPAP pulse sequence. In a) and b) the delay τ was initially set to 1 μs and further incremented by 0.5 ms (i.e., $3\tau_r$). The signal is maximum for $\tau = 1/(4J)$ and the first zero crossing is obtained when τ is equal to $1/(2J)$. The other curves show the J-modulation inside a rotor period around the maximum found here equal to 4.75 ms.*

τ echo delay with the rotation period, the same constraint has been originally expected for IPAP. Contrary to our belief, experimental investigations showed that synchronisation with spinning rotation is not essential for well-calibrated semi-selective pulses. An interference between rotation and semi-selective pulses was only observed at low spinning frequencies when the semi-selective pulses were not completely optimised for the IPAP sequence. This is illustrated in FIGURE 2.2 with two J-modulated curves recorded at 6 kHz rotation frequency with (c and e) and without (d and f) reoptimisation of the π pulse on the I spin directly on the IPAP pulse sequence. A modulation is also observed outside the rotor period when we look at the J-modulation curve as a function of the τ delay. This is shown in FIGURE 2.2b where the τ delay was varied from 1 μs to 25 ms with steps of 0.5 ms (i.e., $3\tau_r$). The power level of the $\pi(I)$ pulse reoptimised with IPAP is 1.7 dB larger than the π pulse optimised with the pulse sequence 2-1. This difference in dB corresponds to a difference in frequency of about 240 Hz. The nutation frequency on the ^{13}C channel used for the reoptimised semi-selective pulse was 1.26 kHz. In conclusion, at low spinning frequencies, problems could arise from the use of shaped pulses, principally due to interference effects with sample rotation. This kind of effects should be explored further.

Results and discussion

Spin-state selection is illustrated in FIGURE 2.3 for all three carbon resonances with respect to each of the coupling partners. The pulse sequence of FIGURE 2.1a with IPAP as selective filter was applied to each of the four J-coupled spin pairs in fully ^{13}C-enriched L-Alanine, e.g., {C' - C$^\alpha$}, {C$^\beta$ - C$^\alpha$}, {C$^\alpha$ - C'}, {C$^\alpha$ - C$^\beta$}. The transitions corresponding to the J-split components of the I spin, with the coupling partner (S spin) being in α or β state, are given on the top of each column. The 2τ delay was experimentally set to match $(2J_{IS})^{-1}$, e.g., 9.26 ms for the C' - C$^\alpha$ spin pair (J-coupling of 54 Hz) and 14.706 ms for the C$^\beta$ - C$^\alpha$ spin pair (J-coupling of 34 Hz). For all resonances and spin pairs, the spin-state selection is remarkably good. In the case of the carboxyl resonance, the MAS range covers a slow spinning regime (6 and 7 kHz) where the doublet due to the J-coupling to the C$^\alpha$ is relatively well resolved in the CPMAS spectrum, an intermediate regime (12 and 18 kHz) where off rotational-resonance effects broaden the transitions leading therefore to unresolved resonances in the carbon spectrum (see FIGURE 1.3),[51, 60, 75] and a fast spinning regime (28 and 35 kHz), well above any rotational-resonance conditions, where the doublet is well resolved. For all these conditions, the separation of the spin states is very good at high spinning frequencies. At the lowest spinning frequencies, a

small contribution from the other spin state passes through the filter. The largest residual represents $\sim 12\,\%$ from the selected spin state. For the methyl resonance, the resolution of the doublet structure in the CPMAS spectrum starts to be visible at about $9\,\mathrm{kHz}$ MAS. Independently of the apparent resolution of the J-coupling with the C^α, the spin-state selection is again very good at all magic-angle-spinning frequencies used here.
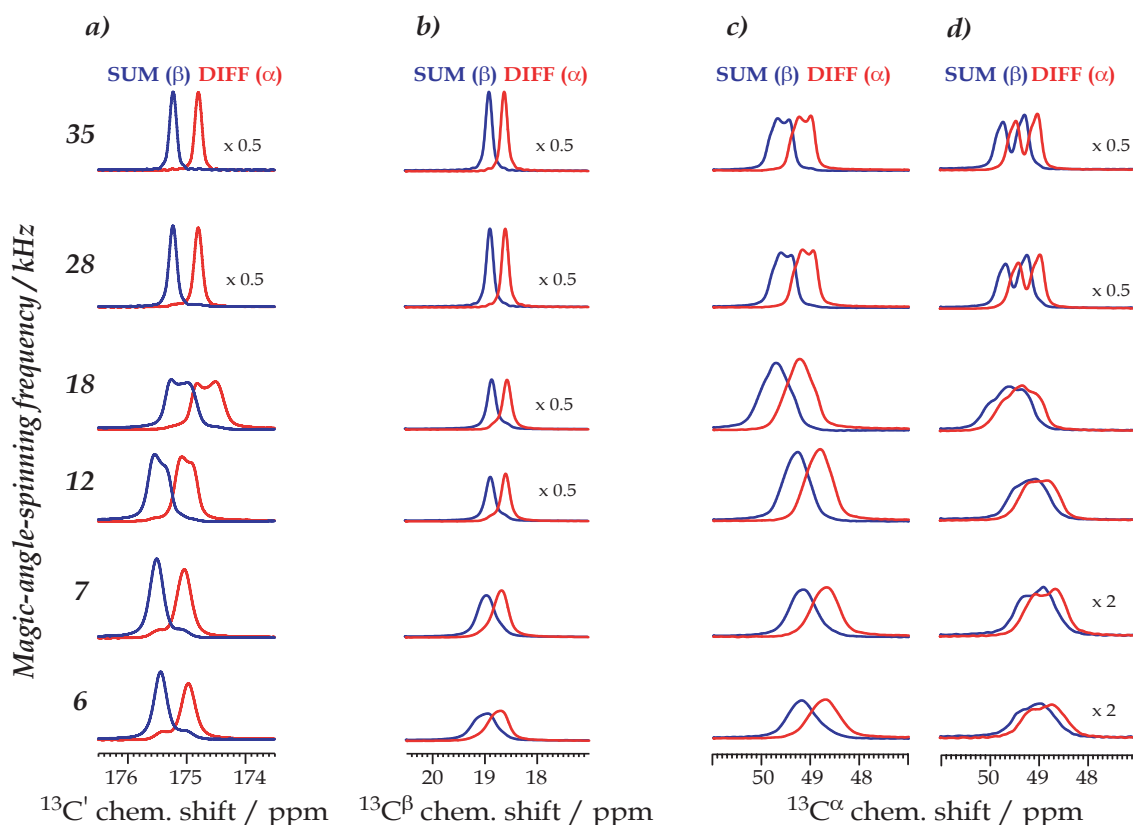

FIGURE 2.3: *Experimental α and β transitions for C' (a), C^β (b), and C^α (c and d) resonances of fully ^{13}C-labelled L-Alanine obtained with the pulse sequence of FIGURE 2.1 with IPAP as selective filter. The sample was purchased from Eurisotop and used without further purification. The last two columns correspond to the C^α resonance with the C' (column c) or the C^β (column d) being in the α or β state. All the experiments were performed on a Bruker 500 Avance spectrometer (proton and carbon frequencies at 500.13 MHz and 125.76 MHz) equipped with a Bruker 2.5 mm double CPMAS probehead. A ramped spin lock on the proton channel was used to broaden the Hartmann-Hahn condition.[23, 24, 71, 72, 73] The CP contact time was set to 1 ms. The proton nutation frequency for the TPPM-15 decoupling sequence[74] was set to 156 kHz. A delay δ of 5 ms was chosen to remove any residual transverse magnetisation. The delay 2τ was set to 9.26 ms for the C' - C^α spin pair (which corresponds to a J-coupling of 54 Hz) and 14.706 ms for C^α - C^β spin pair (i.e., J-coupling of 34 Hz). To ensure the best resolution and to avoid wiggles at high rotation frequencies, the acquisition time was set to 60 ms thus giving a complete decay of the signal, which was further processed without any apodisation function.*

The C^α spin in fully ^{13}C-labelled L-Alanine has two J-coupled partners, C' and C^β. When rotational-resonance conditions are avoided, the CH resonance contains four components corresponding to the carboxyl and methyl carbons in either the α or the β state. This multiplet structure (doublet of doublets) is not at all resolved in the CPMAS spectrum, even at the highest MAS spinning frequency considered here (i.e., 35 kHz, see FIGURE 2.3). A broad (linewidth of more than 100 Hz) and featureless lineshape is obtained for this resonance at all magic-angle-spinning frequencies. Nevertheless, excellent spin-state selection is obtained for the CH resonance using the IPAP filter. Since the C^α spin has two coupled spins, the experiment of FIGURE 2.1a is carried out once for the $\mathrm{C}^\alpha\mathrm{C}'$ spin pair with the 2τ delay matched to $^1J_{C^\alpha C'} = 54$ Hz and once for the $\mathrm{C}^\alpha\mathrm{C}^\beta$ spin pair matched to $^1J_{C^\beta C^\alpha} = 34$ Hz. The results for the $\mathrm{C}^\alpha\mathrm{C}'$ and $\mathrm{C}^\alpha\mathrm{C}^\beta$ spin pairs are shown in FIGURES 2.3c and 2.3d. Depending on the chosen spin pair, the spin-state selection is performed only with respect to one of the

scalar coupled spins (i.e., carboxyl or methyl). Thus, each selected CH spin state still contains two transitions separated by the J-coupling to the third spin. The doublet structure of the separated spin states of the C^α spin is very clear at high MAS frequencies in FIGURES 2.3c and 2.3d.

2.2.2 "Double IPAP" filter

A further possibility for an additional simplification of the CH multiplet can be achieved by applying two successive IPAP filters. This "double IPAP" filter is implemented in the pulse sequence shown in FIGURE 2.4. In a homonuclear three-spin system I - S - K, e.g., $\{C^\alpha$ - C' - $C^\beta\}$, with the I spin being coupled to both S and K spins, the first IPAP filter applied to the I - S spin pair, with $2\tau_{IS}$ matched to $(2J_{IS})^{-1}$, delivers the I-spin states separated with respect to the S spin. Applying a second IPAP filter to the I - K pair system with $2\tau_{IK}$ matched to $(2J_{IK})^{-1}$, the spin states of I spin separated with respect to both S and K spins are then obtained. In practice, four data sets are recorded using the parameters summarised in TABLE 2.1 for the successive IPAP filters.
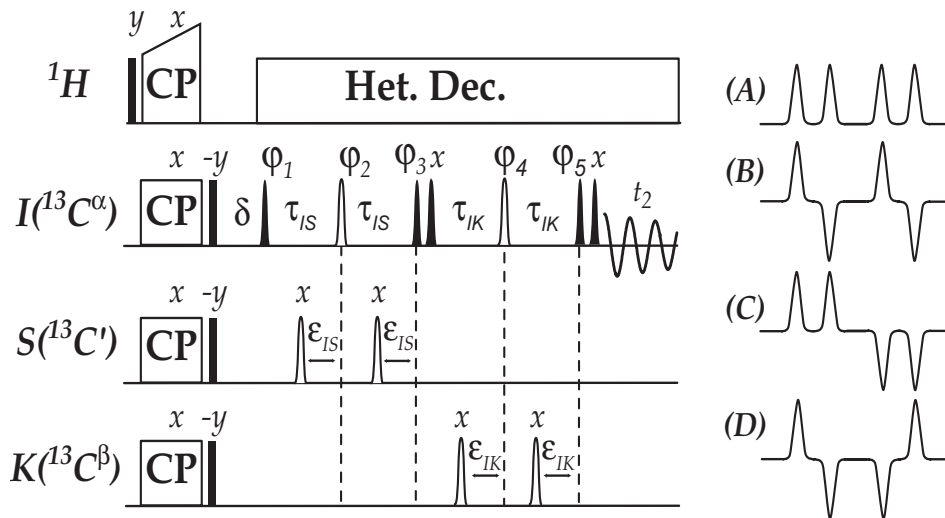

FIGURE 2.4: *Double IPAP pulse sequence to separately measure the four spin states of the I spin coupled to two other spins, denoted S and K. As for the IPAP pulse sequence, the delays $2\tau_{IS}$ and $2\tau_{IK}$ of the consecutive IPAP blocks are set to $(2J_{IS})^{-1}$ and $(2J_{IK})^{-1}$ in order to ensure an optimal spin-state selection. Four experiments are recorded with the parameters ε_{IS}, ε_{IK}, φ_3, and φ_5 set as described in TABLE 2.1. The obtained I-spin resonances are schematically depicted close to the pulse sequence. The phase cycle was as follows: $\varphi_1 = x$ -x, $\varphi_2 = x\,x\,y\,y$ -x -x -y -y, $\varphi_4 = = x\,x\,y\,y$ -x -x -y -y, $\varphi_{rec} = x$ -x -$x\,x$. (See TABLE 2.1 for φ_3 and φ_5.)*

TABLE 2.1: *Experimental parameters for the successive IPAP filters of the double IPAP experiment ($2\tau_{IS} = (2J_{IS})^{-1}$ and $2\tau_{IK} = (2J_{IK})^{-1}$).*

(A) [in-phase/in-phase]	$\varepsilon_{IS} = \tau_{IS}/2$	$\varepsilon_{IK} = \tau_{IK}/2$	$\varphi_3 = x$	$\varphi_5 = x$
(B) [in-phase/anti-phase]	$\varepsilon_{IS} = \tau_{IS}/2$	$\varepsilon_{IK} = 0$	$\varphi_3 = x$	$\varphi_5 = y$
(C) [anti-phase/in-phase]	$\varepsilon_{IS} = 0$	$\varepsilon_{IK} = \tau_{IK}/2$	$\varphi_3 = y$	$\varphi_5 = x$
(D) [anti-phase/anti-phase]	$\varepsilon_{IS} = 0$	$\varepsilon_{IK} = 0$	$\varphi_3 = y$	$\varphi_5 = y$

In terms of product operators,[111] these four experiments lead to the following signals:

$$\begin{cases} \sigma_{(A)} & \propto & I_y \\ \sigma_{(B)} & \propto & 2I_yK_z \\ \sigma_{(C)} & \propto & 2I_yS_z \\ \sigma_{(D)} & \propto & 4I_yS_zK_z \end{cases} \tag{2-2}$$

Schematic spectra illustrating this outcome are drawn next to the pulse sequence in FIGURE 2.4. The following linear combinations of these spectra yield each of the four CH resonance components:

$$\begin{cases} (A) + (B) + (C) + (D): & \sigma_{\alpha\alpha} & \propto & I_yS^\alpha K^\alpha \\ (A) - (B) + (C) - (D): & \sigma_{\alpha\beta} & \propto & I_yS^\alpha K^\beta \\ (A) + (B) - (C) - (D): & \sigma_{\beta\alpha} & \propto & I_yS^\beta K^\alpha \\ (A) - (B) - (C) + (D): & \sigma_{\beta\beta} & \propto & I_yS^\beta K^\beta \end{cases} \tag{2-3}$$

FIGURE 2.5a shows double IPAP spectra for the C^α resonance line of fully ^{13}C-labelled L-Alanine at 28 kHz magic-angle-spinning frequency. It is interesting to note that all four spin states thus isolated in the different subspectra of FIGURE 2.5b have the same linewidth at half-height (within the limit of uncertainty of the experiment), but noticeable different intensities. These intensity differences are not an artifact of the experiment because the sum of the four isolated transitions which corresponds in fact to the (A) experiment in FIGURE 2.5a, has essentially the same lineshape as the one obtained for a standard CPMAS experiment given in the FIGURE 2.5c and recorded with the same experimental parameters. These differential intensities could result from the interference of the ^{14}N quadrupole interaction with the ^{13}C - ^{14}N dipole-dipole interaction.[81]
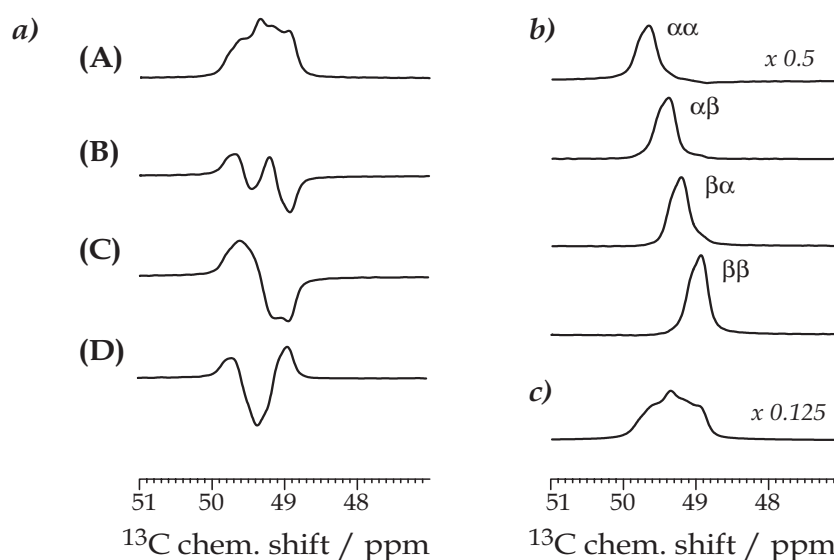
FIGURE 2.5: *Double-IPAP $^{13}C^\alpha$ spectra obtained at 28 kHz rotation frequency using the pulse sequence shown in FIGURE 2.4. a) $^{13}C^\alpha$ signals acquired with the four (A) - (D) experiments necessary for separating the spin states. Gaussian pulses of 800 μs were used for all semi-selective pulses. The delays $2\tau_{IS}$ and $2\tau_{IK}$ were set to match 9.26 ms and 14.706 ms. All other experimental parameters are similar to those indicated in the legend of FIGURE 2.3. b) Linear combinations of the four (A) - (D) spectra which provide the individual αα, αβ, βα, and ββ spin states of the $^{13}C^\alpha$ resonance. The exact combinations of the lines are indicated in the text (see Eq. 2-3). c) $^{13}C^\alpha$ resonance acquired with a standard CPMAS experiment using the same experimental parameters as for the double IPAP experiment.*

At first sight, it may appear strange that we can separate transitions which are not resolved in the carbon spectrum. Similar to the case of the refocused INADEQUATE experiment,[92, 112] it is in fact not the

apparent linewidth, $\Delta^* = 1/(\pi T_2^*)$ which is relevant for the state-selection efficiency of the filter, but the non-refocusable linewidth given by $\Delta' = 1/(\pi T_2')$ and measured in a spin-echo experiment.[92, 113] The time constant T_2' contains all non-refocusable interactions in addition to the spin-spin relaxation time constant T_2. It was shown[92, 114, 115, 116] that in most organic solids the carbon-13 apparent dephasing time T_2^* is dominated by refocusable interactions. In both crystalline and disordered solids, the non-refocusable carbon linewidth was found to be much narrower than the apparent linewidth, and generally smaller than the one bond homonuclear J-couplings.[92] Since the spin-state-selective filters we use here are all based on τ - π - τ evolution periods, it is the non-refocusable linewidth, $1/(\pi T_2')$, which is pertinent for the preparation of the selective spin states.

2.2.3   Selectivity and efficiency of the IPAP filter

It results from the spectra of FIGURE 2.3 that the selection of the spin states should be very useful for improving the resolution of the spectra. In cases where the J-coupling is well resolved, like for example the carboxyl lineshapes of fully ^{13}C-enriched L-Alanine at high spinning speeds, spin-state selection reduces by a factor of 2 the number of peaks. More importantly, for resonances where a relatively large J-coupling is not

resolved, like for example the C$^\alpha$ lineshapes, the selection of single spin states greatly reduces the linewidth. In the case of the CH resonance of L-Alanine (see FIGURE 2.3c) we obtained a linewitth reduction going from 30 to 40 % (depending on the rotor period) compared to that found in CPMAS spectra and measured in the same experimental conditions. The linewidths measured for the CH resonance of L-Alanine are summarised in TABLE 2.2 for the CPMAS spectra and the two separated spin states recorded with respect to the α and β carboxyl spin states at different magic-angle-spinning frequencies. Using the double IPAP pulse sequence, a 66 % resolution enhancement is achieved for the CH resonance when the linewidth of the isolated state transition is compared to the CPMAS lineshape.

TABLE 2.2: *Full widths at half height (Δ) of CH resonance in CPMAS spectra and for both CH selected transitions with respect to the carboxyl spin at different magic-angle-spinning frequencies.*

$\frac{\omega_r}{2\pi}$ / kHz	Δ_{CPMAS} / Hz	Δ_α / Hz	Δ_β / Hz
6	128	90	87
7	124	84	82
12	120	80	79
18	126	86	93
28	110	68	70
35	110	67	68

In order to efficiently implement spin-state selection in solid-state NMR of large and complex systems, like proteins, it is important that the sensitivity loss introduced by the addition of the selection filter be reasonable. Several factors have to be taken into account for the optimisation of the filter sensitivity, such as the total length of the pulse sequence or the choice and length of the semi-selective pulses which have to be as short as possible. Particularly, it was recently noticed that the quality of the decoupling sequence used during the refocusing period of the selection filter is decisive. In a very recent work, De Paëpe and coworkers have shown[26, 113, 116] that decoupling sequences achieving about the same efficiency in the direct dimension can show very different behaviour during the refocusing period. In FIGURE 2.6 we therefore compare the sensitivity of the IPAP spin-state selected spectra of L-Alanine obtained with the pulse sequence of FIGURE 2.1 using different decoupling schemes (i.e., CW,[117] TPPM-15,[74] and eDROOPY[1][26, 113]) for the heteronuclear decoupling. For the carboxyl resonance, the sensitivity loss due to the introduction of the IPAP filter is quite low (0 to 20 %) when eDROOPY is used. Intensity losses range from 30 to 70 % for C$^\beta$ and from 15 to 50 % for C$^\alpha$ depending on the rotation frequency (data not shown). The SPINAL[25] decoupling sequence gave comparable performance to eDROOPY. For all three resonances, the sensitivity of the spin-state selected spectra improves with increasing spinning frequency, and compared to the routinely used CW and TPPM decoupling sequences the sensitivity is significantly improved when eDROOPY or SPINAL are employed.

All these results have been obtained at the same main magnetic field (i.e., B$_0$ = 9.7 T). An interesting

---

[1]Note that eDROOPY decoupling sequence is currently known under the name of CM for *cosine modulation*.
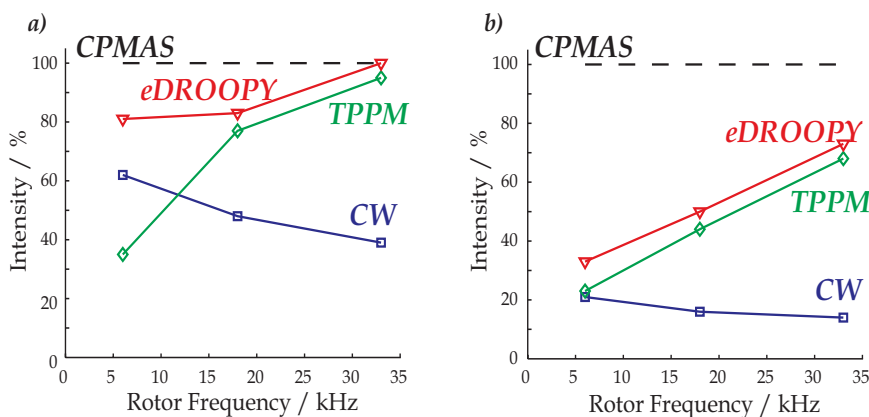
FIGURE 2.6: *Sensitivity of the IPAP experiment using different decoupling sequences with respect to the standard CPMAS experiment recorded with TPPM-15[74] decoupling sequence. The comparison is made for the $^{13}C'$ (a) and $^{13}C^{\beta}$ (b) resonances for 6, 18 and 33 kHz rotation frequencies. For this comparison, both IPAP and CPMAS experiments were acquired with the same total number of transients. For each resonance and spinning rate, the signal intensities were calibrated such to give 100 for the CPMAS experiment. The different decoupling sequences tested here were continuous wave (CW) decoupling,[117] TPPM-15[74] and eDROOPY.[26] The other experimental parameters were identical to those indicated in the legend of FIGURE 2.3.*

behaviour to explored is the performance, in terms of T_2', of the different decoupling schemes at low and high B_0 magnetic fields.

2.3 Other spin-state-selection filters

So far, we have considered in detail the IPAP selection filter on fully ^{13}C-enriched L-Alanine. The other known spin-state-selection filters, S3E[33] and DIPSAP,[34] work with the same type of evolution periods and will be investigated in this section.

The factors to be considered for the choice of the state-selection filter are the length of the filter sequence and its sensitivity to variations of the J-couplings. For example, for systems characterised by a short refocused relaxation time, the S3E filter[33] would be more appropriate due to its short length (two times shorter than IPAP). However, the filter sequence can not be abridged without any cost. Thus, the S3E filter has the drawback of being very sensitive to variations of the J-coupling. The DIPSAP sequence,[34] is a very efficient solution to the problem of large J-mismatch and for the particular cases where spin-state separation is desired for several spin pairs with different J-couplings. The sensitivity to J-mismatch of S3E,[33] IPAP[31,32] and DIPSAP[34] filters has been tackled by Brutscher.[34] The good compromise between the filter length and the tolerance to the J-coupling variations expected for IPAP is the reason why we chose to investigate in detail the IPAP filter.

2.3.1 Spin-state-selective excitation (S3E) filter

The principle of the spin-state-selective excitation was first presented by Meissner *et al.* in 1997.[33] In combination with E.COSY-type techniques,[118,119,120] S3E was established as a method well suited for the measurement of homonuclear and heteronuclear J-couplings of proteins in liquid-state NMR.

The original experiment[33] was adapted for its application to homonuclear systems using semi-selective pulses instead of the non-selective ones for heteronuclear spin systems. An additional π pulse on the S spin was added in order to refocus the transient Bloch-Siegert phase shifts effects[107] which could appear on the evolving spin due to the first π pulse on the S spin.

The circled numbers marked on the S3E filter element drawn in Figure 2.7 indicate time points which are used in the discussion below. The main part of the description of the S3E filter element is based on two works of Meissner and coworkers.[33, 99]

We consider a two-spin system with the spins denoted I and S and experiencing scalar coupling. The function of the S3E filter element can be described using the product operator formalism.[111] Thus, the magnetisation at the time point ① (i.e., after the first $\pi/2$ pulse on the I spin applied either along a 45° or a 5x45° axis) is given by:

$$\begin{cases} (-I_y + I_x)\frac{\sqrt{2}}{2} & \text{for } \varphi_1 = \pi/4 \\ (+I_y - I_x)\frac{\sqrt{2}}{2} & \text{for } \varphi_1 = 5\pi/4 \end{cases} \qquad (2\text{-}4)$$
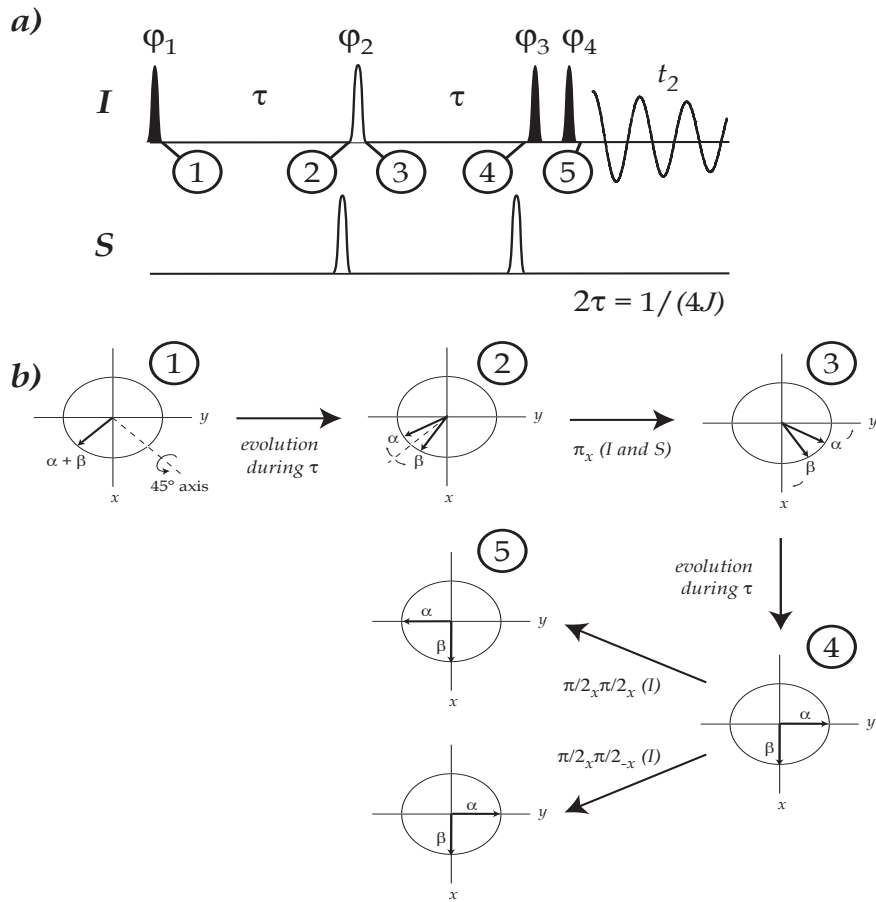
Figure 2.7: *a) S3E filter element adapted for solids for editing α and β components of the I spin in a homonuclear I - S pair system. The circled numbers represents time points discussed in the text. Filled and open shapes represent the $\pi/2$ and π semi-selective pulses. The delay 2τ was set to $1/(4J)$ and the following phase cycle was used in practice: $\varphi_1 = \pi/4 \ \pi/4 \ \pi/4 \ 5\pi/4$, $\varphi_2 = x$, $\varphi_3 = x \ y$, $\varphi_4 = x \ y \ \text{-}x \ \text{-}y$, $\varphi_{rec} = y \ \text{-}y$ -y y (A) - for selecting α transition, and $\varphi_{rec} = x \ \text{-}x$ (B) - for selecting β transition. b) Vector diagram illustrating the spectral editing with S3E.*

These two in-phase terms, shifted one with respect to the other by 90°, evolve under the scalar coupling during the τ - π - τ delay and yield:

$$\begin{cases} (+I_y \cos(2\pi J\tau) - 2I_x S_z \sin(2\pi J\tau)) + (+I_x \cos(2\pi J\tau) + 2I_y S_z \sin(2\pi J\tau))\frac{\sqrt{2}}{2} & \text{for } \varphi_1 = \pi/4 \\ (-I_y \cos(2\pi J\tau) + 2I_x S_z \sin(2\pi J\tau)) + (-I_x \cos(2\pi J\tau) - 2I_y S_z \sin(2\pi J\tau))\frac{\sqrt{2}}{2} & \text{for } \varphi_1 = 5\pi/4 \end{cases}$$
$$(2\text{-}5)$$

at time point ④. Since the filter delay 2τ is set to match $(4J_{IS})^{-1}$, the cosine and sine modulated terms are equal in intensity. Using the product operators notation (i.e., $I^\alpha = \frac{1}{2}\mathbf{1} + I_z$ and $I^\beta = \frac{1}{2}\mathbf{1} - I_z$, with $\mathbf{1}$ the identity operator), the magnetisation can be written as follows:

$$\begin{cases} +I_yS^\alpha + I_xS^\beta & \text{for } \varphi_1 = \pi/4 \\ -I_yS^\alpha - I_xS^\beta & \text{for } \varphi_1 = 5\pi/4 \end{cases} \tag{2-6}$$

In terms of a vector model, the relations of Eq. 2-6 can be represented in the rotating frame of the I spin by two vectors corresponding to the J-coupled spin S being either in the α or in the β state. The vector model diagram is outlined in FIGURE 2.7b only for the first value of the φ_1 phase. At time point ④, two successive $\pi/2$ pulses on the I spin are applied either with opposite or the same phase, in order to preserve or to invert the sign of the one of the two magnetisation vectors. The two magnetisation vectors can be furthermore added or subtracted, by an appropriate set up of the phase cycle, thus leading to individual transitions of the J-split doublet (i.e., I_xS^α, I_yS^β).

In the discussion above, both I_xS^β and I_yS^α components are kept in the transverse plane during the filter duration and an appropriate tunning of the phase cycle allows to select either the α or the β transition. The same results may be obtained if only one $\pi/2$ pulse is applied prior to acquisition (see FIGURE 2.8a), such as to put along z direction the unwanted component. Since the phase cycle of the first and last $\pi/2$ pulse on the I spin is important for canceling out pulse imperfections, the following four-step phase cycle has been used in practice:

$$\begin{array}{llllllll} & & \text{(A) experiment} & & & \text{(B) experiment} & & \\ \varphi_1 & = & \frac{\pi}{4} & \frac{\pi}{4} & \frac{5\pi}{4} & \frac{5\pi}{4} & \frac{\pi}{4} & \frac{\pi}{4} & \frac{5\pi}{4} & \frac{5\pi}{4} \\ \varphi_2 & = & x & & & & x \\ \varphi_3 & = & y & \text{-}y & & & x & \text{-}x \\ \varphi_{rec} & = & y & y & \text{-}y & \text{-}y & x & x & \text{-}x & \text{-}x \end{array} \tag{2-7}$$

The α and β transitions are directly selected by performing the (A) and (B) experiment, respectively. The filter diagram corresponding to the phase cycle given en Eq. 2-7 is outlined in FIGURE 2.8 together with the experimental results obtained for the carboxyl resonance of fully ^{13}C-enriched L-Alanine at 30 kHz spinning frequency.

The $\pi/2$ and π semi-selective pulses were all Gaussian of 300 μs length and 1 % truncation. The sequence was tested at high and low spinning frequencies on the C' resonance and the selection of the spin state was found to be satisfactory in both regimes with however almost perfect selection at high spinning speed. As the filter is very sensitive to the J-mismatch, we determined experimentally the effective scalar coupling by optimising both selection and sensitivity. Thus, we obtained an effective value of 52 Hz at 6 kHz MAS and 53 Hz at 30 kHz MAS by varying the constant associated to the scalar coupling from 50 Hz to 55 Hz with steps of 0.1 Hz (see FIGURE 2.8c and d). The residual on the non-selected transition was about 4 % at 30 kHz and 30 % at 6 kHz rotation frequency. A modulation of approximatively 1.2 Hz frequency was observed at 6 kHz MAS on the signal intensity (FIGURE 2.8c). The modulation is also present at high rotation frequency with the amplitude highly attenuated (FIGURE 2.8d). These last effects are not yet understood.

An obvious advantage of this filter element is its shortness (two times shorter compared to IPAP) which makes it very attractive for systems with rapid transverse relaxation. However, if the filter is not exactly matched to the true coupling value, the observed signal shows residual contribution because the undesired magnetisation component leaks through the filter. An alternative is the use of DISPAP filter, which was devised to be much less sensitive to J-coupling variations.

2.3.2 Double-in-phase single-anti-phase (DIPSAP) filter

The DIPSAP filter was introduced in 2001 by Bernhard Brutscher[34] as an attractive approach for the accurate measurement of small spin-spin coupling constants in molecules placed in anisotropic media.
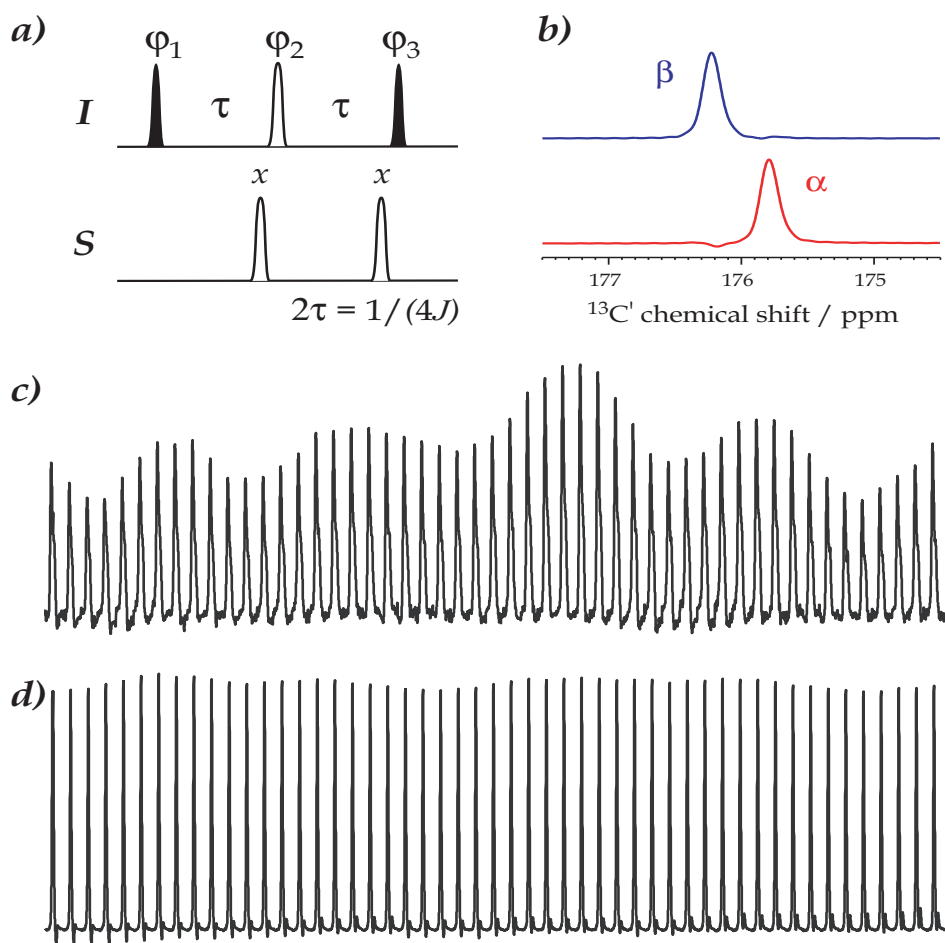
FIGURE 2.8: *a) Version of the S3E filter element adapted for homonuclear spin pairs. Filled and open shapes represent the π/2 and π semi-selective pulses which were all Gaussian shapes, 300 μs length and truncated at 1 %. The delay 2τ was set to 1/(4J). The phase cycle indicated in Eq. 2-7 was used in practice. SPINAL[25] decoupling sequence was applied on protons during the whole length of the filter and the acquisition time at a nutation frequency of 160 kHz. b) The selected α and β transitions of the C' resonance obtained at 30 kHz rotation frequency. Modulation of the C' signal with respect to the scalar coupling at 6 kHz (c) and 30 kHz (d). The curves go from 50 to 55 Hz, with steps of 0.1 Hz.*

Compared to the above mentioned spin-state-selective filters, DIPSAP has a significantly reduced sensitivity to J-mismatch over a wide range of effective coupling constants.

       The spin-state selection with DIPSAP consists in recording three separate experiments with the following settings:

$$
\begin{cases}
\text{(A)} & \varepsilon = \tau/2, \quad \varphi = x \\
\text{(B)} & \varepsilon = 0, \qquad \varphi = x \\
\text{(C)} & \varepsilon = \tau/4, \quad \varphi = y
\end{cases}
\tag{2-8}
$$

The filter length has to be set to $2\tau = 1/J$ (instead of $2\tau = 1/(2J)$ for IPAP). The scalar coupling evolution during the filter is refocused for the (A) experiment while the scalar coupling evolves for an effective period of 2τ and τ for the (B) and (C) experiment, respectively. The subspectra associated to the separated spin states are obtained by the linear combination $k\text{x(A)} + (k-1)\text{x(B)} \pm \text{(C)}$ with $k = 0.73$, the theoretically optimised scaling factor.

       Based on the IPAP approach, the DIPSAP filter achieves the J-mismatch compensation by recording two in-phase spectra, one with a higher and one with a lower intensity than the related anti-phase spectrum.
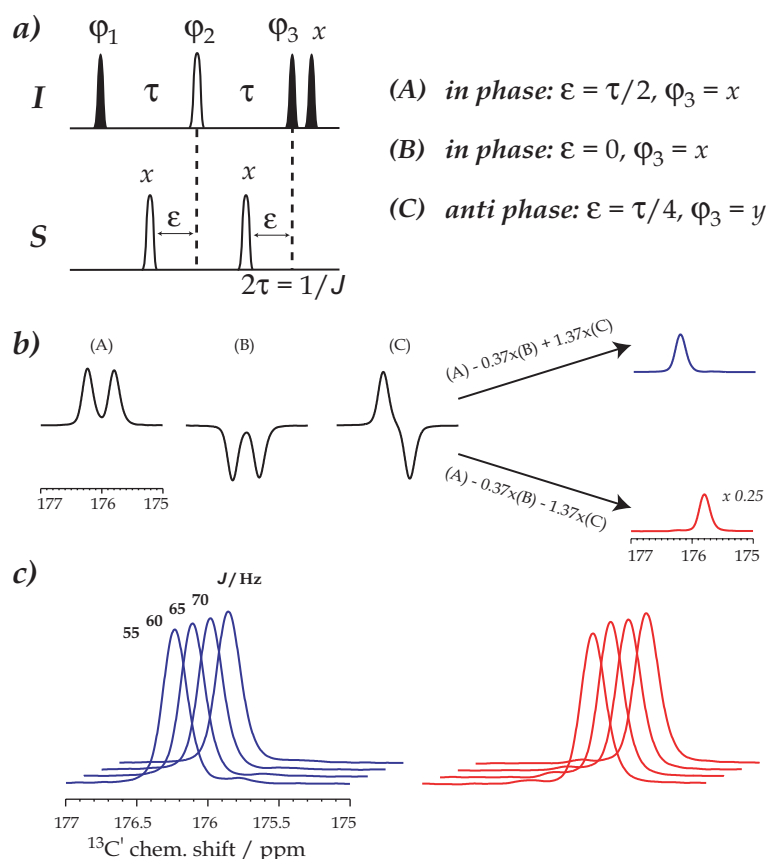
FIGURE 2.9: *a) DIPSAP filter element adapted for homonuclear spin pairs. Filled and open shapes correspond to the semi-selective π/2 and π pulses. They were all chosen Gaussian, 800 μs long and truncated at 1 %. The delay 2τ was set to 1/J. In practice, three experiments have to be recorded with the experimental parameters set up as summarised in Eq. 2-8. For the whole duration of the DIPSAP filter and acquisition period, SPINAL[25] decoupling sequence was used in order to decouple the protons from carbons. The nutation frequency was optimised to 160 kHz. The rotation frequency was 23 kHz MAS. b) Separately recorded (A), (B) and (C) experiments and the individually selected α and β transitions obtained by the linear combinations (i.e., (A) - 0.37x(B) ± 1.37x(C), which corresponds to a k factor of 0.73). c) Selected α and β transitions of the C' resonance illustrating the robustness of DIPSAP sequence with respect to the J-mismatch.*

Thus, the intensity between the in-phase and anti-phase spectra responsible for the detection of the residual peak at the position of the suppressed doublet component should be the same.

The filter element we used for spectral editing with DIPSAP is drawn in FIGURE 2.9a. The semi-selective pulses were all Gaussian, 800 μs long and truncated at 1 %. The scalar coupling was set to 54 Hz for the C' - C^α spin pair and 34 Hz for the C^β - C^α pair system. It was applied to all three carbon resonances of uniformly ^{13}C-enriched L-Alanine at 23 kHz rotation frequency. Only the results obtained for C' resonance are shown in FIGURE 2.9b. The selection is very good for the carboxyl resonance. The same selection efficiency has been expected for the methyl resonance as well. However, a residual of about 15 % leaks through the filter despite setting the effective scalar coupling equal to the value measured in liquid state; it also corresponds to the J-value used for setting the IPAP filter. One possible reason could be the sensitivity to pulse imperfections.

Due to its long duration, the DIPSAP filter element is expected to be less sensitive than IPAP. Since the sequence is highly insensitive to variations of the J-coupling, a judicious choice of the refocusing 2τ period would consist in a good compromise between J-mismatch and sensitivity losses. For example, the selection of

the C' transitions is still acceptable for effective scalar couplings of 70 Hz, which represents a J-mismatch of approximatively 27 % and results in a reduction of the filter length of about 4 ms. However, the filter duration is not the only difference between DIPSAP and IPAP filters which contributes to the sensitivity losses. The additional in-phase spectra recorded for DIPSAP and the unequal numerical weighting of the two in-phase spectra also reduce the sensitivity of the DIPSAP filter.

Now that the spin-state-selective techniques have been introduced, it may be interesting to compare one with respect to the other in terms of sensitivity. The transverse relaxation is another important aspect which must be evaluated. We mentioned previously that the sensitivity of the different spin-state-selective techniques depends on the J-mismatch and the total number of experiments. Since the DIPSAP filter consists in the linear combination of spectra with different numerical weights, it additionally depends on the scaling factor k. The normalised signal amplitude of the spectra recorded for S3E, IPAP and DIPSAP techniques is given by:[34]

$$\begin{cases} \text{(A)} & \cos(\frac{\pi}{4}f_{mis}) & \text{(B)} & -\sin(\frac{\pi}{4}f_{mis}) & & \text{for S3E} \\ \text{(A)} & 1 & \text{(B)} & +\cos(\frac{\pi}{2}f_{mis}) & & \text{for IPAP} \\ \text{(A)} & 1 & \text{(B)} & -\cos(\pi f_{mis}) & \text{(C)} & \cos(\frac{\pi}{2}f_{mis}) & \text{for DIPSAP} \end{cases} \quad (2\text{-}9)$$

where f_{mis} factor is given by the $(J^{eff} - \overline{J})/\overline{J}$. $\overline{J}$ is the J-coupling used for setting the spin-state-selective filter whereas J^{eff} is the effective J-coupling which is assumed here to be constant throughout the sample [2]. In order to calculate the sensitivity of the selected transition we have to consider the same total number of transients (NS) for each spin-state-selection filter and to normalise the signal-to-noise ratio for equal noise level. We obtain therefore the following relations for the normalised signal-to-noise ratio of the selected transition:

$$\begin{cases} [\frac{S}{N}]^{sel} & = & \cos(\frac{\pi}{4}f_{mis})\sqrt{\frac{NS}{2}} & \text{for S3E} \\ [\frac{S}{N}]^{sel} & = & \frac{[1+\cos(\frac{\pi}{2}f_{mis})]}{\sqrt{2}}\sqrt{\frac{NS}{2}} & \text{for IPAP} \\ [\frac{S}{N}]^{sel} & = & \frac{[0.73+0.27\cos(\pi f_{mis})+\cos(\frac{\pi}{2}f_{mis})]}{\sqrt{0.73^2+0.27^2+1}}\sqrt{\frac{NS}{3}} & \text{for DIPSAP} \end{cases} \quad (2\text{-}10)$$

Since both x and y components contribute to the starting magentisation in the S3E technique, its sensitivity is additionally increased by a $\sqrt{2}$ factor relative to IPAP and DIPSAP filters. So, in the case of very small J-mismatch (i.e., f-mismatch ~ 0), the normalised sensitivity of S3E and IPAP spin-state-selective filters will be the same.

2.3.3   INADEQUATE-CR

The original INADEQUATE[103, 104, 105] experiment is undoubtedly one of the most attractive NMR experiments for tracing out the connectivities between pairs of covalently bound carbon atoms. The sensitivity enhancement principle of INADEQUATE experiment was introduced in 1995 by Nielsen and coworkers[35] and consists in concentrating the intensity of the single-quantum doublets to only one of the two lines. Thus, on an equal experimental time basis, the sensitivity of the new approach based on composite refocusing (CR) was found 2 times larger than the conventional method. Moreover, a $\sqrt{2}$ factor can also be recovered by merging[121] the left and right spectra[3] obtained with the CR approach (i.e., INADEQUATE-CR). This sensitivity enhancement makes the technique even appealing for the detection of ^{13}C - ^{13}C DQC in natural abundance samples. Adapted also for solid-state NMR, the INADEQUATE experiment[122, 123] is a valuable probe for through-bond connectivity in both inorganic[124, 125, 126] and organic solids.[106, 114] The refocused INADEQUATE experiment provides enhanced sensitivity as well for the common cases where the refocused linewidth (Δ') is smaller than the apparent linewidth (Δ*), and has been applied to various spin systems.[92, 112, 116, 127, 128, 129]

Compared to the previously introduced spin-state-selection filters, the INADEQUATE-CR approach is limited to homonuclear spin systems and uses non-selective pulses. The pulse sequence we experimentally used

---

[2]Note that it may vary from site to site for particular samples.
[3]Coaddition after shifting by $J_{CC}/2$ and - $J_{CC}/2$.

is drawn in FIGURE 2.10. The INADEQUATE-CR block is identical to the original version introduced in liquid state by Nielsen *et al.* and applied to solids by Verel *et al.*.[36] The first part of the INADEQUATE-CR block converts magnetisation of the ^{13}C spins into DQC. An appropriate choice of the phase cycle selects the ^{13}C - ^{13}C DQC and suppresses the magnetisation coming from isolated ^{13}C spin systems. As the DQCs are not directly observable, they have to be converted back into SQCs. To optimise the sensitivity of the experiment, nothing has to be lost into other coherences during the coherence transfer period. This is done by the composite refocusing block which concentrates the entire magnetisation into only one of the doublet lines of the ^{13}C - ^{13}C two-spin system. It was demonstrated[130,131] that maximum coherence transfer efficiency is performed when $\pi/\sqrt{2}$ selective rotations are applied to one of the doublet lines of the two spins. Since the non-selective experiments are more convenient than experiments employing frequency-selective pulses, an important step in the design of this type of technique is the conversion of the selective rotations into non-selective pulse versions. For the DQ to SQ coherence transfer, a non-selective version exists and is shown in shaded box in FIGURE 2.10. In practice, the two experiments are obtained by setting the filter delay 2τ to $1/2J_{IS}$ which leads to $1.5/J_{IS}$ as total length of the experiment (i.e., 3 times longer than IPAP).
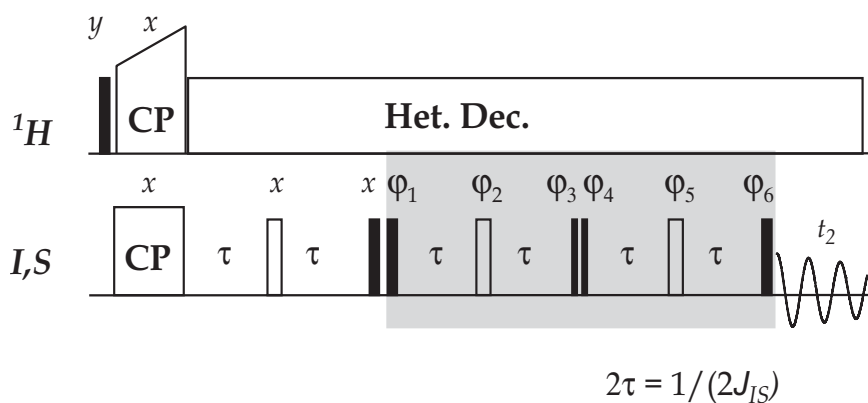

$$2\tau = 1/(2J_{IS})$$

FIGURE 2.10: *The solid-state INADEQUATE-CR pulse sequence. The 2τ was set to $1/(2J_{CC})$ in order to maximise the degree of conversion into double quantum coherence and the composite refocusing. The gray box represents the part performing the composite refocusing. The phase cycle was: $\varphi_1 = x$ -x, $\varphi_2 = y\,x\,x\,y$, $\varphi_3 = 2y\,2(-y)$, $\varphi_4 = 2x\,2(-x)\,2(-x)\,2x$ (α state) $\varphi_3 = 2(-y)\,2y$, $\varphi_4 = 2(-x)\,2x\,2x\,2(-x)$ (β state), $\varphi_5 = 2(x\,x\,y\,y)\,2(y\,y\,x\,x)$, $\varphi_6 = 4(-y)\,4y\,4y\,4(-y)$, $\varphi_{rec} = 8x\,8(-x)$. By adding a z filter before the INADEQUATE-CR block, the residual transverse magnetisation is slightly reduced.*

The pulse sequence was applied to C' - C^α and C^β - C^α spin pairs in uniformly ^{13}C-enriched L-Alanine. The results obtained for the carboxyl and methyl resonances in L-Alanine are shown in FIGURE 2.11 for a variety of spinning frequency. Owing to its long length, a poor sensitivity is expected with respect to the CPMAS experiment. At high spinning frequency, satisfactory sensitivity and selectivity are obtained for the carboxyl resonance. The residual intensity observed at the position of the suppressed line was quantified to $\sim$ 15 % at 28 kHz and $\sim$ 5 % at 33 kHz MAS, respectively. On the other hand, the methyl resonance reveals a completely different behaviour. If the lower sensitivity compared to that obtained for carboxyl can be explained by relaxation losses during 44 ms filter length, which represents 16 ms more than the carboxyl filter duration, no explanation has been found for the completely inefficient state selection over the whole range of spinning rates used. INADEQUATE-CR experiment has been shown to work only for two spin systems[36] and since the methyl resonance is dominated at low spinning speed by three-spin terms (see chapter 1), the selection inefficiency in this regime wouldn't be such unexpected. However, the experiments recorded at high MAS are completely astonishing because at these frequencies the methyl resonance is expected to be dominated by two-spin terms. As for the quite low sensitivity we get at low spinning frequency, it could also be a consequence of the non-synchronisation of the τ delay with the rotation period.

Due to the various pulses, the pulse sequence is prone to artifacts coming from rf inhomogeneity and
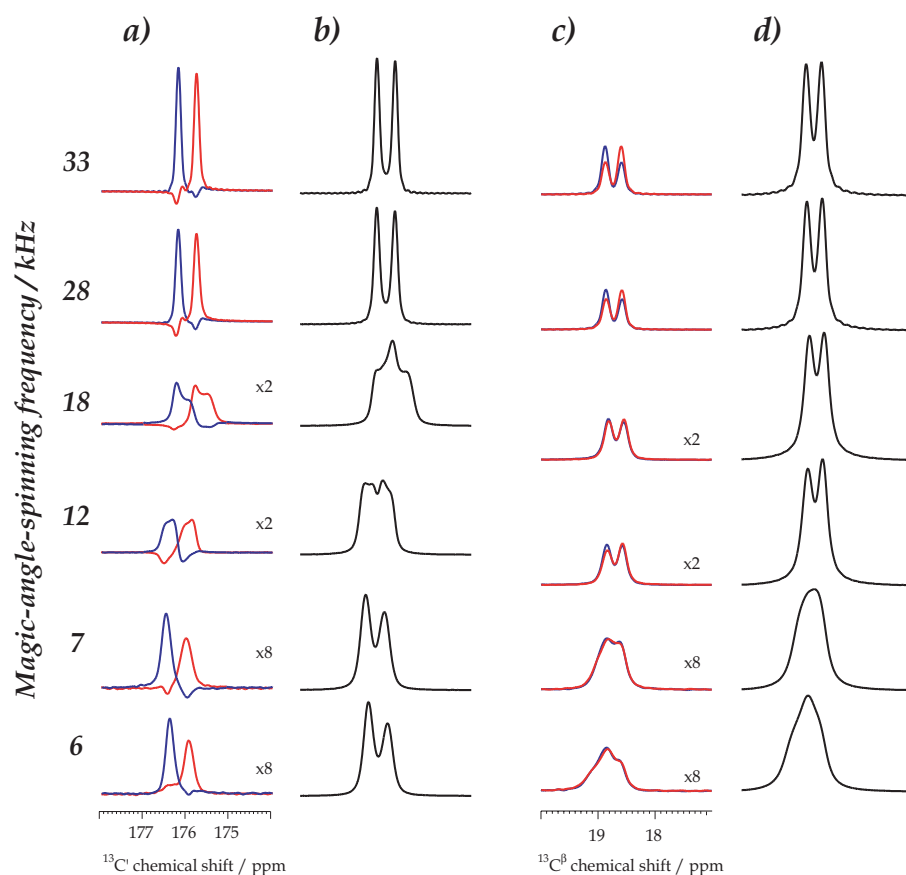
FIGURE 2.11: *INADEQUATE-CR selected spin states for the carboxyl (a) and methyl (c) resonances of uniformly ^{13}C-enriched L-Alanine. These individual transitions are compared to the standard CPMAS C' (b) and C^β (d) resonances acquired with the same number of transients. Using the INADEQUATE-CR approach, a good and sensitive state selection is only obtained for the C' resonance at high spinning frequencies. When off rotational resonance conditions are approached (i.e., at 12 and 18 kHz rotation frequency), the reintroduction of the dipole-dipole carbon interactions results in a broadening of the carbon lines and consequently decreased efficiency. On the other hand, there is no state selection for the methyl resonance at any of the rotation frequencies used. The sensitivity is also lower than that obtained for the C' resonance, but this is due to relaxation losses during the longer filter (i.e., 44 ms for methyl instead of 28 ms for carboxyl spin). All these results were obtained without synchronysing the τ delay with rotation period. This could additionally explain the small sensitivity obtained at low MAS.*

resonance offset effects. These can however be compensated by using composite pulses[132, 133] (i.e., a small number of successive pulses with different phases which has the same effect as a single rf pulse in the ideal case where rotations are all perfect). We tested on carboxyl resonance a couple of π composite pulses without remarking significant improvement in the selection of the spin state. For example, the carboxyl resonance transitions obtained either with a conventional INADEQUATE-CR experiment or with a compensated version of the experiment in which all the π pulses were replaced by the composite pulse $P = (2\pi)_0(\pi)_{120}(\pi)_{60}(\pi)_{120}$ are shown in FIGURE 2.12. The compensated pulse sequence is expected to be less sensitive to both rf field inhomogeneity and resonance offset effects. The rf amplitude on carbon channel was larger enough (i.e., carbon nutation frequency set to approximatively 60 kHz and the main magnetic field is homogeneous) such as to neglect the offset resonance effects.
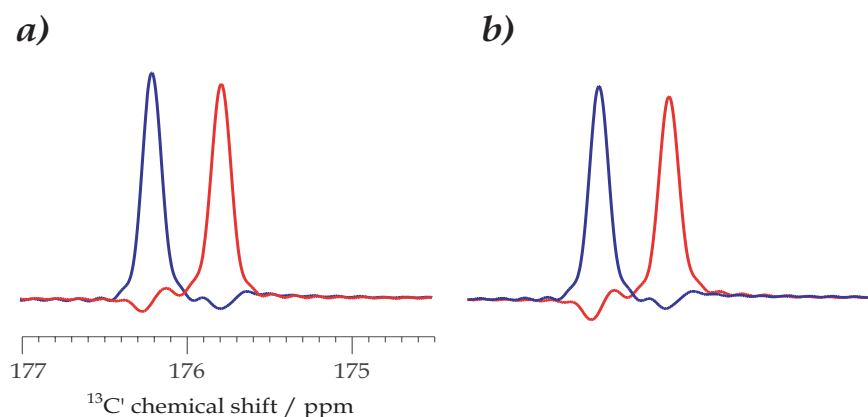
FIGURE 2.12: *C' transitions selected with INADEQUATE-CR pulse sequence with (a) and without (b) composite pulses.*

2.4 Conclusion

It has been illustrated in the present chapter the possibility of using spin-state selection in solid-state NMR. Originally introduced in liquid-state NMR for the measurement of scalar and residual dipolar couplings, the spin-state-selective techniques are found remarkably attractive when applied to homonuclear spin pairs for improving the resolution in spectra of fully isotopically enriched compounds. In addition, they can be used as probes for directly investigating the individual transitions of carbon lineshapes of fully ^{13}C-enriched L-Alanine.

By adapting the heteronuclear liquid-state NMR selection filter IPAP,[31,32] all the transitions of the three carbon resonances in fully ^{13}C-labelled L-Alanine can be individually obtained. The separation of the homonuclear spin-states is very good over a large range of rotation frequencies. Thus, significant resolution enhancement was obtained in the carbon spectra of fully enriched compounds, even for resonances where the multiplet structure is not resolved. The different conditions (i.e., type and length of the semi-selective pulse and choice of the most efficient decoupling scheme) relevant for the sensitivity of the experiment were considered in detail for the IPAP selection filter. As for the other selection filters, they should be affected in a similar way. The introduction of the state-selective filter leads to acceptable intensity losses which can be minimised by the use of appropriate heteronuclear proton decoupling schemes. Therefore, the advances made in optimising spin-state-selection experiment can be used even further for improving the spectral resolution of multidimensional spectra, as will be illustrated in the next chapter.

Application of spin-state-selection techniques to resolution improvement of multidimensional correlation experiments in solid-state NMR spectroscopy of proteins

3.1 Introduction

In the preceding chapter, we have shown that single-transition selection can be achieved, by means of semi-selective pulses, in homonuclear scalar-coupled systems like ^{13}C - ^{13}C spin pairs of uniformly ^{13}C-enriched L-Alanine. The efficiency and the degree of selection of spin-state-selective techniques were found to be sufficient to apply them to biomolecular systems in multidimensional correlation experiments. In addition, a major advantage of state-selection techniques when applied to solids is that they are not restricted to lines with resolved J-splitting.

High-resolution spectra can currently be obtained for microcrystalline uniformly isotopically enriched biomolecules thanks to the important advances made during the last few years in the field of solid-state NMR. As a confirmation, in 2002, the first protein structure has been solved by solid-state NMR.[46] More recently, an almost complete sequential assignment has been reported for the dimeric form of the Crh protein containing 2x85 amino acids (i.e., 2x10.4 kDa molecular weight) involved in carbon catabolite repression in *Bacillus subtilis*.[47] However, spectral resolution remains one of the principal factors limiting the study of larger biological systems.

The ^{13}C - ^{13}C J-couplings constitute a significant contribution to the linewidth in magic-angle-spinning spectra of uniformly ^{13}C-labelled proteins. J-decoupling techniques[37,97] for solid-state NMR using semi-selective pulses can be considered for improving the resolution in indirectly detected dimensions. We will show in this chapter, that resolution enhancement can be achieved in both direct and indirect dimensions if spin-state selection is combined with transition-selective transfer schemes in multidimensional solid-state NMR correlation experiments of ^{13}C-labelled proteins. The single-transition-selection approach will therefore allow to remove the line broadening due to the $^{1}J_{CC}$ spin couplings in both dimensions of a two-dimensional ^{13}C - ^{13}C correlation experiment.

In order to perform a spin-state-selective multidimensional correlation experiment for an IS spin-1/2 system, the selected transition of the first spin, I, evolving during t_1 period has to be transferred to a single transition of the coupled spin, S, by means of an appropriate mixing sequence. In liquid-state NMR, the spin-state-selective coherence transfer is usually obtained through zero-quantum (ZQ) or double-quantum (DQ) π rotations.[99] A ZQ π rotation "conserves" the spin state: $I_x S^\alpha \rightarrow I^\alpha S_x$, and a DQ π rotation "reverses" the spin state: $I_x S^\alpha \rightarrow I^\beta S_x$. $I_x S^l$, with $l = \alpha, \beta$, represents the transition of the I spin when the S spin

is in the state l. In the liquid state, spin-state-selective coherence transfer is obtained using planar mixing, S^3CT building blocks[100] or frequency-switched single-transition cross polarisation.[95, 134] Similar J-based spin-state-selective transfer techniques could be envisaged in the solid state as well. However, since the dipolar interaction is stronger than the indirect spin-spin coupling, a transfer driven by the dipolar coupling would be more efficient and therefore more appropriate for many solid-state applications. As most of the various solid-state dipolar correlation techniques under MAS are based on a ZQ or a DQ average Hamiltonian, they may be directly used for spin-state-selective polarisation or coherence transfer. Common examples of such sequences are proton-driven spin diffusion (PDSD),[50] RFDR,[54] and RIL-ZQT[135, 136] with a ZQ average Hamiltonian, and C7,[56] POST-C7,[57] SPC5,[58] and DREAM[29] with a DQ average Hamiltonian.

3.2 Single-transition transfer

Before extending the spin-state-selection techniques to two-dimensional experiments, we first investigated the selective-transfer step. The pulse sequence used for this purpose is drawn in FIGURE 3.1. Throughout this chapter we restrict to the use of IPAP[31, 32] as spin-state-selective filter but S3E[33] or DIPSAP[34] can also be employed.
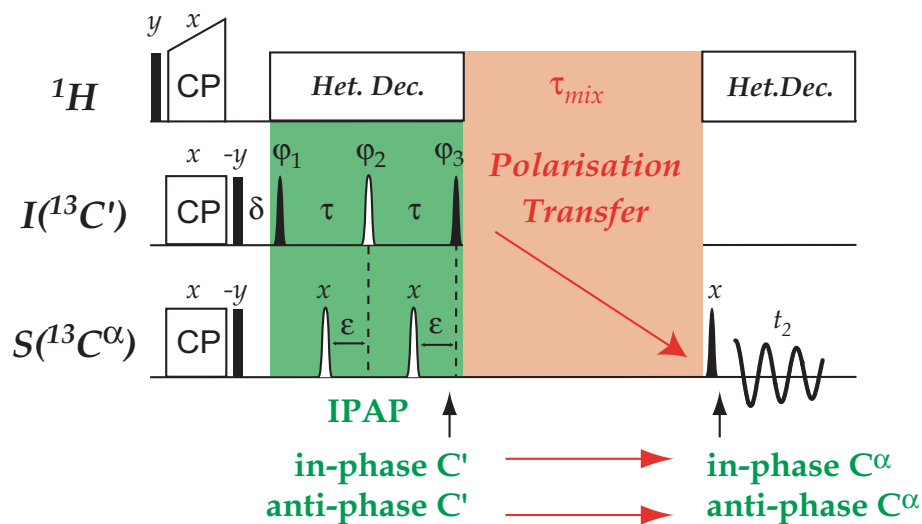

FIGURE 3.1: *1D pulse sequence for checking out the selective transfer step on fully ^{13}C-enriched L-Alanine. $\pi/2$ and π rf pulses are represented by filled and open bars (hard) or shapes (semi-selective). All pulses are applied along the x axis unless indicated. An 16-step phase cycle was applied with $\varphi_1 = 4x\ 4(-x)$, $\varphi_2 = x\ y\ -x\ -y$, $\varphi_3 = 8x\ 8(-x)$, $\varphi_{rec} = x\ -x\ -x\ x\ x\ -x\ x\ x\ -x\ -x\ x\ x\ -x\ x\ -x\ -x\ x$. The magnetisation is selectively prepared on C', transferred to C^α and put in the xy plane for detection. The setup of the IPAP filter is identical to that used in the previous chapter: $\varphi_3 = 2x\ 2(-x)$, $\varepsilon = \tau/2$ – for in phase – and $\varphi_3 = 2y\ 2(-y)$, $\varepsilon = 0$ – for anti phase. Thus, two experiments are recorded for the in-phase and anti-phase settings. The prepared in-phase I magnetisation is transferred and detected as in-phase S magnetisation and anti-phase I magnetisation as anti-phase S magnetisation, respectively.*

In a schematic representation, after cross polarisation, the selective preparation leads to a non-equilibrium Zeeman polarisation at the beginning of the mixing time. In the rotating frame, the polarisation transfer during the mixing period is performed by the dipolar part of the spin Hamiltonian. The polarisation at the end of the mixing period is converted, by the semi-selective pulse applied at the frequency of the S spin, to single-quantum S coherence which is further detected. The spin Hamiltonian during the mixing time is usually described by two terms associated to an evolution in either a ZQ or a DQ subspace.[137] For example, for a ZQ mixing sequence, the evolution occurs only in the ZQ subspace and corresponds to the rotation of a virtual spin-1/2 vector, originally oriented along the z axis of the coordinate system, around the x axis of the ZQ subspace.

In a powder, the individual evolution of each crystallite in the ZQ subspace corresponds to an exact π rotation. However, when we consider the evolution of the ensemble of crystallites, this evolution does not correspond any more to an exact π rotation. Thus, owing to the powder average, the rotation in the ZQ or the DQ subspace does not correspond to an exact π rotation.

Among the many existing homonuclear dipolar recoupling methods which can be used for performing the transfer of polarisation, we chose to use PDSD[50] as ZQ-recoupling sequence and DREAM[29,30] as DQ-mixing scheme. Since no rf is applied during the mixing time of the PDSD sequence, it is appealing for those samples requiring limited rf irradiation time. However, when dealing with spin pairs, this scheme suffers from low transfer efficiency because the polarisation is transferred throughout the sample. This can be optimised by performing the polarisation transfer with adiabatic homonuclear recoupling schemes.[29] The major advantage of the adiabatic methods is their enhanced polarisation transfer efficiency: in theory, an efficiency of 100 % is expected for isolated spin-1/2 pairs. During the last few years, a couple of homonuclear adiabatic polarisation transfer schemes, exploiting either the ZQ[138] or the DQ[29,30] spin Hamiltonian, have been developed. We concentrate here on the homonuclear DQ scheme called DREAM[29,30] (Dipolar Recoupling Enhanced by Amplitude Modulation) which is based on adiabatic amplitude sweep through the DQ-HORROR[139] recoupling condition ($\omega_r = 2\omega_1$). Actually, under fast MAS, the time-independent (i.e., secular) part of the dipolar Hamiltonian, which is usually averaged by the sample spinning, is reintroduced by the irradiating field amplitude modulation. Note that the efficiency of the DREAM mixing sequence increases with increasing spinning frequency.

Since we use IPAP as selection filter, for any of the transfer schemes introduced earlier, a set of two experiments has to be acquired. In practice, for a given mixing time, two spectra corresponding to in-phase and anti-phase IPAP settings are recorded.

In all standard transfer experiments, the efficiency of the polarisation transfer depends on the duration of the mixing period. Let us now try to find out how the selective transfer behaves with respect to the the mixing time. For this purpose, the pulse sequence displayed in FIGURE 3.1 with PDSD as transfer scheme was applied to powdered fully ^{13}C-enriched L-Alanine. The C^α buildup curves with respect to the mixing time are reported in FIGURE 3.2 for in-phase and anti-phase spectra.

For simplicity, in the discussion bellow, a two IS (C'C^α) spin-1/2 system will be first considered. The results drawn in FIGURE 3.2 show that in-phase I magnetisation transfers into in-phase S magnetisation and anti-phase I magnetisation transfers into anti-phase S magnetisation, respectively. We may also remark that in-phase transfer function is different and that it depends on the mixing time. The in-phase S signal grows up with τ_{mix} whereas the anti-phase S signal drops down. This indicates that, during the mixing period, the I_z (C') selected polarisation is gradually transferred through the dipolar coupling to the spin S (C^α) and, after reaching a maximum associated to the optimum mixing time, decays under the effect of the longitudinal relaxation. On the other hand, the anti-phase signal associated with the two-spin order term $2I_zS_z$ is not affected by the dipolar coupling and is only decaying under the effect of longitudinal relaxation.

In terms of product operator formalism,[111] these two transfer processes may be expressed as follows: [1]

$$\begin{cases} I_z & \to & a\,S_z & \text{in-phase experiment} \\ 2I_zS_z & \to & b\,2S_zI_z & \text{anti-phase experiment} \end{cases} \tag{3-1}$$

The functions a and b incorporate the $e^{-\tau_{mix}/T_1}$-term which accounts for the longitudinal relaxation. If now we would have the same transfer function for both in-phase and anti-phase signals, the S transitions could be then separated by simply adding and subtracting the transfer-induced S spectra. We saw that in reality, since only the in-phasesignal is transferred, an accurate spin-state selection will be obtained, by adding and subtracting the in-phase and anti-phase spectra, for only one τ point which actually corresponds to the crossover of the two transfer curves (see FIGURE 3.2). Despite the different transfer functions, a proper spin-state selection can

---

[1]This kind of transfer occurs in a doubly ^{13}C-labelled samples or fully ^{13}C-enriched Glycine.
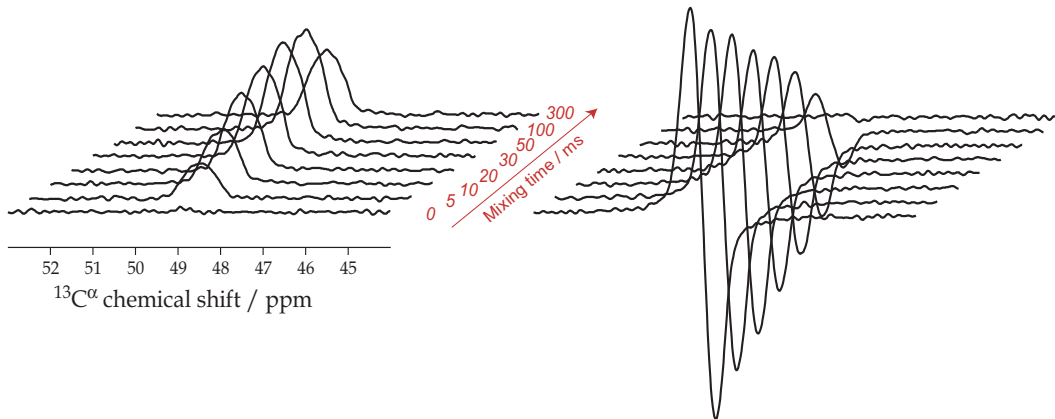
F<small>IGURE</small> 3.2: *C^α buildup curves for in-phase and anti-phase experiments with PDSD[50] as polarisation transfer sequence. The spinning frequency was set to 7 kHz and τ_{mix} was varied from 0 to 300 ms. The experiments were performed on a 11.7 T Bruker Avance spectrometer equipped with a double resonance 4 mm probehead. The spectra were obtained using standard cross polarisation, with a ramped spin lock on the proton channel for broadening Hartmann-Hahn condition.[23, 24, 71, 72, 73] The CP contact time was 1 ms and the proton and carbon rf frequencies were set to 71 and 60 kHz, respectively. The acquisition time was 50 ms and the recycle time 4 s. TPPM-15[74] with a proton nutation frequency of 100 kHz was used during the IPAP filter and acquisition period. The semi-selective pulses were all Gaussian of 1 ms length and truncated at 1 %. A z filter of 5 ms has been applied before the IPAP filter in order to remove any residual transverse magnetisation. The length of the spin-state-selection filter was experimentally optimised to 2τ = 9.32 ms. No exponential broadening was applied prior to Fourier transform.*

be obtained for all τ_{mix} values, if the relative amplitude of the anti-phase spectra with respect to the in-phase spectra is adjusted by an appropriate scaling factor k.

So far, we have restricted our discussion to a pair system and have neglected the third spin (i.e., C^β). This is a rough approximation for the fully ^{13}C-enriched L-Alanine sample we used for the experiments presented in F<small>IGURE</small> 3.2. Thus, a ISK spin-1/2 system, with spin S being indirectly coupled to the spins I and K, would be more adapted for the investigation of the selective polarisation transfer effect from the spin I to the spin S in fully ^{13}C-labelled L-Alanine. Thus, for both in-phase and anti-phase settings, we expect to have a transfer of polarisation from the spin I to the spins S and K. In fact, during the mixing period, the I_z (C') selected polarisation would be transferred through the dipolar coupling to the other spins S_z (C^α) and K_z (C^β), respectively. As for the two-spin order $2I_zS_z$ term, it would give rise to two additional terms: $2I_zK_z$ and $2S_zK_z$. If only the spin S is put back into the plan xy for detection, then the resultant in-phase and anti-phase magnetisations are given by:

$$\begin{cases} \sigma_{\text{in phase}} & \propto \quad a\ S_y \\ \sigma_{\text{anti phase}} & \propto \quad b\ 2S_yI_z + c\ 2S_yK_z \end{cases} \quad (3\text{-}2)$$

with a, b and c again functions depending on the mixing time which characterise the in-phase and anti-phase signals. Thus, the initial in-phase I magnetisation is transferred into in-phase S magnetisation and the starting anti-phase I signal is assumed to give rise to two anti-phase S components, one being anti-phase with respect to the spin I and other being anti-phase with respect to the spin K. The resulting anti-phase S magnetisation is therefore a mixing of these two components with b and c two different functions describing the relaxation decay during the τ_{mix}. So, the product operator description presented above proves that even for a three spin system, the S magnetisation recorded with the anti-phase settings still gives rise to an anti-phase signal. The pulse sequence outlined in F<small>IGURE</small> 3.1 would allow to detect only the anti-phase S component with respect to the spin I if the final semi-selective pulse on the S spin is replaced by one acting simultaneously on S and K.

Let us now investigate the effect of the selective transfer of polarisation from the spin I to the spin K. It can be observed by adapting the pulse sequence in F<small>IGURE</small> 3.1 for detecting the K spin single-quantum

coherence instead of that of spin S. In practice, this is performed by applying a semi-selective $\pi/2$ pulse at the K-spin frequency. The C^β buildup curves therefore obtained are drawn in FIGURE 3.3. They show behaviours similar to that obtained for the C^α resonance. However, the anti-phase C^β signal is decaying more rapidly than the anti-phase C^α one. Since the anti-phase C^β magnetisation contains a single anti-phase component, the rapid decay of the anti-phase signal is probably due to the T_1 methyl relaxation.
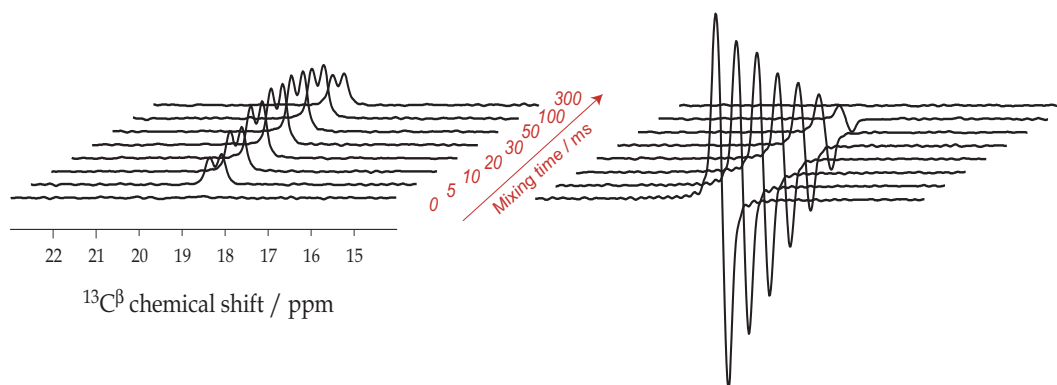

FIGURE 3.3: *C^β buildup curves for in-phase and anti-phase experiments with PDSD[50] as polarisation transfer sequence. The spinning frequency was set to 7 kHz and τ_{mix} was varied from 0 to 300 ms. All other experimental parameters are similar to those indicated in the legend of FIGURE 3.2.*

The DREAM sequence[29] is one of the DQ alternatives to the mixing scheme based on a ZQ spin Hamiltonian previously presented. The sequence is particularly attractive for spin pairs with the isotropic chemical-shift difference significantly smaller than the spinning rate, like for example the $C^\alpha C^\beta$ spin pair in fully ^{13}C-labelled L-Alanine at 30 kHz MAS. The DREAM shape corresponds to a tangential variation of the rf amplitude.[29] It was generated with the ShapeTool package of the XWINNMR Bruker software using 200 points and the following parameters:

$$
\begin{cases}
\frac{\overline{\omega}_1}{2\pi} & = \quad 13.5 \,\text{kHz} \\[2ex]
\frac{\Delta_{rf}}{2\pi} & = \quad 3 \,\text{kHz} \\[2ex]
\frac{d_{est}}{2\pi} & = \quad 1 \,\text{kHz}
\end{cases}
\tag{3-3}
$$

where $\overline{\omega}_1/2\pi$ represents the nutation frequency of the effective irradiation at the HORROR condition. $\Delta_{rf}/2\pi$ is the deviation of the irradiation frequency from the effective HORROR condition and d_{est} defines the shape of the DREAM amplitude. The length of the DREAM sweep was experimentally optimised to 4 ms using the pulse sequence outlined in FIGURE 3.4.

The single-transition polarisation transfer with DREAM requires magnetisation to be in the transverse plane for both in-phase and anti-phase experiments. Then, the simplest way to adapt the sequence outlined in FIGURE 3.1 is to add a $\pi/2$-hard pulse on carbon channel before and after the DREAM sweep. The use of hard pulses, instead of semi-selective ones, has the advantage of keeping the same length for both in-phase and anti-phase sequences and additionally avoids the problem concerned with possible transient Bloch-Siegert phase shifts effects.[107]

FIGURE 3.5 shows the buildup curves for in-phase and anti-phase C^β spectra obtained with DREAM as transfer scheme. Their sum and difference give rise to the buildup curves for the α and β transitions. These results reveal that the state selection is optimal for a mixing time very close to that maximising the DREAM transfer and therefore, for this case here, it is no need for scaling one spectrum with respect the other in order to obtain proper spin-state selection.

The main conclusion of this section is the feasibility of the single-transition transfer. For an isolated
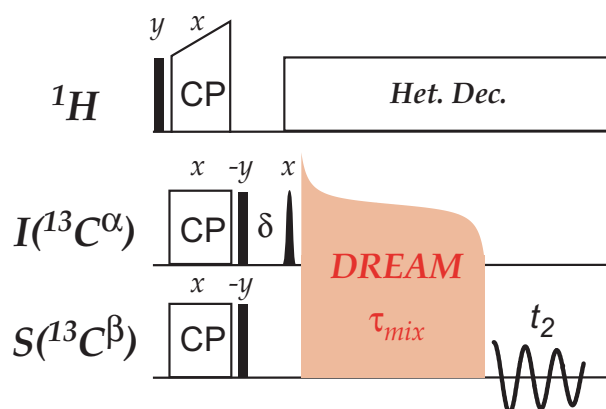
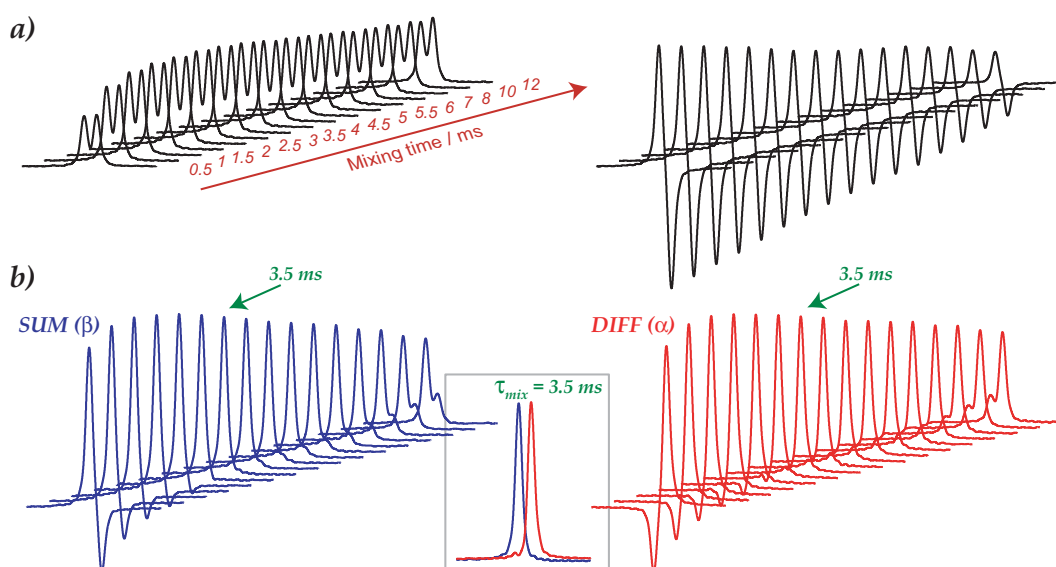FIGURE 3.4: *Pulse sequence for DREAM shape optimisation.*

FIGURE 3.5: *a) C^β buildup curves for in-phase and anti-phase experiments at 30 kHz MAS using DREAM for transferring the polarisation from C^α to C^β. b) α and β transitions obtained by adding and subtracting the in-phase, anti-phase buildup curves. Except the τ_{mix} which is varied from 0.5 to 12 ms with steps of 0.5 ms, all experimental parameters are given in the text. Grey box shows the separated α and β transitions corresponding to 3.5 ms mixing time with DREAM.*

homonuclear spin pair, the dependence of the state selection on the mixing time can be circumvented, if necessary, by using an appropriate scaling factor k. For a homonuclear ISK spin system, like for example the C' - C^α - C^β of fully ^{13}C-enriched L-Alanine, the selective transfer from C' to C^α seems more complicated. Therefore, more theoretical and experimental work should be devoted for understanding the selective polarisation transfer mechanism in three spin-1/2 systems.

3.3 2D COCA-IPAP

3.3.1 Product operator description

Now, that the 1D state-selective transfer was shown to work, we can figure out how to extend the experiment to two dimensions. The simplest way is to add a t_1 evolution period after the IPAP filter. Since the t_1 evolution creates anti-phase (in-phase) magnetisation in the in-phase (anti-phase) experiment and in-phase and anti-phase transfer functions depend on the mixing time, the resulting spectra are combinations of the

transferred in-phase and anti-phase signals with coefficients which depend on the mixing time. Thus, sum and difference of these spectra will yield proper state selection for only one mixing time. Additionally, the use of this approach will limit the access to only the diagonal $\alpha\alpha$ and $\beta\beta$ peaks. In order to get around the limitation related to the different transfer function for in-phase and anti-phase signals, the t_2 acquisition period has been preceded by an element devised for separating the in-phase transfer polarisation from the anti-phase one. In addition, this approach allows to observe all four cross peaks. The length of the pulse sequence can be reduced by building the t_1 evolution into the IPAP block, thus providing a constant-time experiment.[140]

The pulse sequence yielding a spin-state-selective C' - C$^\alpha$ correlation experiment is drawn in FIGURE 3.6.
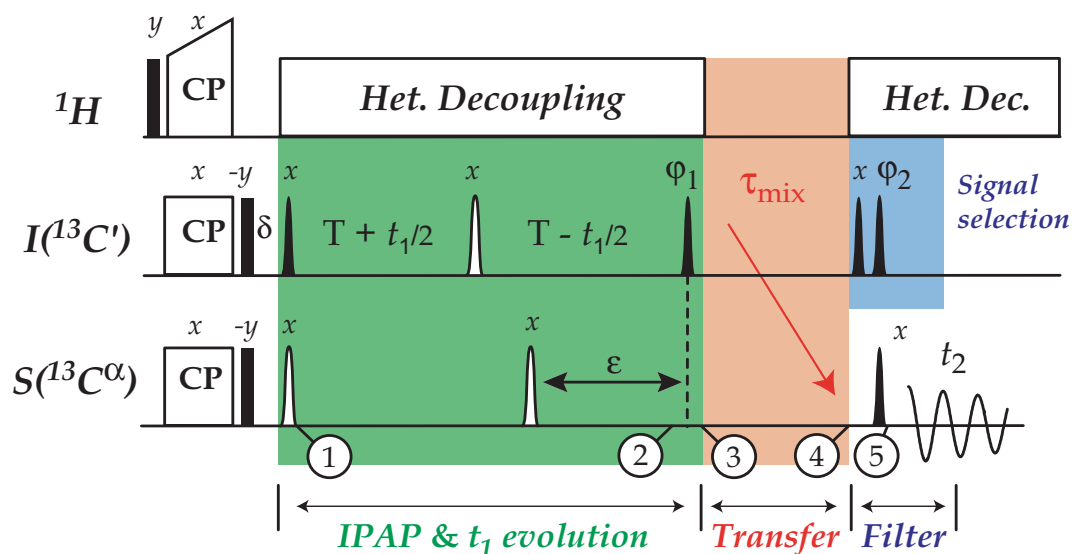

FIGURE 3.6: *Pulse sequence suitable for a C' - C$^\alpha$ correlation experiment. $\pi/2$ and π rf pulses are represented by filled and open bars (hard) or shapes (semi-selective). The C' pulses are applied with the shape of the center lobe of a $\sin x/x$ function, whereas the C$^\alpha$ pulses were rectangular with $\omega_1 = \Delta/\sqrt{15}$ ($\pi/2$) and $\Delta/\sqrt{3}$ (π), with Δ the chemical-shift difference between C' and C$^\alpha$ resonances. All pulses are applied along the x axis unless indicated. An 8-step phase cycle was applied with $\varphi_1 = 4x\ 4(-x)$, $\varphi_2 = x\ y\ -x\ -y$, $\varphi_{rec} = x\ -x\ x\ -x\ -x\ x\ x\ -x\ x$. The constant-time delay 2T was adjusted to $(2J_{C'C^\alpha})^{-1}$.*

The initial spin state is prepared by ^{1}H - ^{13}C cross polarisation. The hard $\pi/2$ ^{13}C pulse and the z filter, coming after the ^{13}C polarisation enhancement, is introduced to remove any residual transverse magnetisation thus ensuring proper z magnetisation for the subsequent part. The rest of the pulse sequence can be divided into three parts:

➡ **IPAP filter** which separates the I components into different subspectra and leads them evolve during the t_1 period;

➡ **Polarisation transfer** block for passing on the selected polarisation of the I spin to the S spin;

➡ **Signal selection** part introduced to chose either the in-phase or the anti-phase signal for each setting of the IPAP block.

In the following paragraphs, the product operator description[111] of the last three parts of the COCA-IPAP pulse sequence will be given. The time points are marked as circled numbers on the pulse sequence diagram (see FIGURE 3.6). For sake of simplicity, we consider a two-spin I - S system which interacts through the scalar coupling. Since the dipolar coupling is restored during the mixing time, it is additionally subjected to the dipolar coupling during this period. Let us first investigate the setup of the in-phase experiment, which is

given by the next settings:

$$\varepsilon = 0; \quad \varphi_1 = \text{-}x. \tag{3-4}$$

The π pulse on the I spin has the effect of refocusing the chemical shift of the I spin and the scalar coupling between the spins I and S during the constant time denoted 2T, while conserving their evolution during the t_1 period. Thus, spin-spin coupling evolution during the t_1 period creates, in addition to the in-phase magnetisation, an anti-phase component. The magnetisation evolution from time point ① to time point ② is therefore given by:

$$
\text{①} \qquad\qquad\qquad\qquad \text{②}
$$

$$
\text{-}I_y \xrightarrow{\ \Omega_I t_1\ }\xrightarrow{\ \pi J t_1\ } \left\{ \begin{array}{l} \text{-}I_y \cos(\Omega_I t_1)\cos(\pi J t_1) \\ +2I_x S_z \cos(\Omega_I t_1)\sin(\pi J t_1) \\ +I_x \sin(\Omega_I t_1)\cos(\pi J t_1) \\ \text{-}2I_y S_z \sin(\Omega_I t_1)\sin(\pi J t_1) \end{array} \right. \tag{3-5}
$$

The next $\pi/2$ pulse with the phase $\varphi_2 = \text{-}x$ will put along z axis only the terms I_y and $2I_y S_z$. The magnetisation at time point ③ is then given by the following two terms:

$$
\left\{ \begin{array}{l} +I_z \cos(\Omega_I t_1)\cos(\pi J t_1) \\ +2I_z S_z \sin(\Omega_I t_1)\sin(\pi J t_1) \end{array} \right. \tag{3-6}
$$

As the transfer functions depend on the mixing time, we discriminate between the in-phase and anti-phase transfers by introducing two coefficients a and b, respectively. This allows to write the polarisation transfer as given below:

$$
\left\{ \begin{array}{l} I_z \cos(\Omega_I t_1)\cos(\pi J t_1) \\ 2\, I_z S_z \sin(\Omega_I t_1)\sin(\pi J t_1) \end{array} \right. \xrightarrow[\tau_{mix}]{\text{Polarisation Transfer}} \left\{ \begin{array}{l} a(\tau_{mix})\, S_z \cos(\Omega_I t_1)\cos(\pi J t_1) \\ b(\tau_{mix})\, 2I_z S_z \sin(\Omega_I t_1)\sin(\pi J t_1) \end{array} \right. \tag{3-7}
$$

The state selection of the transferred S magnetisation is performed by phasing the last $\pi/2$ pulse on I spin in order to select for detection either in-phase or anti-phase S-spin coherence. In fact, the successive $\pi/2$ pulse on I spin have either the effect of a π_x pulse if φ_2 is set to x (see Figure 3.6) or are equivalent to doing nothing if φ_2 is equal to -x. Therefore, the S magnetisation at time point ⑤ is given by:

$$
\left\{ \begin{array}{l} \text{-}\ a(\tau_{mix})\ S_y \cos(\Omega_I t_1)\cos(\pi J t_1) \\ +\ b(\tau_{mix})\ 2I_z S_y \sin(\Omega_I t_1)\sin(\pi J t_1) \end{array} \right. \tag{3-8}
$$

for $\varphi_2 = x$, and by:

$$
\left\{ \begin{array}{l} \text{-}\ a(\tau_{mix})\ S_y \cos(\Omega_I t_1)\cos(\pi J t_1) \\ \text{-}\ b(\tau_{mix})\ 2I_z S_y \sin(\Omega_I t_1)\sin(\pi J t_1) \end{array} \right. \tag{3-9}
$$

for $\varphi_2 = \text{-}x$. Now, the in-phase and anti-phase single quantum S-spin coherences result from addition or subtraction of the two previous terms (see Eqs. 3-8 and 3-9). In summary, setting the φ_2 and the receiver phases equal to:

$$
\left\{ \begin{array}{lll} \varphi_2 & = & x \text{ -}x \\ \varphi_{rec} & = & x\ x \end{array} \right. \tag{3-10}
$$

yields in-phase selection and, anti-phase selection is obtained if:

$$
\left\{ \begin{array}{lll} \varphi_2 & = & x \text{ -}x \\ \varphi_{rec} & = & x \text{ -}x \end{array} \right. \tag{3-11}
$$

which is equivalent to doing:

$$\begin{cases} \varphi_2 & = & x\ x \\ \varphi_{rec} & = & x\ x \end{cases} \tag{3-12}$$

Finally, the S spin chemical shift (Ω_S) and the spin-spin coupling evolutions occur during the t_2 period thus leading to the following signals:

$$\begin{cases} \text{- } a(\tau_{mix})\ S_y \cos(\Omega_I t_1) \cos(\Omega_S t_2) \cos(\pi J t_1) \cos(\pi J t_2) & \text{in-phase selection} \\ \text{+ } b(\tau_{mix})\ 2S_y I_z \sin(\Omega_I t_1) \cos(\Omega_S t_2) \sin(\pi J t_1) \sin(\pi J t_2) & \text{anti-phase selection} \end{cases} \tag{3-13}$$

A schematic representation of the spectra associated to the previous signals is shown in FIGURE 3.7.
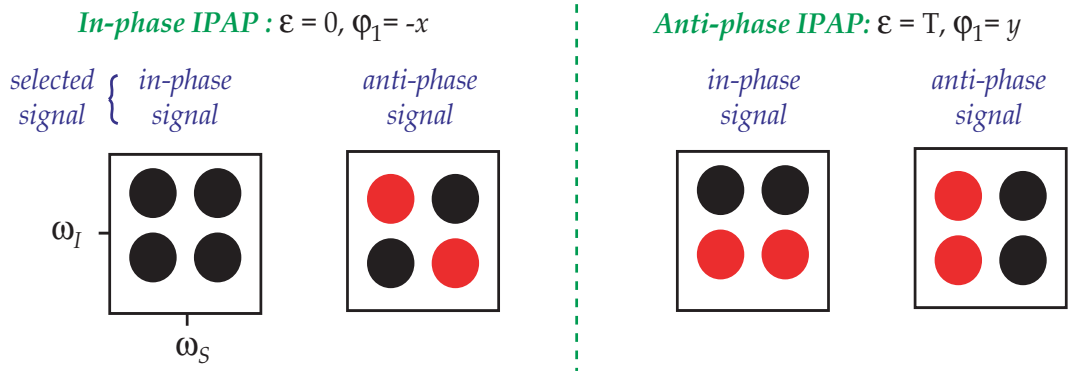

FIGURE 3.7: *Schematic 2D COCA-IPAP spectra expected for the different settings. Black and red filled circles represent positive and negative signals, respectively.*

The second step in the product operator description of the COCA-IPAP pulse sequence consists in considering the settings corresponding to the anti-phase experiment:

$$\varepsilon = T; \quad \varphi_1 = y. \tag{3-14}$$

So, as a consequence of the shift of the last π pulse on the S spin, the spin-spin coupling evolution occurs this time during a period equal to $(t_1 + 2T)$. The J-coupling is thus evolving during the CT period and creates anti-phase magnetisation which is further evolving during t_1 and additionally generates in-phase magnetisation. Magnetisation evolution from time point ① to ⑤, for anti-phase settings, is therefore given by the following expressions:

$$\begin{cases} ① & \to & \text{- } I_y \\ ② & \to & \text{+ } I_y \cos(\Omega_I t_1) \sin(\pi J t_1) \\ & & \text{- } I_x \sin(\Omega_I t_1) \sin(\pi J t_1) \\ & & \text{+ } 2I_x S_z \cos(\Omega_I t_1) \cos(\pi J t_1) \\ & & \text{+ } 2I_y S_z \sin(\Omega_I t_1) \cos(\pi J t_1) \\ ③ & \to & \text{- } I_z \sin(\Omega_I t_1) \sin(\pi J t_1) \\ & & \text{+ } 2I_z S_z \sin(\Omega_I t_1) \sin(\pi J t_1) \\ ④ & \to & \text{- } a(\tau_{mix})\ S_z \sin(\Omega_I t_1) \sin(\pi J t_1) \\ & & \text{+ } b(\tau_{mix})\ 2I_z S_z \cos(\Omega_I t_1) \cos(\pi J t_1) \\ ⑤ & \to & \text{- } a(\tau_{mix})\ S_y \sin(\Omega_I t_1) \cos(\Omega_S t_2) \sin(\pi J t_1) \cos(\pi J t_2) \\ & & \text{+ } b(\tau_{mix})\ 2I_z S_y \cos(\Omega_I t_1) \cos(\Omega_S t_2) \cos(\pi J t_1) \cos(\pi J t_2) \end{cases} \tag{3-15}$$

Note that the chemical shift and J-evolution are both compensated for any length of the π pulse applied on the S spin (i.e., no additional evolution occurs during the π (S) pulse).

3.3.2   Application to uniformly [^{13}C, ^{15}N]-enriched Crh protein

The 2D COCA-IPAP experiment was applied to a microcrystalline sample of fully [^{13}C - ^{15}N]-enriched Crh protein containing 2x85 amino acids. The PDSD scheme has been used for performing the transfer of polarisation. Four experiments (A$_1$), (A$_2$), (B$_1$) and (B$_2$) were separately recorded. The next settings were used for A- and B-type experiments in order to separate the I-spin transitions with IPAP:

$$\begin{cases} \text{(A)} & \varepsilon = \text{T}, \ \varphi_3 = \text{-}x \quad \text{in-phase type experiment} \\ \text{(B)} & \varepsilon = 0, \ \varphi_3 = y \quad \text{anti-phase type experiment} \end{cases} \tag{3-16}$$

Each of the experiments A and B are acquired twice by alternatively setting the phase φ_2 to *x* or *-x*. Addition of the two data sets yields in-phase spectra in ω_2 dimension (A$_1$, B$_1$), and their subtraction gives rise to anti-phase spectra in ω_2 (A$_2$, B$_2$) dimension. The four different single-transition correlation spectra ($\alpha\alpha$, $\alpha\beta$, $\beta\alpha$, $\beta\beta$) can then be obtained by doing the following spectral combinations:

$$(\text{A}_1 + \delta \text{B}_1) \pm k(\text{A}_2 + \delta \text{B}_2) \tag{3-17}$$

with $\delta = +1$ or -1 and k a scaling factor depending on the polarisation transfer functions of both in-phase and anti-phase experiments. If

$$\begin{cases} I_z & \xrightarrow{\quad \text{PDSD} \quad} & aS_z & \text{in-phase signal} \\ 2I_zS_z & \xrightarrow{\quad \text{PDSD} \quad} & b2I_zS_z & \text{anti-phase signal} \end{cases} \tag{3-18}$$

we define the k factor as being b/a (a and b being both functions of τ_{mix}).

FIGURE 3.8 shows the $\alpha\alpha$-subspectrum recorded on the Crh protein using the sequence of FIGURE 3.6, compared to a standard PDSD correlation spectrum. Spin-state selection provides a remarkable increase in resolution in both dimensions. Specifically, the resolution of the 49Gly cross peak is enhanced by 44% and 17% for C$^\alpha$ and C' dimensions, respectively. The resolution enhancement is more pronounced in the C$^\alpha$ dimension because of the longer acquisition time used for direct detection. Note that because the ^{13}C linewidths in solid-state NMR are dominated by refocusable interactions,[92, 115, 113] CT experiments do not provide a significant increase in resolution. However, the insertion of t_1 evolution in the IPAP block allows a shortening of the sequence.

The experiments were all performed on a Bruker Avance spectrometer operating at B$_0$ = 11.7 T static magnetic field equipped with a 4 mm double-resonance probehead. The MAS frequency was 11 kHz and the temperature was regulated to keep the sample temperature constant at 13°C. The CP contact time was 1.8 ms in order to optimise the transfer of polarisation to carbonyls. Decoupling of carbons from protons was performed with SPINAL sequence at $\omega_1/2\pi = 78$ kHz nutation frequency. The mixing time was set to 30 ms.

The combination of the recorded 2D data sets is illustrated in FIGURE 3.9. The spectral combinations $(\text{A}_1 + \delta \text{B}_1) \pm k(\text{A}_2 + \delta \text{B}_2)$ with $\delta = +1$ or -1 and k the adjustable scaling factor, yield all four single-transition-to-single-transition correlation spectra $\alpha\alpha$, $\alpha\beta$, $\beta\alpha$, and $\beta\beta$. For PDSD mixing times of $\tau_{mix} = 30$ ms and τ_{mix} = 15 ms, the scaling factor was found to be $k = 0.7$ and $k = 0.5$, respectively.

Note that for longer PDSD mixing times some polarisation is transferred from the C' to other side-chain carbons (C$^\beta$, C$^\gamma$, C$^\delta$). Since there is no direct scalar coupling between the C' and the side-chain carbons, no frequency shift is expected along the detection dimension (ω_2) between the $\alpha\alpha$ and $\alpha\beta$, or $\beta\alpha$ and $\beta\beta$ subspectra. Thus, the new experiment provides a simple way for distinguishing C$^\alpha$ from other side-chain carbons (e.g., C$^\beta$ of Thr and Ser residues as 62Thr, 31Ser, 56Ser) by comparison of the different subspectra.

3.3.3   Efficiency of 2D-COCA-IPAP experiment

The 2D-COCA-IPAP and conventional PDSD spectra (see FIGURE 3.8) were acquired with the same experimental parameters except for the number of transients. Each of the four COCA-IPAP being recorded
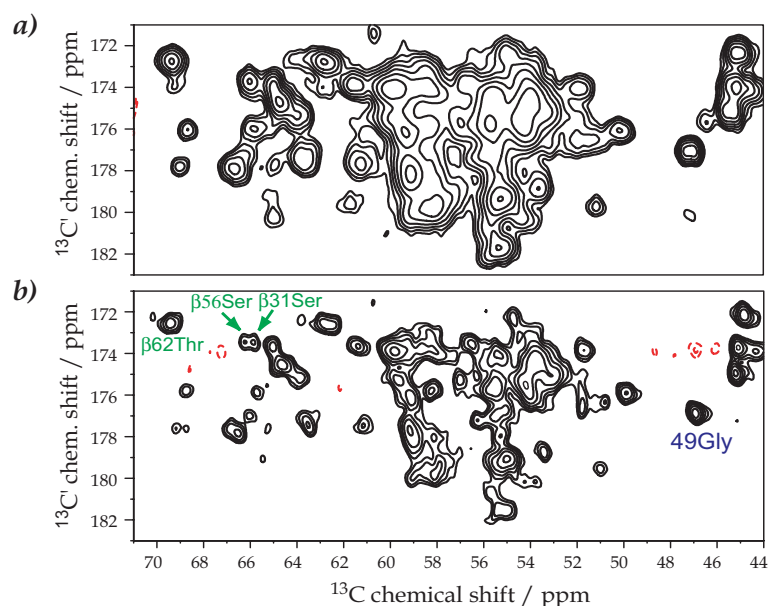
FIGURE 3.8: *C' - C^α region of the standard (a) and the αα-spin-state selective (b) PDSD spectrum of the microcrystalline Crh protein (containing 2x85 amino acids). The second spectrum was obtained from the linear combination $A_1 + B_1 + k(A_2 + B_2)$, with $k = 0.7$. Acquisition times $t_1^{max} = 9.2$ ms with States quadrature detection and $t_2^{max} = 25$ ms were used. A total of 4x48 transients were recorded for the spin-state-selective experiment and 64 for the standard PDSD experiment. The experimental time was 26 h and 4x10 h for the standard and the spin-state-selective spectra, respectively. Cosine apodisation was applied in both dimensions prior to Fourier transformation. For both spectra, the first contour level was set to 15% of the intensity of the 49Gly resonance, with a factor of 1.4 between levels. Cross-peaks discussed in the text are annotated in b).*
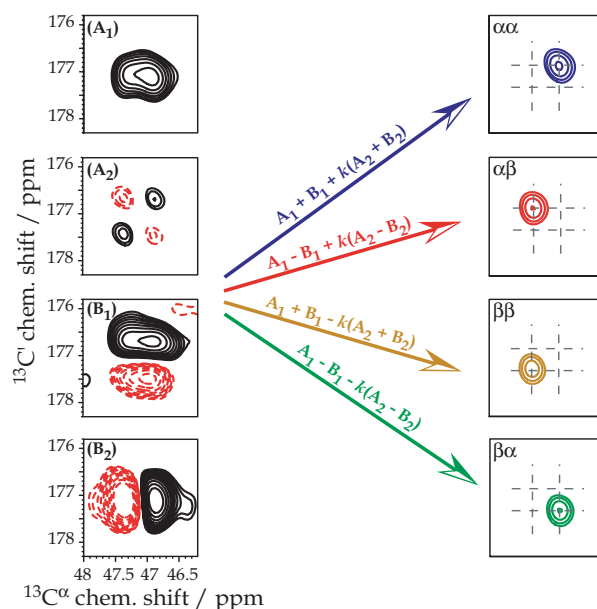

FIGURE 3.9: *Subspectra A_1, A_2, B_1, and B_2 recorded using the spin-state-selective C' - C^α-PDSD experiment of FIGURE 3.6. Experimental details are given in the caption of FIGURE 3.8. Separation of the four cross-peak transitions obtained by linear combination of the subspectra A_1, A_2, B_1, and B_2. For clarity, only the 49Gly cross-peak region is shown. Contours are drawn at the same levels for all spectra.*

with 48 scans, the total number of transients for 2D-IPAP is given by 192. On the other hand, the standard PDSD spectrum was recorded with 64 scans. The two experiments can be directly compared if the number of scans of the standard PDSD experiment is extrapolated (or vice versa) such as to have the same experimental

time for both PDSD and COCA-IPAP.

In order to determine the efficiency of 2D COCA-IPAP correlation experiment with respect to the standard ^{13}C - ^{13}C PDSD experiment, we have to estimate the noise of each transition selected by spectral combinations of the four recorded 2D-IPAP spectra. Since the noise is a random variable described by a Gaussian distribution probability, the noise corresponding to the linear combination of two independent (uncorrelated) NMR experiments E_1, E_2, acquired with the same number of transients (NS) follows a power low:

$$N_{\lambda_1 E_1 + \lambda_2 E_2} = \sqrt{(\lambda_1^2 + \lambda_2^2)\text{NS}} \tag{3-19}$$

with λ_1, λ_2 two numerical coefficients.

The $\alpha\alpha$, $\alpha\beta$, $\beta\alpha$, and $\beta\beta$ cross peaks are obtained by linear combinations of the A_1, A_2, B_1, B_2 spectra with either 1 or k as coefficients:

$$\begin{cases} \alpha\alpha: & A_1 + B_1 + k(A_2 + B_2) \\ \alpha\beta: & A_1 - B_1 + k(A_2 - B_2) \\ \beta\alpha: & A_1 - B_1 - k(A_2 - B_2) \\ \beta\beta: & A_1 + B_1 - k(A_2 + B_2) \end{cases} \tag{3-20}$$

As a result of these spectral combinations, the noise will be the same for all the selected transitions and will depend on the scaling factor k:

$$N_{\alpha\alpha} = N_{\alpha\beta} = N_{\beta\alpha} = N_{\beta\beta} = \sqrt{(1 + k^2)\frac{\text{NS}}{2}} \tag{3-21}$$

with NS the total number of scans recorded for the COCA-IPAP experiment. For a scaling factor k equal to 0.7 and a total number of scans of 64 and 192 for PDSD and IPAP experiments, the IPAP noise is related to that of PDSD experiment by the next relation:

$$\frac{N_{\text{IPAP}}}{N_{\text{PDSD}}} \approx 1.5 \tag{3-22}$$

This theoretical estimation of the noise has been experimentally confirmed by comparison of the traces extracted from both PDSD and IPAP 2D spectra. We can now determine the signal relation by adjusting the noise level such as the noise of the PDSD trace be the same as the noise of the IPAP trace (i.e., S). For the same experimental time and resolution, the relation expressing the efficiency of the IPAP experiment with respect to the standard PDSD experiment, may therefore be written as:

$$\text{Efficiency} = \frac{[\frac{S}{N}]_{\text{IPAP}}^{\text{NS}_1}}{[\frac{S}{N}]_{\text{PDSD}}^{\text{NS}_2}} = \frac{\tilde{S}}{\tilde{N}}\sqrt{\frac{\text{NS}_1}{\text{NS}_2}} \tag{3-23}$$

with $\tilde{S}$ and $\tilde{N}$ being the signal and noise ratios of a single IPAP transition compared to the standard PDSD experiment. NS_1 and NS_2 represent the total number of transients for IPAP and PDSD experiment, respectively.

Using the Eq. 3-23, with $\tilde{N}$ = 1.5, NS_1 = 64, NS_2 = 192 and $\tilde{S}$ the signal ratio measured experimentally for each transition when the noise is put at the same level in both IPAP and PDSD traces, we obtained a mean efficiency of a single transition of 43 % for the 49Gly residue. Moreover, for the same total experimental time we get the four transitions separated in different subspectra. Since the C'C$^\alpha$ J-coupling is known and constant over the protein, the four spin-state-selective subspectra can be shifted in both dimensions such as to bring all transitions at the same position and then add them. Thus, a factor 2 in signal-to-noise ratio is recovered and leads to a spin-state experiment with a sensitivity of 86 % compared to the standard experiment.

The origin of sensitivity losses for the 2D-IPAP experiment is two fold. First, the three additional spectra recorded for the spin-state-selective experiment. Second, the spectral combinations of the four IPAP recorded

spectra with different numerical coefficients. However, since the IPAP filter has been built into a CT element, its signal loss during the filter length can be reduced by using high power ^{1}H decoupling during the filter and faster spinning of the sample. This is possible for protein samples if a powerful cooling system is available.[141] At high spinning frequency the spin diffusion is quenched and techniques like fpRFDR[55] or DREAM[29] have to be considered for performing the transfer of polarisation.

3.4   2D CACB-IPAP

The 2D-IPAP correlation experiment was first applied to the C' - C^α region. Another region particularly important for the carbon assignment is that of the C^α - C^β carbons. Due to the overlapping of the C^α and C^β regions, this kind of experiments present a increased difficulty compared to the C'C^α correlation experiment. Since the C^β resonance of Ser and Thr amino acids are both overlapping the C^α region, their correlation peaks are not expected into the spectrum. For all other residues, very clean band-selective pulses are however necessary to separately excite the C^α or C^β region. Apart its scalar coupling to C^β, the C^α resonance presents an additional broadening due to the scalar coupling to the C' resonance. In order to obtain an optimum increase in resolution with the C^α - C^β spin-state-selective correlation experiment, we have therefore to remove the C^α - C' scalar coupling as well.

The pulse sequence corresponding to the spin-state-selective CACB correlation experiment is drawn in Figure 3.10. Except the C' decoupling during t_1 evolution, this pulse sequence is the same as that used for COCA. A series of existing band-selective pulses developed for solution NMR were tested on the Crh protein (2x85 residues) and all of them give nice results.
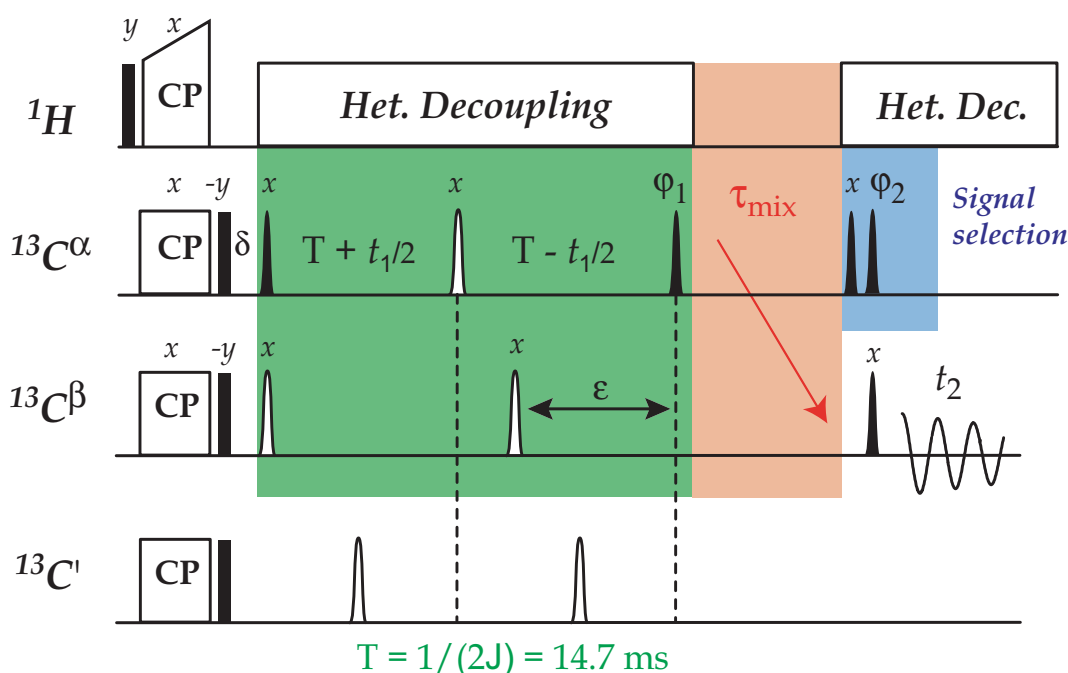

FIGURE 3.10: *Pulse sequence suitable for a C^α - C^β correlation experiment. $\pi/2$ and π rf pulses are represented by filled and open bars (hard) or shapes (semi-selective). The C^α and C^β excitation pulses were BURP-2[142] shapes of 1.95 and 1.19 ms length. The C^α refocalisation pulse was SNOB[143] shape of 920 μs length. The C^α flip-back pulses were universal Q5[144, 145] shapes of 2.25 ms length. The C^β inversion pulse was BURP-1[142] of 1.09 ms length. The C' inversion pulse used for the C' decoupling was $\sin(x)/x$ shape of 300 μs length. An 8-step phase cycle was applied with $\varphi_1 = 4x\,4(\text{-}x)$, $\varphi_2 = x\,y\,\text{-}x\,\text{-}y$, $\varphi_{rec} = x\,\text{-}x\,x\,\text{-}x\,\text{-}x\,x\,\text{-}x\,x$. The constant-time delay 2T is adjusted to $(2J_{C^\alpha C^\beta})^{-1}$.*

A significant gain in resolution with respect to the standard PDPSD experiment is obtained by just ap-

plying a C' decoupling in the indirect dimension using the method introduced by Straus *et al.*[37] The standard PDSD, C' homodecoupled PDSD and spin-state-selective CACB correlation spectra recorded on the Crh protein are given in FIGURE 3.11. An additional gain in resolution obtained this time in both dimensions is again quite clear, even if the scalar coupling removed by the spin-state-selection filter is smaller than in the COCA experiment.
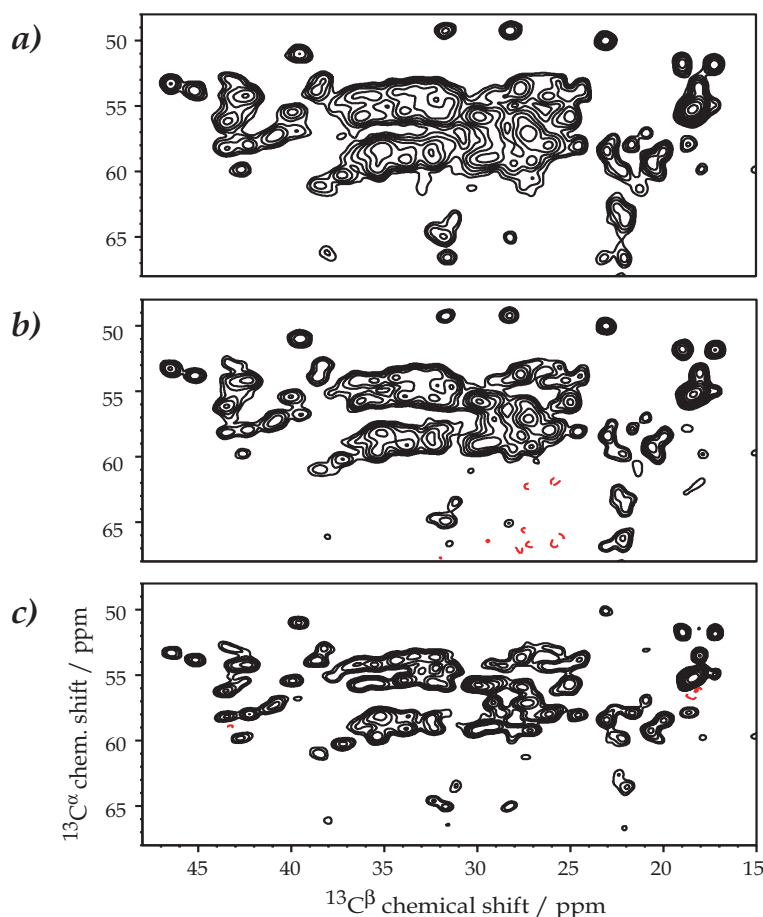

FIGURE 3.11: *C^α - C^β region of the (a) standard, with additional (b) C' homodecoupling and (c) spin-state-selective (coaddition of the 4 transitions shifted by $\pm J/2$) PDSD spectrum of the microcrystalline Crh protein. The third spectrum was obtained with a scaling factor k = 0.6. Acquisition times t_1^{max} = 9.6 ms with States quadrature detection and t_2^{max} = 15 ms were used. A total of 128 transients were recorded for the spin-state-selective experiment and 40 for the standard and homodecoupled PDSD experiments. The experimental time was 26 h, 26h and 4x16 h for the standard, homodecoupled and the spin-state-selective spectra, respectively. Cosine apodisation was applied in both dimensions prior to Fourier transformation. For both spectra, the first contour level was set to 20% from the mean intensity of 44Ala and 54Ala resonances, with a factor of 1.4 between levels.*

However, the spin-state CACB experiment performed as described here is not very sensitive. On the same experimental time and resolution basis, the efficiency of the emerged four transitions of 2D CACB-IPAP compared to standard C' homodecoupled PDSD experiment is only 45 %.

It has been already mentioned that the sensitivity of the spin-state-selective correlation experiment could be enhanced by going to high spinning frequencies. Moreover, high spinning conditions would not only lead to better performance of the selection filter as shown in the chapter 2 for the 1D IPAP experiment, but would also allow the use of better techniques for the transfer of polarisation like for example DREAM[29] transfer sequence.

FIGURE 3.12 shows preliminary results obtained on fully ^{13}C-enriched L-Alanine at 30 kHz MAS with

DREAM. Traces of the separated spin states of the CACB correlation experiment recorded on L-Alanine at 30 kHz MAS with DREAM are compared to traces extracted from the CACB-PDSD correlation experiment recorded on the same sample at 11 kHz MAS. Except polarisation transfer schemes and spinning rates, all other experimental parameters were the same for both experiments. These preliminary results show clearly that the sensitivity of the spin-state-selective correlation experiments can still be significantly improved. This could also lead to an experiment offering at the same time a very good resolution and a good sensitivity.
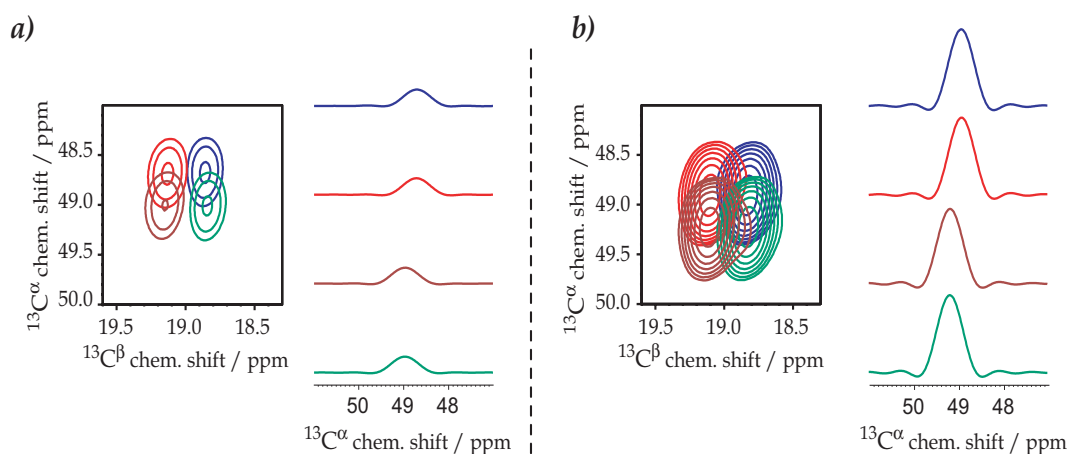

FIGURE 3.12: *CACB-IPAP-PDSD (a) and CACB-IPAP-DREAM (b) $\alpha\alpha$, $\alpha\beta$, $\beta\alpha$, and $\beta\beta$ of the fully ^{13}C-enriched L-Alanine. The PDSD spectrum has been recorded at 11 kHz MAS for a mixing time of 30 ms. The DREAM spectra have been recorded at 30 kHz MAS for a mixing time of 4 ms. A total of 64 transients was recorded for both PDSD and DREAM spectra. Each transition was obtained by linear combinations of A_1, A_2, B_1, and B_2 spectra with a scaling factor k = 1. The sensitivity of the spin-state-selective experiment with DREAM is two times larger than that of IPAP-PDSD. This sensitivity improvement factor has been corrected for the difference introduced by the cross-polarisation efficiency.*

3.5 Conclusion

In this chapter, we have introduced a new experimental approach which provides significant resolution enhancement in multidimensional solid-state NMR correlation experiments. Resolution enhancement is achieved by using transition-selective excitation and transfer techniques. Spin-state-selective polarisation transfer is obtained using standard ZQ or DQ solid-state NMR mixing sequences. The new experiments can be easily extended to higher-dimensional experiments. In addition, spin-state-selective correlation experiments allow the distinction of "direct" transfer peaks, involving covalently-bound nuclei, and "relayed" transfer peaks.

We have showed that significant resolution enhancement can be obtained in homonuclear multidimensional solid-state NMR correlation experiments by transition selection and spin-state-selective polarisation transfer techniques. The selection and transfer of single states allows the removal of the J-coupling contribution from the linewidth in both the direct and indirect spectral dimensions. This was demonstrated with a new spin-state selective C' - C$^{\alpha}$ and C$^{\alpha}$ - C$^{\beta}$ correlation experiments, applied to a microcrystalline Crh protein counting 2x85 amino acids. With these new sequences, all four components of the C' - C$^{\alpha}$ and C$^{\alpha}$ - C$^{\beta}$ cross-peaks were separated into different subspectra, obtained by linear combination of four recorded data sets.

Heteronuclear directly detected techniques for protein backbone assignment by liquid-state NMR

4.1 Introduction

So far, we have dealt with developments in NMR methodology for samples in the solid state. We have first discussed the asymmetry and differential broadening effects induced by the interference of CSA and dipolar interactions in fully enriched powdered compounds. Spin-state-selection techniques have proved to be well adapted to accurately measure the J-induced differential broadening and, by allowing to select only one component of the J-multiplet, to increase the spectral resolution. This interesting feature has been further exploited in 2D ^{13}C - ^{13}C correlation experiments. In order to illustrate that significant increase in resolution can therefore be obtained, the 2D ^{13}C - ^{13}C experiments based on the spin-state-selection scheme have been applied to the microcrystalline Crh protein.

In comparison to solids NMR, liquid-state NMR takes advantage of the rapid isotropic motion which averages the magnetic interactions thus leading to high-resolution spectra. It is important to notice that the interactions are only averaged to their isotropic part and not completely removed. Note also that the fluctuations induced by the molecular tumbling remain and they represent the main contributions of spin-relaxation rates.[27] For complete motional averaging to occur, the motion has to be isotropic and also rapid enough with respect to the frequency of the interactions characterising the spin system (i.e., chemical shift, CSA, DD, etc). In general, for molecular systems with tumbling correlation times of $\tau_c < 50$ ns, the motional averaging is efficient enough and high-resolution NMR spectra may be obtained. Since the correlation time is directly related to molecular weight, the liquid-state NMR spectra are expected to show broad lines for those systems with molecular weights above 50 kDa (i.e., $\tau_c > 50$ ns). However, by using TROSY-based techniques, fast relaxation may be favourably exploited. Indeed, interference between CSA and DD relaxation mechanisms gives rise to different relaxation rates for the two components of NH moieties or aromatic CH groups, thus producing an effect of differential line broadening. TROSY in either partially or uniformly deuterated proteins[40, 146, 147] in combination with cross relaxation-induced polarization transfer (CRIPT) and cross relaxation-enhanced polarization transfer (CRINEPT) techniques[148, 149] allows NMR studies of even larger proteins. However, uniform deuteration also imposes severe limitations on the structural information that can be obtained by conventional triple-resonance experiments. Moreover, even if the ^{1}H - ^{15}N correlation spectrum of a protein contains important information, the NMR-based tridimensional structure cannot be calculated directly from a single ^{1}H - ^{15}N spectrum.

A valuable alternative to overcome fast ^{1}H relaxation is the use of direct ^{13}C detection, which takes advantage of the slowly relaxing ^{13}C magnetisation compared to ^{1}H. Nowadays, all the liquid-state NMR

experiments for heteronuclear backbone assignment are commonly performed via ^{1}H (i.e., using the so-called inverse mode). Most of them can in principle be performed using direct heteronuclear excitation and detection without involving protons at any place in the pulse sequence. However, the design strategy of these experiments for backbone assignment using heteronuclei only is different from that for ^{1}H-based experiments. Indeed, most of the experiments used nowadays for backbone assignment are based on the HN group, that actively exploits TROSY effects.[150, 151] Passing to direct heteronuclear detection, ^{15}N is not the best starting point for sensitivity reasons. The experiments tailored for backbone sequential assignment without involving protons should rather start and end on ^{13}C nuclei, either on C$^\alpha$ (interesting in H$^\alpha$-deuterated proteins) or on carbonyls C' (attractive at intermediate magnetic fields) atoms, in an "out-and-back"[1] scheme,[154] or should start on one of them and end on the other in an "out-and-stay" approach.[155]

The detection method via ^{1}H is less favorable in solids, because the ^{1}H - ^{1}H dipolar coupling (usually > 20 kHz) is dominant so that it cannot be averaged by the magic-angle-spinning at spinning frequencies which are nowadays feasible or tolerable to the sample. Furthermore, since at moderate spinning rates it is usually possible to satisfactorily average out CSAs as well as ^{13}C - ^{13}C and ^{13}C - ^{15}N dipolar couplings in labelled (microcrystalline) compounds, most of the techniques for ^{13}C, ^{15}N assignment of solid samples are based on ^{13}C detection.

In this chapter, we will introduce two techniques devised for protein backbone assignment in solution NMR and based on direct ^{13}C detection approach.

4.2 Triple-resonance CBCACO experiment

4.2.1 Pulse sequence description

We first present the CBCACO technique which yields correlations between three carbon nuclei belonging to the same residue (i.e., *intra-residue* ^{13}CO - ^{13}C$^\alpha$ - ^{13}C$^{\alpha,\beta}$ correlations). The pulse sequence for the 3D CBCACO experiment is illustrated in Figure 4.1.

The sequence consists basically in two evolution periods and one block INEPT for performing the transfer of magnetisation to carbonyls which are further detected. The evolution periods were built into the experiment in a constant time (CT) manner.[140]

The first $\pi/2$ pulse excites both C$^\alpha$ and C$^\beta$ spins. They are evolving, from time point ① to ② under the influence of their chemical shifts and of C$^\alpha$ - C$^\beta$ (and for C$^\beta$ also C$^\gamma$ - C$^\beta$) scalar couplings. The $\pi/2$ pulse after time point ② retains in-phase C_y^α and C_y^β coherences and converts the anti-phase $2C_x^\beta C_z^\alpha$ coherence into $2C_x^\alpha C_z^\beta$. These are then converted into anti-phase $2C_x^\alpha C_z'$ coherence during the interval from time point ③ to ④. Up to this time point, the experiment closely looks like the CBCA(CO)NH experiment.[157] However, in this case the anti-phase $2C_z^\alpha C_x'$ coherence is refocused to in-phase C_y' coherence and further detected (from time point ⑤ to ⑥). This avoids the long delays necessary for the CO - N transfer present in the conventional CBCA(CO)NH experiment. The C' - C$^\alpha$ scalar coupling that complicates the spectra during the acquisition dimension is removed by band-selective homodecoupling. Among the three planes, one contains the same information like the COCAMQ spectrum,[158] other additionally provides the C$^\beta$ frequencies and the third one shows in a COSY-type spectrum[159, 160] the C$^\alpha$ - C$^\alpha$ diagonal peaks together with the C$^\alpha$ - C$^\beta$ cross-peaks.

A characteristic feature of direct ^{13}C detection is the presence of many homonuclear couplings which complicate the spectra in the acquisition dimension. These couplings may be useful for coherence transfer or determination of residual dipolar couplings but are definitely detrimental to achieve good resolution in the

---

[1]In general, an experiment is called "out-and-back" if the initially excited spin is identical to the detected one. As almost all the conventional triple-resonance schemes published since the introduction of this concept in 1990 by Bax and coworkers[152, 153] are ^{1}H-based, for most of them, proton is the excited and detected spin.
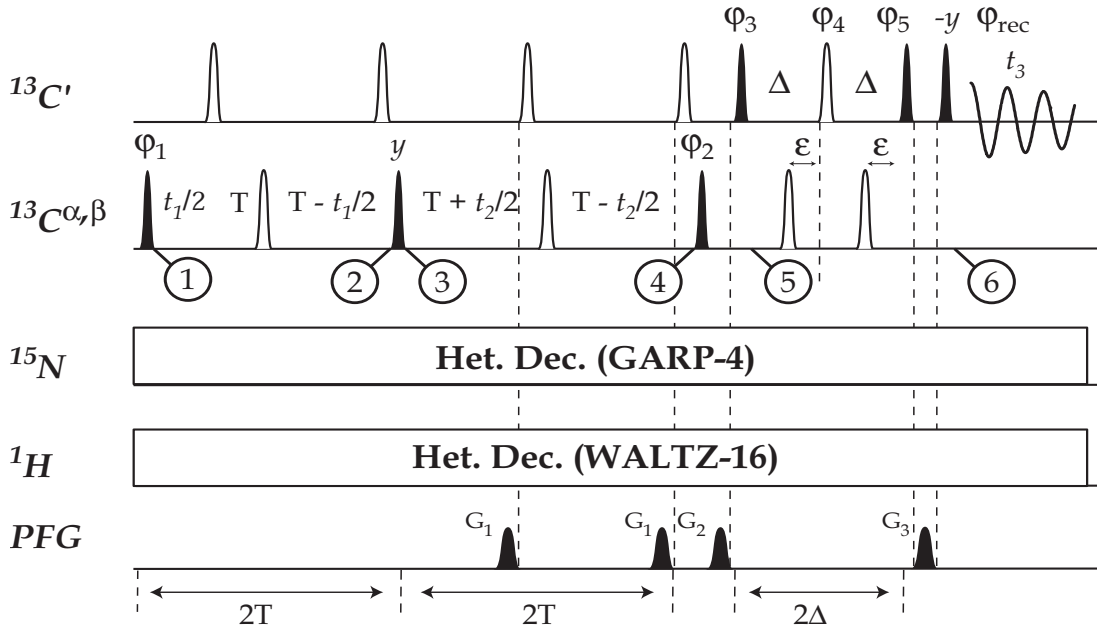
FIGURE 4.1: *3D CBCACO pulse sequence ($^{13}C'$ - $^{13}C^{\alpha,\beta}$ - $^{13}C^{\alpha}$). Filled and open Gaussian shapes represent selective $\pi/2$ and π pulses, respectively. Universal Gaussian cascades were used[144, 145] 332 μs long for the $\pi/2$ pulses and 300 μs long for the π pulses, except for the first two $^{13}C^{\alpha,\beta}$ pulses which were 274 μs ($\pi/2$) and 220 μs (π) long and centered at 35 ppm, in order to cover the C^{α} - C^{β} spectral region. The carrier frequencies for pulses applied on $^{13}C'$, $^{13}C^{\alpha}$, ^{15}N and ^{1}H were of 175, 35, 120 and 3.5 ppm, respectively. Before the first pulse, the carrier on the carbon channel is switched from 175 to 35 ppm and it is switched back to 175 ppm before the first $\pi/2$ C' pulse. The phase cycle was as follows: φ_1 = 2x 2(-x), φ_2 = y, φ_3 = x -x, φ_4 = 4x 4y, φ_{rec} = x -x -x x -x x x -x. All the pulses are applied along the x axis unless indicated. The variations in the phase cycle to obtain the in-phase component were φ_5 = 8y 8(-y), last $\pi/2$ pulse = y, φ_{rec} = x -x -x x -x x x -x and for the anti-phase component φ_5 = 8x 8(-x), last $\pi/2$ pulse = x, φ_{rec} = x -x -x x -x x x -x -x x x x x -x -x x. The pulsed field gradients were 1 ms long, sine shaped, with maximum intensities of G_1 = 11 G/cm, G_2 = 21 G/cm and G_3 = 19 G/cm. The delays were T = 3.5 ms, Δ = 4.5 ms. Phase-sensitive spectra in the $^{13}C^{\alpha,\beta}(t_1)$ and $^{13}C^{\alpha}(t_2)$ dimensions are obtained by incrementing φ_1 and φ_2 in a States-TPPI manner.[156]*

acquisition dimension. Band-selective homodecoupling[161, 158] is one of methods already proposed to solve this problem.

The CBCACO experiment offers an additional possibility to remove the scalar coupling during the acquisition dimension as it is perfectly suited to implement spin-state-selective approaches like IPAP,[31, 32] without including additional building blocks into the experiment. Two $\pi/2$ carbonyl pulses with the gradient in between are added to apply the IPAP selection filter. The variant of the experiment shown in the FIGURE 4.1 with $\varepsilon = \Delta/2$ is the one to obtain the anti-phase component. By shifting the last two C^{α} π pulses from right to left by a $1/(8J_{C'C^{\alpha}})$ delay and changing the phase of the last $\pi/2$ pulse by 90°, the last block can be used to retain the in-phase C'_y coherence instead of converting it into the anti-phase $2C_z^{\alpha}C'_y$ coherence. The use of two π pulses on the C^{α} nucleus ensures removal of transient Bloch-Siegert effects.[107] Therefore, for each t_1 (and t_2) increment, two FIDs are acquired in an interleaved fashion, one for the in-phase signal, other for the anti-phase one, and stored separately. The complete phase cycle on the last C' π pulse is important for removing artifacts due to pulse imperfections. The two FIDs separately stored for each t_1 (and t_2) increment can be summed and subtracted to separate the two multiplet components and thus simplify the spectra. The two spectra obtained in this way can further be shifted one respect to the other by $J/2$ in order to superimpose the two multiplet components that appear in the two spectra. These can then be summed again to increase the sensitivity of the spectrum. This approach works provided the C' - C^{α} scalar coupling is uniform throughout the sample. We tested this approach on the 2D version of the experiment and compared with the other existing

methods to eliminate the C' - C^α indirect coupling (band-selective[161, 158] homodecoupling and Maximum Entropy Reconstruction[162, 163]). It can also be implemented in the 3D version of the experiment.

4.2.2   Results and discussion

All the experiments shown in this chapter were carried out on a 16.4 T Bruker Avance spectrometer operating at 700.06 MHz for ^{1}H and 176.03 MHz for ^{13}C equipped with a prototype TXO probe designed specifically for carbon directly detected experiments. The inner coil is tuned to ^{13}C while the outer coil is double tuned to ^{1}H and ^{15}N. The probe, optimised for ^{13}C sensitivity (with a signal-to-noise of about 500:1 on the standard ASTM sample (i.e., 40 % dioxane in benzene-d6 with 0.2 % CrAcAc)), is characterised by a short ^{13}C $\pi/2$ pulse (12.5 μs) at the expense of longer pulses on ^{1}H (23 μs) and ^{15}N (65 μs).

Apart from the 2D IPAP-CBCACO experiments described above, all other carbon experiments were recorded with the band-selective homodecoupling turned on during 20 % of the total acquisition time, in order to decouple the C' from the C^α signals.[158, 161] The ^{13}C decoupling field strength was set to 1.91 kHz. Adiabatic Chirp[164] pulses of 10 ms length, smoothed at 25 % and supercycled in a p5m4 manner[165, 166] have been chosen for composite pulse decoupling. In the decoupled spectra, the ^{13}C carrier for acquisition was set in between the spectral part of interest to avoid possible folding of artifacts into the spectrum. Strip transformation was then used to process at high resolution only the spectral region of interest. Composite pulse decoupling on ^{1}H and ^{15}N was applied during the whole duration of the experiments with the nutation frequency set to 1.665 kHz for ^{1}H (WALTZ-16)[167, 168] and 625 Hz for ^{15}N (GARP-4),[169] respectively. The carrier frequencies for pulses applied on ^{15}N and ^{1}H were of 120 and 3.5 ppm, respectively, unless otherwise specified.

In order to check sample integrity, ^{1}H - ^{15}N HSQC experiments were acquired with standard parameters.[170] The COCAMQ[158] spectrum was recorded to facilitate and confirm the assignment into the C' - C^α plane of the 3D spectrum. A recycle delay of 1 s, 256 dummy scans, 96 transients and 58 ms acquisition time were used to acquire the 2D spectrum. The total acquisition time in the indirect dimension was t_1^{max} = 28 ms. Spectral windows of 200 and 51.6 ppm were acquired in the C' and C^α dimensions corresponding to a matrix of 4096x512 complex points. The carrier on the carbon channel was switched from 98 to 50 ppm before the first $\pi/2$ C^α pulse and switched back to 98 ppm after the second $\pi/2$ C^α pulse.

Oncomodulin, a calcium binding diamagnetic protein containing 109 residues, has been used to evaluate the performance of these experiments. The calcium loaded form of the protein has been assigned through the "standard" approach based on triple resonance experiments and its solution structure is being solved through standard restraints.[171] The protein concentration in the final NMR sample was about 2.5 mM. The sample was dissolved in 100 mM NaCl at pH 6.0 water solution and 10 % D2O was added for the lock signal. All the spectra detailed below were recorded at 283 K.

The 2D spectrum of the CBCACO experiment is drawn in Figure 4.2. The spectrum shows the characteristic C' - C^β correlations, in addition to the C' - C^α ones. Therefore, if compared to the information contained in a COCAMQ spectrum, the additional cross peaks present in the CBCACO spectrum (for a total of two cross peaks per residue, except for Glys), provide information to identify the spin systems of all amino acids present in the protein. Assignment of a spin system to a particular residue type can be done on the basis of the characteristic chemical shift of the C^β resonance, or on its absence (Gly residues). Moreover, a larger chemical shift dispersion of C^β resonances, compared to the C^α ones, contributes to resolution enhancement.

In the present case, except for two spin systems in complete overlap (residues 61Glu and 62Glu, for which C', C^α and C^β are degenerate), all spin systems expected on the basis of the primary sequence of the protein were identified with the CBCACO experiment. If only the COCAMQ experiment is used, 5 pairs of residues have their C' - C^α correlation in overlap which means an uncertainty for 10 residues. Due to their different C^β shifts, these residues can be identified in the CBCACO experiment despite the C^α overlap.

Correlations involving side chains of Asp, Asn, Glu and Gln residues are also detected with this exper-
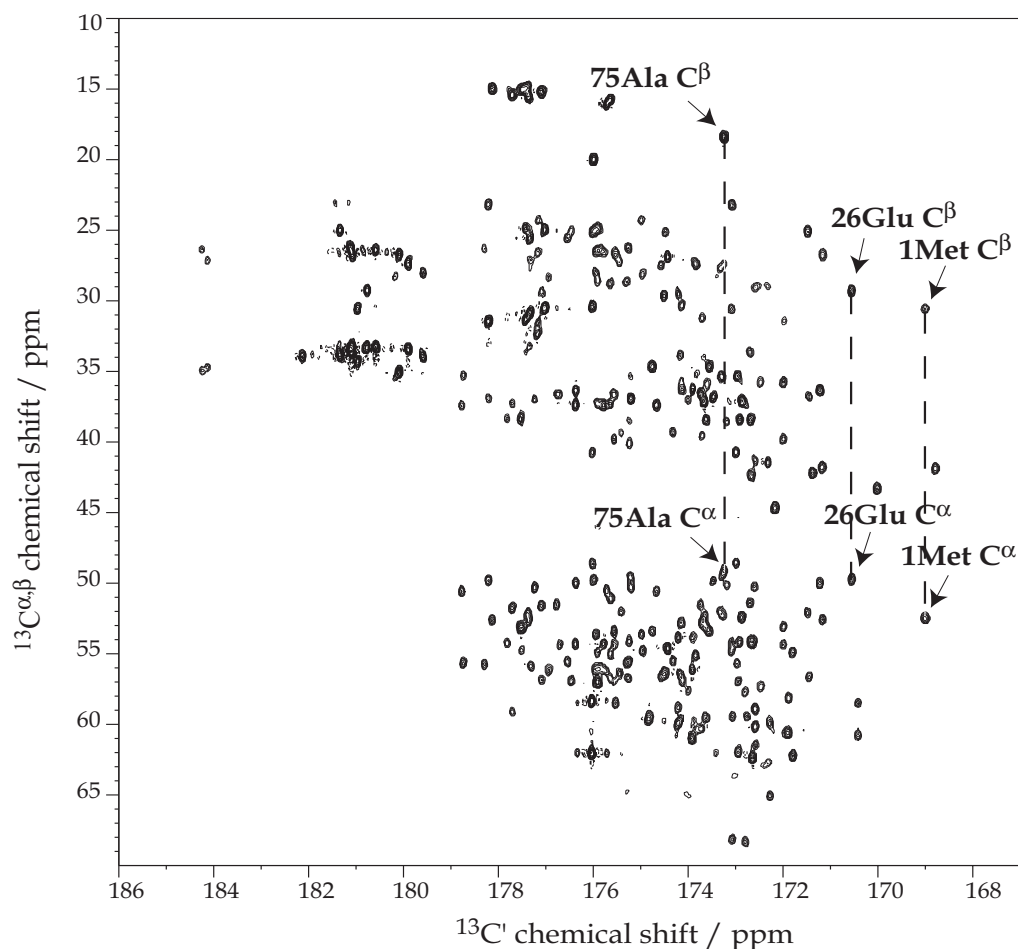
FIGURE 4.2: *2D spectrum (^{13}C' - $^{13}C^{\alpha,\beta}$) of the [U - $^{13}C,^{15}N$]-labelled oncomodulin protein at 283 K recorded on a Bruker Avance spectrometer operating at 700.06 MHz ^1H frequency with a prototype TXO probe. The experiment was acquired with band-selective homodecoupling of C^α during acquisition of the carbonyls. The ^{13}C was decoupled at 1.91 kHz with a train of adiabatic Chirp[164] π pulses of 10 ms length and smoothed at 25 %. Acquisition times t_1^{max} = 5.45 ms, t_2^{max} = 58 ms, recycle delay 1.3 s, 128 transients and 256 dummy scans were used. Spectral windows of 200 and 100 ppm were acquired in the C' and $C^{\alpha,\beta}$ dimensions, respectively. A matrix of 4096x192 complex points in the C' and $C^{\alpha,\beta}$ dimensions was acquired. ^1H and ^{15}N were decoupled at 1.667 kHz with WALTZ-16[167, 168] and 625 Hz with GARP-4,[169] respectively. The experimental time was 10 h. Prior to Fourier transformation, 8192x512 expansion by linear prediction in the indirect dimension together with zero filling and squared sine multiplication functions shifted by $\pi/4$ and $\pi/2$ were applied in t_2 and t_1 dimensions, respectively. A couple of C^α - C^β connected cross peaks are marked on the figure.*

iment in a specific region of the spectrum centered at δ_2 = 180 ppm, δ_1 = 30 ppm.

The 2D CBCACO experiment was expanded in a 3D version by evolving the C^α chemical shift in the third dimension. The 3D version of the experiment was used to separate two spin systems with degenerate carbonyl shifts. Moreover, the 3D spectrum allowed us to resolve residues that have the C' - C^α correlation in overlap. Some examples of cross sections extracted from the 3D CBCACO experiment are reported in FIGURE 4.3 which shows C^α - $C^{\alpha,\beta}$ (a), C' - $C^{\alpha,\beta}$ (b), and C' - C^α (c) planes containing correlations corresponding to 26Glu.

The CBCACO experiment provides information to connect the backbone assignment with side-chain assignment through identification of the C^β spin, in addition to C^α and C'. On the basis of the chemical shift of C^β it is possible to identify the kind of amino acid associated with a specific spin system and the large spread in the C^β chemical shifts also allows to obtain a good resolution in the C' - C^β region.
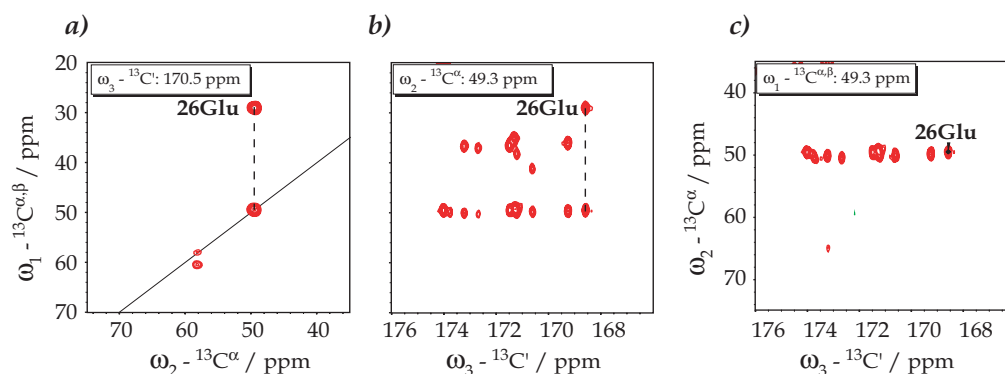
FIGURE 4.3: *Contour plots of a) [$C^{\alpha,\beta}$, C^α], b) [$C^{\alpha,\beta}$, C'], c) [C^α, C'] planes from the 3D CBCACO correlation spectra recorded with band-selective homodecoupling of C^α during acquisition of the carbonyls. In the [$C^{\alpha,\beta}$, C^α] plane, the C^α - C^β correlation of 26Glu is drawn in dotted line. The [$C^{\alpha,\beta}$, C'] plane corresponding to the backbone chemical shifts in the third dimension is shown in (c) and the correlation is marked on the spectrum. The experiment was recorded using 16 transients. Spectral windows of 99.3, 80 and 100 ppm were acquired in the C', C^α and $C^{\alpha,\beta}$ dimensions, respectively. The acquisition time was 59 ms. The maximum t_1 and t_2 evolution periods were 3.46 ms and 2.27 ms, respectively. All other experimental parameters are the same as those indicated in caption of FIGURE 4.1. The 3D CBCACO spectrum was processed with the XWINNMR 3.5 software. Prior to Fourier transformation the raw data were multiplied by squared sine functions shifted by $\pi/4$ and $\pi/2$ in t_2 and t_1 and further transformed with 2048x256x256 points using forward linear prediction and zero filling functions. Contours are drawn at the same levels for all the planes.*

4.2.3 Homodecoupling efficiency

All homonuclear experiments and the carbon directly detected experiments, in particular, show structured signals in the direct dimension due to the presence of the scalar coupling with the covalently bound nuclei. The scalar coupling in the indirect dimension can be removed by applying a semi-selective π pulse in the middle of the evolution period on the nucleus to which the evolving spin is coupled or by CT evolution.[140] The potential of carbon directly detected experiments for sequence specific assignment can be greatly enhanced by removing C - C couplings in the acquisition dimension. Band-selective homodecoupling (HD) provides a valuable solution to this problem.[158] Spin-state-selective filters[31, 32, 172] can also be implemented for this purpose. Another alternative is the virtual decoupling approach (based on the Maximum Entropy Reconstruction algorithm) first introduced to NMR by Hoch and Stern.[162, 163] This approach has to be used with caution and has been included in our study for the sake of completeness. Comparison of the three selected decoupling methods chosen (HD, IPAP and MER) points out that in terms of sensitivity the homonuclear IPAP spectrum is the most sensitive. Note that IPAP is expected to give optimal results if the J-coupling is uniform throughout the sample. This is generally the case for the C' - C^α scalar coupling. The efficiency of band-selective homodecoupling, instead, is independent on the value of the coupling constants and only depends on the resonance frequency of the decoupled nucleus.

The 2D CBCACO spectra used for the comparison of the different decoupling methods were all acquired with the same spectral widths and number of increments and were transformed with 8192x256 complex points by zero filling and multiplied by squared sine functions shifted by $\pi/4$ and $\pi/2$ in t_2 and t_1 dimensions. However they had to be processed with different software packages because none of the existing ones includes all the features necessary to the present analysis. The NMRPipe software package[173] was used because it allows us to easily shift one spectrum with respect to another one in the frequency domain through a shift function (C' - $C^{\alpha,\beta}$ non-decoupled, homocoupled and IPAP spectra). It can also be performed with the XWINNMR software by doing a first order correction of *shift**360/(*sweep width*) degrees in the time domain. The NMR Rowland Toolkit[174] software package was used for applying the maximum entropy reconstruction approach in order to "virtually decouple" the spectrum (C' - $C^{\alpha,\beta}$ non-decoupled, homocoupled and MER spectra).

Three 2D CBCACO experiments (^{13}C' - ^{13}C$^{\alpha,\beta}$) were acquired with the same parameters (except for the spin-state-selective method) in order to compare the efficiency in removing the C' - C$^\alpha$ coupling in the direct acquisition dimension. The IPAP experiment was acquired with one half the number of scans compared to the other two experiments used for the comparison (coupled and band-selective HD CBCACO) since in the former IPAP case two FIDs are acquired and stored separately and actually correspond to one FID of the other two experiments. The total measurement time for all kind of experiments was the same, thus allowing the direct comparison of the different results.

The 2D CBCACO spectra were recorded with 128 transients (64 for each of the two parts of the IPAP) and 256 dummy scans. On the carbon channel, the irradiation frequency offset was switched from 98 to 35 ppm in the beginning of the sequence and switched back to 98 ppm before the first $\pi/2$ C' pulse. The maximum acquisition time in the indirect dimension was t_1^{max} = 5.45 ms. Spectral windows of 200 and 100 ppm were acquired in the C' and C$^{\alpha,\beta}$ dimensions. A matrix of 4096x192 complex points was recorded.

To avoid possible errors due to any software dependent scaling factors and/or window functions we chose to compare spectra processed with the same software package. Thus, we first evaluated the C' - C$^{\alpha,\beta}$ non-decoupled, HD and IPAP spectra processed with the NMRPipe software package and, secondly, the C' - C$^{\alpha,\beta}$ non-decoupled, HD and MER spectra processed with the NMR Rowland Toolkit software package. For the first one, the traces were extracted using an appropriate NMRPipe function, while for the second case, the extraction was performed with the XEASY software package[175] after converting the Rowland data into the XEASY format. In spite of using the same processing parameters for all the spectra, the resultant traces seem to highly depend on the software used for processing and/or extraction of the traces.

The maximum entropy reconstruction method was performed along the direct dimension. The following parameters were found to give the best decoupled and sensitive spectrum: 25 iterations (*nloops*), 1000 points (*nuse*) for the linear sampling of each FID, 900 for the reconstruction scaling factor (*def*), 5x10^{-6} (*aim*) the difference between the input FID and the reconstructed one and 50 (*Jvalue*) the size in Hz of the constant coupling to be deconvoluted.

In order to compare the efficiency of the different approaches to remove the C' - C$^\alpha$ indirect coupling in the various spectra, several 1D traces of isolated cross peaks were extracted and compared in terms of signal-to-noise ratios (S/N). The following definition was used to calculate the S/N ratios:

$$\frac{\text{S}}{\text{N}} = \frac{M}{(2noise)} \tag{4-1}$$

where M is the highest intensity in the signal region and $noise$ is the root-mean-square of the noise amplitude. For the coupled spectrum this implicitly means considering the highest component of the multiplet, which in most cases is slightly asymmetric. To estimate the noise factor the algorithm described in XWINNMR software was employed. The signal region was chosen equal to 1.22 ppm such as only the peak of interest to be taken into account. The width of the noise region was selected equal to that of the signal. We verified that increasing these regions did not lead to appreciable variations in the S/N ratio. All the S/N ratios were calculated with a home written routine in the Matlab software.[79] The analysis was performed on a subset of well isolated peaks by extracting a 1D trace from the 2D spectra.

Since the quality of the spectra, both in terms of resolution and sensitivity, depends on the method chosen to eliminate the C' - C$^\alpha$ J-splitting present in the acquisition dimension, we have analysed the efficiency of the HD, IPAP and MER decoupling methods. As an example, Figure 4.4 compares traces from the 2D CBCACO spectra for four isolated peaks (1Met (C$^\beta$), 34Ser (C$^\alpha$), 55Gln (C$^\beta$), 108His (C$^\beta$)). The complete S/N analysis is reported in Table 4.1.

The results clearly indicate that the IPAP approach is the one that gives the best S/N ratio. The gain in S/N ratio compared to the most intense component of the coupled spectrum is close to that theoretically expected of $\sqrt{2}$. It is worthwhile to note that for band-selective homodecoupling, the low S/N ratio is mainly
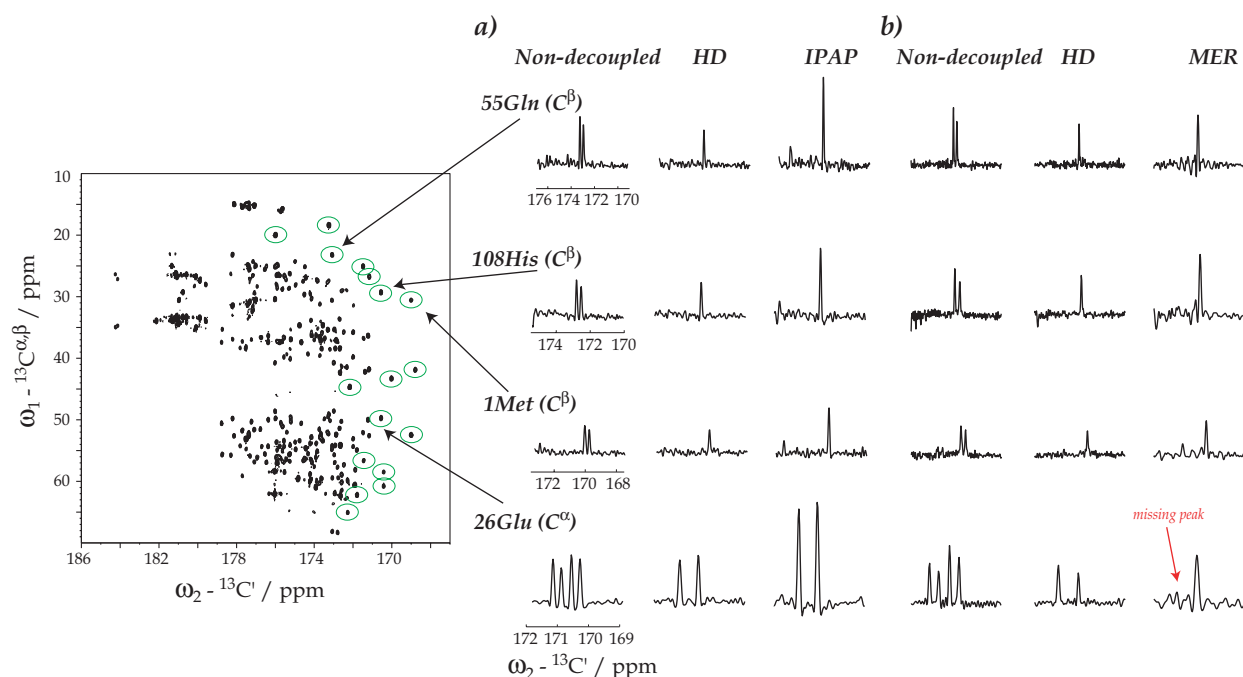
FIGURE 4.4: *1D traces of four selected residues (1Met (C$^\beta$), 26Glu (C$^\alpha$), 55Gln (C$^\beta$), 108His (C$^\beta$)) extracted from the CBCACO 2D spectra processed with a) NMRPipe[173] and b) NMR Rowland toolkit.[174] The three columns report traces extracted from spectra that only differ in the C' - C$^\alpha$ decoupling method used in the acquisition dimension: non-decoupled, homodecoupled and IPAP or MER. The spectra were scaled one with respect to the other by keeping the noise constant in all the traces. The S/N values determined for a set of well isolated peaks falling in clean areas of the spectra are reported in TABLE 4.1.*

determined by the increased noise in the spectrum, intrinsic to this acquisition method, rather than by unsatisfactory decoupling efficiency. MER apparently gives higher signal than the homodecoupled and non-decoupled spectra at the expense of a non-uniform noise surrounding the reconstructed peaks, and a certain unreliability in the presence of the peak itself.

The IPAP filter, which can be implemented in the CBCACO experiment at no cost in terms of extra relaxation (i.e., it is not necessary to extend the overall duration of the experiment), also yields a measurement of the C' - C$^\alpha$ coupling. This can be useful to determine C' - C$^\alpha$ couplings, again when protons are not detectable or not available because the protein is perdeuterated. Thus, even in the absence of proton assignment, residual dipolar couplings can be measured using this method, provided a sufficient degree of partial alignment can be induced either through external media or through the presence of heavily anisotropic metal ions. Residual dipolar coupling restraints, together with paramagnetic constraints such as pseudocontact shifts, relaxation rate enhancements and cross correlations, can provide effective structural information for structure refinement.[158, 176]

The CBCACO experiment may also be useful for studying large proteins. The experiments commonly used for the assignment of large proteins make use of the NH TROSY effect to exploit the advantageous transverse relaxation properties. For this purpose, the higher the magnetic field the larger the effect, up to about 23.4 T (1 GHz proton Larmor frequency) where the maximum efficiency is expected to be reached. This is in contrast with optimal conditions for C' relaxation as this is dominated by the CSA interaction that increases with the square of the magnetic field (i.e., faster than the increase in the magnitude of the cross-correlation rate responsible for the TROSY effect, that scales linearly with the external magnetic field). In the CBCACO experiment the TROSY effect is not used so there is no need to seek very high fields. Moreover, the delay during which C' is transverse is significantly shorter than in the CBCA(CO)NH experiment (9 ms vs 33 ms) and thus the adverse contribution to relaxation at high fields is reduced by a factor of about 3. The choice of the most appropriate magnetic field for the CBCACO experiment, should therefore result from a suitable compromise

TABLE 4.1: *Signal-to-noise ratios determined for 17 isolated peaks in the 2D CBCACO processed either with the NMRPipe software[173] (Ref, HD and IPAP) or NMR Rowland Toolkit software[174] (Ref, HD and MER), where Ref is the abbreviation of the non-decoupled spectrum. The mean and the standard deviation were calculated over the 17 peaks for all the spectra. The values for the non-decoupled version refer to the highest component of the doublet.*

Amino acid	NMRPipe			Rowland Toolkit		
	S/N (Ref)	S/N (HD)	S/N (IPAP)	S/N (Ref)	S/N (HD)	S/N (MER)
75Ala (C^β)	38.1	27.6	40.8	36.3	23.8	41.5
90Ala (C^β)	31.4	22.6	42.7	33.3	25.9	44.5
55Gln (C^β)	14.8	12.9	23.1	15.6	13.4	16.4
19Cys (C^β)	20.0	15.8	20.3	15.2	14.4	17.7
108His (C^β)	13.3	12.5	17.0	14.1	10.2	15.2
26Glu (C^β)	17.5	16.0	22.7	20.2	15.6	20.8
1Met (C^β)	8.9	8.0	12.5	9.5	6.9	14.1
57Gly (C^α)	17.0	13.2	20.5	17.1	12.8	10.7
96Gly (C^α)	21.8	15.7	34.1	21.5	17.1	21.8
94Gly (C^α)	23.3	17.2	32.9	17.7	20.4	19.6
26Glu (C^α)	16.8	14.6	19.7	17.3	9.7	17.3
1Met (C^α)	18.4	13.0	22.7	16.4	11.9	13.8
25Phe (C^α)	12.6	8.8	16.4	11.5	7.9	13.3
34Ser (C^α)	8.8	6.7	13.2	11.6	7.3	12.6
34Ser (C^β)	13.5	10.3	16.2	12.5	9.0	13.9
40Ser (C^β)	19.7	14.3	23.3	20.5	14.2	16.3
4Thr (C^β)	13.7	8.1	18.0	11.4	8.6	12.5
$\langle$S/N$\rangle \pm \Delta$(S/N)	18.2 ± 7.5	14.0 ± 5.3	23.3 ± 9.0	17.7 ± 7.3	13.5 ± 5.6	18.8 ± 9.7

between a high enough B_0 to obtain the necessary sensitivity and resolution but still maintain C' relaxation within acceptable limits.
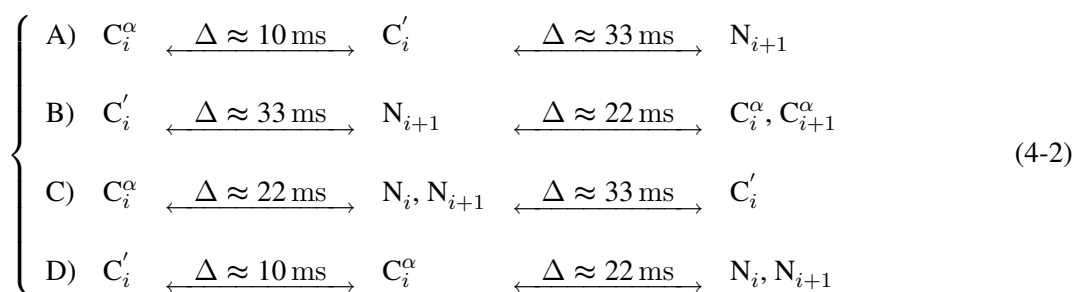
Another interesting application of the CBCACO experiment is in the assignment of side chains of Asp, Asn, Glu and Gln. Indeed, this information can be very useful when studying surface properties of proteins, such as protein-protein interactions, since these residues are often found on protein surfaces and are involved in inter-molecular recognition.

The CBCACO experiment may be also useful for studying unfolded systems and can complement the CBCA(CO)NH[177] experiment when the NH exchanges is broadened beyond detection by relaxation effects that cannot be recovered through the TROSY approach.

4.3 Triple-resonance CANCO experiment

4.3.1 Alternatives for coherence transfer

Various ways for connecting the backbone heterenuclei are open when the problem of sequential connectivity is approached from a ^{13}C-start, ^{13}C-detect point of view. The usual starting point of standard 2D and 3D experiments is the H^{N} - N transfer step, which takes advantage of the high sensitivity due to large separation in the ^{1}H energy levels and the TROSY effect. In contrast to these techniques based on ^{1}H detection, the ^{13}C schemes offer two possibilities for the starting nucleus and a wider range of transfer pathways. The design of ^{13}C-start, ^{13}C-detect sequences for backbone sequential connectivities requires a close investigation of the possible coherence transfer steps. For example, for obtaining sequential correlations of heteronuclei in an "out-and-back" scheme, four different coherence transfer steps can be imagined[2]. Following the transfer scheme reported in FIGURE 4.5a, they can be represented as follows:

$$
\begin{cases}
\text{A)} \quad \text{C}_i^\alpha \quad \xleftarrow{\Delta \approx 10\,\text{ms}} \quad \text{C}_i' \quad \xleftarrow{\Delta \approx 33\,\text{ms}} \quad \text{N}_{i+1} \\[2ex]
\text{B)} \quad \text{C}_i' \quad \xleftarrow{\Delta \approx 33\,\text{ms}} \quad \text{N}_{i+1} \quad \xleftarrow{\Delta \approx 22\,\text{ms}} \quad \text{C}_i^\alpha, \text{C}_{i+1}^\alpha \\[2ex]
\text{C)} \quad \text{C}_i^\alpha \quad \xleftarrow{\Delta \approx 22\,\text{ms}} \quad \text{N}_i, \text{N}_{i+1} \quad \xleftarrow{\Delta \approx 33\,\text{ms}} \quad \text{C}_i' \\[2ex]
\text{D)} \quad \text{C}_i' \quad \xleftarrow{\Delta \approx 10\,\text{ms}} \quad \text{C}_i^\alpha \quad \xleftarrow{\Delta \approx 22\,\text{ms}} \quad \text{N}_i, \text{N}_{i+1}
\end{cases}
\tag{4-2}
$$

We have aimed at obtaining a transfer pathway which offers, in the same plane, intra- and inter-residue connectivities between ^{13}C$^\alpha$ and ^{15}N nuclei, minimises the evolution delays and detects the slower-relaxing nucleus. Among these alternatives, the last one is therefore the most attractive because it reduces the relaxation losses taking advantage of the largest ^{13}C - ^{13}C scalar coupling available and yields both intra- and inter-residue connectivities. The magnetisation transfer, in the sequence displayed in FIGURE 4.5, takes place as follows: in-plane INEPT-like transfer from C' to C$^\alpha$, followed by the evolution of C$^\alpha$ chemical shift (t_1), a HMQC transfer to two neighbouring nitrogens, N chemical shift evolution (t_2), and back transfer to C$^\alpha$ and then C' nucleus, followed by the detection (t_3), with ^{15}N decoupling turned on during acquisition.

The weakness of this approach is resulting from the necessity of keeping the magnetisation of the aliphatic carbons transverse during the whole duration of the transfer which implies considerable relaxation losses. Additionally, the choice of an "out-and-back" approach increases the number of transfer periods. Since the spectrum recorded with this pulse sequence showed only 65 % from the expected correlations (which corresponds to all the intra-residue correlations and 31 % sequential correlations), we will further focus on the "out-and-stay" schemes and analyse in detail the $\text{C}_i^\alpha \rightarrow \text{N}_i, \text{N}_{i+1} \rightarrow \text{C}_{i-1}', \text{C}_i'$ transfer option which is very attractive for the detection of sequential correlations.

The transfer delays for this pulse sequence were tuned to maximise, at the same time, $\text{C}_i^\alpha \rightarrow \text{N}_i$ and $\text{C}_i^\alpha \rightarrow \text{N}_{i+1}$ transfers for the range (i.e., between 7 and 14 Hz) of inter-residue $J_{C^\alpha N}$ coupling values encountered in proteins. This property has been exploited in order to produce, in the C$^\alpha$ plane, two peaks of different intensities. FIGURE 4.6 depicts extreme cases of different intra- and inter-residue J-couplings found in proteins. The intra-residue $J_{C^\alpha N}$ value is constant (11 Hz), while the inter-residue J-coupling value can vary between 7 and 14 Hz. If the intra-residue value of the J-coupling is larger (see blue curves in FIGURE 4.6), the transfer will be more efficient for the intra-residue correlations and the intensity of the corresponding peak can be up to 2 times larger than that of the inter-residue one. On the other hand, if the inter-residue J-coupling is larger

---

[2]The nuclear spins of the i$^{\text{th}}$ amino-acid residue are specified as N$_i$ for the amide ^{15}N spin, C$_i^\alpha$ and C'$_i$ for α-carbon and carbonyl spins. Throughout this section, intra-residue and inter-residue ^{13}C$^\alpha$ - ^{15}N scalar coupling constants are named J_1 (i.e., $^1J_{C_i^\alpha N_i}$) and J_2 (i.e., $^2J_{C_i^\alpha N_{i+1}}$), respectively. Additionally, inter-residue ^{15}N - ^{13}C' and ^{13}C$^\alpha$ - ^{13}C$^\beta$ scalar coupling constants are designated J_{NC} (i.e., $^1J_{N_iC'_{i-1}}$) and J_{AB} (i.e., $^1J_{C_i^\alpha C_i^\beta}$), respectively.
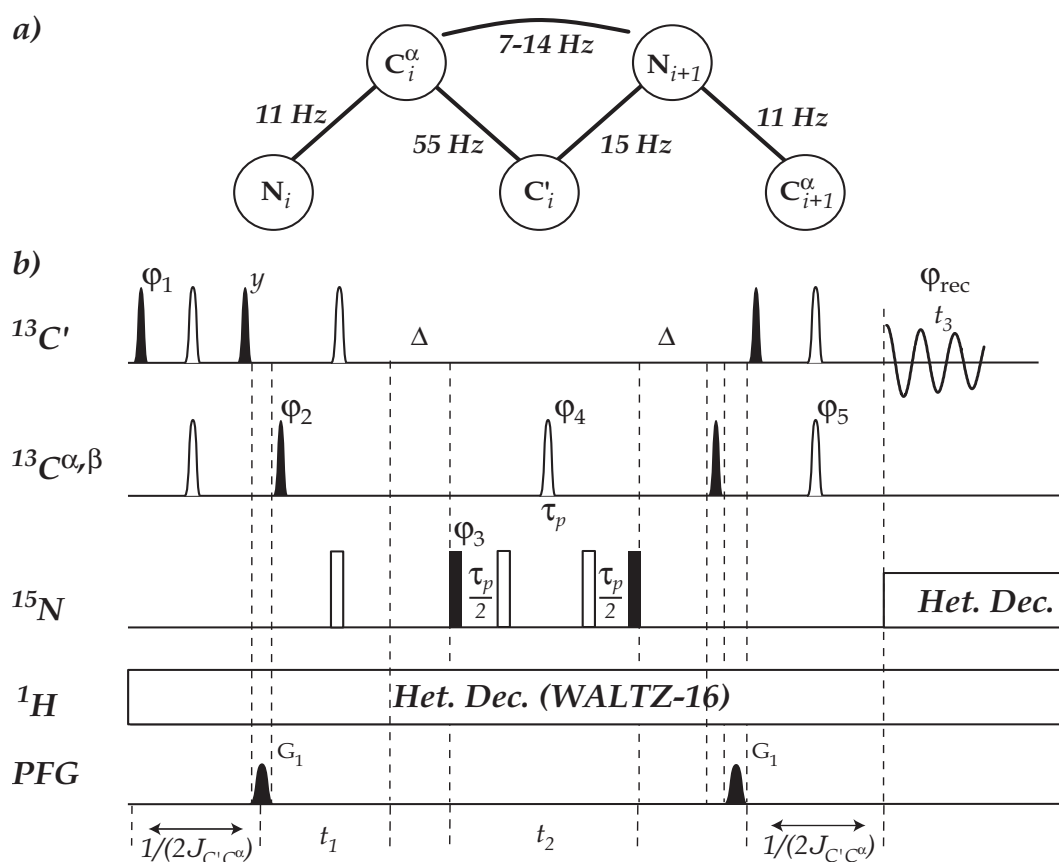
a)

b)

FIGURE 4.5: *a) Coherence transfer pathway in a protein. b) Pulse sequence corresponding to the CO(CA)N transfer pathway noted D) in the equation 4-2.*

(see green curves in FIGURE 4.6), the transfer is then more efficient for the inter-residue connectivities and the ratio of the peak intensities can be up to 0.5 (i.e., inter/intra). It results from the curves shown in FIGURE 4.6 that a transfer time of 22 ms will optimise both intra- and inter-residue connectivities for the whole range of inter-residue $J_{C^\alpha N}$ values encountered in proteins.

The pulse sequence, corresponding to the intra- and inter-residue transfers depicted above, will be described in the following section.

4.3.2   Pulse sequence description

The 3D CANCO experiment correlates the chemical shifts of C^α nuclei with the shifts of the two neighbouring nitrogen nuclei and subsequently with those of the carbonyls adjacent to these nitrogen atoms. This produces patterns in which for each N spin two resonances appear, corresponding to the two nearest C^α carbons (C_i^α,N_{i+1},C_i' and C_{i+1}^α,N_{i+1},C_i')[3] in the (ω_1, ω_2, ω_3) dimensions. The magnetisation transfer pathway

---

[3]For ease of presentation, the C_i^α,N_{i+1},C_i' connectivities are referred to as intra-residue and the C_{i+1}^α,N_{i+1},C_i' connectivities are referred to as inter-residue.
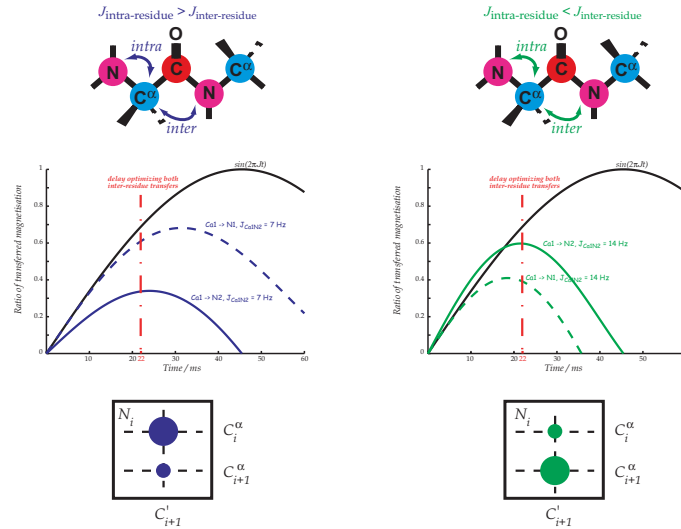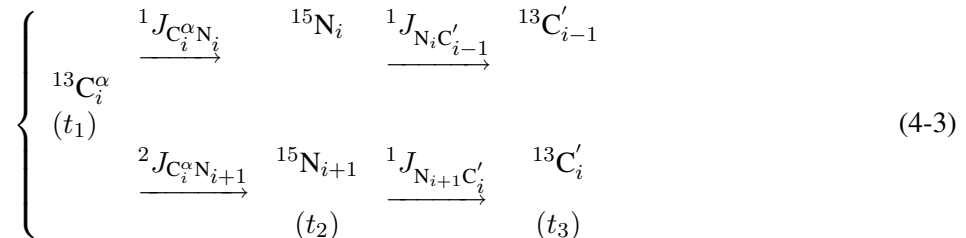
FIGURE 4.6: *Dependency of $C^\alpha \rightarrow N$ magnetisation transfer efficiency on the transfer delay. The transfer curve corresponding to a single $C^\alpha N$ J-coupling is drawn in black. The other inter- and intra-residue transfer curves are drawn in either continue or dashed lines. The transfer curves are drawn in blue for the case when the intra-residue $J_{C^\alpha N}$ coupling value is larger than the inter-residue one. For the opposite case, the transfer curves are drawn in green.*

can be represented as:

$$
\begin{cases}
& \xrightarrow{{}^1 J_{C_i^\alpha N_i}} \quad {}^{15}N_i \quad \xrightarrow{{}^1 J_{N_i C'_{i-1}}} \quad {}^{13}C'_{i-1} \\
{}^{13}C_i^\alpha & \\
(t_1) & \\
& \xrightarrow{{}^2 J_{C_i^\alpha N_{i+1}}} \quad {}^{15}N_{i+1} \quad \xrightarrow{{}^1 J_{N_{i+1} C'_i}} \quad {}^{13}C'_i \\
& \qquad\qquad\qquad (t_2) \qquad\qquad\qquad\qquad (t_3)
\end{cases}
\tag{4-3}
$$

The pulse sequence developed for obtaining sequential correlation of backbone heteronuclei follows the transfer scheme reported in FIGURE 4.7a. The description of the actual pulse sequence and the magnetisation transfer pathway in terms of product operator formalism[111] are detailed below.

The pulse sequence of the CANCO experiment is drawn in FIGURE 4.7b. The time points we evaluate herein are marked by circled numbers. The first semi-selective pulse on C^α is followed by a CT-evolution period,[140] optimised to refocus C^α - C^β scalar couplings, during which magnetisation is labelled with the C^α chemical shift. The evolution of the two C^α - N J-couplings during part of the CT period allows to transfer the magnetisation to the two nearest nitrogen spins. At the same time, the C'N scalar coupling is refocused. Thus, the magnetisation from time point ① to time point ② is represented by:

$$
\begin{aligned}
-C_{iy}^\alpha \quad \rightarrow \quad & -2C_{ix}^\alpha N_{iz} \cos(\pi J_{AB}(\delta + \varepsilon)) \overbrace{\sin(\pi J_1 \delta) \cos(\pi J_2 \delta) \cos(\Omega(C_i^\alpha) t_1)}^{T_1} \\
& -2C_{ix}^\alpha N_{(i+1)z} \cos(\pi J_{AB}(\delta + \varepsilon)) \underbrace{\cos(\pi J_1 \delta) \sin(\pi J_2 \delta) \cos(\Omega(C_i^\alpha) t_1)}_{T_2}
\end{aligned}
\tag{4-4}
$$

where the terms noted T_1 and T_2 are introduced for ease of writing. For $\delta + \varepsilon = 1/J_{AB}$, $\cos(\pi J_{AB}(\delta + \varepsilon)) = -1$ for all the amino acids having a C^β. On the contrary, for Gly residues the previous cosine term is equal to $+1$, thus ensuring a phase discrimination between Gly and other residues. The following product operator description is not restricted to the particular case of Gly residues, which can be easily obtained by changing the
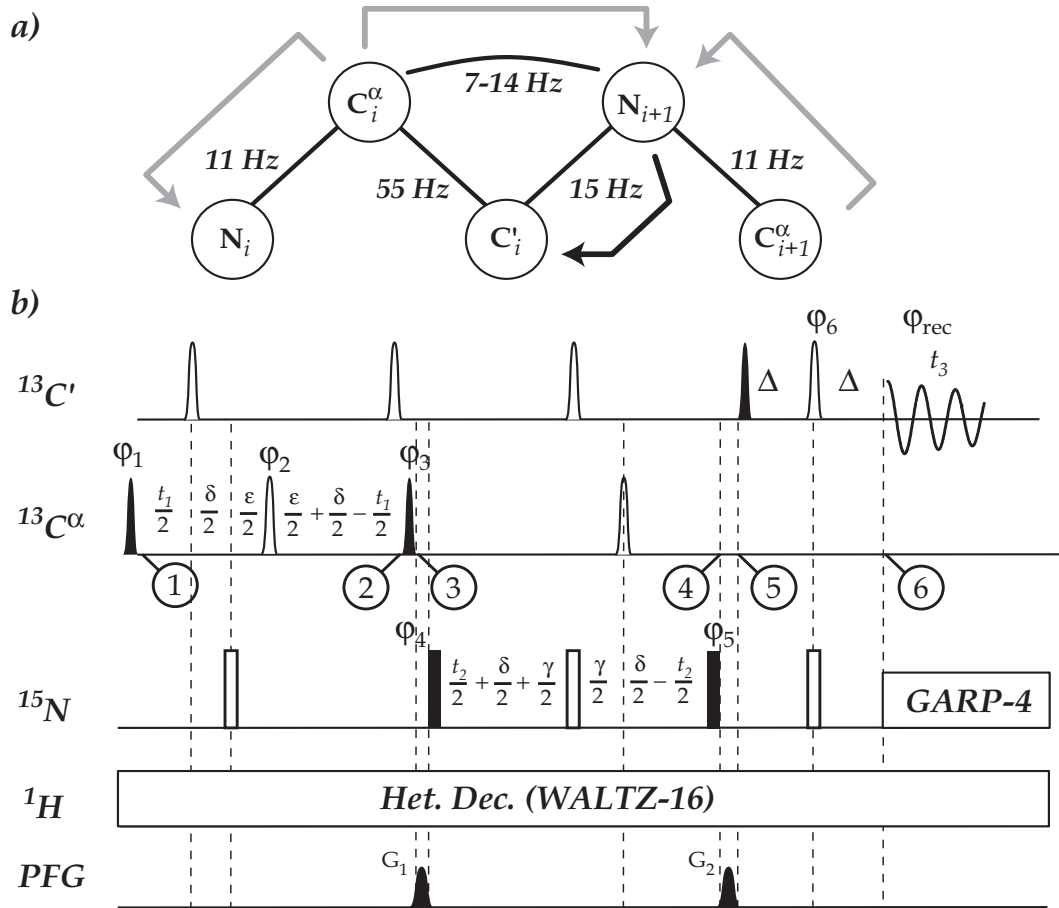
a)

b)

FIGURE 4.7: *a) Coherence transfer pathway in the CANCO sequence: the transfers occurring during the first step of the sequence are indicated by gray arrows, those effected during the second step by black arrows. b) Pulse sequence suited for CANCO correlation experiment.*

sign of the magnetisation. The C^{α} - N coherence transfer is performed between ② and ③ time points and, in terms of product operators, the magnetisation is as follows:

$$\begin{cases} 2C^{\alpha}_{ix}N_{iz}T_1 & \rightarrow & 2C^{\alpha}_{iz}N_{iy}T_1 \\ 2C^{\alpha}_{ix}N_{(i+1)z}T_2 & \rightarrow & 2C^{\alpha}_{iz}N_{(i+1)y}T_1 \end{cases} \tag{4-5}$$

During the second CT evolution period, the chemical-shift labelling of the nitrogen spins is accomplished, the magnetisation is refocused with respect to C^{α} and J-coupling transfer to carbonyls takes place. At the end of the t_2 evolution period (i.e., ④ time point) the observable magnetisation is described by the following two terms:

$$\begin{cases} -2C'_{(i-1)z}N_{iy}\sin(\pi J_{NC}(\delta+\gamma))\overbrace{\sin(\pi J_1\delta)\cos(\pi J_2\delta)\cos(\Omega(N_i)t_2)}^{T_3}T_1 \\ -2C'_{iz}N_{(i+1)y}\sin(\pi J_{NC}(\delta+\gamma))\underbrace{\cos(\pi J_1\delta)\sin(\pi J_2\delta)\cos(\Omega(N_i)t_2)}_{T_4}T_2 \end{cases} \tag{4-6}$$

where again the terms noted T_3 and T_4 are introduced for ease of writing. By choosing $\delta + \gamma = 1/(2J_{NC})$, $\sin(\pi J_{NC}(\delta+\gamma)) = 1$. The coherence transfer from nitrogens to carbonyls is performed from time point ④ to

time point ⑤ and the magnetisation at the time point ⑤ is given by:

$$
\left\{
\begin{array}{l}
2\mathrm{C}'_{(i-1)y}\mathrm{N}_{iz}\mathrm{T}_1\mathrm{T}_3 \\
2\mathrm{C}'_{iy}\mathrm{N}_{(i+1)z}\mathrm{T}_2\mathrm{T}_4
\end{array}
\right.
\tag{4-7}
$$

The last part of the sequence consists of refocusing of C' magnetisation with respect to nitrogen and detection of carbonyls. This yields to the following expression of the magnetisation at time point ⑥:

$$
\left\{
\begin{array}{l}
-\mathrm{C}'_{(i-1)x}\sin(2\pi J_{\mathrm{NC}}\Delta)\mathrm{T}_1\mathrm{T}_3 \\
-\mathrm{C}'_{ix}\sin(2\pi J_{\mathrm{NC}}\Delta)\mathrm{T}_2\mathrm{T}_4
\end{array}
\right.
\tag{4-8}
$$

If $\Delta = 1/(4J_{\mathrm{NC}})$, $\sin(2\pi J_{\mathrm{NC}}\Delta) = 1$ and the observable magnetisation is thus modulated by the next two terms:

$$
\left\{
\begin{array}{ll}
e^{\mathrm{i}\Omega(\mathrm{C}'_{i-1})t_3}e^{\mathrm{i}\Omega(\mathrm{N}_i)t_2}e^{\mathrm{i}\Omega(\mathrm{C}^\alpha_i)t_1}[\sin(\pi J_1\delta)\cos(\pi J_2\delta)]^2 & \text{(inter-residue term)} \\
e^{\mathrm{i}\Omega(\mathrm{C}'_i)t_3}e^{\mathrm{i}\Omega(\mathrm{N}_{i+1})t_2}e^{\mathrm{i}\Omega(\mathrm{C}^\alpha_i)t_1}[\cos(\pi J_1\delta)\sin(\pi J_2\delta)]^2 & \text{(intra-residue term)}
\end{array}
\right.
\tag{4-9}
$$

The choice of the "out-and-stay" transfer approach is not arbitrary because it allows the N - C' transfer to be performed at the same time as the refocusing of ^{15}N magnetisation with respect to C$^\alpha$ which considerably reduces the duration of the pulse sequence and ensures increase in sensitivity. Additionally, the starting C$^\alpha$ magnetisation can be enhanced by irradiating protons during part of the recycle delay. This results in a sensitivity enhancement which depends on the C - H cross-relaxation rate. However, this method is not useful in ^{2}H-labelled molecules.

The initial CT delay was set to $1/J_{\mathrm{AB}}$ in order to refocus the C$^\alpha$ - C$^\beta$ scalar coupling. An alternative could be using a semi-selective π pulse at the C$^\alpha$ frequency (with respect to the C$^\beta$ frequency), which results however in a decreased sensitivity of amino acids for which the C$^\alpha$ and C$^\beta$ chemical shifts are very similar (i.e., Thr, Ser) or of amino acids for which the C$^\alpha$ resonances have large deviations from the mean C$^\alpha$ chemical shift of proteins (i.e., Gly, Pro, Ala, Val).[178]

Phase cycling eliminates artifacts due to imperfections of the associated π pulses and coherences resulting from incomplete J-coupling evolution. The pulsed field gradients are complementary to the phase cycling, eliminating any in-plane magnetisation once the intended J-coupling transfers are achieved and the magnetisation of interest is parallel to the main magnetic field.

4.3.3   Results and discussion

The 3D CANCO experiment was also tested on oncomodulin protein ($11.5\,\mathrm{kDa}$, 109 amino acids). A pair of 2D experiments, namely the COCA and CON[158] multiple-quantum experiments, were also acquired to complement the 3D CANCO data.

Most of the experimental parameters for the 3D CANCO experiment are similar to those used for CBCACO. Phase cycling of φ_1, φ_3, φ_4 and φ_5 eliminates magnetisation that does not follow the desired C$^\alpha$ - N - C' pathway, φ_2 and φ_6 eliminate artifacts due to imperfections of the associated π pulse. Phase-sensitive spectra in the ^{13}C$^\alpha$ (t_1) and ^{15}N (t_2) dimensions are obtained by incrementing the phases φ_1 and φ_4 in a States-TPPI manner.[156] For ^{1}H decoupling, the WALTZ-16[167, 168] sequence was used, with applied field strength of $1.667\,\mathrm{kHz}$. For ^{15}N decoupling, the GARP-4[169] sequence was used, with applied field strength of 625 Hz.

The 3D CANCO experiment was acquired using 640 transients and a recycle delay of $1.2\,\mathrm{s}$. Spectral windows of 220, 40 and 64 ppm were acquired in the ^{13}C', ^{15}N and ^{13}C$^\alpha$ dimensions, respectively. The acquisition time was $59\,\mathrm{ms}$. A matrix of 4096x16x64 complex points in ^{13}C', ^{15}N and ^{13}C$^\alpha$ dimensions was acquired and transformed to 4096x128x128 points using linear prediction and zero filling. The maximum t_1 and t_2 evolution periods were $2.8\,\mathrm{ms}$ and $4.86\,\mathrm{ms}$, respectively.
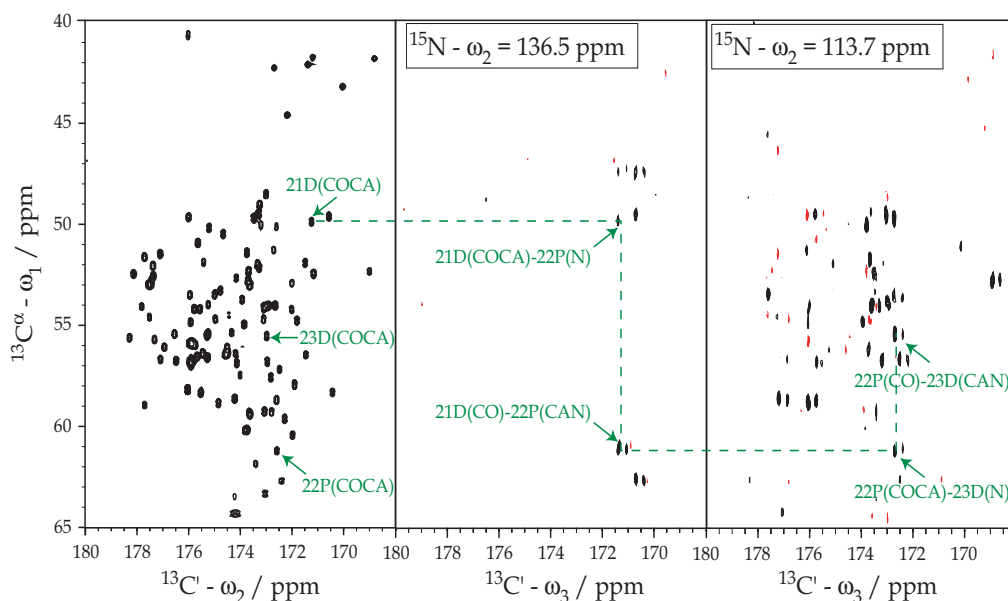
FIGURE 4.8: *Schematic representation of the methodology for establishing sequential correlations in the series of residues 21Asp - 22Pro - 23Asp of oncomodulin protein, using 2D CACOMQ and 3D CANCO spectrum. Two planes of the 3D spectrum are displayed, corresponding to the ^{15}N frequency of 22Pro and 23Asp.*

FIGURE 4.8 illustrates the sequential assignment approach for the series of three residues 21Asp - 22Pro - 23Asp. The ^{15}N chemical shifts of the two prolines present in oncomodulin (22Pro, at 135.3 ppm and 27Pro, at 135.6 ppm) were actually assigned using this 3D spectrum. Indeed, all types of residues can be detected with the 3D CANCO sequence, in contrast with other sequences that, being based on the NH group, do not allow a direct assignment of proline residues.

The 3D experiment displays the signals of 99 C_{i+1}^{α}, N_{i+1}, C_i' inter-residue correlations (which represents 92.5 % of the assigned expected correlations) and 85 C_i^{α}, N_{i+1}, C_i' intra-residue correlations (representing 79.4 % of the assigned expected correlations). All missing C_i^{α}, C_i' correlations were identified in the 2D COCAMQ experiment and were connected to the adjacent residue with the aid of a 2D CON experiment.

The ^{15}N resonances of 22Pro (136.5 ppm), 27Pro (135.6 ppm), 52Asp (118.6 ppm), 64Leu (116.6 ppm), 65Lys (116.9 ppm) and 109Ser (122 ppm), the $^{13}C^{\alpha}$ resonances of 59Leu (58.8 ppm), 60Asp (56 ppm), 63Glu (55.48 ppm), 64Leu (54 ppm) and 109Ser (58.09 ppm), as well as the $^{13}C'$ resonances of 64Leu (175.2 ppm) and 86Leu (174.4 ppm) were not assigned by the use of standard proton spectra[171] and could be assigned by using the ^{13}C-detected spectra described herein.

As pointed out earlier, an important feature of this pulse sequence is its increased sensitivity for inter-residue correlations, which are favoured with respect to intra-residue correlations, as the former originate from transfer with the higher C^{α} - N scalar coupling constant (of $\approx$ 14 Hz), while the last originate from coherence transfer with the smaller C^{α} - N coupling constant (of $\approx$ 7 Hz). This is a remarkable feature, as in the majority of the existing proton-based pulse sequences that provide both correlations simultaneously the inter-residue correlations are unfavourable, making it difficult to establish sequential connectivities when the quality of the spectra is poor.

Resonances which involve a step in coherence transfer on the proline nitrogen spins (intra- and inter-correlations for residues preceding prolines) are favoured in terms of sensitivity, as the relaxation rates of proline nitrogens are lower[4]. On the other hand, the sensitivity is lower when transfer from C^{α} of glycines is involved, as these nuclei are coupled to two protons, but this is a concern also for the classical proton-based

---

[4]It has to be noticed that they are coupled to an additional carbon, while all other nitrogens are coupled to a proton.

pulse sequences. In the 3D spectrum recorded on the oncomodulin sample, out of the twelve overall expected correlations originating on Gly C^α nuclei only three C^α_{i+1}, N_{i+1}, C'_i and two C^α_i, N_{i+1}, C'_i correlations were observed. As previously mentioned, due to the absence of the scalar coupling during the first CT-evolution period, signals originating from Gly C^α are very easily distinguished, as they have opposite phase with respect to all other signals that evolve with the cosine period during this step.

As the chemical shifts of C^α and C^β of alanine are at the extreme ranges of the irradiated region, magnetisation originating from Ala C^α nuclei might also result in less sensitive transfers.[178] The remaining three missing inter-correlations might be accounted for by slightly different values of the inter-residual coupling between ^{15}N and $^{13}C^\alpha$ carbons, for which the transfer delay was not optimal, or by the occurrence of conformational exchange phenomena. The magnetisation transfer pathway hinders the observation of an intra-residue correlation for the last residue in a protein (as magnetisation would have to be transferred via the nitrogen nucleus of the next residue), but the inter-residue correlation between the penultimate and the last residue is expected, as well as both the correlations involving the first residue.

4.4 Conclusion

The experimental approaches described in this chapter are designed for the complete assignment of the backbone heteronuclei without involving protons. In the absence of TROSY effects, which become operative at high fields, the present approaches become interesting. In paramagnetic molecules, the TROSY effect may be ineffective in some parts of the macromolecule because of paramagnetic relaxation, and then the heteronuclear direct detection sequences are preferable.

Principles of spin-echo modulation by J-couplings in magic-angle-spinning solid-state NMR

5.1 Introduction

The modulation of spin echoes by the indirect scalar coupling (J-coupling) between nuclear spins is a well-known phenomenon in solution-state NMR. The observation of spin-echo modulation by Hahn and Maxwell in 1951[28] was one of the first experiments that demonstrated the existence of the J-coupling and established its nature as an indirect coupling between the magnetic dipole moments of the nuclei, with the participation of the bonding electrons. Since then, the J-modulation of spin echoes has been the basis of innumerable useful methods, including some of the earliest two-dimensional NMR experiments,[13] polarisation transfer techniques such as INEPT,[21] and double-quantum-filtering experiments such as INADEQUATE.[103, 104]

Many solution-state NMR experiments incorporating J-modulated spin echoes have been adapted for solid-state NMR. For homonuclear spin systems, the INADEQUATE experiment[122, 123, 124] is a valuable probe of through-bond connectivities in both inorganic[124, 125, 126] and organic solids.[106, 179] The refocused INADEQUATE experiment, which incorporates two spin echoes, delivers enhanced sensitivity for the common case where the refocused linewidth is smaller than the normal linewidth, and has been widely applied.[92, 112, 127, 128, 116, 129] The J-couplings have also been exploited in solids by double-quantum filtered correlation experiments.[180, 181, 182] It was illustrated in the previous chapters that the J-modulated spin echoes are important elements of spin-state-selective experiments, which provide enhanced resolution and sensitivity in the spectra of ^{13}C labelled systems. Two-dimensional spin-echo experiments, utilizing the modulation of spin echoes by homonuclear J-couplings, have been widely performed in magic-angle-spinning solids, for example in the ^{31}P studies of inorganic and organometallic systems.[129, 183, 184, 185, 186, 187, 188, 189, 190, 191, 192, 193] Spin echoes modulated by heteronuclear J-couplings are also widely utilised.[194, 195, 196, 197, 198, 199, 200, 201, 202, 203]

A particularly promising application of J-coupling measurements in solids is the study of hydrogen bonding. Brown *et al.* showed that ^{15}N - ^{15}N hydrogen-bond mediated J-couplings can be measured using ^{15}N spin-echo MAS experiments with a precision sufficient to identify differences in hydrogen bonding strength.[114] Similarly, the quantitative determination of a ^{13}C - ^{1}H J-coupling associated with an H-agostic bond allowed the calculation of the C - C - H bond angle.[200]

Clearly, such precise experiments depend upon a good understanding of the J-modulation of spin echoes in solids. However, many of the experiments described above have been performed without solid theoretical support. Instead, the validity of this approach has largely been based on the good agreement of the extracted J-couplings with values known from solution-state NMR or with values determined from observable multiplet patterns in magic-angle-spinning spectra. In this chapter, we attempt to give a reasonably com-

prehensive theory of spin-echo modulation by homonuclear *J*-couplings in magic-angle-spinning solids, for the case of isolated spin-1/2 pairs. We make no attempt here to compare the spin-echo modulation experiment with other methods for estimating the *J*-coupling in MAS NMR, such as the TOBSY range of pulse sequences.[141, 204, 205, 206, 207, 208, 209, 210, 211, 212, 213]

The modulation of spin echoes is well-understood for coupled spin-1/2 pairs in isotropic liquids. The Hahn-Maxwell paper[28] already provided the essential theoretical description, including the well-known disappearance of the *J*-modulation when the isotropic shifts of the two coupled spins are the same (case of magnetic equivalence), and the more complicated modulation patterns in the so-called strong coupling case, where the isotropic shift difference is comparable to the *J*-coupling.

The situation is potentially much more complicated for spin-1/2 pair systems in magic-angle-spinning solids, since the nuclear spins experience strong anisotropic interactions such as the CSA and direct DD coupling. These interactions are often much larger than the *J*-coupling, usually do not commute with it, and are modulated in time as the sample rotates. It is therefore reasonable to expect a complex spin-echo behaviour for solids under MAS, compared to isotropic liquids. Any observed modulation would be expected to depend on the interplay of many factors in addition to the *J*-coupling, such as the CSA tensors, the DD interactions, and their mutual orientation. Although such complications could be rich and informative, they would, if present, be a practical obstacle to the measurement and exploitation of *J*-couplings in solids, since many of the participating interactions are hard to characterise by independent measurements.

There have been several theoretical studies of the behaviour of spin-1/2 pairs in solids under MAS, concentrating especially on the spectral lineshapes.[20, 184, 185, 186, 188, 189, 191, 214, 215, 216, 217, 218, 219, 220, 221, 222, 223] In their classic paper on magic-angle spinning, Maricq and Waugh[20] used average Hamiltonian theory[224] to analyse the one-dimensional MAS lineshapes of coupled spin-1/2 pairs, in the case that the isotropic chemical shifts are the same while the CSA tensors have different orientations. This special case, often known as "$n = 0$ rotational resonance", has subsequently been investigated by various research groups.Maricq and Waugh[20] identified the significance of the interference term involving the chemical-shift anisotropy and the dipole-dipole coupling between the spins, using second-order average Hamiltonian theory. They predicted that the spectral splitting induced by the *J*-coupling, which is absent in solution-state NMR for the case of identical isotropic shifts, may reappear under certain conditions in MAS solid-state NMR. However, a clear experimental demonstration of this was not given. The Maricq and Waugh theory was reformulated and expanded by Kubo *et al.*[184] and Challoner *et al.*,[185] who presented a more thorough comparison with experiment, including an investigation of *J*-modulated 2D experiments in systems with coupled ^{31}P nuclei. These authors clearly demonstrated the *J*-recoupling phenomenon in two-dimensional spectra. *J*-recoupling has now been widely studied and exploited.[185, 188, 189, 190, 192, 193] It has also been shown that the sign of the *J*-coupling can be determined from a fitting of the one-dimensional MAS lineshapes.[220, 225]

Herein, we explore the theory and consequences of the *J*-recoupling effect in more detail. In contrast to Maricq and Waugh,[20] Kubo *et al.*,[184] Challoner *et al.*[185] and Kuwahara *et al.*,[222, 223] we will concentrate on the *J*-modulation of spin echoes, rather than the one-dimensional and two-dimensional lineshapes, which are more complicated. We will also generalise the theory and consider important cases which are not discussed thoroughly in the earlier studies, such as the transitions between the various modulation regimes, and the influence of rotational resonance on the *J*-modulation.

The conclusions of this theoretical study are optimistic with respect to the exploitation of *J*-couplings in solids. We will show that for a wide range of conditions, rather simple *J*-modulation behaviour is expected, even in the presence of large CSA and DD interactions, and even for cases which would give rise to relatively complex behaviour in liquids, such as when the isotropic shifts are slightly different. We also highlight the rare regimes where a simple *J*-modulation of spin echoes is not expected.

5.2 Theoretical description

We assume throughout this chapter a model of isolated spin-1/2 pairs experiencing chemical shift anisotropy and interacting by a through-space DD coupling and by a scalar J-coupling. Anisotropic contributions to the J-coupling are absorbed into the DD term, which transforms in an identical fashion. The spin-1/2 pairs are assumed not to interact with each other. This situation is approximated in practice by, for example, organic solids in which $^{13}C_2$ pairs have been introduced chemically, and in which the $^{13}C_2$ pairs are dilute. We assume that interactions with heteronuclei such as protons are strongly suppressed by decoupling irradiation, and that any residual heteronuclear couplings may be taken into account by imposing an exponential decay on the theoretical results. Relaxation and other damping processes are taken into account in the same way. Lineshape effects induced by transverse relaxation, as described in Helmle *et al.*,[226] are not considered.

The pulse sequence under discussion is sketched in FIGURE 5.1. Transverse magnetisation is generated by a strong $\pi/2$ pulse (or by cross polarisation) and allowed to evolve for the first half of the spin-echo interval, denoted τ. In the discussion below, we assume that the $\pi/2$ pulse has phase 90°. A strong π pulse is applied, and the transverse magnetisation is allowed to evolve for a further interval τ before the NMR signal is detected and Fourier transformed, to give the NMR spectrum. The π pulse is considered here to be ideal, infinitely short, and to have phase 0. The circled numbers in FIGURE 5.1 indicate time points which are used in the discussion below.
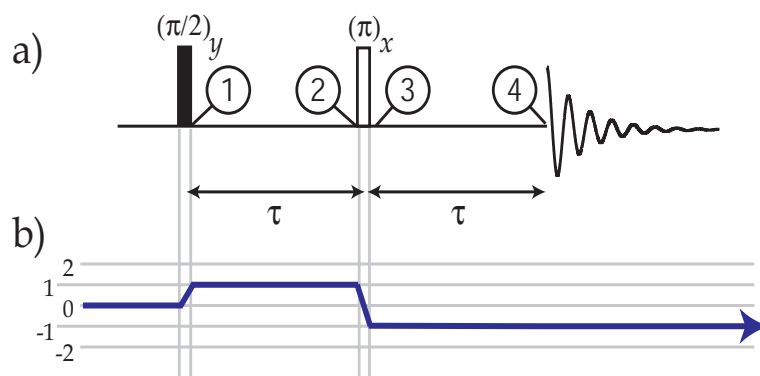
FIGURE 5.1: *a) Spin-echo pulse sequence. The intervals τ are integer multiples of the MAS rotation period τ_r. b) Coherence transfer pathway[2] showing that the quadrature-detected NMR signals derive from $(+1)$-quantum coherences during the first half of the spin-echo interval and (-1)-quantum coherences during the second half of the spin-echo interval.*

It will be assumed throughout that τ is an integer multiple of the sample rotation period $\tau_r = |2\pi/\omega_r|$, where ω_r is the angular rotation frequency of the sample. If this synchronisation condition is not satisfied, the CSA introduces additional modulation effects, which are described elsewhere.[223, 227, 228] The form of the NMR spectrum may vary in a complicated way as the total echo interval is increased. In the discussion below, we ignore the details of the spectral lineshapes, and concentrate solely on the *integrated* spectral amplitude as a function of the total echo interval. The integrated spectral amplitude is identical to the time-domain signal at the instant of the echo maximum, denoted $s(2\tau)$.

The time-domain echo modulation function $s(2\tau)$ may be Fourier transformed to obtain the *echo modulation spectrum*. The theory below is mainly concerned with the echo-modulation pattern generated by a single molecular orientation. In a powder sample, there is a superposition of contributions from many different molecular orientations, as discussed later.

5.2.1 Nuclear spin Hamiltonian

The theory of homonuclear spin-1/2 pairs in MAS solids has been discussed many times in the literature.[61, 226] The main results will be now quickly summarized. The nuclear spin Hamiltonian representing the homonuclear spin-1/2 pair system may be written as follows:

$$\mathcal{H} = \mathcal{H}_j + \mathcal{H}_k + \mathcal{H}_{jk} \tag{5-1}$$

where the one-spin Hamiltonians are:

$$\begin{cases} \mathcal{H}_j &= \omega_j S_{jz} \\ \mathcal{H}_k &= \omega_k S_{kz} \end{cases} \tag{5-2}$$

and the two-spin Hamiltonian is:

$$\mathcal{H}_{jk} = \omega_A 2 S_{jz} S_{kz} + \omega_B \frac{1}{2}[S_j^+ S_k^- + S_j^- S_k^+] \tag{5-3}$$

Here ω_j and ω_k are the instantaneous chemical-shift frequencies of the two spins, while ω_A and ω_B depend on the direct and indirect spin-spin couplings according to the following relation:

$$\begin{cases} \omega_A &= \pi J + d \\ \omega_B &= 2\pi J - d \end{cases} \tag{5-4}$$

The term d is the secular part of the DD coupling between the spins, and depends on the instantaneous angle θ_{jk} between the internuclear vector and the magnetic field. The secular DD coupling d is given by:

$$d = b_{jk} \tfrac{1}{2} \left(3 \cos^2 \theta_{jk} - 1 \right) \tag{5-5}$$

where the DD coupling constant is defined as follows:

$$b_{jk} = -\frac{\mu_0}{4\pi} \gamma_j \gamma_k \hbar \frac{1}{r_{jk}^3} \tag{5-6}$$

and r_{jk} is the internuclear distance.

Since the spin interaction terms vary *periodically* as the sample rotates, they may be written as Fourier series. All these terms being derived from spherical tensors of maximum rank 2, the modulated interactions may be written as follows:

$$\omega_Q(t) = \sum_{m=-2}^{+2} \omega_Q^{(m)} e^{\mathrm{i}m\omega_r t} \tag{5-7}$$

where $\omega_Q^{(-m)}$ is given by:

$$\omega_Q^{(-m)} = \omega_Q^{(m)*} \tag{5-8}$$

and Q refers to any of the subscripts A, B, j or k. A complete description of the Fourier components, including their orientation and time-dependence, is given in the work of Helmle *et al.*.[226] For our purposes, we need only note the following properties:

$$\begin{cases} \omega_j^{(0)} &= \omega_j^{iso} \\ \omega_k^{(0)} &= \omega_k^{iso} \\ \omega_A^{(0)} &= \pi J \\ \omega_B^{(0)} &= 2\pi J \end{cases} \tag{5-9}$$

where the isotropic chemical-shift frequencies of the two spins are denoted ω_j^{iso} and ω_k^{iso}. It proves to be convenient to represent the spin Hamiltonian using single-transition operators,[229, 230] defined by the following relations:

$$\begin{cases} I_x^{rs} &=& \frac{1}{2}(|r\rangle\langle s| + |s\rangle\langle r|) \\ I_y^{rs} &=& \frac{1}{2i}(|r\rangle\langle s| - |s\rangle\langle r|) \\ I_z^{rs} &=& \frac{1}{2}(|r\rangle\langle r| + |s\rangle\langle s|) \\ \frac{1}{2}\mathbf{1}^{rs} &=& \frac{1}{2}(|r\rangle\langle r| + |s\rangle\langle s|) \end{cases} \tag{5-10}$$

where the kets represent orthonormal spin states. A Zeeman product basis set is defined by:

$$\begin{cases} |1\rangle &=& |+\frac{1}{2}, +\frac{1}{2}\rangle \\ |2\rangle &=& |+\frac{1}{2}, -\frac{1}{2}\rangle \\ |3\rangle &=& |-\frac{1}{2}, +\frac{1}{2}\rangle \\ |4\rangle &=& |-\frac{1}{2}, -\frac{1}{2}\rangle \end{cases} \tag{5-11}$$

where $S_{jz}|M_j, M_k\rangle = M_j|M_j, M_k\rangle$ and $S_{kz}|M_j, M_k\rangle = M_k|M_j, M_k\rangle$. The spin Hamiltonian may be written using single-transition operators in the Zeeman product basis as follows:

$$\mathcal{H} = \omega_\Sigma I_z^{14} + \omega_A \mathbf{1}^{14} - \omega_\Sigma \mathbf{1}^{13} + \mathcal{H}^{23} \tag{5-12}$$

where $\mathcal{H}^{23}$ is given by the next expression:

$$\mathcal{H}^{23} = \omega_\Delta I_z^{23} + \omega_B I_x^{23} \tag{5-13}$$

with ω_Σ and ω_Δ the instantaneous sum and difference of the chemical shift frequencies, defined as follows:

$$\begin{cases} \omega_\Sigma &=& \omega_j + \omega_k \\ \omega_\Delta &=& \omega_j - \omega_k \end{cases} \tag{5-14}$$

Eq. 5-12 is the starting point for a discussion of the dynamical properties of the spin-1/2 pair. It contains four mutually commuting terms.
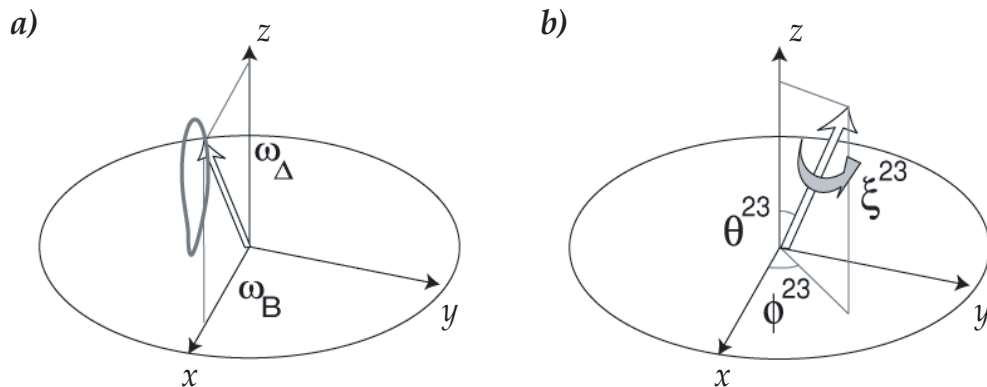
FIGURE 5.2: *a) Pseudofield in the subspace of the spin eigenstates $|2\rangle$ and $|3\rangle$. The z component of the pseudofield is given by the instantaneous chemical-shift difference ω_Δ. The x component of the pseudofield is given by the coupling term ω_B. Both components are periodically modulated in the case of MAS, so the tip of the pseudofield vector executes a periodic trajectory in the xz plane (shown by the loop). b) Net rotation in the $\{|2\rangle, |3\rangle\}$ subspace induced by the pseudofield over one sample rotation period. The rotation is by an angle ξ^{23} about an axis with polar angles $\{\theta^{23}, \phi^{23}\}$. Note that the net rotation axis is not constrained to the xz plane.*

The term $\mathcal{H}^{23}$ in Eq. 5-13 is of particular importance. This Hamiltonian represents the interaction of the fictitious spin-1/2 with a pseudo-field in the xz plane of the $\{|2\rangle, |3\rangle\}$ subspace. The z component of the pseudo-field is proportional to the instantaneous chemical-shift difference ω_Δ, while the x component is proportional to the spin-spin coupling ω_B, which contains a time-dependent DD coupling contribution as well as the constant J-coupling contribution (see Eq. 5-4). This pseudofield is sketched in Figure 5.2a. The two pseudofield components ω_B and ω_Δ are both time-dependent, so the direction and magnitude of the pseudofield vary during the rotor cycle. The tip of the pseudofield traces out a periodic loop in the xz plane.

5.2.2   Evolution operators

The spin system propagator solves the time-dependent Schrödinger equation:

$$\frac{\mathrm{d}}{\mathrm{d}t} U(t, t_0) = -\mathrm{i}\mathcal{H}(t)U(t, t_0) \tag{5-15}$$

where t_0 is the time origin of the propagation. From Eq. 5-10 and 5-12, the general form of this propagator is:

$$
\begin{aligned}
U(t, t_0) \;=\; & [e^{-\mathrm{i}\Phi_\Sigma(t,t_0)-\mathrm{i}\Phi_A(t,t_0)}|1\rangle\langle 1| + \\
& e^{-\mathrm{i}\Phi_A(t,t_0)}(|2\rangle\langle 2| + |3\rangle\langle 3|) + \\
& e^{-\mathrm{i}\Phi_\Sigma(t,t_0)-\mathrm{i}\Phi_A(t,t_0)}|4\rangle\langle 4|]U^{23}(t, t_0)
\end{aligned}
\tag{5-16}
$$

where $U^{23}(t, t_0)$ is given by the equation:

$$\frac{\mathrm{d}}{\mathrm{d}t} U^{23}(t, t_0) = -\mathrm{i}\mathcal{H}^{23}(t)U^{23}(t, t_0) \tag{5-17}$$

and the integrated phase functions are as follows:

$$
\begin{cases}
\Phi_\Sigma(t_b, t_a) & = \quad \int_{t_a}^{t_b} \omega_\Sigma(t)dt \\
\Phi_A(t_b, t_a) & = \quad \int_{t_a}^{t_b} \omega_A(t)dt
\end{cases}
\tag{5-18}
$$

From Eq. 5-9, the phase functions evaluated over one rotor period are given by the relations:

$$
\begin{cases}
\Phi_\Sigma(\tau_r + t_0, t_0) & = \quad \omega_\Sigma^{iso}\tau_r \\
\Phi_A(\tau_r + t_0, t_0) & = \quad \pi J\tau_r
\end{cases}
\tag{5-19}
$$

The evolution under the Hamiltonian $\mathcal{H}^{23}$, over one rotor period, may be written with full generality as:

$$U^{23}(\tau_r + t_0, t_0) = e^{-\mathrm{i}\mathbf{I}^{23}\cdot\omega^{23}(t_0)\tau_r} \tag{5-20}$$

This relation represents a rotation in the $\{|2\rangle, |3\rangle\}$ subspace about a vector operator $\omega^{23}(t_0)$, whose direction depends in general upon the time origin t_0 of the evolution.

If both τ intervals span an integer multiple of the rotation period, and the duration of the π pulse is negligible, the position of the sample at the beginning of the two τ intervals is the same. It is therefore possible to drop the indexing with t_0 in the following discussion. The net rotation in the $\{|2\rangle, |3\rangle\}$ subspace over one rotor period may be therefore written as follows:

$$e^{-\mathrm{i}\mathbf{I}^{23}\cdot\omega^{23}\tau_r} = e^{-\mathrm{i}\phi^{23}I_z^{23}} e^{-\mathrm{i}\theta^{23}I_y^{23}} e^{-\mathrm{i}\xi^{23}I_z^{23}} e^{+\mathrm{i}\theta^{23}I_y^{23}} e^{+\mathrm{i}\phi^{23}I_z^{23}} \tag{5-21}$$

with $\{\theta^{23}, \phi^{23}\}$ being the polar angles of the rotation axis, and the net rotation angle, over one rotor period, being given by the next equation:

$$\xi^{23} = \omega^{23}\tau_r \tag{5-22}$$

The three rotation angles in the $\{|2\rangle, |3\rangle\}$ subspace are sketched in FIGURE 5.2b. The theory below describes how these three angles determine the form of the echo modulation, and how they depend on the spin-system parameters and experimental conditions.

The infinitesimal rotations induced by $\mathcal{H}^{23}(t)$ are always about an axis in the xz plane of the $\{|2\rangle, |3\rangle\}$ subspace. However, since these infinitesimal rotations do not commute with each other in general, the net rotation axis represented by the direction of the vector operator ω^{23} is *not* constrained to the xz plane (see FIGURE 5.2b). The eigenstates of the rotation operator in Eq. 5-21 are given by the next equations:

$$\begin{cases} |2'\rangle & = & +e^{-i\frac{1}{2}\phi^{23}}\cos(\frac{1}{2}\theta^{23})|2\rangle + e^{+i\frac{1}{2}\phi^{23}}\sin(\frac{1}{2}\theta^{23})|3\rangle \\ |3'\rangle & = & -e^{-i\frac{1}{2}\phi^{23}}\sin(\frac{1}{2}\theta^{23})|2\rangle + e^{+i\frac{1}{2}\phi^{23}}\cos(\frac{1}{2}\theta^{23})|3\rangle \end{cases}$$ (5-23)

and these states are satisfying the next eigenequations:

$$\begin{cases} e^{-i\mathbf{I}^{23}\cdot\omega^{23}\tau r}|2'\rangle & = & e^{-i\frac{1}{2}\xi^{23}}|2'\rangle \\ e^{-i\mathbf{I}^{23}\cdot\omega^{23}\tau r}|3'\rangle & = & e^{+i\frac{1}{2}\xi^{23}}|3'\rangle \end{cases}$$ (5-24)

The eigenstates of the propagator in Eq. 5-16 are therefore given by the states $|2'\rangle$ and $|3'\rangle$, and the two outer states:

$$\begin{cases} |1'\rangle & = & |1\rangle \\ |4'\rangle & = & |4\rangle \end{cases}$$ (5-25)

So, the full propagation operator over each half of the spin echo may be written as follows:

$$U(\tau) = \sum_{s=1}^{4} e^{-i\omega'_s \tau}|s'\rangle\langle s'|$$ (5-26)

where the four eigenvalues of the evolution operator are given by:

$$\begin{cases} \omega'_1 & = & \frac{1}{2}\omega_\Sigma^{iso} + \frac{1}{2}\pi J \\ \omega'_2 & = & -\frac{1}{2}\pi J + \frac{1}{2}\omega^{23} \\ \omega'_3 & = & -\frac{1}{2}\pi J - \frac{1}{2}\omega^{23} \\ \omega'_4 & = & -\frac{1}{2}\omega_\Sigma^{iso} + \frac{1}{2}\pi J \end{cases}$$ (5-27)

These four eigenvalues of the evolution operator, given by Eq. 5-27, and the associated eigenstates, given by Eq. 5-23 and Eq. 5-25, can be viewed as the "effective energy levels" for the spin-1/2 pair during the echo intervals. So far, the only assumptions are that each half of the spin echo occupies an integer multiple of rotor periods, and that the π pulse duration may be ignored.

5.2.3   Spin-echo modulation

Transverse magnetisation, as generated by the initial $\pi/2$ pulse or cross polarisation, may be described as a superposition of (±1)-quantum coherences between the Zeeman eigenstates. Since the π pulse in the middle of the spin echo inverts the coherence order, and the final quadrature detected signal has coherence order -1, we need only consider the $(+1)$-quantum coherences at time point ① in FIGURE 5.1. The initial transverse magnetisation may therefore be written as follows:

$$I_x = a_①^{12}|1'\rangle\langle 2'| + a_①^{13}|1'\rangle\langle 3'| + a_①^{24}|2'\rangle\langle 4'| + a_①^{34}|3'\rangle\langle 4'| \cdots$$ (5-28)

where the (-1)-quantum coherence operators such as $|2'\rangle\langle1|$ have not been specifically stated, since they eventually lead to no observable signal. From Eq. 5-23 and Eq. 5-25, the amplitudes of the four $(+1)$-quantum coherences at time point ① are given by the following relations:

$$\begin{cases} a^{12}_① & \doteq & \langle1'|I_x|2'\rangle & \equiv & \frac{1}{2}[e^{-i\frac{1}{2}\phi^{23}}\cos(\frac{1}{2}\theta^{23}) + e^{+i\frac{1}{2}\phi^{23}}\sin(\frac{1}{2}\theta^{23})] \\ a^{13}_① & \doteq & \langle1'|I_x|3'\rangle & \equiv & \frac{1}{2}[e^{+i\frac{1}{2}\phi^{23}}\cos(\frac{1}{2}\theta^{23}) - e^{-i\frac{1}{2}\phi^{23}}\sin(\frac{1}{2}\theta^{23})] \\ a^{24}_① & \doteq & \langle2'|I_x|4'\rangle & \equiv & \frac{1}{2}[e^{+i\frac{1}{2}\phi^{23}}\cos(\frac{1}{2}\theta^{23}) + e^{-i\frac{1}{2}\phi^{23}}\sin(\frac{1}{2}\theta^{23})] \\ a^{34}_① & \doteq & \langle3'|I_x|4'\rangle & \equiv & \frac{1}{2}[e^{-i\frac{1}{2}\phi^{23}}\cos(\frac{1}{2}\theta^{23}) - e^{+i\frac{1}{2}\phi^{23}}\sin(\frac{1}{2}\theta^{23})] \end{cases} \tag{5-29}$$

And during the first spin echo interval, the coherences propagate at the following frequencies:

$$\begin{cases} \omega^{12} & \doteq & \omega'_2 - \omega'_1 & \equiv & -\frac{1}{2}\omega^{iso}_\Sigma - \pi J + \frac{1}{2}\omega^{23} \\ \omega^{13} & \doteq & \omega'_3 - \omega'_1 & \equiv & -\frac{1}{2}\omega^{iso}_\Sigma - \pi J - \frac{1}{2}\omega^{23} \\ \omega^{24} & \doteq & \omega'_4 - \omega'_2 & \equiv & -\frac{1}{2}\omega^{iso}_\Sigma + \pi J - \frac{1}{2}\omega^{23} \\ \omega^{34} & \doteq & \omega'_4 - \omega'_3 & \equiv & -\frac{1}{2}\omega^{iso}_\Sigma + \pi J + \frac{1}{2}\omega^{23} \end{cases} \tag{5-30}$$

The coherence amplitudes at the end of the first half of the spin-echo sequence are given by the relation below:

$$a^{rs}_② = a^{rs}_① e^{i\omega^{rs}\tau} \tag{5-31}$$

Since the evolution eigenstates $|2'\rangle$ and $|3'\rangle$ are mixed Zeeman product eigenstates (see Eq. 5-23), the effect of the strong, ideal, π pulse may be relatively complicated. The detailed deduction of the π-rotation transformations summarised below can be found in Appendix B (see page 102):

$$\mathcal{R}_x(\pi)|1'\rangle = -|4'\rangle \tag{5-32}$$

$$\mathcal{R}_x(\pi)|2'\rangle = -\cos\phi^{23}\sin\theta^{23}|2'\rangle + (-\cos\phi^{23}\cos\theta^{23} + i\sin\phi^{23})|3'\rangle \tag{5-33}$$

$$\mathcal{R}_x(\pi)|3'\rangle = (-\cos\phi^{23}\cos\theta^{23} - i\sin\phi^{23})|2'\rangle + \cos\phi^{23}\sin\theta^{23}|3'\rangle \tag{5-34}$$

$$\mathcal{R}_x(\pi)|4'\rangle = -|1'\rangle \tag{5-35}$$

where the rotation operator is defined by:

$$\mathcal{R}_x(\pi) \doteq e^{-i\pi I_x} \tag{5-36}$$

The π-rotation equations show that rotation operator, when applied to an eigenstate $|s'\rangle$, does rotate the eigenvalue of I_x operator around the x axis by an angle π. From this, one may derive now the following correspondence between coherence amplitudes before and after the π pulse:

$$\begin{cases} a^{21}_③ & \doteq & \langle2'|I_x|1'\rangle & \equiv & +\cos\phi^{23}\sin\theta^{23}a^{24}_② + (\cos\phi^{23}\cos\theta^{23} + i\sin\phi^{23})a^{34}_② \\ a^{31}_③ & \doteq & \langle3'|I_x|1'\rangle & \equiv & -\cos\phi^{23}\sin\theta^{23}a^{34}_② + (\cos\phi^{23}\cos\theta^{23} - i\sin\phi^{23})a^{24}_② \\ a^{42}_③ & \doteq & \langle2'|I_x|4'\rangle & \equiv & +\cos\phi^{23}\sin\theta^{23}a^{12}_② + (\cos\phi^{23}\cos\theta^{23} - i\sin\phi^{23})a^{13}_② \\ a^{43}_③ & \doteq & \langle3'|I_x|4'\rangle & \equiv & -\cos\phi^{23}\sin\theta^{23}a^{13}_② + (\cos\phi^{23}\cos\theta^{23} + i\sin\phi^{23})a^{12}_② \end{cases} \tag{5-37}$$

Notice that every (-1)-quantum coherence derives its amplitude from two $(+1)$-quantum coherences existing before the π pulse. During the second half of the spin echo, the four (-1)-quantum coherences evolve under their eigenfrequencies $\omega^{rs} = -\omega^{sr}$, as given in Eq. 5-30, according to next relation:

$$a^{rs}_④ = a^{rs}_③ e^{i\omega^{rs}\tau} \tag{5-38}$$

The echo amplitude is therefore modulated in general by eight frequency components, each derived from one of the four pairs of coherence transfer processes induced by the π pulse. The echo amplitude may be estimated from the following expression:

$$s(2\tau) = a^{21}_④\langle1'|I_x|2'\rangle + a^{31}_④\langle1'|I_x|3'\rangle + a^{42}_④\langle2'|I_x|4'\rangle + a^{43}_④\langle3'|I_x|4'\rangle \tag{5-39}$$

This simplifies (see Appendix B for details) to the following expression:

$$s(2\tau) = s_-(2\tau) + s_0(2\tau) + s_+(2\tau) \tag{5-40}$$

where all three modulation components are given by next expressions:

$$\begin{cases} s_-(2\tau) &= a_- \cos[(\pi J - \frac{1}{2}\omega^{23})2\tau] \\ s_0(2\tau) &= a_0 \cos[(\pi J)2\tau] \\ s_+(2\tau) &= a_+ \cos[(\pi J + \frac{1}{2}\omega^{23})2\tau] \end{cases} \tag{5-41}$$

with the amplitudes:

$$\begin{cases} a_- &= \frac{1}{2}\cos\phi^{23}\sin\theta^{23}(1 + \cos\phi^{23}\sin\theta^{23}) \\ a_0 &= (1 - \cos^2\phi^{23}\sin^2\theta^{23}) \\ a_+ &= \frac{1}{2}\cos\phi^{23}\sin\theta^{23}(-1 + \cos\phi^{23}\sin\theta^{23}) \end{cases} \tag{5-42}$$

The eight modulation components implied by the Eqs. 5-37 and 5-39 condense into the six components expressed in the Eqs. 5-40 and 5-41, since two pairs of components are degenerate. An echo-modulation spectrum is generated by taking the Fourier transform of the echo amplitude $s(2\tau)$ with respect to the echo interval 2τ. From Eq. 5-41, the "ideal" component $s_0(2\tau)$ generates a doublet with a splitting of $2\pi J$ and amplitude a_0. Similarly, the "satellite" components $s_\pm(2\tau)$ contribute doublets with splittings of $2\pi J \pm \omega^{23}$ and amplitudes $a_\pm$ to the echo-modulation spectrum.
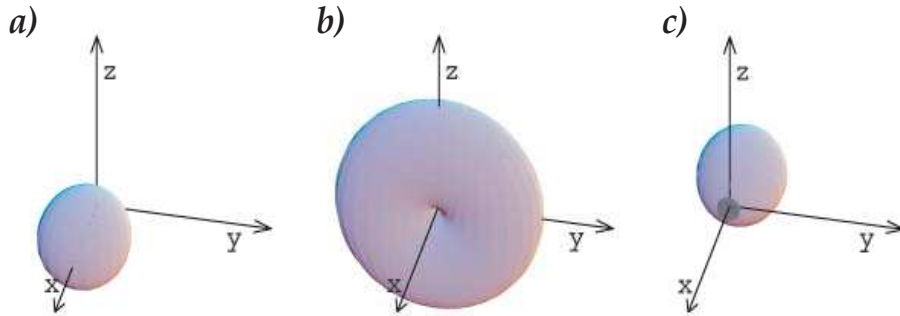
FIGURE 5.3: *Amplitudes a_-, a_0 and a_+ of the spin-echo modulation components, plotted as functions of the polar angles of the rotation axis $\{\theta^{23}, \phi^{23}\}$. In each case the distance of the surface from the origin is proportional to the signal-component amplitude. The small regions of negative amplitude have a dark shade. a) Amplitude a_- of the $s_-(2\tau)$ satellite component, which contributes a doublet with splitting $2\pi J - \omega^{23}$ to the echo-modulation spectrum. b) Amplitude a_0 of the "ideal" $s_0(2\tau)$ component, which contributes a doublet with splitting $2\pi J$ to the echo-modulation spectrum. c) Amplitude a_+ of the $s_-(2\tau)$ satellite component, which contributes a doublet with splitting $2\pi J + \omega^{23}$ to the echo-modulation spectrum.*

The ideal J-modulated component s_0 originates from the four coherence transfer pathways $|3'\rangle\langle 4'| \Rightarrow |2'\rangle\langle 1'|$, $|2'\rangle\langle 4'| \Rightarrow |3'\rangle\langle 1'|$, $|1'\rangle\langle 3'| \Rightarrow |4'\rangle\langle 2'|$, and $|1'\rangle\langle 2'| \Rightarrow |4'\rangle\langle 3'|$ induced by the π pulse. The remaining four coherence transfer pathways induced by the π pulse account for the s_+ ($|3'\rangle\langle 4'| \Rightarrow |3'\rangle\langle 1'|$, $|1'\rangle\langle 3'| \Rightarrow |4'\rangle\langle 3'|$) and s_- ($|2'\rangle\langle 4'| \Rightarrow |2'\rangle\langle 1'|$, $|1'\rangle\langle 2'| \Rightarrow |4'\rangle\langle 2'|$) "satellite" components (see Appendix B). The spin system parameters and experimental conditions determine how *prominent* the ideal J-modulated components are, with respect to the other terms. However, *its frequency is always conserved*. This conclusion is borne out by the numerical simulations presented later. By definition, the J-splitting of the ideal component s_0 is independent of the molecular orientation, while the frequencies of the satellite components $s_\pm$ are orientation-dependent. In a powder, this property helps to differentiate between the ideal component and the satellites. The satellites tend to be broad in a powder, while the ideal J-modulated component stays sharp. The presence of satellite components in the Fourier transforms of spin-echo data was noted previously by Kuwahara *et al.*.[222, 223]

Modulation components corresponding to the pure J-coupling were also identified by Kubo *et al.*[184] and Challoner *et al.*.[185] However, those analyses were performed by making approximations, while the present result is completely general for isolated spin-1/2 pairs in a magic-angle-spinning solid.

FIGURE 5.3 sketches the dependence of the modulation amplitudes a_-, a_0 and a_+ on the direction of the net rotation axis in the $\{|2\rangle, |3\rangle\}$ subspace, as described by Eq. 5-42. The amplitude of the ideal J-modulated component has the form of a doughnut in the yz plane (FIGURE 5.3b), while the satellite amplitudes have the form of lobes along the $\pm$ x axis (FIGURE 5.3a and c). Pure J-modulation of the spin echo is therefore observed when the net rotation axis lies anywhere in the yz plane, while the satellites become prominent when the net rotation axis is roughly parallel to the positive or negative x axis in the $\{|2\rangle, |3\rangle\}$ subspace.

Maricq and Waugh[20] and Challoner *et al.*[185] analysed the problem using average Hamiltonian theory[224] applied directly to $\mathcal{H}^{23}$. This approach is only feasible in the fast spinning limit but cannot be reliably used at spinning frequencies comparable to, or less than, the anisotropic chemical shifts. The problem may be treated with greater generality using an interaction frame transformation of the type employed in the work of Levitt *et al.*.[61] In analogy with Eq. 5-7, we define the Fourier components of the chemical shift frequency difference as follows:

$$\omega_\Delta(t) = \sum_{m=-2,+2} \omega_\Delta^{(m)} e^{im\omega_r t} \tag{5-43}$$

The isotropic and anisotropic parts of the chemical shift frequency difference are defined through:

$$\begin{cases} \omega_\Delta^{iso} = \omega_\Delta^{(0)} = \omega_j^{iso} - \omega_k^{iso} \\ \omega_\Delta^{aniso}(t) = \sum_{m \neq 0} e^{im\omega_r t} \end{cases} \tag{5-44}$$

The time-dependent rotation operator in $\{|2\rangle, |3\rangle\}$ subspace is defined by:

$$\mathbf{V}(t,0) = e^{-i(\Phi_\Delta^{aniso}(t,0) + n\omega_r t)I_z^{23}} \tag{5-45}$$

where the integrated phase angle is:

$$\Phi_\Delta^{aniso}(t_b, t_a) = \int_{t_b}^{t_b} \omega_\Delta^{aniso}(t)dt \tag{5-46}$$

Here n is the closest integer to the ratio $\omega_\Delta^{iso}/\omega_r$ which is the closest order of rotational resonance [51, 61, 226, 231, 232, 233, 234, 235].

The interaction frame spin Hamiltonian may be defined through:

$$\mathcal{H} = \mathbf{V}\mathcal{H}^{23}\mathcal{V} - (n\omega_r + \omega_\Delta^{aniso})I_z^{23} \tag{5-47}$$

Since the interaction frame operator defined by Eq. 5-45 is periodic, with period τ_r, and most of the large chemical shift interactions have been removed from the interaction frame Hamiltonian in Eq. 5-47, it is therefore possible to apply average Hamiltonian theory[224] as long as the spinning frequency is larger than the coupling terms. Note that any value of the CSA may be tolerated.

From the Fourier theorem, the periodic phase function Φ_Δ^{aniso} may be expressed as an infinite series:

$$\Phi_\Delta^{aniso} = \sum_{k=-\infty}^{+\infty} a_\Delta^{(k)} e^{ik\omega_r t} \tag{5-48}$$

The complex amplitudes $a_\Delta^{(k)}$ may be regarded as spinning sidebands generated by the periodic modulation of the chemical shift difference. In this frame, the Hamiltonian may be written as follows:

$$\tilde{\mathcal{H}} = \tilde{\omega}_B \tfrac{1}{2} |3\rangle\langle 2| + \tilde{\omega}_B^* \tfrac{1}{2} |2\rangle\langle 3| + \Delta\omega_n I_z^{23} \tag{5-49}$$

where $\Delta\omega_n$ is the offset from the nearest rotational resonance:

$$\Delta\omega_n = \omega_\Delta^{iso} - n\omega_r \tag{5-50}$$

The interaction frame coupling term may be expressed using a Fourier series:

$$\tilde{\omega_B} = \sum_{k=-\infty}^{+\infty} \tilde{\omega}_B^{(k)} e^{\mathrm{i}k\omega_r t} \tag{5-51}$$

where the Fourier components are given by:

$$\tilde{\omega}_B^{(k)} = \sum_{m=-2}^{+2} \omega_B^{(m)} a_\Delta^{(m-k-n)*} \tag{5-52}$$

and $\omega_B^{(m)}$ are defined in Eq. 5-7. This represents a convolution of the dipolar sideband pattern with the sideband pattern generated by the anisotropic chemical shift difference, shifted by the nearest rotational resonance order n. If the spinning frequency is fast compared to the coupling terms, Eq. 5-49 may be replaced by its time average over the modulation period, which is:

$$\overline{\tilde{\mathcal{H}}^{23(1)}} = \tilde{\omega}_B^{(0)}\tfrac{1}{2}|3\rangle\langle 2| + \tilde{\omega}_B^{(0)*}\tfrac{1}{2}|2\rangle\langle 3| + \Delta\omega_n I_z^{23} \tag{5-53}$$

and the resonant component of the interaction frame coupling is given by the next relation:

$$\tilde{\omega}_B^{(0)} = \sum_{m=-2}^{+2} \omega_B^{(m)} a_\Delta^{(m-n)*} \tag{5-54}$$

It contains products of spin-spin coupling sideband amplitudes and sideband amplitudes generated by the difference chemical shift. From Eq. 5-53, it is possible to derive the polar angles of the net rotation in $\{|2\rangle, |3\rangle\}$ subspace:

$$\begin{cases} \tan\theta^{23} &= |\tilde{\omega}_B^{(0)}|\Delta\omega_n \\ \phi^{23} &= \arg\tilde{\omega}_B^{(0)} \end{cases} \tag{5-55}$$

These angles govern the amplitudes a_0 and $a_\pm$, according to Eq. 5-42 and Figure 5.3. The frequency shifts of the $s_\pm$ satellite components with respect to the ideal s_0 component are determined by the frequency ω^{23}, which is given by:

$$\omega^{23} = \left[|\tilde{\omega}_B^{(0)}|^2 + |\Delta\omega_n|^2\right]^{1/2} \tag{5-56}$$

This set of equations can be used to derive the spin-echo modulation in different experimental regimes.

5.2.4   Echo-modulation regimes

The implications of this theoretical treatment for the measurement of J-couplings under different experimental or chemical conditions will be briefly summarised in the next paragraphs. The experimental regimes are distinguished by the rotation axes and angles in the $\{|2\rangle, |3\rangle\}$ subspace, determined by the 2-level Hamiltonian $\mathcal{H}^{23}$ in Eq. 5-13, and sketched in Figure 5.2b.

Five different regimes may be distinguished, depending on how the spinning frequency is related to the chemical shift anisotropies and the difference between the isotropic shift frequencies.

a) Very fast MAS

The very fast MAS regime is reached if the rotation frequency is much larger than chemical shift anisotropies and isotropic shift difference; conditions which may be expressed as follows:

$$|\omega_r| > |\frac{d\omega_\Delta}{2\pi J}|, |\omega_\Delta^{iso}| \tag{5-57}$$

If the CSA interactions are large, it is difficult to attain the fast MAS regime with current spinning technology. For example, consider the following typical parameters for ^{13}C-labelled sp^2 sites in organic solids: CSA interactions of the order of $10\,\mathrm{kHz}$, J-coupling of $50\,\mathrm{Hz}$, and DD coupling of the order of -2 kHz. With these parameters, the condition $|\omega_r| > |d\omega_\Delta^{aniso}/2\pi J|$ is only satisfied for spinning frequencies of around $100\,\mathrm{kHz}$ and above.

On the other hand, the separation in isotropic chemical-shift frequencies may be much larger than the J-coupling, equal to zero or comparable to the J-coupling. The first case gives rise to a spin-echo modulation oscillating only at the J-coupling frequency. For the particular case of degenerated isotropic shifts, no spin-echo modulation is expected. Indeed, this corresponds to the A$_2$ case of magnetic equivalence in isotropic liquids. If the MAS frequency is high enough (see Numerical simulations section), the homonuclear J-coupling has no spectral effects in spin-1/2 pair systems with identical isotropic chemical shifts. Lastly, at high enough MAS frequency, more complicated modulation phenomena are expected for systems with isotropic shift difference comparable to the J-coupling. These are however exactly analogous to those observed for AB systems in isotropic liquids and are not usually relevant in solids.

To summarise, in the very fast regime, two cases have to be retained for the spin-echo modulation:

$$\begin{array}{rcll} s(2\tau) & = & \cos[\pi J(2\tau)] & \text{(very fast MAS; \textit{large} isotropic shift separation)} \quad (5\text{-}58) \\ s(2\tau) & = & 1 & \text{(very fast MAS; \textit{degenerate} isotropic shifts)} \quad\quad (5\text{-}59) \end{array}$$

b) Moderate MAS, small isotropic shift difference

Now, let us consider the situation when the MAS frequency is not sufficiently high with respect to the difference in chemical-shift anisotropies:

$$|\omega_r| < |\frac{d\omega_\Delta}{2\pi J}| \tag{5-60}$$

Additionally, if the CSA tensors of the two homonuclear spins are identical in all respects, then the chemical-shift difference is equal to zero at all times. This special case is called here *total magnetic equivalence* and will be discussed further below. In most cases, the CSA tensors of the two spins have different orientation and/or principal values, which leads to finite values for the instantaneous chemical-shift difference.

The CSA has therefore the effect of stabilising the spin-echo J-modulation by ensuring that instantaneous chemical shifts are different for most of the time, except in the case of total magnetic equivalence, where the two CSA tensors are identical in all respects. On the contrary, it is less obvious to find an explanation for why DD coupling also has a stabilising effect on the J-modulation.

The moderate regime is thus reached if the next conditions are satisfied:

$$|\omega_\Delta^{iso}| \lesssim |\omega_\Delta^{aniso}| < |\omega_r| < |\frac{d\omega_\Delta}{2\pi J}| \tag{5-61}$$

These conditions are generally satisfied for a wide range of practical spinning frequencies, and even applies when there is a small isotropic chemical-shift difference, which, in liquids, leads to the relatively complicated AB case.

The spin-echo modulation, in the moderate spinning regime, is dominated by the pure J-coupling component:

$$s(2\tau) \;\approx\; \cos[\pi J(2\tau)] \quad \text{(moderate MAS; near } n = 0 \text{ rotational resonance)} \quad (5\text{-}62)$$

c) Moderate MAS, large isotropic shift difference

In many cases, the difference in isotropic chemical shifts between the two spins is larger than the chemical-shift anisotropies and this leads to slightly different behaviour.

Consider the case where the spinning frequency is large compared to the chemical-shift anisotropies, at the same time as being comparable to the isotropic shift frequency difference:

$$|\omega_\Delta^{aniso}| < |\omega_\Delta^{iso}| \sim |\omega_r| \lesssim |\frac{d\omega_\Delta}{2\pi J}| \qquad (5\text{-}63)$$

In this regime, the behaviour of the spin system depends on the nearest rotational resonance order n, i.e., the closest integer to the ratio $\omega_\Delta^{iso}/\omega_r$.

The expected spin-echo modulation behaviour for a powder off and on rotational resonance, is given by the next relations:

$$
\begin{aligned}
s(2\tau) &\approx \cos[\pi J(2\tau)] & \text{(moderate MAS; off rotational resonance)} & \quad (5\text{-}64)\\
s(2\tau) &\approx \tfrac{1}{2}\cos[\pi J(2\tau)] + \tfrac{1}{2}g(2\tau) & \text{(moderate MAS; on } n \neq 0 \text{ rotational resonance)} & \quad (5\text{-}65)
\end{aligned}
$$

where $g(2\tau)$ represents the broad $s_\pm$ satellites. The function $g(2\tau)$ is a rapidly decaying function of the echo interval 2τ, and has the property $g(0) = 1$. In determing the off rotational-resonance echo modulation, the small satellite contributions, considered by Kuwahara *et al.*,[222,223] have been ignored.

d) Slow MAS

Now consider the situation where the spinning frequency is smaller than the chemical-shift anisotropies, so that the one-dimensional spectra contain many spinning sidebands generated by the modulation of the CSA. We refer to this case as the "slow-spinning" regime. It is defined by the next approximated boundaries:

$$|d|, |\pi J| \lesssim |\omega_r| \lesssim |\omega_\Delta^{aniso}| \qquad (5\text{-}66)$$

Far from rotational resonance, the spin-echo modulation in the slow MAS regime is similar to that observed in the moderate-spinning, large chemical-shift-difference regime described in Eq. 5-63. If there is a finite isotropic shift difference, the J-modulated component s_0 dominates, and the expected modulation behaviour is again dominated by the pure J-component. If the isotropic shift difference is small or zero, or in the vicinity of a rotational resonance, there are strong satellite modulation components s_+ and s_- for some molecular orientations. However, these are rendered less prominent in a powdered solid since their frequencies are strongly orientation-dependent. The expected modulation behaviour in the slow MAS regime is therefore:

$$
\begin{aligned}
s(2\tau) &\cong \cos[\pi J(2\tau)] & \text{(slow MAS, far from rotational resonance)} & \quad (5\text{-}67)\\
s(2\tau) &\cong \tfrac{1}{2}\cos[\pi J(2\tau)] + \tfrac{1}{2}g(2\tau) & \text{(slow MAS, on rotational resonance, including } n = 0) & \quad (5\text{-}68)
\end{aligned}
$$

where the rapidly decaying function $g(2\tau)$ again takes into account the broad satellites $s_\pm(2\tau)$.

The ^{31}P spin systems discussed by Challoner *et al.*[185] fall within the slow-spinning regime, because the spectra contain a large number of CSA spinning sidebands. However, the theory of Challoner *et al.*,[185] which predicted a pure J-modulated spin echo, is restricted to the moderate-spinning regime, and appears to be unsatisfactory in this experimental situation. The discrepancies between experiment and theory may have been obscured by the orientational broadening of the $s_\pm$ components, as previously described.

e) Very slow MAS

The interaction-frame average Hamiltonian description[224] breaks down if the spinning frequency is less than or comparable to the spin-spin couplings:

$$|\omega_r| \lesssim |d|, |\pi J| \tag{5-69}$$

Although it is not possible to derive any rotation parameters, the general conclusions of Eq. 5-41 and Eq. 5-42 still apply. The echo modulation still contains an ideal J-modulated components s_0, whose frequency is orientation-independent, and satellite components $s_\pm$, whose frequencies are strongly orientation-dependent. The satellite components are, as usual, expected to become very broad in a powder sample. As for the ideal component amplitude s_0, it may be estimated by assuming that the rotation axes are quasi-isotropically distributed in the 2D space.

The expected echo modulation function in this regime is given by:

$$s(2\tau) \quad \cong \quad \tfrac{2}{3}\cos[\pi J(2\tau)] + \tfrac{1}{3}g(2\tau) \quad \text{(very slow MAS)} \tag{5-70}$$

where the rapidly decaying function $g(2\tau)$ again takes into account the broad satellite components $s_\pm(2\tau)$.

Once more we note the astonishing propensity of the J-modulation to resist, or even be stabilised by, potentially competing interactions that are orders of magnitude larger in amplitude.

f) Total magnetic equivalence

If the chemical shift frequencies of the coupled sites are identical *at all instants during the sample rotation period*, the term ω_Δ vanishes identically, and the spin echoes are unmodulated:

$$s(2\tau) \quad = \quad 1 \quad \text{(total magnetic equivalence)} \tag{5-71}$$

This case is encountered when the coupled sites have the same chemical-shift tensors in all respects, including principal axes orientations. It is referred to here as *total magnetic equivalence*. The most easily envisaged case is when the sites of the participating spins are related by a crystal inversion operation.

In solution NMR, the term *magnetic equivalence* refers to the situation where two or more spins have the same isotropic shift, and also have identical J-couplings to all other spins.[2] The term *total magnetic equivalence*, as used here, implies a stronger condition, in which the chemical shifts of the coupled spins, both isotropic and anisotropic, are the same for *all molecular orientations*, as well as fulfilling the ordinary scalar coupling conditions for magnetic equivalence. Haeberlen[236] and Mehring[14] employ an alternative definition of magnetic equivalence in solids, based on crystal symmetry operations. However, as noted by Haeberlen,[236] this definition is problematic: nuclei which are magnetically equivalent in solids (according to the Haeberlen-Mehring definition) are not necessarily magnetically equivalent in isotropic solution (according to the accepted solution-state definition). Here we choose to use the solution-state definition of magnetic equivalence, avoid the Haeberlen-Mehring definition entirely, and introduce the new term *total magnetic equivalence* which is a

restricted version of solution-state magnetic equivalence, and which is applicable to anisotropic phases. Total magnetic equivalence should be distinguished from the situation in Eq. 5-59, which applies when only the isotropic shifts are the same, while the chemical shift anisotropy tensors are different. The Eq. 5-59 is only valid in the very fast spinning regime, while in the case of total magnetic equivalence, the spin-echo modulation is expected to disappear at *all* spinning frequencies.

Summary of the modulation regimes

FIGURE 5.4 is intended to summarize and clarify the conclusions of the previous subsections. Three general regimes of echo modulation are identified, labelled A, B and C. The experimental cases discussed below are indicated by symbols. The regimes are:

Regime A.
  In this regime, the net rotation in the $\{|2\rangle, |3\rangle\}$ subspace occurs around an axis which is close to the x axis (see FIGURE 5.2b). In this regime, the s_- satellite dominates, while the J-modulated component s_0 is small or absent.

Regime B.
  In this regime, the net rotation in the $\{|2\rangle, |3\rangle\}$ subspace occurs around an axis which is close to the yz plane. In this regime, the J-modulated component s_0 is dominant. This is the most favourable regime for accurate determination of the J-coupling by spin-echo modulation measurements.

Regime C.
  In this regime, the phase of the net rotation axes is strongly orientation-dependent, and all three modulation components s_-, s_0 and s_+ are present. Nevertheless, in a powder, the ideal J-component s_0 is most prominent since the others have orientation-dependent frequencies and become broad. It is therefore still possible to estimate the J-coupling accurately by spin-echo modulation measurements.
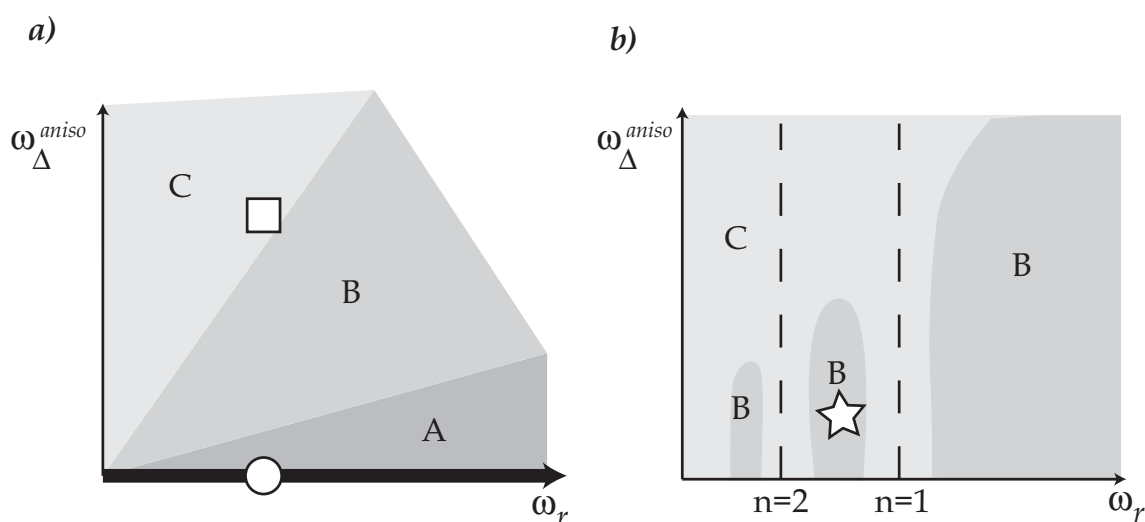
FIGURE 5.4: *The three regimes of spin-echo modulation, plotted as a function of spinning frequency (horizontal axis) and difference in chemical-shift anisotropies (vertical axis). In* regime A*, the J-modulation is absent or weak. In* regime B*, the J-modulation is prominent and relatively pure in form. In* regime C*, the J-modulated component is accompanied by satellites which are broad in a powder. The symbols indicate the experimental cases presented in* FIGURE 5.9*. a) Case of vanishing isotropic-shift difference. The thick horizontal line represents total magnetic equivalence. b) Finite isotropic-shift difference. The rotational resonances are shown by vertical lines.* Regime A *vanishes in this case.*

FIGURE 5.4a refers to the case of vanishing isotropic shift difference (ω_Δ^{iso}). The diagram shows the incidence of the three regimes, as a function of spinning frequency (horizontal axis) and the difference in chemical shift anisotropies (vertical axis). The bold horizontal line indicates total magnetic equivalence (regime A at all spinning frequencies). The boundary between regime A and B corresponds to the condition $|\omega_r| \sim |d\omega_\Delta|/|2\pi J|$.

As one passes from A to B, the low-frequency modulation component s_- becomes weaker, and the true J-modulation component s_0 becomes increasingly prominent. The boundary between regime B and C corresponds to the condition $|\omega_r| \sim |\omega_\Delta^{aniso}|$. As one passes from B to C, the additional modulation components $s_\pm$ become stronger. However, these components are generally broad in powder samples.

Figure 5.4b shows the regime boundaries in the presence of a substantial isotropic shift difference. The positions of the rotational resonances are indicated by the vertical dashed lines. The vicinity of the rotational resonances corresponds to regime C. Regime B is split into "islands" between the rotational resonances, while regime A vanishes. The width of the rotational resonance regions is proportional to the homonuclear dipole-dipole coupling.

The main conclusions of this section are that for isolated homonuclear spin-1/2 pairs, a prominent J-modulated spin-echo component should be visible in rotating solids, except under the conditions corresponding to regime A (very fast MAS, or total magnetic equivalence). In regime B, a damped oscillation of the spin echoes is observed, with an oscillation frequency equal to the J-coupling. In regime C, the initial part of the echo modulation is contaminated by the broad components $s_\pm(2\tau)$. Nevertheless, *an accurate estimate of the J-coupling by spin-echo modulation should be possible in the very wide range of cases covered by regimes B and C.*

5.3   Numerical simulations

In this section we present numerical simulations of spin-echo modulations for isolated spin-1/2 pairs in solids under magic-angle spinning.

All simulations were performed with SIMPSON[89] and correspond to isolated $^{13}C_2$ pairs at a magnetic field of $B_0 = 9.34$ T, leading to a ^{13}C Larmor frequency of $\omega_0/2\pi = -100$ MHz. A $\pi/2 - \tau - \pi - \tau$ spin-echo sequence was simulated, using an ideal and infinitely short π pulse and starting with transverse magnetization for both spins. The integrated signal amplitude was obtained from the intensity of the complex signal at the end of the second τ interval, i.e., the first point of the free-induction decay. The powder average was performed using a a set of 143 molecular orientational angles $\{\alpha_{MR}, \beta_{MR}\}$ generated by the ZCW algorithm[86, 87, 88] and 10 evenly-spaced values for the third Euler angle γ_{MR}. These angles define the relative orientation of a molecular reference frame M, defined so that the z axis is along the internuclear vector, and a rotor reference frame R, defined so that the z axis is along the spinning axis. We verified that increasing the number of orientations did not lead to appreciable changes in the integrated signal. The simulations took no account of the interactions with heteronuclei such as protons. The simulated modulation curves $s(2\tau)$ were multiplied by an exponential function $\exp\{-\lambda 2\tau\}$, corresponding to Lorentzian spectral broadening with a width at half-height of $\lambda/2\pi = 10.5$ Hz, in order to emulate signal decay through relaxation or other irreversible damping mechanisms.

Figure 5.5 shows the dependence of the spin-echo modulation on spinning frequency, with all other parameters kept fixed. The simulation parameters for the first two columns are specified in Table 5.1. Note that the isotropic chemical shifts of the two sites are identical. The simulation at 1 kHz spinning (Figure 5.5a) shows a clear J-splitting, which persists up to a spinning frequency of 18 kHz (Figure 5.5c). At a spinning frequency of 33 kHz (Figure 5.5d), a central peak appears in the Fourier transform of the echo modulation, shown in the second column. This peak marks the appearance of a significant s_- component, and signifies the transition from *regime B* to *regime A* in Figure 5.4. At higher spinning frequencies, the central peak grows at the expense of the pure J-modulated component s_0. At the highest simulated spinning frequency of 100 kHz (Figure 5.5f), the J-modulation almost vanishes, and the spin system behaves to a good approximation as a system of two magnetically-equivalent spins-1/2 in an isotropic liquid.

The third column in Figure 5.5 shows simulations for the parameters in Table 5.1, except that the DD coupling is set to zero. A similar behaviour is observed as for the second column, except that the transition from *regime B* to *regime A* occurs at a much lower spinning frequency, between 3 kHz and 18 kHz. This confirms
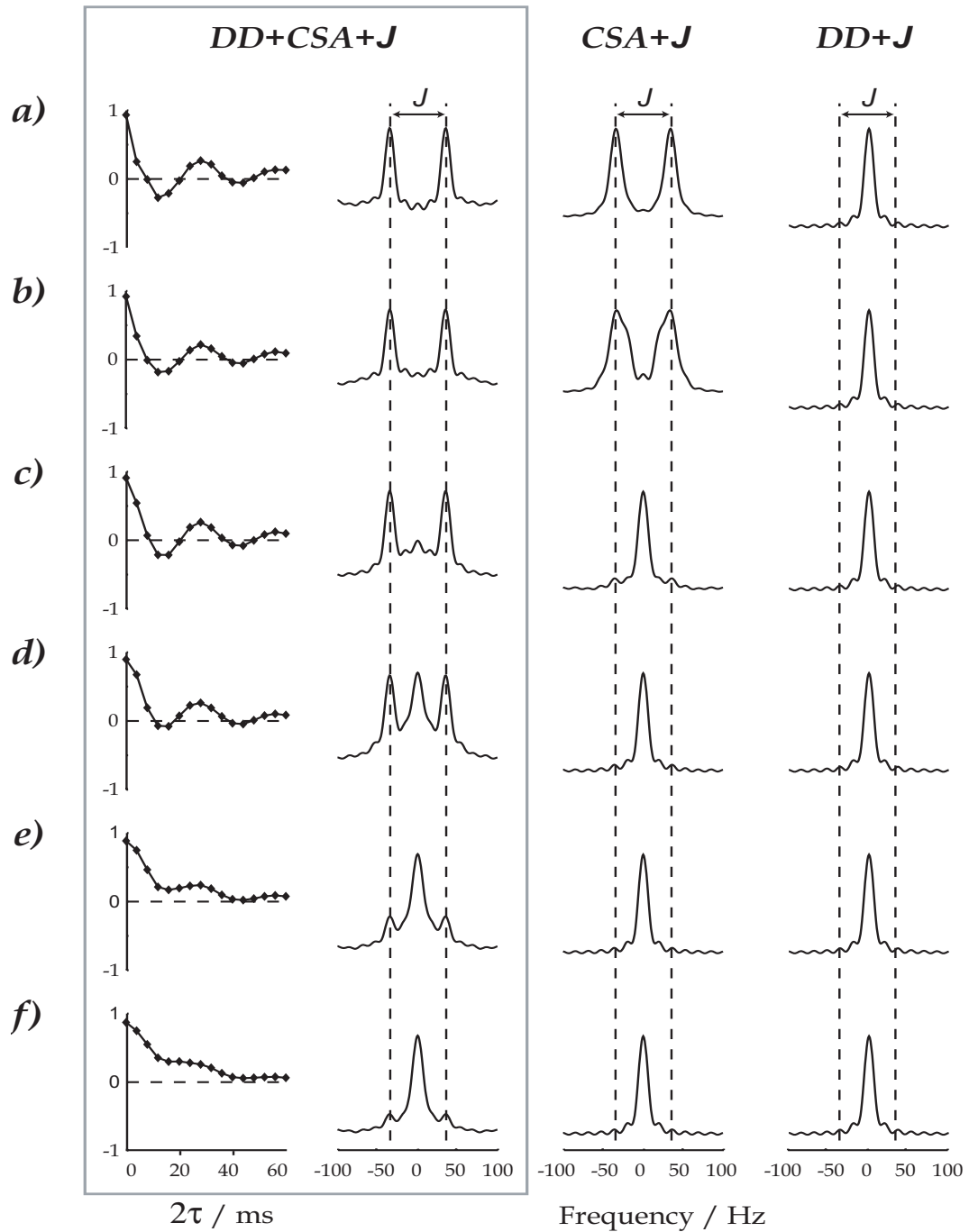
FIGURE 5.5:   *Spin-echo simulations for an ensemble of spin-1/2 pairs showing the effect of increasing spinning frequency from 1 to 100 kHz at a magnetic field $B_0 = 9.34$ T. The spinning frequencies are given by (a) 1 kHz, (b) 3 kHz, (c) 18 kHz, (d) 33 kHz, (e) 70 kHz and (f) 100 kHz. The first two columns show the time-domain echo modulations and their Fourier transforms, employing all the spin-interaction parameters listed in TABLE 5.1. The third column shows the Fourier transforms of the echo modulations, simulated using the same parameters as in the first two columns, except that the DD coupling is set to zero. The fourth column shows the Fourier transforms of the echo modulations, simulated using the same parameters as in the first two columns, except that the CSA is set to zero.*

the importance of the CSA-DD interference in maintaining the J-modulation in systems of spin-1/2 pairs with identical isotropic shifts.

The fourth column in FIGURE 5.5 shows simulations for the parameters in TABLE 5.1, except that the CSA

tensors of both sites are set to zero. Since the isotropic shifts are identical, this case corresponds to total magnetic equivalence. As expected, the J-modulation is quenched at all spinning frequencies (*regime A* throughout).

TABLE 5.1: *Parameters for the CSA and DD tensors, and J-coupling constants used in numerical simulations.* [a]

CSA parameters	site j	site k
δ^{iso}	134 ppm	134 ppm
δ^{aniso}	81.7 ppm	81.7 ppm
η	0.93	0.93
Ω_{PM}	$\{39°, 77°, \text{-} 53°\}$	$\{82°, 24°, 29°\}$
DD parameters	site $\{j, k\}$	
$d/2\pi$	- 3166 Hz	
Ω'_{PM}	$\{0°, 0°, 0°\}$	
J parameters	site $\{j, k\}$	
J	70 Hz	

[a] The chemical shifts are defined using the deshielding convention. The isotropic chemical shift, anisotropic chemical shift and asymmetry parameter are defined through $\delta^{iso} = \frac{1}{3}(\delta_{xx} + \delta_{yy} + \delta_{zz})$, $\delta^{aniso} = \delta_{zz} - \delta^{iso}$ and $\eta = (\delta_{yy} - \delta_{xx})/\delta^{aniso}$, where the chemical-shift principal values are ordered according to $|\delta_{zz} - \delta^{iso}| \geq |\delta_{xx} - \delta^{iso}| \geq |\delta_{yy} - \delta^{iso}|$. These parameters resemble those for [11,12-^{13}C$_2$]-all-E-retinal given in the work of Carravetta *et al.*.[237] The Euler angles specify the relative orientations of the principal axes system P of the relevant spin interaction and the molecular axes system M. The z axis of the M system is defined to be parallel to the ^{13}C-^{13}C internuclear vector.

FIGURE 5.6 shows the effect of increasing the isotropic shift difference between the two sites, at a slow spinning frequency of $\omega_r/2\pi = 3$ kHz. In the first two columns, all of the spin system parameters are as in TABLE 5.1, except for the isotropic shift frequency difference $\omega_\Delta^{iso}/2\pi$ which increases from 0 in (a) to 400 Hz in (f). As may be seen, the spin-echo modulation is almost unaffected by this increase in the chemical shift difference.

All simulations in the first two columns of FIGURE 5.6 correspond to *regime B*. In FIGURE 5.6a, the rotation axis in $\{|2\rangle, |3\rangle\}$ subspace is dominated by the term representing the interference between CSA and DD interactions, and lies close to the y axis. In FIGURE 5.6f, the isotropic-shift difference dominates, so that the rotation axis is close to the z axis in $\{|2\rangle, |3\rangle\}$ subspace. In the intermediate plots, the net rotation axis is close to the yz plane.

The third column in FIGURE 5.6 shows simulations for the same parameter sets as in the second column, except that the DD coupling is set to zero. Therefore, the CSA-DD contribution is eliminated. The modulation is again rather clean at high isotropic-shift differences, but additional modulation peaks are observed for small isotropic-shift differences. The contrast between the second and third column in FIGURE 5.6 again illustrates the important role of the CSA-DD interference in stabilizing the J-modulation.

The fourth column in FIGURE 5.6 shows simulations for the same parameter sets as in the second column, except that the CSA is set to zero. Case (a) in column 4 corresponds to total magnetic equivalence, where the J-modulation is absent (*regime A*). A cross-over to *regime B* is observed in the region of $\omega_\Delta^{iso}/2\pi = 80$ Hz
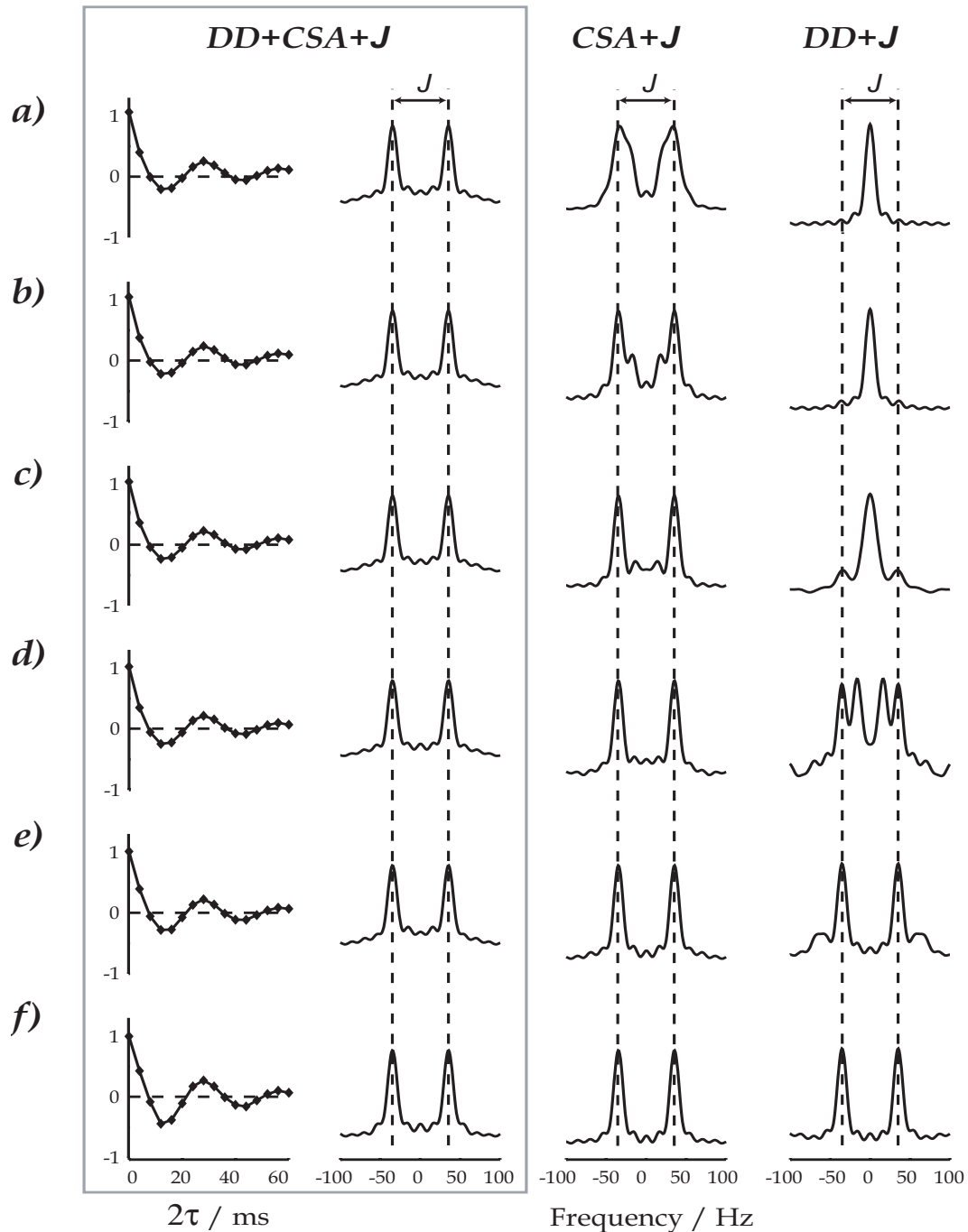
FIGURE 5.6: *Spin-echo simulations for an ensemble of spin-1/2 pairs showing the effect of increasing isotropic shift difference at a fixed spinning frequency $\omega_r/2\pi = 3$ kHz and magnetic field $B_0 = 9.34$ T. The first two columns show the time-domain echo modulations and their Fourier transforms, with simulation parameters as in TABLE 5.1, except for the difference in the isotropic shift frequencies $\omega_\Delta^{iso}/2\pi$, which takes the values a) 0 Hz, b) 20 Hz, c) 40 Hz, d) 80 Hz, e) 200 Hz and f) 400 Hz. The third column shows the Fourier transforms of the echo modulations, simulated using the same parameters as in the first two columns, except that the dipole-dipole coupling is set to zero. The fourth column shows the Fourier transforms of the echo modulations, simulated using the same parameters as in the first two columns, except that the CSA is set to zero.*

(FIGURE 5.6d), marked by non-zero frequencies for the inner s_- satellites and the appearance of the J-modulated s_0 components. At the moderate isotropic-shift difference of $\omega_\Delta^{iso}/2\pi = 400$ Hz (FIGURE 5.6f), the J-modulation is clean (*regime B*). The contrast between columns 2 and 4 illustrates the significance of the CSA in stabilizing

the J-coupling modulation in the *regime B* for a range of isotropic shift differences going from 0 to 200 Hz.
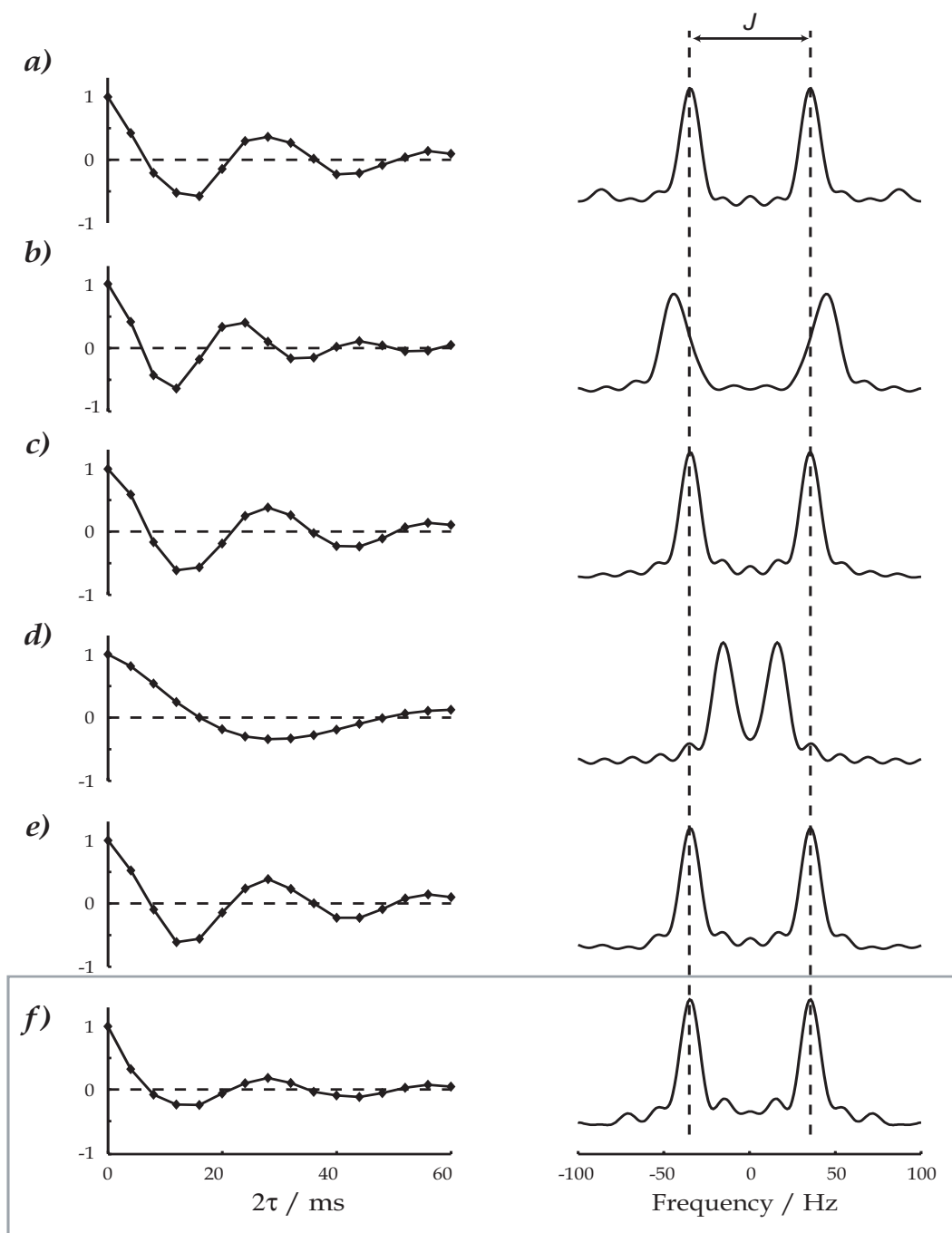
FIGURE 5.7: *Simulations of spin-echo modulations for an ensemble of spin-1/2 pairs showing the effects of molecular orientation. The time-domain modulations are shown in the left column and their Fourier transforms in the right column. The simulated spinning frequency is $\omega_r/2\pi = 3$ kHz and the magnetic field is $B_0 = 9.34$ T. All simulation parameters are as in TABLE 5.1. The Euler angles $\{\alpha_{MR}, \beta_{MR}, \gamma_{MR}\}$ specifying the relative orientation of the molecule-fixed frame M and the rotor-fixed frame R are a) $\{0°, 75°, 180°\}$; b) $\{0°, -53°, 180°\}$; c) $\{38°, 103°, 180°\}$; d) $\{63°, 210°, 180°\}$; e) $\{-140°, 13°, 180°\}$. The powder average modulation is shown in f).*

In FIGURE 5.7, the dependence of the spin-echo modulation on the molecular orientation, in *regime C*, is explored. All simulations are again for the parameters in TABLE 5.1, at a slow spinning frequency of $\omega_r/2\pi = 3$ kHz. Rows (a)-(e) are for a variety of single molecular orientations, while row (f) is the powder average over

many orientations. The simulations for a single orientation display modulation peaks from all three components s_-, s_0 and s_+. The amplitudes and frequencies of the s_- and s_+ peaks are strongly orientation-dependent, while only the amplitude of the ideal s_0 is orientation-independent. For example, the J-modulated peaks of the single orientation simulations shown in (a), (c) and (e) all coincide, although they have very different amplitudes. When a full orientational average is taken (FIGURE 5.7f), the J-modulated components s_0 interfere constructively, while the $s_\pm$ peaks are strongly broadened.

The powder-average spin-echo trajectory in FIGURE 5.7f has a deceptive simplicity. Nevertheless, the peak splitting in the Fourier-transformed echo modulation does provide an accurate estimate of the J-coupling.

5.4   Experiments

In this section we show experimental results for three $^{13}C_2$-labelled samples, which illustrate the spin-echo modulation phenomena discussed above.

The three samples used were:

a) Diammonium [2,3-$^{13}C_2$]-fumarate, co-crystallized at a molar ratio of 1:10 with natural abundance diammonium fumarate. The molecular structure of the $^{13}C_2$-fumarate anion is illustrated in FIGURE 5.8a. We refer to this sample as 10%-$^{13}C_2$-DAF;

b) Ammonium hydrogen [2,3-$^{13}C_2$]-maleate (for the structure of the anion, see FIGURE 5.8b). We refer to this sample as $^{13}C_2$-AHM;

c) [$^{13}C_2$,^{15}N]-glycine (FIGURE 5.8c).

The fumarate anion in DAF lies on a centre of inversion symmetry in the crystal structure[238] and hence the two ^{13}C sites display total magnetic equivalence. In AHM, on the other hand, the two ^{13}C sites are related by a reflection plane,[239] not an inversion, and have CSA tensors with the same principal values but different orientations. In the DAF case, the coupled nuclei are magnetically equivalent in general, while in the AHM case, the coupled nuclei are not magnetically equivalent in general but they can approach the magnetic equivalence at very high spinning frequency. In glycine, the labelled ^{13}C sites have very different chemical shifts.
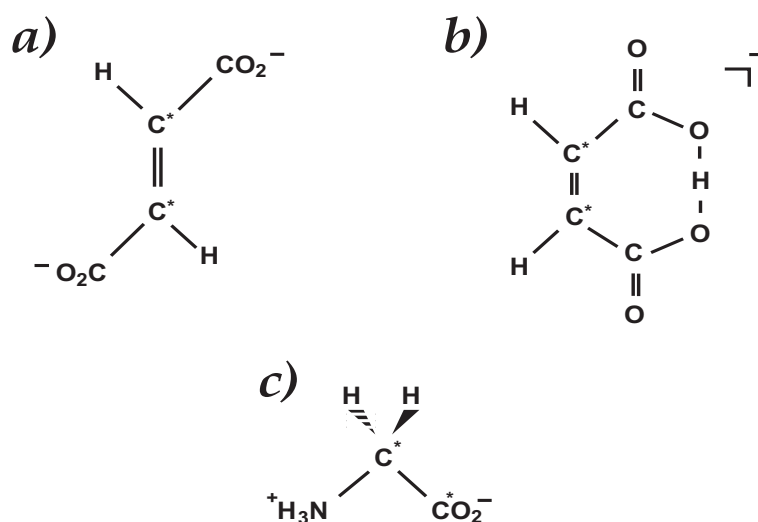
FIGURE 5.8: *Molecular structures of the $^{13}C_2$-labelled species used for experimental tests. a) The anion of diammonium [2,3-$^{13}C_2$]-fumarate; b) The anion of ammonium hydrogen [2,3-$^{13}C_2$]-maleate; c) [$^{13}C_2$,^{15}N]-glycine.*

All experiments were performed using $4\,\text{mm}$ zirconia magic-angle-spinning rotors on a Varian Infinity+ spectrometer at a magnetic field strength of $9.4\,\text{T}$. Ramped cross-polarization[240] was used to generate proton-enhanced ^{13}C transverse magnetization. The echo intervals were performed in the presence of SPINAL-64 proton decoupling[25, 241, 113] throughout, using a decoupler field corresponding to a proton nutation frequency of $100\,\text{kHz}$ for all samples. The SPINAL pulse length, in theory equal to $165°$, was experimentally optimised for each sample using a spin-echo experiment with a $2\tau = 31\,\text{ms}$ to determine the pulse length giving the most signal. The so-determined values were, 5.3, 5.3 and 4.9 μs for DAF, AHM and glycine samples, respectively. In all cases the ^{13}C π pulse had a duration of $6\,\mu s$, and its centre was always placed so as to coincide with an integer number of rotation periods after the end of cross-polarization. A MAS spinning frequency of $10000 \pm 5\,\text{Hz}$ was used in all cases. Sixteen transients were collected for glycine and eight for DAF and AHM samples. The recycle delay was set to 6, 4 and 25 s for glycine, DAF and AHM samples. An eight-step nested phase cycle[2] was used to select changes of coherence order of ± 1 and ± 2 on the ^1H 90° and ^{13}C 180° pulse, respectively. Only the -2 (for ^{13}C 180°) change in coherence order produces detectable signal.

Experimental results for the 10%-$^{13}\text{C}_2$-DAF sample are shown in Figure 5.9a. A monotonic decrease in the echo amplitude can be observed (left column). Fourier transformation of the echo trajectory gives a single zero-frequency peak (right column). The truncation artefacts are due to practical limitations on the maximum decoupling interval. The lack of echo modulation is consistent with the total magnetic equivalence of the two ^{13}C sites (see Eq. 5-71). The ^{13}C pairs in this sample lie on the horizontal axis in Figure 5.4a, i.e., well within *regime A* (indicated by a circle). For this sample, the echo decay trajectory was very sensitive to minor experimental perturbations such as probe tuning and temperature. We do not understand fully the origins of this unstable behaviour but note that total magnetic equivalence requires a delicate balance of many large spin interactions. Experimental results for the $^{13}\text{C}_2$-AHM sample are shown in Figure 5.9b, left column. A rather weak oscillation is observed in the echo decay. The echo trajectory $s(2\tau)$ fits well to the function:

$$s^{fit}(2\tau) = p\, e^{-2\tau/T_2^0} + (1-p)\cos(\pi J 2\tau)e^{-2\tau/T_2^J} \tag{5-72}$$

using fit parameters listed in Table 5.2 (solid line). The fitted J-coupling of $J = 64.9 \pm 1.8\,\text{Hz}$ agrees reasonably well with the solution-state J-coupling estimate of $J = 67\,\text{Hz}$.[234]

Table 5.2: *Parameters used in Eq. 5-72 to fit the experimental spin-echo modulation curves shown in Figure 5.9.*

sample	J / Hz	p	T_2^0/ ms	T_2^J / ms
10%-$^{13}\text{C}_2$-DAF	indeterminate	1.0	38 ± 1	indeterminate
$^{13}\text{C}_2$-AHM	64.9 ± 1.8	0.49 ± 0.08	10.0 ± 2.0	13.0 ± 2.0
[$^{13}\text{C}_2$,^{15}N]-glycine (CO peak)	54.6 ± 0.1	0.20 ± 0.02	13.4 ± 2.0	36.9 ± 1.0
[$^{13}\text{C}_2$,^{15}N]-glycine (C$^\alpha$ peak)	54.6 ± 0.1	0.37 ± 0.01	5.3 ± 0.1	17.0 ± 0.2

Fourier transformation of $s(2\tau)$ provides a large central peak flanked by the two components of the J-split doublet (Figure 5.9b, right column). This behaviour is consistent with the different principal axes orientations of the two large CSA tensors, which bring the spin system into *regime C* of Figure 5.4a (indicated by a square). After allowing for decay due to relaxation and other mechanisms, the theoretical model in Eq. 5-68 resembles the experimental form of the spin echo trajectory in Eq. 5-72. Note that the fitted p value of 0.49 ± 0.08 in Table 5.2 agrees with the theoretical expectation of $p = 0.5$ from Eq. 5-68.

The [$^{13}\text{C}_2$,^{15}N]-glycine sample displays prominent oscillations in the spin echo trajectory (Figure 5.9c and d, left column). The carboxyl and α-carbon peak amplitudes may both be fitted to the function in Eq. 5-72, with the same value of the J-coupling ($J = 54.6 \pm 0.1\,\text{Hz}$), which agrees well with the solution-state value
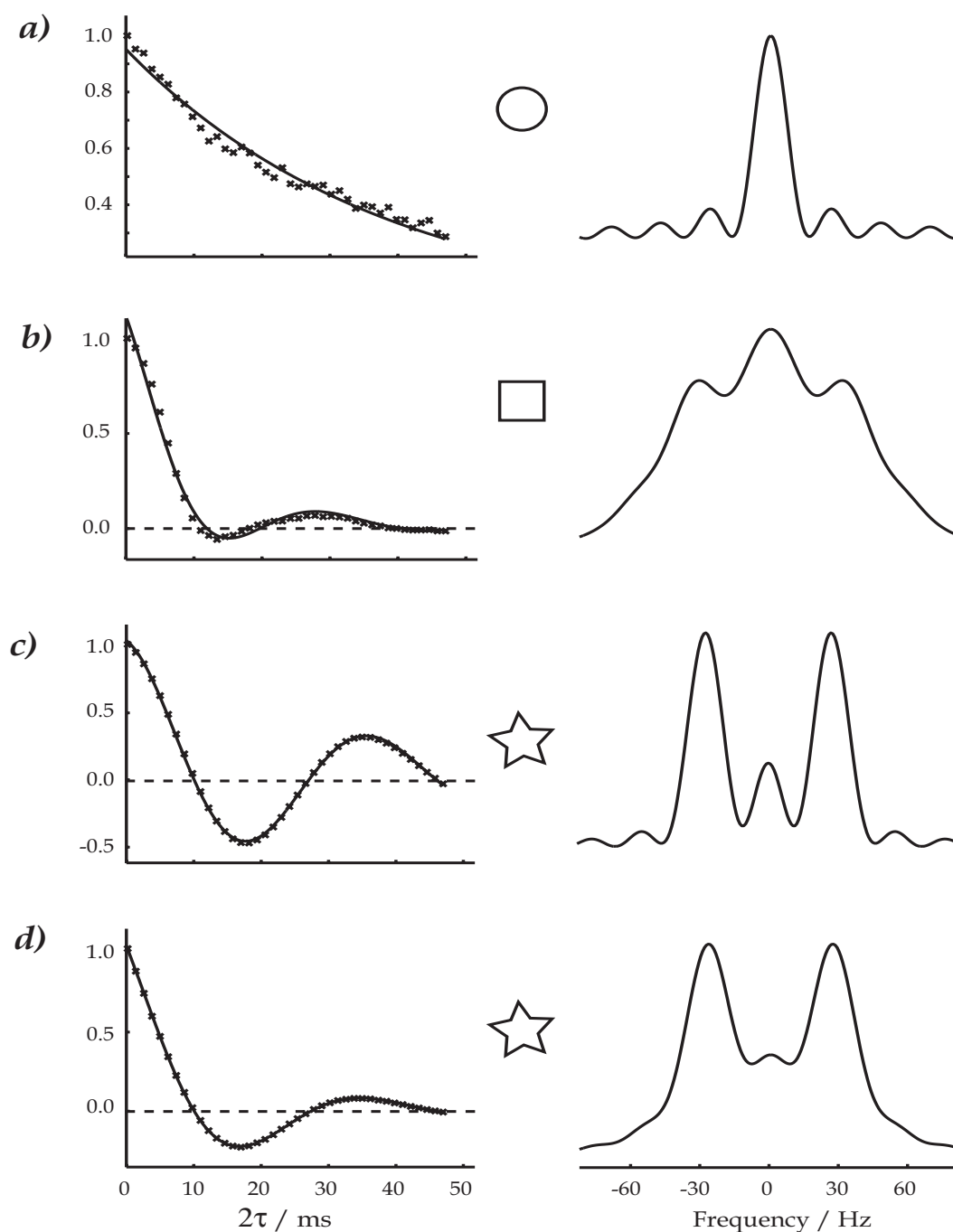
FIGURE 5.9: *Left column, crosses: experimental echo amplitudes, plotted as a function of the full echo interval 2τ. Left column, solid lines: best fits to the function in Eq. 5-72, using the parameters listed in TABLE 5.2. Right column: Fourier transforms of the echo amplitude function. Some of the plots display truncation artifacts due to practical limitations on the total decoupling time. The symbols represent the echo modulation regime for each sample, as indicated in FIGURE 5.4. a) diammonium [2,3-^{13}C$_2$]-fumarate; b) Ammonium hydrogen [2,3-^{13}C$_2$]-maleate; c) [^{13}C$_2$,^{15}N]-glycine, amplitude of the carbonyl ^{13}C peak; d) [^{13}C$_2$,^{15}N]-glycine, amplitude of the α-^{13}C peak.*

of $J = 53.6\,\text{Hz}$.[242] Fourier transformation of the echo trajectories provides well-resolved J-split doublets (FIGURE 5.9c and d, right column). The isotropic chemical shift difference between the ^{13}C sites in glycine is 132.5 ppm, which corresponds to 13.322 kHz at the magnetic field used. It follows that the spinning frequency of 10 kHz is between the $n = 1$ and $n = 2$ rotational resonances, which places this spin-1/2 pair system in *regime B* of FIGURE 5.4b (indicated by a star). The theoretical modulation of Eq. 5-64 is in good agreement with

the experiment.

5.5   Conclusion

The measurement of homonuclear *J*-couplings in solids has the potential for becoming an important experimental method for studying conformational and structural effects, as well as hydrogen bonding. In this paper we have examined the principles of spin-echo modulation by homonuclear *J*-couplings in systems containing isolated pairs of spins-$1/2$. We find that the modulation of spin echoes is described by a superposition of several modulation components, one of which corresponds to a pure *J*-modulation. In a wide range of circumstances, the pure *J*-modulated component is the most prominent one. In some cases, the satellite components have small amplitude, while in many experimental situations, the satellite components are broadened in a powder due to a spread in modulation frequencies. It is often possible to determine the *J*-coupling accurately by examining the frequency of the dominant modulation component.

Care must nevertheless be used, since there are some situations in which the pure *J*-modulated components are weak or absent. In the rare case of total magnetic equivalence, the pure *J*-modulated component vanishes entirely, and the spin echoes are completely unmodulated. In summary, the message is one of qualified optimism for the quantitative exploitation of homonuclear *J*-couplings in solids. Except in the unusual case of total magnetic equivalence, the modulation of spin echoes may be used to estimate these couplings rather easily, with high accuracy and reliability. Nevertheless, one should be aware that in some regimes the apparently simple form of the powder-average *J*-modulation is misleading. The detailed spin system evolution is sometimes complicated and strongly orientation-dependent.

Our optimism as to the use of spin-echo modulations for measuring *J*-couplings does not imply that *all* solution-state NMR experiments based on *J*-couplings are directly transferable to the solid-state NMR context. Firstly, the theory presented above is only directly applicable to systems of spin-1/2 pairs. Secondly, further theoretical work is required on other pulse sequences exploiting homonuclear *J*-couplings in MAS solids, such as INADEQUATE-type experiments,[106, 92, 116, 112, 122, 123, 124, 125, 126, 127, 128, 129, 179] z-filtered spin-echo experiments,[114, 129] and double-quantum-filtered experiments.[180, 181, 182] We also anticipate that this theory may be used to elucidate the mechanism of RFDR[54, 55, 243] which involves multiple spin echoes. The strong participation of the *J*-couplings in RFDR has previously been noted by Brinkmann *et al.*[244]

Conclusion and perspectives

Most of the experiments presented in this thesis exploit the presence of the J-coupling during a τ - π - τ echo sequence. Scalar couplings have a great potential in both solid-state and solution NMR spectroscopy. Amongst other interactions like chemical-shift anisotropy, dipole-dipole interaction, etc, the through-bond magnetic interactions between nuclei, known as scalar couplings or J-couplings represent an extremely valuable source of information appearing encoded in the NMR spectra. The scalar couplings can furnish important chemical and structural information. However, they can be difficult to interpret particularly if signal overlap becomes a problem. Since they are not averaged by the molecular tumbling in solution, they are also used for performing the transfer of magnetisation between the nuclei in multidimensional experiments. In solids, the transfer of magnetisation through the dipolar coupling is commonly used due to its bigger efficiency with respect to that driven by the scalar coupling.

Recent improvements in NMR technology and the development of powerful sequences for decoupling and recoupling different interactions under magic-angle spinning, lead to high-resolution spectra in fully ^{13}C, ^{15}N-labelled compounds. Due to the carbon-13 labelling, the carbon spectra show however broad lines due to the presence of the ^{13}C - ^{13}C J-couplings. When resolution is good enough to resolve the fine structure of the ^{13}C-lines induced by the J-coupling, unusual and asymmetric carbone lineshapes were observed. The primary aim of this thesis was to understand the different contributions responsible for this broadening and asymmetry of the carbone lines. A second objective came up with the study of carbon lineshapes in fully ^{13}C-enriched L-Alanine and consisted in seeking techniques for improving spectral resolution by removing the broadening induced by the scalar couplings. The ideas of spin-state selection came from solution NMR which once again proved to be a valuable source of inspiration for new solid-state NMR experiments. Solution NMR as well can take advantage from the advances made in solid-state NMR spectroscopy, mainly for the design of experiments for the assignment of heteronuclei. The techniques based on the direct detection of carbon nuclei are good examples. Finally, many solution NMR experiments incorporating J-modulated spin echoes have been adapted for solid-state NMR. The theoretical investigation of spin-echo modulation by J-couplings in magic-angle-spinning solid-state NMR showed that for a wide range of conditions the pure J-modulation is preserved during a τ - π - τ echo sequence, even in the presence of large chemical-shift anisotropy and dipole-dipole interactions.

Many issues remain open for a future work. Namely, the spin-state-selective polarisation transfer mechanism for which more experimental work and theoretical investigations need to be devoted. Preliminary results indicate a possible interference between magic-angle spinning and the semi-selective pulses which in the case of the homonuclear IPAP experiment may lead less effcient spin-state selection. A more detailed study is needed to clarify this problem.

Preliminary results obtained on fully ^{13}C-labelled L-Alanine show that the sensitivity of spin-state-

selective correlation experiment can be enhanced by going to fast magic-angle-spinning frequencies. At these spinning rates, the spin-state-selective correlation experiment may be combined with adiabatic polarisation transfer techniques, like the DREAM sequence developed by Meier an coworkers, for obtaining at the same time a very good resolution with additionally a good sensitivity. The feasibility of spinning proteins at such spinning speeds was demonstrated recently by Ernst *et al.*.[141] In the light of these recent results, the application of spin-state-selective correlation experiments to the assignment of ^{13}C resonances in microcrystalline fully ^{13}C, ^{15}N-enriched proteins looks promising.

"I wonder how many people in this city
live in furnished rooms
Late at night when I look out at the buildings
I swear I see a face in every window
looking back at me,
and then I turn away
I wonder how many go back to their desks
and write this down."

I wonder how many people in this city, Leonard Cohen

5.1 Appendix A: Geometric rotations and Eulerian representation

We consider here only rotations conserving one point of the space, which is assumed to be the origin of the Cartesian coordinate system. One rotation can then be characterised by the set of Euler angles α, β, γ. They specify the orientation of a new coordinate frame $(O\mathbf{e}'_1\mathbf{e}'_2\mathbf{e}'_3)$ with respect to a fixed set of cartesian axes in tridimensional space.

The Euler angles (α, β, γ) are defined by a sequence of three successive rotations of the space axes (i.e., "passive rotations"[1, 11]). Using the clockwise rotation convention, the Euler rotation angles can be represented as shown in FIGURE 5.10. Starting from the right handed trihedron $\mathbf{e}_1$, $\mathbf{e}_2$, $\mathbf{e}_3$, we rotate clockwise (i.e., as viewed from the positive direction of the axis of rotation) by an angle α about the $\mathbf{e}_3$ axis to a first intermediate set of axes $\mathbf{f}_1$, $\mathbf{f}_2$, $\mathbf{e}_3$. We then rotate clockwise by an angle β about the axis $\mathbf{f}_1$ to a second intermediate set of axes $\mathbf{f}_1$, $\mathbf{f}'_2$, $\mathbf{e}'_3$. Finally, we rotate clockwise through an angle γ about the axis $\mathbf{e}_3$ to obtain the system $\mathbf{e}'_1$, $\mathbf{e}'_2$, $\mathbf{e}'_3$.
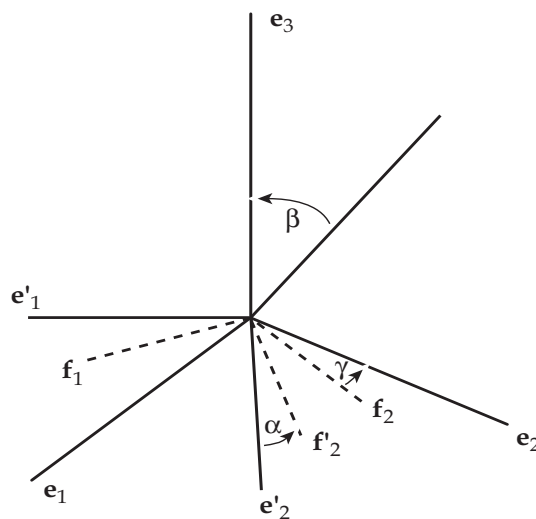
FIGURE 5.10: *The Euler angles*

The rotation matrices for the three steps are:

$$a(\alpha) = \begin{pmatrix} \cos\alpha & -\sin\alpha & 0 \\ \sin\alpha & \cos\alpha & 0 \\ 0 & 0 & 1 \end{pmatrix} \quad a(\beta) = \begin{pmatrix} 1 & 0 & 0 \\ 0 & \cos\beta & -\sin\beta \\ 0 & \sin\beta & \cos\beta \end{pmatrix} \quad a(\gamma) = \begin{pmatrix} \cos\gamma & -\sin\gamma & 0 \\ \sin\gamma & \cos\gamma & 0 \\ 0 & 0 & 1 \end{pmatrix} \quad (5\text{-}73)$$

and the matrix for the resultant transformation is:

$$(a_{ij}) = a(\alpha, \beta, \gamma) = a(\alpha)a(\beta)a(\gamma)$$

$$= \begin{pmatrix} \cos\alpha\cos\gamma - \sin\alpha\cos\beta\sin\gamma & -\cos\alpha\sin\gamma + \sin\alpha\cos\beta\sin\gamma & \sin\alpha\sin\beta \\ \sin\alpha\cos\gamma + \cos\alpha\cos\beta\sin\gamma & -\sin\alpha\sin\gamma + \cos\alpha\cos\beta\cos\gamma & -\cos\alpha\sin\gamma \\ \sin\beta\sin\gamma & -\sin\beta\cos\gamma & \cos\beta \end{pmatrix} \quad (5\text{-}74)$$

with $0 \leq \alpha \leq 2\pi$, $0 \leq \alpha \leq \pi$, $0 \leq \alpha \leq 2\pi$. Note that the elements of the rotation matrix (a_{ij}) represents also the direction cosines, each of the frame axes make with the axes of the new frame and can be written as follows:

$$(a_{ij}) = \begin{pmatrix} l_1 & m_1 & n_1 \\ l_2 & m_2 & n_2 \\ l_3 & m_3 & n_3 \end{pmatrix} \quad (5\text{-}75)$$

Let consider a P point, located in the $Oe_1e_2e_3$ frame at a position given by x, y, and z. In the new frame, it will be described by the coordinates x', y', z'. Assuming either the Euler angles or the direction cosines are know, the new coordinates can be calculated using the following relation:

$$\begin{pmatrix} x' \\ y' \\ z' \end{pmatrix} = (a_{ij}) \begin{pmatrix} x \\ y \\ z \end{pmatrix} \quad (5\text{-}76)$$

To determine the set of Euler angles specify the relative orientations of the interaction principal axes system of a tensor and the molecular reference frame from direction cosines, the following relations has to be used:

$$\begin{cases} n_3 = \cos\beta & \Rightarrow & \beta = \arccos(n_3) \\ \frac{n_1}{n_2} = -\tan\alpha & \Rightarrow & \alpha \arctan[-\frac{n_1}{n_2}] \\ \frac{l_3}{m_3} = \tan\gamma & \Rightarrow & \gamma \arctan[-\frac{l_3}{m_3}] \end{cases} \quad (5\text{-}77)$$

5.2   Appendix B: Rotation transformation and spin-echo amplitude

We prove here (i) the π-rotation transformations of Eqs. 5-33, 5-34 (see subsection 5.2.3) and (ii) the simplification of the $s(2\tau)$ echo amplitude into three modulation components.

(i) The matrix representation of rotation operators in the Zeeman product basis of a two spin-1/2 system, is given by the direct product of the individual rotation operators:[2]

$$
\begin{aligned}
R_\phi(\beta) &= R_{1,\phi}(\beta)R_{2,\phi}(\beta) \\[2mm]
&= \begin{pmatrix} c & -\mathrm{i}se_- \\ -\mathrm{i}se_+ & c \end{pmatrix} \otimes \begin{pmatrix} c & -\mathrm{i}se_- \\ -\mathrm{i}se_+ & c \end{pmatrix} \\[2mm]
&= \begin{pmatrix}
c^2 & -\mathrm{i}sce_- & -\mathrm{i}sce_- & -s^2 e_-^2 \\
-\mathrm{i}sce_+ & c^2 & -s^2 & -\mathrm{i}sce_- \\
-\mathrm{i}sce_+ & -s^2 & c^2 & -\mathrm{i}sce_- \\
-s^2 e_+^2 & -\mathrm{i}sce_+ & -\mathrm{i}sce_+ & c^2
\end{pmatrix}
\end{aligned}
$$

where

$$
c = \cos(\tfrac{1}{2}\beta), \qquad s = \sin(\tfrac{1}{2}\beta), \qquad e_\pm = e^{\pm\mathrm{i}\phi}
$$

and with ϕ being either 0, for a rotation of angle β around the x axis, or $\pi/2$, for a rotation of angle β around the y axis. We derive then the following expressions for the π-rotation operators in the Zeeman product basis:

$$
R_x(\pi) = \begin{pmatrix}
0 & 0 & 0 & -1 \\
0 & 0 & -1 & 0 \\
0 & -1 & 0 & 0 \\
-1 & 0 & 0 & 0
\end{pmatrix}
$$

$$
R_y(\pi) = \begin{pmatrix}
0 & 0 & 0 & \mathrm{i} \\
0 & 0 & -1 & 0 \\
0 & -1 & 0 & 0 \\
-\mathrm{i} & 0 & 0 & 0
\end{pmatrix}
$$

Therefore a π rotation around the x axis, when applied on the eigenstate matrix, will have the following effect:

$$
\begin{pmatrix} |1\rangle_r \\ |2\rangle_r \\ |3\rangle_r \\ |4\rangle_r \end{pmatrix} = R_z(\pi) \begin{pmatrix} |1\rangle \\ |2\rangle \\ |3\rangle \\ |4\rangle \end{pmatrix} = \begin{pmatrix} -|4\rangle \\ -|3\rangle \\ -|2\rangle \\ -|1\rangle \end{pmatrix} \tag{5-78}
$$

where the subscript r, design the state after the rotation.

Under a π rotation around the x axis, the states $|2'\rangle, |3'\rangle$ (see Eq.) are becoming as follows:

$$
\begin{aligned}
R_x(\pi)|2'\rangle &= [e^{-\mathrm{i}\frac{1}{2}\phi^{23}} \cos(\tfrac{1}{2}\theta^{23})] \underbrace{R_x(\pi)|2\rangle}_{-|3\rangle} + [e^{\mathrm{i}\frac{1}{2}\phi^{23}} \sin(\tfrac{1}{2}\theta^{23})] \underbrace{R_x(\pi)|3\rangle}_{-|2\rangle} \\
&= -e^{\mathrm{i}\frac{1}{2}\phi^{23}} \sin(\tfrac{1}{2}\theta^{23})|2\rangle - e^{-\mathrm{i}\frac{1}{2}\phi^{23}} \cos(\tfrac{1}{2}\theta^{23})|3\rangle] \\[2mm]
R_x(\pi)|3'\rangle &= [-e^{-\mathrm{i}\frac{1}{2}\phi^{23}} \sin(\tfrac{1}{2}\theta^{23})] \underbrace{R_x(\pi)|2\rangle}_{-|3\rangle} + [e^{\mathrm{i}\frac{1}{2}\phi^{23}} \cos(\tfrac{1}{2}\theta^{23})] \underbrace{R_x(\pi)|3\rangle}_{-|2\rangle} \\
&= -e^{\mathrm{i}\frac{1}{2}\phi^{23}} \cos(\tfrac{1}{2}\theta^{23})|2\rangle + e^{-\mathrm{i}\frac{1}{2}\phi^{23}} \sin(\tfrac{1}{2}\theta^{23})|3\rangle
\end{aligned} \tag{5-79}
$$

From Eq. 5-23, we can express the eigenstates $|2\rangle, |3\rangle$ in the Zeeman product basis with respect to the evolution eigenstates $|2'\rangle, |3'\rangle$:

$$
\begin{cases}
|2\rangle = e^{\mathrm{i}\frac{1}{2}\phi^{23}} \cos(\tfrac{1}{2}\theta^{23})|2'\rangle - e^{\mathrm{i}\frac{1}{2}\phi^{23}} \sin(\tfrac{1}{2}\theta^{23})|3'\rangle \\
|3\rangle = e^{-\mathrm{i}\frac{1}{2}\phi^{23}} \sin(\tfrac{1}{2}\theta^{23})|2'\rangle + e^{-\mathrm{i}\frac{1}{2}\phi^{23}} \cos(\tfrac{1}{2}\theta^{23})|3'\rangle
\end{cases} \tag{5-80}
$$

The expressions of Eqs. 5-33 and 5-34 can then be derived by replacing the relations above in Eq. 5-79:

$$
\begin{aligned}
R_x(\pi)|2'\rangle &= -\underbrace{[e^{i\frac{1}{2}\phi^{23}} + e^{-i\frac{1}{2}\phi^{23}}]}_{2\cos\phi^{23}}\underbrace{\sin(\tfrac{1}{2}\theta^{23})\cos(\tfrac{1}{2}\theta^{23})}_{\frac{1}{2}\sin\theta^{23}}|2'\rangle \\
&\quad +[e^{i\frac{1}{2}\phi^{23}}\sin^2(\tfrac{1}{2}\theta^{23}) - e^{-i\frac{1}{2}\phi^{23}}\cos^2(\tfrac{1}{2}\theta^{23})]|3'\rangle \\
&= -\cos\phi^{23}\sin\theta^{23}|2'\rangle + (-\cos\phi^{23}\cos\theta^{23} + i\sin\phi^{23})|3'\rangle \\[6pt]
R_x(\pi)|3'\rangle &= -[e^{i\frac{1}{2}\phi^{23}}\cos^2(\tfrac{1}{2}\theta^{23}) - e^{-i\frac{1}{2}\phi^{23}}]\sin^2(\tfrac{1}{2}\theta^{23}))|2\rangle \\
&\quad -[e^{i\frac{1}{2}\phi^{23}} + e^{-i\frac{1}{2}\phi^{23}}]\sin(\tfrac{1}{2}\theta^{23})\cos(\tfrac{1}{2}\theta^{23})|3'\rangle] \\
&= (-\cos\phi^{23}\sin\theta^{23} - i\sin\phi^{23})|2'\rangle + \cos\phi^{23}\sin\theta^{23}|3'\rangle
\end{aligned}
\tag{5-81}
$$

(ii) The spin-echo modulation is given by the signal expression at the time point ④:

$$
s(2\tau) = \underbrace{a_{\textcircled{4}}^{21}\langle 1'|I_x|2'\rangle}_{A} + \underbrace{a_{\textcircled{4}}^{31}\langle 1'|I_x|3'\rangle}_{B} + \underbrace{a_{\textcircled{4}}^{42}\langle 2'|I_x|4'\rangle}_{C} + \underbrace{a_{\textcircled{4}}^{43}\langle 3'|I_x|4'\rangle}_{D}
$$

where A, B, C and D are notations of the different terms of the relation above.

In the Zeeman product basis of the spin-1/2 pair system, the matrix representation of the I_x operator is given by:

$$
\begin{aligned}
I_x &\doteq I_{1x} \otimes \mathbf{1} + \mathbf{1} \otimes I_{2x} \\[6pt]
&\equiv \frac{1}{2}\begin{pmatrix} 0\begin{pmatrix}1&0\\0&1\end{pmatrix} & 1\begin{pmatrix}1&0\\0&1\end{pmatrix} \\ 1\begin{pmatrix}1&0\\0&1\end{pmatrix} & 0\begin{pmatrix}1&0\\0&1\end{pmatrix} \end{pmatrix} + \frac{1}{2}\begin{pmatrix} 1\begin{pmatrix}0&1\\1&0\end{pmatrix} & 0\begin{pmatrix}0&1\\1&0\end{pmatrix} \\ 0\begin{pmatrix}0&1\\1&0\end{pmatrix} & 1\begin{pmatrix}0&1\\1&0\end{pmatrix} \end{pmatrix} \\[6pt]
&= \frac{1}{2}\begin{pmatrix} 0 & 1 & 1 & 0 \\ 1 & 0 & 0 & 1 \\ 1 & 0 & 0 & 1 \\ 0 & 1 & 1 & 0 \end{pmatrix}
\end{aligned}
$$

For convenience, let make the following notations:

$$
\begin{cases}
|2'\rangle = \underbrace{e^{-i\frac{1}{2}\phi^{23}}\cos\tfrac{1}{2}\theta^{23}}_{a}|2\rangle + \underbrace{e^{+i\frac{1}{2}\phi^{23}}\sin\tfrac{1}{2}\theta^{23}}_{b}|3\rangle \\[12pt]
|3'\rangle = \underbrace{-e^{-i\frac{1}{2}\phi^{23}}\sin\tfrac{1}{2}\theta^{23}}_{c}|2\rangle + \underbrace{e^{+i\frac{1}{2}\phi^{23}}\cos\tfrac{1}{2}\theta^{23}}_{d}|3\rangle
\end{cases}
$$

Since $|1'\rangle = |1\rangle$ and $4'\rangle = |4\rangle$, the expression of the first two terms of the spin-echo modulation can be written as follows:

$$A = a^{21}_{\circled{4}}\langle 1|I_x[a|2\rangle + b|3\rangle]$$

$$B = a^{31}_{\circled{4}}\langle 1|I_x[c|2\rangle + d|3\rangle]$$

$$= a^{21}_{\circled{4}}[a\underbrace{\langle 1|I_x|2\rangle}_{=\frac{1}{2}} + b\underbrace{\langle 1|I_x|3\rangle}_{=\frac{1}{2}}]$$

$$= a^{31}_{\circled{4}}[c\underbrace{\langle 1|I_x|2\rangle}_{=\frac{1}{2}} + d\underbrace{\langle 1|I_x|3\rangle}_{=\frac{1}{2}}]$$

$$= \tfrac{1}{2}a^{21}_{\circled{4}}[a + b]$$

$$= \tfrac{1}{2}a^{31}_{\circled{4}}[c + d]$$

$$C = a^{42}_{\circled{4}}[a^*|2\rangle + b^*|3\rangle]|I_x|4\rangle$$

$$D = a^{43}_{\circled{4}}[c^*|2\rangle + d^*|3\rangle]|I_x|4\rangle$$

$$= a^{42}_{\circled{4}}[a^*\underbrace{\langle 2|I_x|4\rangle}_{=\frac{1}{2}} + b^*\underbrace{\langle 3|I_x|4\rangle}_{=\frac{1}{2}}]$$

$$= a^{43}_{\circled{4}}[c^*\underbrace{\langle 2|I_x|4\rangle}_{=\frac{1}{2}} + d^*\underbrace{\langle 3|I_x|4\rangle}_{=\frac{1}{2}}]$$

$$= \tfrac{1}{2}a^{42}_{\circled{4}}[a^* + b^*]$$

$$= \tfrac{1}{2}a^{43}_{\circled{4}}[c^* + d^*]$$

where * means taking the complex conjugate of the element.
The main steps of the $a^{21}_{\circled{4}}$ derivation are summarized in the next equation:

$$a^{21}_{\circled{4}} = a^{21}_{\circled{3}}e^{\mathrm{i}\omega^{21}\tau}$$

$$= [\cos\phi^{23}\sin\theta^{23}a^{24}_{\circled{2}} + (\cos\phi^{23}\cos\theta^{23} + \mathrm{i}\sin\phi^{23})a^{34}_{\circled{2}}]e^{\mathrm{i}\omega^{21}\tau}$$

$$= [\cos\phi^{23}\sin\theta^{23}a^{24}_{\circled{1}}e^{\mathrm{i}\omega^{24}\tau} + (\cos\phi^{23}\cos\theta^{23} + \mathrm{i}\sin\phi^{23})a^{34}_{\circled{1}}e^{\mathrm{i}\omega^{34}\tau}]e^{\mathrm{i}\omega^{21}\tau}$$

$$= \cos\phi^{23}\sin\theta^{23}\tfrac{1}{2}(e^{\mathrm{i}\frac{1}{2}\phi^{23}}\cos\tfrac{1}{2}\theta^{23} + e^{-\mathrm{i}\frac{1}{2}\phi^{23}}\sin\tfrac{1}{2}\theta^{23})e^{\mathrm{i}(\pi J - \frac{1}{2}\omega^{23})2\tau}$$
$$+ (\cos\phi^{23}\cos\theta^{23} + \mathrm{i}\sin\phi^{23})\tfrac{1}{2}(e^{-\mathrm{i}\frac{1}{2}\phi^{23}}\cos\tfrac{1}{2}\theta^{23} - e^{\mathrm{i}\frac{1}{2}\phi^{23}}\sin\tfrac{1}{2}\theta^{23})e^{\mathrm{i}\pi J 2\tau}$$

The other amplitudes may be determined in the same manner. Their final expressions are given below:

$$a^{31}_{\circled{4}} = -\cos\phi^{23}\sin\theta^{23}\tfrac{1}{2}(e^{-\mathrm{i}\frac{1}{2}\phi^{23}}\cos\tfrac{1}{2}\theta^{23} - e^{\mathrm{i}\frac{1}{2}\phi^{23}}\sin\tfrac{1}{2}\theta^{23})e^{\mathrm{i}(\pi J + \frac{1}{2}\omega^{23})2\tau}$$
$$+ (\cos\phi^{23}\cos\theta^{23} - \mathrm{i}\sin\phi^{23})\tfrac{1}{2}(e^{\mathrm{i}\frac{1}{2}\phi^{23}}\cos\tfrac{1}{2}\theta^{23} + e^{-\mathrm{i}\frac{1}{2}\phi^{23}}\sin\tfrac{1}{2}\theta^{23})e^{\mathrm{i}\pi J 2\tau}$$

$$a^{42}_{\circled{4}} = \cos\phi^{23}\sin\theta^{23}\tfrac{1}{2}(e^{-\mathrm{i}\frac{1}{2}\phi^{23}}\cos\tfrac{1}{2}\theta^{23} + e^{\mathrm{i}\frac{1}{2}\phi^{23}}\sin\tfrac{1}{2}\theta^{23})e^{-\mathrm{i}(\pi J - \frac{1}{2}\omega^{23})2\tau}$$
$$+ (\cos\phi^{23}\cos\theta^{23} - \mathrm{i}\sin\phi^{23})\tfrac{1}{2}(e^{\mathrm{i}\frac{1}{2}\phi^{23}}\cos\tfrac{1}{2}\theta^{23} - e^{-\mathrm{i}\frac{1}{2}\phi^{23}}\sin\tfrac{1}{2}\theta^{23})e^{-\mathrm{i}\pi J 2\tau}$$

$$a^{43}_{\circled{4}} = -\cos\phi^{23}\sin\theta^{23}\tfrac{1}{2}(e^{\mathrm{i}\frac{1}{2}\phi^{23}}\cos\tfrac{1}{2}\theta^{23} - e^{-\mathrm{i}\frac{1}{2}\phi^{23}}\sin\tfrac{1}{2}\theta^{23})e^{-\mathrm{i}(\pi J + \frac{1}{2}\omega^{23})2\tau}$$
$$+ (\cos\phi^{23}\cos\theta^{23} + \mathrm{i}\sin\phi^{23})\tfrac{1}{2}(e^{-\mathrm{i}\frac{1}{2}\phi^{23}}\cos\tfrac{1}{2}\theta^{23} + e^{\mathrm{i}\frac{1}{2}\phi^{23}}\sin\tfrac{1}{2}\theta^{23})e^{-\mathrm{i}\pi J 2\tau}$$

Finally, the expressions of the four terms of the spin-echo modulation may be written as:

$$A = \tfrac{1}{2}a^{21}_{\textcircled{4}}[a+b] = \tfrac{1}{2}a^{21}_{\textcircled{4}}(e^{-i\frac{1}{2}\phi^{23}}\cos\tfrac{1}{2}\theta^{23} + e^{i\frac{1}{2}\phi^{23}}\sin\tfrac{1}{2}\theta^{23})$$

$$= \tfrac{1}{4}\cos\phi^{23}\sin\theta^{23}(1+\cos\phi^{23}\sin\theta^{23})e^{i(\pi J - \frac{1}{2}\omega^{23})2\tau}$$

$$+\tfrac{1}{4}(\cos\phi^{23}\cos\theta^{23} + i\sin\phi^{23})(e^{-i\phi^{23}}\cos^2\tfrac{1}{2}\theta^{23} - e^{i\phi^{23}}\sin^2\tfrac{1}{2}\theta^{23})e^{i\pi J 2\tau}$$

$$B = \tfrac{1}{2}a^{31}_{\textcircled{4}}[c+d] = \tfrac{1}{2}a^{31}_{\textcircled{4}}(e^{i\frac{1}{2}\phi^{23}}\cos\tfrac{1}{2}\theta^{23} - e^{-i\frac{1}{2}\phi^{23}}\sin\tfrac{1}{2}\theta^{23})$$

$$= -\tfrac{1}{4}\cos\phi^{23}\sin\theta^{23}(1-\cos\phi^{23}\sin\theta^{23})e^{i(\pi J + \frac{1}{2}\omega^{23})2\tau}$$

$$+\tfrac{1}{4}(\cos\phi^{23}\cos\theta^{23} - i\sin\phi^{23})(e^{i\phi^{23}}\cos^2\tfrac{1}{2}\theta^{23} - e^{-i\phi^{23}}\sin^2\tfrac{1}{2}\theta^{23})e^{i\pi J 2\tau}$$

$$C = \tfrac{1}{2}a^{42}_{\textcircled{4}}[a^* + b^*] = \tfrac{1}{2}a^{42}_{\textcircled{4}}(e^{i\frac{1}{2}\phi^{23}}\cos\tfrac{1}{2}\theta^{23} + e^{-i\frac{1}{2}\phi^{23}}\sin\tfrac{1}{2}\theta^{23})$$

$$= \tfrac{1}{4}\cos\phi^{23}\sin\theta^{23}(1+\cos\phi^{23}\sin\theta^{23})e^{-i(\pi J - \frac{1}{2}\omega^{23})2\tau}$$

$$+\tfrac{1}{4}(\cos\phi^{23}\cos\theta^{23} - i\sin\phi^{23})(e^{i\phi^{23}}\cos^2\tfrac{1}{2}\theta^{23} - e^{-i\phi^{23}}\sin^2\tfrac{1}{2}\theta^{23})e^{-i\pi J 2\tau}$$

$$D = \tfrac{1}{2}a^{43}_{\textcircled{4}}[c^* + d^*] = \tfrac{1}{2}a^{43}_{\textcircled{4}}(e^{-i\frac{1}{2}\phi^{23}}\cos\tfrac{1}{2}\theta^{23} - e^{i\frac{1}{2}\phi^{23}}\sin\tfrac{1}{2}\theta^{23})$$

$$= -\tfrac{1}{4}\cos\phi^{23}\sin\theta^{23}(1-\cos\phi^{23}\sin\theta^{23})e^{-i(\pi J + \frac{1}{2}\omega^{23})2\tau}$$

$$+\tfrac{1}{4}(\cos\phi^{23}\cos\theta^{23} + i\sin\phi^{23})(e^{-i\phi^{23}}\cos^2\tfrac{1}{2}\theta^{23} - e^{i\phi^{23}}\sin^2\tfrac{1}{2}\theta^{23})e^{-i\pi J 2\tau}$$

The $s_-(2\tau)$ component can be obtained by adding the $e^{\pm i(\pi J - \frac{1}{2}\omega^{23})2\tau}$-terms in the expressions of A and C:

$$s_-(2\tau) = \tfrac{1}{4}\cos\phi^{23}\sin\theta^{23}(1+\cos\phi^{23}\sin\theta^{23})[e^{i(\pi J - \frac{1}{2}\omega^{23})2\tau} + e^{-i(\pi J - \frac{1}{2}\omega^{23})2\tau}]$$

$$= \underbrace{\tfrac{1}{2}\cos\phi^{23}\sin\theta^{23}(1+\cos\phi^{23}\sin\theta^{23})}_{a_-}\cos[(\pi J - \tfrac{1}{2}\omega^{23})2\tau]$$

The $s_+(2\tau)$ component can be obtained by adding the $e^{\pm i(\pi J + \frac{1}{2}\omega^{23})2\tau}$-terms in the expressions of B and D:

$$s_-(2\tau) = -\tfrac{1}{4}\cos\phi^{23}\sin\theta^{23}(1-\cos\phi^{23}\sin\theta^{23})[e^{i(\pi J + \frac{1}{2}\omega^{23})2\tau} + e^{-i(\pi J + \frac{1}{2}\omega^{23})2\tau}]$$

$$= \underbrace{\tfrac{1}{2}\cos\phi^{23}\sin\theta^{23}(-1+\cos\phi^{23}\sin\theta^{23})}_{a_+}\cos[(\pi J + \tfrac{1}{2}\omega^{23})2\tau]$$

Adding together all the $e^{\pm i\pi J 2\tau}$-terms in the expressions of A, B, C and D, we get the pure J-modulated component:

$$
\begin{aligned}
s_0(2\tau) &= \tfrac{1}{2}\cos\phi^{23}\cos\theta^{23}[e^{i\phi^{23}}\underbrace{(\cos^2\tfrac{1}{2}\theta^{23}-\sin^2\tfrac{1}{2}\theta^{23})}_{\cos\theta^{23}}+e^{-i\phi^{23}}\underbrace{(\cos^2\tfrac{1}{2}\theta^{23}-\sin^2\tfrac{1}{2}\theta^{23})}_{\cos\theta^{23}}]\cos(\pi J2\tau) \\[2mm]
&\quad +i\tfrac{1}{2}\sin\phi^{23}[-e^{i\phi^{23}}\underbrace{(\cos^2\tfrac{1}{2}\theta^{23}+\sin^2\tfrac{1}{2}\theta^{23})}_{1}+e^{-i\phi^{23}}\underbrace{(\cos^2\tfrac{1}{2}\theta^{23}+\sin^2\tfrac{1}{2}\theta^{23})}_{1}]\cos(\pi J2\tau) \\[2mm]
&= \tfrac{1}{2}[\cos\phi^{23}\cos\theta^{23}\cos\theta^{23}\underbrace{(e^{i\phi^{23}}+e^{-i\phi^{23}})}_{2\cos\phi^{23}}-i\sin\phi^{23}\underbrace{(e^{i\phi^{23}}-e^{-i\phi^{23}})}_{2i\sin\phi^{23}}]\cos(\pi J2\tau) \\[2mm]
&= [\cos^2\phi^{23}\cos^2\theta^{23}+\sin^2\phi^{23}]\cos(\pi J2\tau) \\[2mm]
&= \underbrace{(1-\cos^2\phi^{23}\sin^2\theta^{23})}_{a_0}\cos(\pi J2\tau)
\end{aligned}
$$

References

[1] C. Cohen-Tannoudji, B. Diu, and F. Laloë. *Mécanique Quantique*, volume I. Hermann, Paris, **1996**.

[2] Malcolm H. Levitt. *Spin dynamics. Basics of Nuclear Magnetic Resonance*. Wiley-Interscience, Chichester, first edition, **2001**.

[3] O. Stern. Ein Weg zur experimentellen Prüfung der Richtungsquantelung im Magnetfeld. *Z. Phys.*, 7:249–253, **1921**.

[4] W. Gerlach and O. Stern. Der Experimentelle Nachweis des magnetischen Moments des Silberatoms. *Z. Phys.*, 8:110–111, **1921**.

[5] E.M. Purcell, H.C. Torrey, and R.V. Pound. Resonance absorption by nuclear magnetic moments in a solid. *Phys. Rev.*, 69:37–38, **1946**.

[6] F. Bloch, W.W. Hansen, and M. Packard. Nuclear induction. *Phys. Rev.*, 69:127–127, **1946**.

[7] Jr. W. Pauli. Exclusion principle. *Naturw.*, 12:741–744, **1924**.

[8] G. Breit and I.I. Rabi. Measurement of nuclear spin. *Phys. Rev.*, 38:2082–2082, **1931**.

[9] R. Frisch and O. Stern. *Z. Phys.*, 85:4–4, **1933**.

[10] K. Wüthrich. *NMR of Proteins and Nucleic Acids*. Wiley-Interscience, New York, first edition, **1986**.

[11] Klaus Schmidt-Rohr and Hans Wolfgang Spiess. *Multidimensional Solid-State NMR and Polymers*. Academic Press, London, first edition, **1994**.

[12] A. Abragam. *The Principles of Nuclear Magnetism*. Clarendon Press, Oxford, first edition, **1961**.

[13] R.R. Ernst, G. Bodenhausen, and A. Wokaun. *Principles of nuclear magnetic resonance in one and two dimensions*. Oxford University Press, United Kingdom, second edition, **1987**.

[14] M. Mehring. *Principles of High Resolution NMR in Solids*. Springer, Berlin, second edition, **1983**.

[15] S.J. Opella and J.S. Waugh. 2-dimensional ^{13}C NMR of highly oriented polyethylene. *J. Chem. Phys.*, 66:4919–4924, **1977**.

[16] S.J. Opella, P.L. Stewart, and K.G. Valentine. Protein-structure by solid-state NMR-spectroscopy. *Q. Rev. of Biophys.*, 19:7–49, **1987**.

[17] E.R. Andrew, A. Bradbury, and E.G. Eades. Nuclear magnetic resonance spectra from a crystal rotating at high speed. *Nature*, 182:1659–1659, **1958**.

[18] E.R. Andrew, A. Bradbury, and E.G. Eades. Removal of dipolar broadening of nuclear magnetic resonance spectra of solids by specimen rotation. *Nature*, 183:1802–1803, **1959**.

[19] I.J. Lowe. Free induction decays of rotating solids. *Phys. Rev. Lett.*, 2:285–287, **1959**.

[20] M.M. Maricq and J.S. Waugh. NMR in rotating solids. *J. Chem. Phys.*, 70:3300–3316, **1979**.

[21] G.A. Morris and R. Freeman. Enhancement of nuclear magnetic-resonance signals by polarization transfer. *J. Am. Chem. Soc.*, 101:760–762, **1979**.

[22] D.P. Burum and R.R. Ernst. Net polarization transfer via a *J*-ordered state for signal enhancement of low-sensitivity nuclei. *J. Magn. Reson.*, 39:163–168, **1980**.

[23] S.R. Hartmann and E.L. Hahn. Nuclear double resonance in the rotating frame. *Phys. Rev.*, 128:2042–2053, **1962**.

[24] S. Hediger, B.H. Meier, and R.R. Ernst. Adiabatic passage Hartmann-Hahn cross-polarization in NMR under magic-angle sample-spinning. *Chem. Phys. Lett.*, 240:449–456, **1995**.

[25] B.M. Fung, A.K. Khitrin, and K. Ermolaev. An improved broadband decoupling sequence for liquid crystals and solids. *J. Magn. Reson.*, 142:97–101, **2000**.

[26] G. De Paëpe, P. Hodgkinson, and L. Emsley. Improved heteronuclear decoupling schemes for solid-state magic angle spinning NMR by direct spectral optimisation. *Chem. Phys. Lett.*, 376:259–267, **2003**.

[27] M. Goldman. *Quantum description of high-resolution NMR in liquids*. Clarendon Press, Oxford, sixth edition, **2000**.

[28] E.L. Hahn and D.E. Maxwell. Chemical shift and field independent frequency modulation of the spin echo envelope. *Phys. Rev.*, 84:1246–1247, **1951**.

[29] R. Verel, M. Baldus, and B.H. Meier. A homonuclear spin-pair filter for solid-state NMR based on adiabatic-passage techniques. *Chem. Phys. Lett.*, 287:421–428, **1998**.

[30] R. Verel, M. Ernst, and B.H. Meier. Adiabatic recoupling in solid-state NMR: the DREAM scheme. *J. Magn. Reson.*, 150:81–99, **2001**.

[31] M. Ottiger, F. Delaglio, J.L. Marquardt, N. Tjandra, and A. Bax. Measurement of dipolar couplings for methylene and methyl sites in weakly oriented macromolecules and their use in structure determination. *J. Magn. Reson.*, 134:365–369, **1998**.

[32] P. Andersson, J. Weigelt, and G. Otting. Spin-state selection filters for the measurement of heteronuclear one-bond coupling constants. *J. Biomol. NMR*, 12:435–441, **1998**.

[33] A. Meissner, J.Ø. Duus, and O.W. Sørensen. Spin-state-selective excitation. Application for E.COSY-type measurement of *J*(HH) coupling constants. *J. Magn. Reson.*, 128:92–97, **1997**.

[34] B. Brutscher. Accurate measurement of small spin-spin couplings in partially alligned molecules using o novel *J*-mismatch compensated spin-state-selection filter. *J. Magn. Reson.*, 151:332–338, **2001**.

[35] N.C. Nielsen, H. Thøgersen, and O.W. Sørensen. Doubling the sensitivity of INADEQUATE for tracing out the carbon skeleton of molecules by NMR. *J. Am. Chem. Soc.*, 117:11365–11366, **1995**.

[36] R. Verel, J.D. van Beek, and B.H. Meier. INADEQUATE-CR experiments in the solid state. *J. Magn. Reson.*, 140:300–303, **1999**.

[37] S.K. Straus, T. Bremi, and R.R. Ernst. Resolution enhancement by molecular *J* decoupling in solid-state MAS NMR. *Chem. Phys. Lett.*, 262:709–715, **1996**.

[38] M. Ernst and B.H. Meier. Adiabatic polarisation transfer methods in MAS spectroscopy. In *Encyclopedia of Nuclear Magnetic Resonance*, volume 9, pages 23–32. John Wiley and Sons, New York, Second edition, **2002**.

[39] R. Freeman. Beg, borrow, or steal. Finding ideas for new NMR experiments. *Concepts Magn. Reson. Part A*, 17:71–85, **2003**.

[40] K. Pervushin, R. Riek, G. Wider, and K. Wüthrich. Attenuated T_2 relaxation by mutual cancellation of dipole-dipole coupling and chemical shift anisotropy indicates an avenue to NMR structures of very large biological macromolecules in solution. *Proc. Natl. Acad. Sci. U. S. A.*, 94:12366–12371, **1997**.

[41] S.K. Straus, T. Bremi, and R.R. Ernst. Experiments and strategies for the assignment of fully $^{13}C/^{15}N$-labelled polypeptides by solid-state NMR. *J. Biomol. NMR*, 12:39–50, **1998**.

[42] A. McDermott, T. Polenova, A. Böckmann, K.W. Zilm, E.K. Paulsen, R.W. Martin, and G.T. Montelione. Partial NMR assignments for uniformly ($^{13}C,^{15}N$)-enriched BPTI in the solid state. *J. Biomol. NMR*, 16:209–212, **2000**.

[43] J. Pauli, B. van Rossum, H. Föster, H.J.M. de Groot, and H. Oschkinat. Sample optimization and identification of signal patterns of amino acid side chains in 2D RFDR spectra of the aplha-spectrin SH3 domain. *J. Magn. Reson.*, 143:411–416, **2000**.

[44] J. Pauli, B. van Rossum, H. de Groot, and H. Oschkinat. Backbone and side-chain ^{13}C and ^{15}N signal assignments of the alpha-spectrin SH3 domain by magic angle spinning solid-state NMR at 17.6 Tesla. *ChemBioChem*, 2:272–281, **2001**.

[45] B.J. van Rossum, F. Castellani, K. Rehbein, J. Pauli, and H. Oschkinat. Assignment of the non-exchanging protons of the alpha-spectrin SH3 domain by two- and three-dimensional ^1H-^{13}C solid-state magic-angle spinning NMR and comparison of solution and solid-state proton chemical shifts. *ChemBioChem*, 2:906–914, **2001**.

[46] F. Castellani, B. van Rossum, A. Diehl, M. Schubert, K. Rehbein, and H. Oschkinat. Structure of a protein determined by solid-state magic-angle-spinning NMR spectroscopy. *Nature*, 420:98–102, **2002**.

[47] A. Böckmann, A. Lange, A. Galinier, S. Luca, N. Giraud, M. Juy, H. Heise, R. Montserret, F. Penin, and M. Baldus. Solid-state NMR sequential resonance assignments and conformational analysis of the 2 x 10.4 kDa dimeric form of *bacillus subtilis* protein, Crh. *J. Biomol. NMR*, 2:906–914, **2003**.

[48] M. Edén and M.H. Levitt. Pulse sequence symmetries in the nuclear magnetic resonance of spinning solids: Application to heteronuclear decoupling. *J. Chem. Phys.*, 111:1511–1519, **1999**.

[49] M. Ernst. Heteronuclear spin decoupling in solid-state NMR under magic-angle sample spinning. *J. Magn. Reson.*, 162:1–34, **2003**.

[50] N. Bloembergen. On the interaction of nuclear spins in a crystalline lattice. *Physica*, 15:386–426, **1949**.

[51] D.P. Raleigh, M.H. Levitt, and R.G. Griffin. Rotational resonance in solid-state NMR. *J. Chem. Phys.*, 146:71–76, **1988**.

[52] T. Gullion and J. Schaefer. Rotational–echo double–resonance NMR. *J. Magn. Reson.*, 81:196–200, **1989**.

[53] R. Tycko and G. Dabbagh. Measurement of nuclear magnetic dipole-dipole couplings in magic angle spinning NMR. *J. Chem. Phys.*, 173:461–465, **1990**.

[54] A.E. Bennett, J.H. Ok, R.G. Griffin, and S. Vega. Chemical–shift correlation spectroscopy in rotating solids: radio frequency–driven dipolar recoupling and longitudinal exchange. *J. Chem. Phys.*, 96:8624–8627, **1992**.

[55] Y. Ishii. ^{13}C - ^{13}C dipolar recoupling under very fast magic angle spinning in solid-state nuclear magnetic resonance: application to distance measurements, spectral assignments and high-through-put secondary-structure determination. *J. Chem. Phys.*, 114:8473–8483, **2001**.

[56] Y.K. Lee, N.D. Kurur, M. Helme, O.G. Johannessen, N.C. Nielsen, and M.H. Levitt. Efficient dipolar recoupling in the NMR of rotating solids. A sevenfold symmetrical radiofrequency pulse sequence. *Chem. Phys. Lett.*, 242:304–309, **1995**.

[57] M. Hohwy, H.J. Jakobsen, M. Edén, M.H. Levitt, and N.C. Nielsen. Broadband dipolar recoupling in nuclear magnetic resonance of rotating solids: A compensated C7 pulse sequence. *J. Chem. Phys.*, 108:2686–2694, **1998**.

[58] M. Howhy, C.M. Rienstra, C.P. Jaroniec, and R.G. Griffin. Fivefold symmetric homonuclear dipolar recoupling in rotating solids: Application to double quantum spectroscopy. *J. Chem. Phys.*, 110:7983–7992, **1999**.

[59] A.E. Bennett, R.G. Griffin, and S. Vega. *Recoupling of homo- and heteronuclear dipolar interactions in rotating solids*, volume 33. Sprienger, Berlin Heidelberg, first edition, **1994**.

[60] T. Nakai and C. A. McDowell. Calculation of rotational resonance NMR spectra using Floquet theory combined with perturbation treatment. *Mol. Phys.*, 88:1263–1275, **1996**.

[61] M.H. Levitt, D.P. Raleigh, F. Creuzet, and R.G. Griffin. Theory and simulations of homonuclear spin pair systems in rotating solids. *J. Chem. Phys.*, 92:6347–6364, **1990**.

[62] T. Nakai and C.A. McDowell. Application of Floquet theory to the nuclear-magnetic-resonance spectra of homonuclear 2-spin systems in rotating solids. *J. Chem. Phys.*, 96:3452–3466, **1992**.

[63] R.K. Harris, K.J. Packer, and A.M. Thayer. Slow magic-angle rotation ^{13}C NMR-studies of solid phosphonium iodides - the interplay of dipolar, shielding and indirect coupling tensors. *J. Magn. Reson.*, 62:284–297, **1985**.

[64] T. Nakai and C.A. McDowell. An analysis of NMR spinning side-band of homonuclear 2-spin systems using Floquet theory. *Mol. Phys.*, 77:569–584, **1992**.

[65] B. Brutscher. Principles and applications of cross-correlated relaxation in biomolecules. *Concepts Magn. Reson.*, 12:207–229, **2000**.

[66] A. Kumar, R.C.R. Grace, and P.K. Madhu. Cross-correlations in NMR. *Prog. Nucl. Magn. Reson. Spectrosc.*, 37:191–319, **2000**.

[67] C.J. Hartzell, P.C. Stein, T.J. Lynch, L.G. Werbelow, and W.L. Earl. Differential line broadening in the NMR-spectrum of methanol adsorbed on sol-gel silica. *J. Am. Chem. Soc.*, 111:5114–5119, **1989**.

[68] E. Oldfield, F. Adebodun, J. Chung, B. Montez, K.D. Park, H.B. Le, and B. Philips. ^{13}C nuclear-magnetic-resonance spectroscopy of lipids - differential line broadening due to cross-correlation effects as a probe of membrane-structure. *Biochemistry*, 30:11025–11028, **1991**.

[69] J. Chung, E. Oldfield, A. Thevand, and L. Werbelow. A magic-angle sample-spinning nuclear-magnetic-resonance spectroscopic study of interference effects in the nuclear-spin relaxation of polymers. *J. Magn. Reson.*, 100:69–81, **1992**.

[70] E. Oldfield, J. Chung, H.B. Le, T. Bowers, J. Patterson, and G.L. Turner. Differential line broadening in coupled ^{13}C magic-angle sample-spinning nuclear-magnetic-resonance spectra of solid polymers. *Macromolecules*, 25:3027–3030, **1992**.

[71] A. Pines, M.G. Gibby, and J.S. Waugh. Proton-enhanced NMR of dilute spins in solids. *J. Chem. Phys.*, 59:569–590, **1973**.

[72] S. Hediger, B.H. Meier, N.D. Kurur, G. Bodenhausen, and R.R. Ernst. NMR cross-polarization by Adiabatic Passage through the Hartmann-Hahn condition (APHH). *Chem. Phys. Lett.*, 223:283–288, **1994**.

[73] O.B. Peersen, X.L. Wu, and S.O. Smith. Enhancement of CPMAS signals by variable-amplitude cross-polarisation-compensation for inhomogeneous B_1 fields. *J. Magn. Reson. Ser. A*, 106:127–131, **1994**.

[74] A.E. Bennett, C.M. Rienstra, M. Auger, K.V. Lakshmi, and R.G. Griffin. Heteronuclear decoupling in rotating solids. *J. Chem. Phys.*, 103:6951–6958, **1995**.

[75] M.H. Levitt, T.G. Oas, and R.G. Griffin. Rotary resonance recoupling in heteronuclear spin pair systems. *Isr. J. Chem.*, 28:271–282, **1988**.

[76] T.G. Oas, R.G. Griffin, and M.H. Levitt. Rotary resonance recoupling of dipolar interactions in solid-state nuclear-magnetic-resonance spectroscopy. *J. Chem. Phys.*, 89:692–695, **1988**.

[77] K.W. Zilm and D.M. Grant. ^{13}C dipolar spectroscopy of small organic-molecules in argon matrices. *J. Am. Chem. Soc.*, 103:2913–2922, **1981**.

[78] P. Hodgkinson and L. Emsley. Numerical simulation of solid-state NMR experiments. *Prog. Nucl. Magn. Reson. Spectrosc.*, 36:201–239, **2000**.

[79] Matlab, The Mathworks, Inc. Natick, MA. http://www.mathworks.com/products/matlab/.

[80] M. Bak, R. Schults, T. Vosegaard, and C. Nielsen. Specification and visualisation of anisotropic interaction tensors in polypeptides and numerical simulations in biological solid-state. *J. Magn. Reson.*, 154:28–45, **2002**.

[81] A. Naito, S. Ganapathy, K. Akasaka, and C.A. McDowell. Chemical shielding tensor and ^{13}C - ^{14}N dipolar splitting in single-crystals of L-Alanine. *J. Chem. Phys.*, 74:3190–3197, **1981**.

[82] C.H. Ye, R.Q. Fu, J.Z. Hu, L. Hou, and S.W. Ding. ^{13}C chemical-shift anisotropies of solid amino-acids. *Magn. Reson. Chem.*, 31:699–704, **1993**.

[83] M.H. Levitt and M. Eden. Numerical simulation of periodic nuclear magnetic resonance problems: fast calculation of carousel averages. *Mol. Phys.*, 95:879–890, **1998**.

[84] M.H. Levitt. The sign of frequencies and phases in NMR. *J. Magn. Reson.*, 126:164–182, **1997**.

[85] H.J. Simpson and R.E. Marsh. Crystal structure of L-Alanine. *Acta Crystallogr.*, 20:550–555, **1966**.

[86] S.K. Zaremba. Good lattice points, discrepancy, and numerical integration. *Ann. Mat. Pura Appl.*, 73:293–317, **1966**.

[87] H. Conroy. Molecular Schrödinger equation VIII. A method for evaluation of multidimensional integrals. *J. Chem. Phys.*, 47:5307–5318, **1967**.

[88] V.B. Cheng, H.H. Suzukawa, and M. Wolsberg. Investigations of a nonrandom numerical-method for multidimensional integration. *J. Chem. Phys.*, 59:3992–3999, **1973**.

[89] M. Bak, J.T. Rasmussen, and N.C. Nielsen. SIMPSON: A general simulation program for solid-state NMR spectroscopy. *J. Magn. Reson.*, 147:296–330, **2000**.

[90] C. Filip, S. Hafner, I. Schnell, D.E. Demco, and H.W. Spiess. Solid-state nuclear magnetic resonance spectra of dipolar-coupled multi-spin systems under fast magic angle spinning. *J. Chem. Phys.*, 110:423–440, **1999**.

[91] M. Howhy, H. Bildsøe, H.J. Jakobsen, and N.C. Nielsen. Efficient spectral simulations in NMR of rotating solids. The γ-COMPUTE algorithm. *J. Magn. Reson.*, 136:6–14, **1999**.

[92] A. Lesage, M. Bardet, and L. Emsley. Through-bond carbon-carbon connectivities in disordered solids by NMR. *J. Am. Chem. Soc.*, 121:10987–10993, **1999**.

[93] N. Janes, S. Ganapathy, and E. Oldfield. ^{13}C chemical shielding tensors in L-Threonine. *J. Magn. Reson.*, 54:111–121, **1983**.

[94] D.P. Shoemaker, J. Donohue, V. Shomaker, and R.B. Corey. The crystal structure of L-Threonine. *J. Am. Chem. Soc.*, 72:2328–2349, **1950**.

[95] F. Ferrage, T.R. Eykyn, and G. Bodenhausen. Highly selective excitation in biomolecular NMR by frequency-switched single-transition cross-polarization. *J. Am. Chem. Soc.*, 124:2076–2077, **2002**.

[96] B. Reif, M. Henning, and C. Griesinger. Direct measurement of angless between bond vectors in high-resolution NMR. *Science*, 276:1230–1233, **1997**.

[97] T.I. Igumenova and A.E. McDermott. Improvement of resolution in solid state NMR spectra with *J*-decoupling: an analysis of lineshape contributions in uniformly ^{13}C-enriched amino acids and proteins. *J. Magn. Reson.*, 164:270–285, **2003**.

[98] T. Fäcke and S. Berger. Alpha/beta-ge-SELINCOR-TOCSY, a new method for the determination of H,C coupling constants. *J. Magn. Reson. Ser. A*, 119:260–263, **1996**.

[99] A. Meissner, J.Ø. Duus, and O.W. Sørensen. Integration of spin-state-selective excitation into 2D NMR correlation experiments with heteronuclear ZQ/2Q pi rotations for ^1J(XH)-resolved E.COSY-type measurements of heteronuclear coupling constants in proteins. *J. Biomol. NMR*, 10:89–94, **1997**.

[100] M.D. Sørensen, A. Meissner, and O.W. Sørensen. Spin-state-selective coherence transfer via intermediate states of two-spin coherence in IS spin systems: application to E.COSY-type measuremnt of *J* coupling constants. *J. Biomol. NMR*, 10:181–186, **1997**.

[101] F. Ferrage, T.R. Eykyn, and G. Bodenhausen. Coherence transfer by single-transition cross-polarization: Quantitation of cross-correlation effects in nuclear magnetic resonance. *J. Chem. Phys.*, 113:1081–1087, **2000**.

[102] T.R. Eykyn, F. Ferrage, E. Winterfors, and G. Bodenhausen. Single-transition coherence transfer by adiabatic cross polarization in nmr. *ChemPhysChem*, 1:217–221, **2000**.

[103] A. Bax, R. Freeman, and S.P. Kempsell. Natural abundance ^{13}C - ^{13}C coupling observed via double-quantum coherence. *J. Am. Chem. Soc.*, 102:4849–4851, **1981**.

[104] A. Bax, R. Freeman, T.A. Frenkiel, and M.H. Levitt. Assignment of ^{13}C NMR-spectra via double-quantum coherence. *J. Magn. Reson.*, 43:478–483, **1981**.

[105] A. Bax, R. Freeman, and T.A. Frenkiel. An NMR technique for tracing out the carbon skeleton of an organic-molecule. *J. Am. Chem. Soc.*, 103:2102–2104, **1981**.

[106] A. Lesage, C. Auger, S. Caldarelli, and L. Emsley. Determination of through-bond carbon-carbon connectivities in solid-state NMR using the INADEQUATE experiment. *J. Am. Chem. Soc.*, 119:7867–7868, **1997**.

[107] L. Emsley and G. Bodenhausen. Phase-shifts induced by transient Bloch-Siegert effects in NMR. *Chem. Phys. Lett.*, 168:297–303, **1990**.

[108] C. Bauer, R. Freeman, T. Frenkiel, J. Keeler, and A.J. Shaka. Gaussian pulses. *J. Magn. Reson.*, 58:442–457, **1984**.

[109] L. Emsley. Selective pulses. In *Encyclopedia of Nuclear Magnetic Resonance*, volume 7, pages 4228–4235. John Wiley and Sons, Chichester, First edition, **1996**.

[110] Bruker. http://www.bruker.de/.

[111] O.W. Sørensen, G.W. Eich, M.H. Levitt, G. Bodenhausen, and R.R. Ernst. Product operator-formalism for the description of NMR pulse experiments. *Prog. Nucl. Magn. Reson. Spectrosc.*, 16:163–192, **1983**.

[112] D. Sakellariou, S.P. Brown, A. Lesage, S. Hediger, M. Bardet, C.A. Meriles, A. Pines, and L. Emsley. High-resolution NMR spectra of disordered solids. *J. Am. Chem. Soc.*, 125:4376–4380, **2003**.

[113] G. De Paëpe, A. Lesage, and L. Emsley. The performance of phase modulated heteronuclear dipolar decoupling schemes in fast magic angle spinning NMR experiments. *J. Chem. Phys.*, 119:4833–4841, **2003**.

[114] S.P. Brown, M. Pérez-Torralba, D. Sanz, R.M. Claramunt, and L. Emsley. Determining hydrogen-bond strengths in the solid state by NMR. *Chem. Commun.*, pages 1852–1853, **2002**.

[115] B.A. Cowans and J.B. Grutzner. Examination of homogeneous broadening in solids via rotationally synchronised spin-echo NMR-spectroscopy. *J. Magn. Reson. Ser. A*, 105:10–18, **1993**.

[116] G. De Paëpe, N. Giraud, A. Lesage, P. Hodgkinson, A. Böckmann, and L. Emsley. Transverse dephasing optimized solid-state NMR spectroscopy. *J. Am. Chem. Soc.*, 125:13938–13939, **2003**.

[117] F. Bloch. Theory of line narrowing by double-frequency irradiation. *Phys. Rev.*, 111:841–853, **1958**.

[118] C. Griesinger, O.W. Sørensen, and R.R. Ernst. Two-dimensional correlation of connected NMR transitions. *J. Am. Chem. Soc.*, 107:6394–6395, **1985**.

[119] C. Griesinger, O.W. Sørensen, and R.R. Ernst. Correlation of connected transitions by two-dimensional NMR spectroscopy. *J. Chem. Phys.*, 85:6837–6852, **1986**.

[120] C. Griesinger, O.W. Sørensen, and R.R. Ernst. Aspects of the E.COSY technique. Measurement of scalar spin-spin coupling constants in peptides. *J. Magn. Reson.*, 75:474–492, **1987**.

[121] M. Sattler, J. Schleucher, O. Schedletzky, S.J. Glaser, C. Griesinger, N.C. Nielsen, and O.W. Sørensen. $\alpha\&\beta$ HSQC, an HSQC-type experiment with improved resolution for I_2S groups. *J. Magn. Reson. Ser. A*, 119:171–179, **1996**.

[122] T.A. Early, B.K. John, and L.F. Johnson. Observation of homonuclear double-quantum correlations in plastic crystals using cross polarisation and magic-angle spinning. *J. Magn. Reson.*, 75:134–138, **1987**.

[123] R. Benn, H. Grondey, and L.F. Johnson. The detection of connectivities of rare spin-1/2 nuclei in the solid-state using natural abundance samples - ^{13}C and ^{29}Si INADEQUATE and COSY type experiments. *Chem. Commun.*, pages 102–103, **1988**.

[124] C.A. Fyfe, Y. Feng, H. Gies, H. Grondey, and G.T. Kokotailo. Natural-abundance 2-dimensional solid-state ^{29}Si NMR investigation of the 3-dimensional bonding connectivities in the zeolite catalyst ZSM-5. *J. Am. Chem. Soc.*, 112:3264–3270, **1990**.

[125] C.A. Fyfe, H. Grondey, Y. Feng, and G.T. Kokotailo. Natural-abundance 2-dimensional Si-29 MAS NMR investigation of the 3-dimensional bonding connectivities in the zeolite catalyst ZSM-5. *J. Am. Chem. Soc.*, 112:8812–8820, **1990**.

[126] S.C. Christiansen, D.Y. Zhao, M.T. Janicke, C.C. Landry, G.D. Stucky, and B.F. Chmelka. Molecularly ordered inorganic frameworks in layered silicate surfactant mesophases. *J. Am. Chem. Soc.*, 123:4519–4529, **2001**.

[127] G. Grasso, T.M. De Swiet, and J.J. Titman. Electronic structure of the polymer phase of CsC_{60}: Refocused INADEQUATE experiments. *J. Pys. Chem. B*, 106:8676–8680, **2002**.

[128] F. Fayon, G. Le Saout, L. Emsley, and D. Massiot. Through-bond phosphorus-phosphorus connectivities in crystalline and disordered phosphates by solid-state NMR. *Chem. Commun.*, pages 1702–1703, **2002**.

[129] F. Fayon, I.J. King, R.K. Haris, R.K.B. Gover, J.S.O. Evans, and D. Massiot. Characterisation of the room-temperature structure of SnP_2O_7 by ^{31}P through-space and through-bond NMR correlation spectroscopy. *Chem. Mat.*, 15:2234–2239, **2003**.

[130] N.C. Nielsen, H. Thøgersen, and O.W. Sørensen. A systematic strategy for design of optimum coherent experiments applied to effcient interconversion of double- and single-quantum coherences in nuclear magnetic resonance. *J. Chem. Phys.*, 105:3962–3968, **1996**.

[131] A. Meissner and O.W. Sørensen. Exercise in modern NMR pulse sequence design: INADEQUATE CR. *Concepts Magn. Reson.*, 14:141–154, **2002**.

[132] M.H. Levitt. Composite pulses. In *Encyclopedia of Nuclear Magnetic Resonance*, volume 2, pages 1396–1410. John Wiley and Sons, Chichester, First edition, **1996**.

[133] M.H. Levitt. Composite pulses. *Prog. Nucl. Magn. Reson. Spectrosc.*, 18:61–122, **1986**.

[134] F. Ferrage, T.R. Eykyn, and G. Bodenhausen. Frequency-switched single-transition cross-polarization: a tool for selective experiments in biomolecular NMR. *ChemPhysChem*, 5:76–84, **2004**.

[135] M. Baldus, M. Tomaselli, B.H. Meier, and R.R. Ernst. Broadband polarisation transfer experiments for rotating solids. *Chem. Phys. Lett.*, 230:329–336, **1994**.

[136] M. Baldus and B.H. Meier. Broadband polarisation transfer under magic-angle spinning: application to total through-space-correlation nmr spectroscopy. *J. Magn. Reson.*, 128:172–193, **1997**.

[137] B.H. Meier. Polarization transfer and spin diffusion in solid-state NMR. In *Andvances in Magnetic and Optical Resonance*, volume 18, pages 1–116. Academic Press, Berlin, First edition, **1994**.

[138] R. Verel, M. Baldus, M. Nijman, J.W.M. van Os, and B.H. Meier. Adiabatic homonuclear polarisation transfer in magic-angle-spinning solid-state nmr. *Chem. Phys. Lett.*, 280:31–39, **1997**.

[139] N.C. Nielsen, H. Bildsoe, H.J. Jakobsen, and M. H. Levitt. Double-quantum homonuclear rotary resonance - efficient dipolar recovery in magic-angle-spinning nuclear-magnetic-resonance. *J. Chem. Phys.*, 101:1805–1812, **1994**.

[140] A. Bax, A.F. Mehlkopf, and J. Smidt. Homonuclear broadband–decoupled absorption–spectra, with linewidths which are independent of the transverse relaxation rate. *J. Magn. Reson.*, 35:167–169, **1979**.

[141] M. Ernst, A. Detken, A. Böckmann, and B.H. Meier. Nmr spectra of microcrystalline protein at 30 kHz MAS. *J. Am. Chem. Soc.*, 125:15807–15809, **2003**.

[142] H. Geen and R. Freeman. Band-selective radiofrequency pulses. *J. Magn. Reson.*, 93:93–141, **1991**.

[143] E. Kupçe and R. Freeman. Adiabatic pulses for wide-band inversion and broad-band decoupling. *J. Magn. Reson. Ser. A*, 115:273–276, **1995**.

[144] Lyndon Emsley. *Shaped selective pulses and their applications in Nuclear Magnetic Resonance spectroscopy and imaging*. PhD thesis, University of Lausanne - Faculty of Science, Switzerland, **1991**.

[145] L. Emsley and G. Bodenhausen. Optimization of shaped selective pulses for NMR using a quaternion description of their overall propagators. *J. Magn. Reson.*, 97:135–148, **1992**.

[146] M. Salzmann, K. Pervushin, G. Wider, H. Senn, and K. Wüthrich. TROSY in triple-resonance experiments: New perspectives for sequential NMR assignment of large proteins. *Proc. Natl. Acad. Sci. U. S. A.*, 95:13585–13590, **1998**.

[147] M. Salzmann, G. Wider, K. Pervushin, H. Senn, and K. Wüthrich. TROSY-type triple-resonance experiments for sequential NMR assignments of large proteins. *J. Am. Chem. Soc.*, 121:844–848, **1999**.

[148] R. Riek, G. Wider, K. Pervushin, and K. Wüthrich. Polarisation transfer by cross-correlated relaxation in solution NMR with very large molecules. *Proc. Natl. Acad. Sci. U. S. A.*, 96:4918–4923, **1999**.

[149] R. Riek, J. Fiaux, E.B. Bertelsen, A.L. Horwich, and K. Wüthrich. Solution NMR techniques for large molecular and supramolecular structures. *J. Am. Chem. Soc.*, 124:12144–12153, **2002**.

[150] K. Pervushin. Impact of transverse relaxation optimised spectroscopy (TROSY) on NMR as a technique in structural biology. *Q. Rev. of Biophys.*, 33:161–197, **2000**.

[151] C. Fernandez and G. Wider. TROSY in NMR studies of the structure and function of large biological macromolecules. *Curr. Opin. Struct. Biol.*, 13:570–580, **2003**.

[152] M. Ikura, L.E. Kay, and A. Bax. A novel-approach for sequential assignment of ^{1}H, ^{13}C, and ^{15}N spectra of large proteins - heteronuclear triple-resonance 3-dimensional NMR spectroscopy - application to oncomodulin. *Biochemistry*, 29:4659–4667, **1990**.

[153] L.E. Kay, M. Ikura, R. Tschudin, and A. Bax. 3-dimensional triple-resonance NMR-spectroscopy of isotopically enriched proteins. *J. Magn. Reson.*, 89:496–514, **1990**.

[154] S.J. Archer, M. Ikura, D.A. Torchia, and A. Bax. An alternative 3D-NMR technique for correlating backbone ^{15}N with side-chain H$^\beta$-resonances in large proteins. *J. Magn. Reson.*, 95:636–641, **1991**.

[155] L.E. Kay, M. Ikura, and A. Bax. The design and optimisation of complex NMR experiments. Application to a triple-resonance scheme correlating H$^\alpha$, N^H, and ^{15}N chemical-shifts in ^{15}N - ^{13}C-labelled proteins. *J. Magn. Reson.*, 91:84–92, **1991**.

[156] D. Marion, M. Ikura, R. Tschudin, and A. Bax. Rapid recording of 2d NMR spectra without phase cycling - application to the study of hydrogen-exchange in proteins. *J. Magn. Reson.*, 85:393–399, **1989**.

[157] S. Grzesiek and A. Bax. Correlating backbone amide and side-chain resonances in larger proteins by multiple relayed triple resonance NMR. *J. Am. Chem. Soc.*, 114:6291–6293, **1992**.

[158] W. Bermel, I. Bertini, I.C. Felli, R. Pierattelli, and R. Kümmerle. ^{13}C direct detection experiments on the paramagnetic oxidised monomeric copper, zinc superoxide dismutase. *J. Am. Chem. Soc.*, 125:16423–16429, **2003**.

[159] J. Jeener. Ampère International Summer School. Basko Polje, Yugoslavia, **1971**.

[160] W.P. Aue, E. Bartholdi, and R.R Ernst. 2-dimensional spectroscopy - application to nuclear magnetic resonance. *J. Chem. Phys.*, 64:2229–2249, **1976**.

[161] G. Wider. Technical aspects of NMR spectroscopy with biological macromolecules and studies of hydration in solution. *Prog. Nucl. Magn. Reson. Spectrosc.*, 32:193–275, **1998**.

[162] J.C. Hoch and A.S. Stern. Maximum entropy reconstruction. In *Encyclopedia of Nuclear Magnetic Resonance*, volume 5, pages 2980–2988. John Wiley and Sons, Chichester, first edition, **1996**.

[163] J.C. Hoch and A.S. Stern. Maximum entropy reconstruction, spectrum analysis and deconvolution in multidimensional nuclear magnetic resonance. *Method. Emzymol.*, 338:159–178, **2001**.

[164] J.M. Böhlen and G. Bodenhausen. Experimental aspects of Chirp NMR spectroscopy. *J. Magn. Reson. Ser. A*, 102:293–301, **1993**.

[165] T. Fujiwara and K. Nagayama. Composite inversion pulses with frequency switching and their application to broadband decoupling. *J. Magn. Reson.*, 77:53–6, **1988**.

[166] R. Tycko, A. Pines, and J. Guckenheimer. Fixed-point theory of iterative schemes in NMR. *J. Chem. Phys.*, 83:2775–2802, **1985**.

[167] A.J. Shaka, J. Keeler, T. Frenkiel, and R. Freeman. An improved sequence for broadband decoupling sequence: WALTZ-16. *J. Magn. Reson.*, 52:335–338, **1983**.

[168] A.J. Shaka, J. Keeler, and R. Freeman. Evaluation of a new broadband decoupling sequence - WALTZ-16. *J. Magn. Reson.*, 53:313–340, **1983**.

[169] A.J. Shaka, P.B. Barker, and R. Freeman. Computer-optimized decoupling scheme for wideband applications and low-level operation. *J. Magn. Reson.*, 64:547–552, **1985**.

[170] L.E. Kay, P. Keifer, and T. Saarinen. Pure absorption gradient enhanced heteronuclear single quantum correlation spectroscopy with improved sensitivity. *J. Am. Chem. Soc.*, 114:10663–10665, **1992**.

[171] Bertini *et al.* unpublished results, **2004**.

[172] M. Ottiger, F. Delaglio, and A. Bax. Measurement of *J* and dipolar couplings from simplified two-dimensional NMR spectra. *J. Magn. Reson.*, 131:373–378, **1998**.

[173] F. Delaglio, S. Grzesiek, G. Vuister, G. Zhu, J. Pfeifer, and A. Bax. NMRPIPE - a multidimensional spectral processing system based on UNIX pipes. *J. Biomol. NMR*, 6:277–293, **1995**.

[174] Rowland NMR Toolkit. http://www.rowland.org/rnmrtk/toolkit.html.

[175] C. Bartels, T.H. Xia, M. Billeter, P. Güntert, and K. Wüthrich. The program XEASY for computer-suppprted NMR spectral analysis of biological macromolecules. *J. Biomol. NMR*, 6:1–10, **1995**.

[176] F. Arnesano, L. Banci, I. Bertini, I.C. Felli, C. Luchinat, and A.R. Tompsett. A strategy for the NMR characterization of type II copper(II) proteins: the case o f the copper trafficking protein CopC from pseudomonas syringae. *J. Am. Chem. Soc.*, 125:7200–7208, **2003**.

[177] S. Grzesiek and A. Bax. Measurement of amide proton-exchange rates and NOEs with water in ^{13}C/^{15}N-enriched calcineurin-B. *J. Biomol. NMR*, 3:627–638, **1993**.

[178] D.S. Wishart and B.D. Sykes. The ^{13}C chemical-shift index - A simple method for the identification of protein secondary structure using ^{13}C chemical-shift data. *J. Biomol. NMR*, 4:171–180, **1994**.

[179] S.P. Brown, M. Pérez-Torralba, D. Sanz, R.M. Claramunt, and L. Emsley. The direct detection of a hydrogen bond in the solid state by NMR through the observation of a hydrogen-bond mediated ^{15}N - ^{15}N J coupling. *J. Am. Chem. Soc.*, 124:1152–1153, **2002**.

[180] L.J. Mueller, D.W. Elliott, K.C. Kim C.A. Reed, and P.D.W. Boyd. Establishing through-bond connectivity in solids with NMR: structure and dynamics in HC60+. *J. Am. Chem. Soc.*, 124:9360–9361, **2002**.

[181] M. Bechmann, X. Helluy, C. Marichal, and A. Sebald. Double-quantum filtered MAS NMR in the presence of chemical shielding anisotropies and direct dipolar and J couplings. *Solid State Nucl. Magn. Reson.*, 21:71–85, **2002**.

[182] R.A. Olsen, J. Struppe, D.W. Elliott, and R.J. Thomas. Through-bond C-13-C-13 correlation at the natural abundance level: refining dynamic regions in the crystal structure of vitamin-D-3 with solid-state NMR. *J. Am. Chem. Soc.*, 125:11784–11785, **2003**.

[183] T. Allman. The observation of two-dimensional NMR-spectra of crystalline solids - the ^{31}P CPMAS COSY and J-resolved spectra of a phosphine complex Hg(II). *J. Magn. Reson.*, 83:637–642, **1989**.

[184] A. Kubo and C.A. McDowell. One-dimensional and two-dimensional ^{31}P cross-polarisation magic-angle-spinning nuclear-magnetic-resonance studies on 2-spin systems with homonuclear dipolar coupling and J coupling. *J. Chem. Phys.*, 92:7156–7170, **1990**.

[185] R. Challoner, T. Nakai, and C.A. McDowell. J-coupling in chemically equivalent spin pairs as studied by solid-state nuclear-magnetic-resonance. *J. Chem. Phys.*, 94:7038–7045, **1991**.

[186] G. Wu and R.E. Wasylishen. Homonuclear ^{31}P J-resolved 2D spectra of rhodium(I) phosphine complexes in solid-sate. *Inorg. Chem.*, 31:145–148, **1992**.

[187] G. Wu and R.E. Wasylishen. Applications of 2-dimensional ^{31}P CPMAS NMR techniques for studying metal phosphine complexes in solid-state. *Organometallics*, 11:3242–3248, **1992**.

[188] K. Eichele, G. Wu, and R.E. Wasylishen. Unusual AB spectra in high-resolution magic-angle-spinning NMR-studies of solids. *J. Magn. Reson. Ser. A*, 101:157–161, **1993**.

[189] G. Wu and R.E. Wasylishen. J-recoupling patterns arising from 2 chemically equivalent nuclear spins in magic-angle spinning spectra of solids. *J. Chem. Phys.*, 98:6138–6149, **1993**.

[190] G. Wu and R.E. Wasylishen. Direct determination of J coupling between 2 crystallographically equivalent spins from 2-dimensional J-resolved nuclear-magnetic-resonance spectra under variable-angle-spinning conditions. *J. Chem. Phys.*, 100:5546–5549, **1994**.

[191] C.W. Liu, H.J. Pan, J.P. Fackler, G. Wu, and R.E. Wasylishen. Studies of [AG(PPH(3))(2)]NO3, [AG(P(CH2CH2CN)(3))(2)]NO3 and [AG(P(C(6)H(4)ME-M)(3))(2)]NO3 by X-ray-diffraction and solid-state nucmear-magnetic-resonance. *J. Chem. Soc., Dalton Trans.*, pages 3691–3697, **1995**.

[192] G. Wu and R.E. Wasylishen. Measurement of indirect spin-spin coupling-constants between crystallographically equivalent nuclei - determination of (2)J(P-31, P-31) in solid AG[P(M-TOLYL)(3)]2NO3. *Magn. Reson. Chem.*, 33:734–738, **1995**.

[193] G. Wu and R.E. Wasylishen. Observation of ^{31}P - ^{31}P indirect spin-spin coupling in copper-bis(phosphine) complexes by two-dimensional solid-state NMR. *Inorg. Chem.*, 35:3113–3116, **1996**.

[194] C.A. Fyfe, K.C. Wong-Moon, Y. Huang, and H. Grondey. INEPT experiments in solid-state NMR. *J. Am. Chem. Soc.*, 117:10397–10398, **1995**.

[195] H.M. Kao and C.P. Gray. Determination of the ^{31}P - ^{27}Al J-coupling constant for trimethylphosphine bound to the Lewis acid site of zeolite HY. *J. Am. Chem. Soc.*, 119:627–628, **1997**.

[196] B. Alonso and C. Sanchez. Structural investigation of polydimethylsiloxane-vanadate hybrid materials. *J. Mater. Chem.*, 10:377–386, **2000**.

[197] A. Lesage, P. Charmont, S. Steuernegal, and L. Emsley. Complete resonance assignment of a natural abundance solid peptide by through-bond heteronuclear correlation solid-state NMR. *J. Am. Chem. Soc.*, 122:9739–9744, **2000**.

[198] A. Lesage and L. Emsley. Through-bond heteronuclear single-quantum correlation spectroscopy in solid-state NMR, and comparison to other through-bond and through-space experiments. *J. Magn. Reson.*, 148:449–454, **2001**.

[199] S. Hediger, A. Lesage, and L. Emsley. A new NMR method for the study of local mobility in solids and application to hydration of biopolymers in plant cell walls. *Macromolecules*, 35:5078–5084, **2002**.

[200] A. Lesage, L. Emsley, M. Chabanas, C. Copéret, and J.-M. Basset. Observation of a H-agostic bond in a highly active rhenium-alkylidene olefin metathesis heterogeneous catalyst by two-dimensional solid-state NMR spectroscopy. *Angew. Chem. Int. Ed.*, 4:4535–4538, **2002**.

[201] B. Alonso and D. Massiot. Multi-scale NMR characterisation of mesostructured materials using H-1 -¿ C-13 through-bond polarisation transfer, fast MAS, and H-1 spin diffusion. *J. Magn. Reson.*, 163:347–352, **2003**.

[202] A. Lesage, D. Sakellariou, S. Hediger, B. Elena, P. Charmont, S. Steuernagel, and L. Emsley. Experimental aspects of proton NMR spectroscopy in solids using phase-modulated homonuclear dipolar decoupling. *J. Magn. Reson.*, 163:105–113, **2003**.

[203] D. Massiot, F. Fayon, B. Allonso, J. Trebosc, and J.P. Amoureux. Chemical bonding differences evidenced from J-coupling in solid state NMR experiments involving quadrupolar nuclei. *J. Magn. Reson.*, 164:160–164, **2003**.

[204] M. Baldus and B.H. Meier. Total correlation spectroscopy in the solid state. The use of scalar couplings to determine the through-bond connectivity. *J. Magn. Reson. Ser. A*, 121:65–69, **1996**.

[205] M. Baldus, R.J. Iuliucci, and B.H. Meier. Probing through-bond connectivities and through-space distances in solids by magic-angle-spinning nuclear magnetic resonance. *J. Am. Chem. Soc.*, 119:1121–1124, **1997**.

[206] S. Dusold, J. Kummerlen, and A. Sebald. A P-31 NMR study of solid compounds MxP2O7. *J. Chem. Phys. A*, 101:5895–5900, **1997**.

[207] R.J. Iuliucci and B.H. Meier. Carbon-13 chemical shift tensors in polycyclic aromatic compounds. 7.[1] Symmetry augmented chemical shift chemical shift correlation spectroscopy and single crystal study of triphenylene. *J. Am. Chem. Soc.*, 120:9059–9062, **1998**.

[208] X. Helluy, C. Marichal, and A. Sebald. Through-bond indirect and through-space direct dipolar coupling P-31 MAS NMR constraints for spectral assignment in the cubic 3 x 3 x 3 superstructure of Ti2O7. *J. Chem. Phys. B*, 104:2836–2845, **2000**.

[209] A.S.D. Heindrichs, H. Geen, C. Giordani, and J.J. Titman. Improved scalar shift correlation NMR spectroscopy in solids. *Chem. Phys. Lett.*, 335:104–112, **2001**.

[210] J.C.C. Chan and G. Brunklaus. R sequences for the scalar-coupling mediated homonuclear correlation spectroscopy under fast magic-angle spinning. *Chem. Phys. Lett.*, 349:104–112, **2001**.

[211] A. Detken, A.H. Hardy, M. Ernst, M. Kainosho, T. Kawakami, S. Aimoto, and B.H. Meier. Methods for sequential resonance assignment in solid, uniformly C-13, N-15 labelled peptides: Quantification and application to antamanide. *J. Biomol. NMR*, 20:203–221, **2001**.

[212] E.H. Hardy, R. Verel, and B.H. Meier. Fast MAS total through-bond correlation spectroscopy. *J. Magn. Reson.*, 148:459–464, **2001**.

[213] E.H. Hardy, A. Detken, and B.H. Meier. Fast-MAS total through-bond correlation spectroscopy using adiabatic pulses. *J. Magn. Reson.*, 165:208–218, **2003**.

[214] S. Hayashi and K. Hayamizu. Spinning-rate-dependent line-shape in P-31 magic-angle spinning NMR-spectra of inorganic phosphates. *Chem. Phys. Lett.*, 161:158–162, **1989**.

[215] R. Challoner, T. Nakai, and C.A. McDowell. Anisotropy of J in homonuclear spin-pair systems in rotating solids. *J. Magn. Reson.*, 94:433–438, **1991**.

[216] W.P. Power and R.E. Wasylishen. Anisotropies of the P-31 chemical-shift and P-31-Pt-195 indirect spin spin coupling in plitunum(II) phosphines. *Inorg. Chem.*, 31:2176–2183, **1992**.

[217] E. Lindner, R. Fawzi, H.A. Mayer, K. Eichele, and W. Hiller. Effect of ring size on NMR parameters - cyclic bisphosphine complexes of molybdenum, tungsten, and platinum - bond angle dependence of metal shieldings, metal phosphorous coupling-constants, and the P-31 chemical-shift anisotropy in the solid-state. *Organometallics*, 11:1033–1043, **1992**.

[218] G. Wu and R.E. Wasylishen. NMR lineshapes arising from a pair of nonequivalent homonuclear spins in magic-angle-spinning experiments. *J. Magn. Reson. Ser. A*, 102:183–189, **1993**.

[219] E. Klaus and A. Sebald. P-31 CP/MAS NMR-spectroscopy of transition-etal phosphane complexes - J-recoupling between chemically equivalent P-31 nuclei in polycrystalline compounds of the type trans-[(PR(3))(2)MX(2)], M = PD, PT. *Angew. Chem. Int. Ed.*, 34:667–669, **1995**.

[220] S. Dusold, E. Klaus, A. Sebald, M. Bak, and N.C. Nielsen. Magnitudes and relative orientations of chemical shielding, dipolar and J coupling tensors for isolated P-31-P-31 spin pairs determined by iterative fitting of P-31 MAS NMR spectra. *J. Am. Chem. Soc.*, 119:7121–7129, **1997**.

[221] E. Kundla and E. Lippmaa. Field-dependence of the magic-angle-spinning nuclear-magnetic-resonance line-shapes of paired spin-1/2 nuclei in solids. *J. Chem. Phys.*, 102:1569–1578, **1995**.

[222] D. Kuwahara, T. Nakai, J. Ashida, and S. Miyajima. Novel satellites in a two-dimensional spin-echo NMR experiment for homonuclear dipole-coupled spins in rotating solids. *Chem. Phys. Lett.*, 305:35–38, **1999**.

[223] D. Kuwahara, T. Nakai, J. Ashida, and S. Miyajima. Real figure of two-dimensional spin-echo NMR spectra for a homonuclear two-spin system in rotating solids. *Mol. Phys.*, 99:939–956, **2001**.

[224] U. Haeberlen and J.S. Waugh. Coherent averaging effects in magnetic resonance. *Phys. Rev.*, 175:453–467, **1968**.

[225] S. Dusold, W. Milius, and A. Sebald. Iterative lineshape fitting of MAS NMR spectra: A tool to investigate homonuclear J coupling in isolated spin pairs. *J. Magn. Reson.*, 135:500–513, **1998**.

[226] M. Helmle, Y.K. Lee, P.J.E. Verdegem, X. Feng, T. Karlsson, J. Lugtenburg, H.J.M. de Groot, and M.H. Levitt. Anomalous rotational resonance spectra in magic-angle spinning NMR. *J. Magn. Reson.*, 140:379–403, **1999**.

[227] E.T. Olejniczak, S. Vega, and R.G. Griffin. Multiple pulse NMR in rotating solids. *J. Chem. Phys.*, 81:4804–4817, **1984**.

[228] A.C. Kolbert, D.P. Raleigh, M.H. Levitt, and R.G. Griffin. Two-dimensional spin-echo nuclear magnetic-resonance in rotating solids. *J. Chem. Phys.*, 90:679–689, **1989**.

[229] A. Wokaun and R.R. Ernst. Selective excitation and detection in multilevel spin systems - application of single transition operators. *J. Chem. Phys.*, 67:1752–1758, **1977**.

[230] S. Vega. Fictitious spin 1-2 operator formalism for multiple quantum NMR. *J. Chem. Phys.*, 68:5518–5527, **1978**.

[231] E.R. Andrew, A. Bradbury, R.G. Eades, and V.T. Wynn. Nuclear cross-relaxation induced specimen rotation. *Phys. Lett.*, 4:99–100, **1963**.

[232] E.R. Andrew, S. Clough, L.F. Farnell, T.D. Gledhill, and I. Roberts. Resonant rotational broadening of nuclear magnetic resonance spectra. *Phys. Lett.*, 21:505–505, **1966**.

[233] B.H. Meier and W.L. Earl. A double-quantum filter for rotating solids. *J. Am. Chem. Soc.*, 109:7937–7942, **1987**.

[234] S. Dusold, M. Maisel, and A. Sebald. Magnitudes and orientations of interaction tensors determined from rotational resonance MAS NMR lineshapes of a four-C-13-spin system. *J. Magn. Reson.*, 141:78–90, **1999**.

[235] P.R. Costa, B. Sun, and R.G. Griffin. Rotational resonance NMR: separation of dipolar coupling and zero quantum relaxation. *J. Magn. Reson.*, 164:92–103, **2003**.

[236] U. Haeberlen. *High Resolution NMR in Solids. Selective Averaging.* Academic Press, New York, First edition, **1976**.

[237] M. Carravetta, M. Edén, O.G. Johannessen, H. Luthman, P.J.E. Verdegem, J. Lugtenburg, A. Sebald, and M.H. Levitt. Estimation of carbon-carbon bond lengths and medium-range internuclear: Distances by solid-state nuclear magnetic resonance. *J. Am. Chem. Soc.*, 123:10628–10638, **2001**.

[238] H. Hosomi, Y. Ito, and S. Ohba. Ammonium and isopropylammonium salts of the fumaric acid dianion. *Acta Crystallogr.*, pages 142–145, **1998**.

[239] L. Golic and I. Leban. The crystal-structure of ammonium hydrogen maleate. *Croat. Chem. Acta*, 55:41–45, **1982**.

[240] G. Metz, X. Wu, and S.O. Smith. Ramped-amplitude cross-polarisation in magic-angle-spinning NMR. *J. Magn. Reson. Ser. A*, 110:219–227, **1994**.

[241] T. Bräuniger, P. Wormald, and P. Hodgkinson. Improved proton decoupling in NMR spectroscopy of crystalline solids using the SPINAL-64 sequence. *Monatsh. Chem.*, 133:1549–1554, **2002**.

[242] L.B. Krivdin and G.A. Kalabin. Structural applications of one-bond carbon-carbon spin-spin coupling constants. *Prog. Nucl. Magn. Reson. Spectrosc.*, 21:293–448, **1989**.

[243] D.K. Sodickson, M.H. Levitt, S. Vega, and R.G. Griffin. Broad-band dipolar recoupling in the nuclear-magnetic-resonance of rotating solids. *J. Chem. Phys.*, 98:6742–6748, **1993**.

[244] A. Brinkmann, J. Schmedt auf der G¨unne, and M.H. Levitt. Homonuclear zero-quantum recoupling in fast magic-angle spinning nuclear magnetic resonance. *J. Magn. Reson.*, 56:79–96, **2002**.

Abbreviations

AHT	Average Hamiltonian Theory
Asn	ʟ-Asparagine
Asp	ʟ-Aspartic Acid
CP	Cross Polarisation
CPMAS	Cross Polarisation Magic-Angle Spinning
Crh	Catabolite repression histidine
CR	Composite Refocusing
CSA	Chemical Shift Anisotropy
CW	Continuous Wave
DD	Dipole-Dipole
DIPSAP	Double In Phase Single Anti Phase
DREAM	Dipolar Recoupling Enhanced by Amplitude modulation
DQC	Double Quantum
DQC	Double-Quantum Coherence
eDROOPY	Experimental Decoupling is Robust for Offset Or Power inhomogeneitY
FID	Free Induction Decay
FT	Fourier Transformation
GARP	Globally Optimised Alternating Phase Rectangular Pulse
Gln	ʟ-Glutamine
Glu	ʟ-Glutamic Acid
Gly	Glycine
HHCP	Hartmann-Hahn Cross Polarisation
His	ʟ-Histidine
HMQC	Heteronuclear Multiple Quantum Coherence
HSQC	Heteronuclear Single Quantum Coherence
INADEQUATE	Incredible Natural Abundance Double Quantum Transfer Experiment
INEPT	Insensitive Nuclei Enhanced by Polarisation Transfer
IPAP	In Phase Anti Phase
MAS	Magic-Angle Spinning
Met	Methionine
MQ	Multiple Quantum
NMR	Nuclear Magnetic Resonance

PDSD	Proton-Driven Spin Diffusion
ppm	Parts per million
RAMP-CP	Ramped-Amplitude Cross Polarisation
RIL-ZQT	Rotating Inverse-Laboratory Zero Quantum Transfer
rf	Radio Frequency
SE	Spin Echo
Ser	L-Serine
SNR or S/N	Signal-to-noise ratio
SPINAL	Small Phase Incremental Alternation
SQC	Single-Quantum Coherence
TPPM	Two Pulse Phase Modulation
TXO	Triple-Resonance Observe
U	Uniformly
Val	L-Valine
WALTZ	Composite-pulse decoupling sequence containing the elements R $=(\beta)_0(2\beta)_\pi(3\beta)_0$, with $\beta \cong \pi/2$
z-filter	Pulse sandwich for elimination of signal components with dispersive phase

Symbols and constants

$\hat{\mathcal{H}}$	Hamiltonian Operator
$\lvert\alpha,\ \alpha\rangle,\cdots$	spin states for a two-spin 1/2 system
η	anisotropy parameter
$\gamma_I,\ \gamma_S$	gyromagnetic ratio of the I, respectively S spins
τ_r	MAS rotor period
τ_c	rotational correlation time

Name: Luminita Duma
Date of birth: 11th October 1976
Nationality: Romanian

Education:

➥ 1991-1995: "Gh. M. Murgoci" College, Chemistry-Physics Department, Braila, Romania. Graduated in 1995, mark 8.60 (out of 10).

➥ 1995-1998: University of Bucharest, Faculty of Physics, Romania. French courses of study.

➥ 1998-2001: Ecole Normale Supérieure, Science Materials Department, Lyon, France.

Degrees:

➥ 1999 - Licence de Physique at Ecole Normale Supérieure de Lyon (ENS-Lyon), France.

➥ 2000 - Maitrise de Physique at ENS-Lyon, France.

➥ 2001 - MSc of Nuclear Physics at Claude Bernard University, Lyon, France.
        (DEA de "Particules, Noyaux, Atomes et Photons")
        - Magistère de Physique at ENS-Lyon, France.

Present status:

Preparation of a Doctoral thesis in the group of Prof. L. Emsley, Chemistry Laboratory of ENS-Lyon, France

Articles :

➥ Luminita Duma, Sabine Hediger, Bernhard Brutscher, Anja Böckmann and Lyndon Emsley, In preparation.

➥ Ivano Bertini, Luminita Duma, Lyndon Emsley, Isabella C. Felli, Roberta Pierattelli and Paul R. Vasos, Protonless biomolecular NMR: the CBCACO experiment, Submitted.

➥ Luminita Duma, Wai Cheu Lai, Marina Carravetta, Lyndon Emsley, Steven P. Brown, Malcolm H. Levitt, Principles of spin-echo modulation by J-couplings in magic-angle-spinning solid-state NMR, *ChemPhysChem*, **5**, pp. 815-833 (2004).

➥ Ivano Bertini, Luminita Duma, Isabella C. Felli, Michael Fey, Claudio Luchinat, Roberta Pierattelli and Paul R. Vasos, A heteronuclear direct-detection NMR spectroscopy experiment for protein-backbone assignment, *Angewandte Chemie International Edition*, **43**, pp. 2257-2259 (2004).

➥ Luminita Duma, Sabine Hediger, Bernhard Brutscher, Anja B̈ockmann and Lyndon Emsley, Resolution Enhancement in Multidimensional Solid-State NMR Experiments of ^{13}C-Labeled Proteins Using Transition Selection, *Journal of the American Chemical Society*, **125**, pp. 11816-11817 (2003).

➥ Luminita Duma, Sabine Hediger, Anne Lesage, and Lyndon Emsley, Spin-State Selection in Solid-State NMR, *Journal of Magnetic Resonance*, **164**, pp. 187-195 (2003).

➥ Luminita Duma, Sabine Hediger, Anne Lesage, Dimitris Sakellariou, and Lyndon Emsley, Carbon-13 lineshapes in solid-state NMR of labeled compounds. Effects of coherent CSA-dipolar cross-correlation, *Journal of Magnetic Resonance*, **162**, pp. 90-101 (2003).

➥ Anne Lesage, Luminita Duma, Dimitris Sakellariou, and Lyndon Emsley, Improved resolution in proton NMR spectroscopy of powdered solids, *Journal of the American Chemical Society*, **123**, pp. 5747-5752 (2001).

Oral presentations and seminars:

➥ 2nd August 2004: "Resolution enhancement in multidimensional solid-state NMR of proteins using spin-state-selective techniques", NMR Symposium at the 46th Rocky Mountain Conference on Analytical Chemistry (August 1 - 5, 2004), University of North Carolina, United States - Polymers, Gels and Soft Materials Session.

➥ 19th September 2003: "Differential broadening and spin-state-selective experiments in solid-state NMR, Seminar at the Structural Biology Department, University of Basel, Switzerland.

➥ 10th September 2003: "Resolution enhancement in solid-state NMR of labeled biomolecules using spin-state selective techniques", Seminar at the CERM Laboratory, University of Florence, Italy.

➥ 30th June 2003: "Effects of coherent CSA-Dipolar cross-correlation on ^{13}C NMR of Labeled Compounds", 16th International Meeting on NMR Spectroscopy (29th June - 3rd July), University of Cambridge, UK - Postgraduate Session.

"Adieu, dit le renard. Voici mon secret.
Il est très simple : on ne voit bien qu'avec le cœur.
L'essentiel est invisible pour les yeux."

Antoine de Saint-Exupery, Le Petit Prince

Acknowledgments

Dear Reader, it is just the good time to present the awards of the *Mythanks*. The first award goes to you, Dear Reader, for taking some of your very precious time to read this manuscript.

The award *Mythanks* for the golden jury goes to Prof. Geoffrey Bodenhausen, Prof. Hartmut Oschkinat, Prof. Alain Milon, Dr. Iannick Crémillieux, and Prof. Lyndon Emsley. I am grateful to Prof. Bodenhausen at the Department of Chemistry, École Normale Supérieure of Paris, and Prof. Oschkinat at the Department of NMR - Supported Structural Biology, University of Berlin, for accepting the difficult task of referee for this thesis. I am also grateful to Prof. Milon at the Department of NMR and interactions between proteins and membranes, University of Toulouse, and Dr. Cré at the NMR Laboratory, University of Lyon, for accepting to participate in the jury of this thesis.

The award *Mythanks* goes now to all past and present members of the Chemistry Laboratory and particularly to the NMR group. Many thanks for the very stimulating atmosphere you created. I really enjoyed the time I spent in Lyon.

The award *Mythanks* goes also to Dr. Stefan Steuernagel. I thank Stefan for many useful hints on the spectrometer and on pulse sequence programming.

I would like to present the award *Mythanks* to Dr. Jay Baltisberger for the very stimulating discussions we had on various NMR subjects and computing problems.

The award *Mythanks* goes now to Prof. Ivano Bertini and all the members of the CERM laboratory. I thank Prof. Bertini for giving me the opportunity to work and to participate in the research activities of his group. I am grateful to all members of the group and particularly to Prof. Roberta Pierattelli, Dr. Isabella Felli, Prof. Claudio Luchinat and Dr. Paul Vasos. I would like to thank you-all for introducing me to the captivating world of solution NMR spectroscopy. I would like to thank Claudia, Francesca, Elisa, Adele, Gabriele, Karel, Simone, and Nicola for their friendship and warm support.

I would like to present the award *Mythanks* to Dr. Bernhard Brutscher. Many thanks for the remarquable insights into spin-state-selective techniques.

I would like to present the award *Mythanks* to Anne Galinier, Francois Penin and Anja Böckmann for providing us the Crh protein.

The award *Mythanks* for the golden J-coupling team: Prof. Malcolm Levitt, Prof. Lyndon Emsley, Dr. Steven Brown, Linda Lai, Dr. Marina Carravetta. I wish to express my warmest thanks to Malcolm for inspiring discussions on J-couplings and for the fruitful collaboration. Many thanks to Steven, Linda and Marina for their endless enthusiasm. I wish to thank Lyndon for encouraging me to work on this project.

A special award *Mythanks* for my office partners, Sylvian Cadars, Nicolas Giraud, Bénédicte Eléna and Dr. Gaël De Paëpe for the wonderful atmosphere they provided inside and outside the ENS. Many thanks to Sylvian for his patience and disponibility and for all the encouraging words during the difficult period of working on this manuscript. Last but not least, a warm award *Mythanks* goes to Dr. Patrick Charmont and Dr. Dimitris Sakellariou. Thank you Patrick for your humour and your almost contagious passion for nice and expensive cars. Thank you Dimitri for your very precious preliminary work on the carbon lineshapes' project.

A special award *Mythanks* goes now to Dr. Anne Lesage. I wish to thank Anne for her constant help on the spectrometer and many stimulating discussions.

A special award *Mythanks* for Prof. Lyndon Emsley. I wish to thank Lyndon for giving me the great opportunity to work in his group, for his endless encouragement and support.

I would like to present a special award *Mythanks* to Dr. Sabine Hediger. I thank Sabine for introducing me to the fascinating world of solid-state NMR spectroscopy, for her great enthusiasm and encouragement during all these years I spent in Lyon.

A special award *Mythanks* goes now to my dear friends and family. I express my greatest thanks to Mylène, Cécile, Ştefana, Stephanie, Tomasz, François, Ion, for their endless encouragement and friendship. Mylène, thanks for always being so optimistic and for inspiring the same optimism to the people around you. I express my sincere thanks to my parents for believing in my dreams and for supporting me all the time. Thank you Caroline, Élodie, Franck, Virginie, Tudor, Doru et Ioana.

So many have offered support, suggestions, criticisms, and very important feedback over the last two years. I remain grateful to you all.

I would like to present the award *Mythanks* to the French Research Ministry who supported this work and to the Marie Curie Fellowship Association who supported the trainning in the CERM laboratory.

Finally, a special award *Mythanks* to the unpredictable and amazing "partner" of work we use to have when dealing with NMR. My friends call "him" *Spectroman* and they are right, "he" deserves the award *Mythanks* for the best spectrometer.

Lyon, July, 2004   Luminita Duma

Last revised: Paris, October, 2006

List of Figures

List of Tables